Università degli studi di Modena e Reggio Emilia

**Dipartimento di Ingegneria "Enzo Ferrari" - DIEF**

# Multiscale phenomena in turbulent boundary layers

Gabriele Boga

Corso di Dottorato di Ricerca in Ingegneria Industriale e del Territorio
"Enzo Ferrari" - XXXVII Ciclo

Tesi di dottorato in Fluidodinamica

**Relatore:**
**Prof. Andrea Cimarelli**

**Coordinatore del Corso:**
**Prof. Alberto Muscio**

**Anno accademico 2023/2024**

*Ai miei genitori,*
*Rita e Riccardo*

# Abstract

Wall-turbulent flows are of great interest for both industrial and environmental applications. Their dynamics is governed by the combined role of inner and outer self-sustaining mechanisms involving different scale motions. The near-wall region is the site of a high rate of turbulent energy production, and its dynamics is governed by motions scaling in inner units. On the other hand, for high Reynolds numbers, the outer overlap layer is thought to become relevant, being the site of self-sustaining mechanisms of large flow structures following mixed inner/outer scaling. The complex interactions involved, which determine the overall momentum transfer, are not yet fully understood, and their understanding underpins the development of more reliable turbulence models and new control strategies. In wall-turbulent flows, the strong inhomogeneity and anisotropy imposed by the presence of the wall deeply modify the classical picture of turbulence. The near-wall region is in fact the site of a strong reverse energy transfer process in the wall-parallel directions, feeding long and wide scales that dissipate energy through sharp gradients in the wall-normal direction. A similar scenario, albeit more moderate in intensity, is observed in the Turbulent/Non-Turbulent Interface (TNTI) region. In the present work, we make use of both classical statistical tools and dynamic numerical experiments aimed at shedding light on the observed phenomena. The multiscale nature of the mechanisms involved requires the use of two-point formalisms such as the one provided by the second-order structure function. Furthermore, the rotational and dissipative nature of turbulence makes enstrophy an appealing observable, especially for the study of the TNTI region and of the vortex stretching mechanism that is connected to the energy cascade process. The main focus of the work is the assessment of the two-point energy and enstrophy budgets in a turbulent boundary layer, with particular attention on the near-wall and TNTI regions. Furthermore, a dynamical approach is also proposed in order to establish the role of the inner and outer cycles. This approach consists in using different scalar fields transported by modified velocity fields in which the inner and outer cycles are alternatively suppressed. Both the analysis and the numerical experiments are conducted on the flow setup of a tem-

porally evolving boundary layer via direct numerical simulations up to a friction Reynolds number of $Re_\tau = 1500$. This flow configuration, characterised by the presence of a wall and of a TNTI, exhibits spatial homogeneity in two directions (streamwise and spanwise), while retaining a qualitatively unaltered dynamics with respect to the one observed in the spatially evolving boundary layer.

# Table of Contents

## Guide for the Reader

The experienced reader may consider skipping some parts of the thesis concerning the theoretical background and introduction. For this reason, we report here on the location of the main results.

Section 2.3 shows the results obtained by applying the generalized Kolmogorov equation and the two-point enstrophy budget frameworks on direct numerical simulations of homogeneous isotropic turbulence. Chapter 3 describes the flow configuration and the simulation settings of the temporal boundary layer (on which most of the analyses contained in this thesis work are carried out). In this chapter, the main flow features are also described and some of the main topics concerning wall turbulence are briefly investigated. Chapters 4 and 5 contain the main novelty of the thesis work, addressing the generalised Kolmogorov equation and the two-point enstrophy budget formalisms on the temporal boundary layer (after the analysis of the corresponding single-point budgets). Finally, the dynamical experiments which try to establish the role of the inner and outer cycles in the temporal boundary layer are presented in appendix A.

# Chapter 1

# Introduction

The phenomenon of turbulence affects our daily lives, with its benefits and drawbacks. Thanks to its mixing nature, turbulence helps us in speeding up processes that would otherwise require a remarkably long time. Among these processes are the dilution and dispersion of contaminants, such as the pollution emitted by factories, exhaust pipes or ashes ascending from a volcanic plume, which, without the process of turbulent entrainment, would travel in concentrated harmful clouds, taking a huge time to dilute in the surrounding air. Analogously, turbulent entrainment is exploited in internal combustion engines, where fuel is mixed with fresh air at a rate that would not be achievable through laminar diffusion alone. At a more macroscopic scale, turbulence plays a fundamental role in the climatic balance of our planet's atmosphere and oceans and, further widening the picture, is even deeply connected with star formation and the dynamics of the interstellar medium in galaxies. Turbulence also gives us spectacular views, such as the wrinkled edges of clouds or the fine structures generated by the waves breaking as they approach the coast. Nevertheless, the phenomenon of turbulence also constitutes a problem for many applications. Just to name a few, it is sufficient to think that in many cases turbulence causes an increase in aerodynamic drag, it greatly increases the power required to move a fluid through a pipeline and its chaotic nature makes it extremely difficult to make predictions (such as weather forecasting) and to control a turbulent flow. But one of the most fascinating things about turbulence is that, despite the enormous effort spent on the subject, it is still an unsolved problem in physics.

The lack of a unifying theory, however, has not stopped engineers, physicists and mathematicians from producing knowledge, also based on empirical observations, deductions and heuristic arguments. The need to be able to estimate the drag coefficient of a car, the aerodynamic loads acting on a building or bridge, and to be able to make weather forecasts or to predict the effect of a certain change on the urban climate of a certain city, has prompted the development of feasible models. These include reduced-order models such as the LES and RANS approaches, in which the dynamic of

turbulence is partially or completely modelled. The discriminator of what is modelled and what is resolved in these models is based on dimension of the scale motions considered, with the RANS context being the extreme, where all the scales of a turbulent motion are modelled. The models used in these two contexts benefit from an understanding of the fundamental dynamics of turbulence at all its scales, which is primarily accessible through direct numerical simulations and experiments. In the former, the main limiting factor is the computational cost, while experiments present challenges in the set-up and suffer from limitations in measurement accuracy, but with the obvious advantage of dealing with real flows. The investigations carried out in this thesis work are completely performed by means of numerical simulations, as they allow a complete access to the velocity and pressure fields at every instant and in every region of the fluid domain. Another advantage of the numerical approach is the possibility of performing experiments in which the physics of the problem is modified, observing how the applied modifications (impossible to implement in a real experiment) affect the development of the flow studied. In other words, simulations allow one to play with the physics of the problem.

Many of the flows of engineering and environmental interest are characterized by the presence of a solid wall, which may be represented by the fuselage of an aircraft, the wall of a hydraulic duct or by the earth's surface for the atmospheric motions. This simple constraint can already pose a challenge for the reduced order models mentioned above, as the presence of a solid boundary profoundly changes the classical picture of turbulence. In fact, in the near-wall region it is possible to observe the injection of energy in small-scale fluctuating motions that is eventually transferred towards motions with larger characteristic scales. This phenomenon may pose a problem for LES models as it would require the modelling of a source of energy arising from unresolved scales. In addition to this complexity, the mode of energy dissipation itself is also changed by the presence of a solid wall. These challenges, together with its implications on practical applications, make wall turbulence a case of great interest.

Similarly, in many flows of interest for applications, it is common to encounter the coexistence of flow regions that are in a turbulent regime, with others that are non-turbulent. These two regions are separated by the Turbulent/Non-Turbulent Interface (TNTI), in the proximity of which it is possible to observe some confinement effects that, in some sense, resemble the dynamics observed in the presence of a solid wall.

The present thesis work mainly focuses on how some of the features of turbulence are modified in the presence of a solid wall and in the proximity of

a TNTI. In particular, the study is conducted by means of direct numerical simulations and numerical experiments on the flow configuration of the temporal boundary layer, characterised by the simultaneous presence of the wall and of the TNTI. Particular focus is placed on the multiscale phenomena at the basis of energy transfer and production, together with the scale-by-scale dynamics of enstrophy, that is linked to energy dissipation. These topics are addressed through the study of the generalized Kolmogorov equation and its equivalent two-point enstrophy budget. Finally, a dynamic approach is also proposed aimed at establishing the role of the different scales involved in the near-wall and outer cycles of wall turbulence.

The thesis is organized as follows. In chapter 2, the framework of the generalized Kolmogorov equation and of the two-point enstrophy budget are presented together with some basic notions regarding wall turbulence and the TNTI. In this chapter, we also present the results derived from the two-point energy and enstrophy budgets framework applied to direct numerical simulations of homogeneous and isotropic turbulence at different Reynolds numbers. This is intended to both facilitate the understanding of the phenomena described by starting with one of the most basic flow configurations and to set a reference before diving into the study of the a more complex flow configuration. In chapter 3, the temporal boundary layer is described, by presenting the flow settings used and by showing some of the main flow features commonly investigated in wall turbulence. In chapters 4 and 5 we address the main topics mentioned above on the flow configuration of the temporal boundary layer. In particular, chapter 4 is dedicated to the study of energy transfers and production mechanisms, with a focus on the confinement effects given by the wall and by the TNTI. Chapter 5 follows in the wake of the previous chapter, providing another view of the phenomena observed through the investigation of the enstrophy dynamics. Concluding remarks are given in chapter 6. Finally, numerical experiments aimed at understanding the role of inner and outer cycles in the temporal boundary layer are presented in appendix A, while appendix B contains an off-topic on High Performance Computing topics that I dealt with during the first part of my PhD, following my previous work.

# Chapter 2

# Theoretical framework

Since the seminal work of Kolmogorov (1941), no revolutionary steps have been made in the development of a universal theory of turbulence. Many of the theoretical results concern isotropic homogeneous turbulence, while a unique theory capable of explaining most of the phenomena occurring in every day flows is completely missing. This lack results in an advancement of the knowledge in this field that is sustained also by the study of individual cases of interest. Considerable effort has been certainly spent in investigating the canonical flows, which consist in relatively simple flow configurations that allow to grasp some essential features and concepts that are also applicable to more general cases. Among this family of flow configurations, it is possible to identify a group of cases of interest for the study of wall turbulence. The main flows investigated in this context are the channel flow, the pipe flow and the boundary layer. Among these three configurations the only one presenting a Turbulent/Non-Turbulent Interface (TNTI), across which the turbulent entrainment phenomenon occurs, is the boundary layer. This thesis work will mainly focus on this flow configuration, applying the framework of the Generalized Kolmogorov Equation (GKE) in order to try to shed light on the complex phenomena occurring in wall turbulence and near the TNTI region. This same framework will also be extended to enstrophy, which constitutes a more appropriate observable for the study of the TNTI and which can provide additional information regarding the constrained dynamics in the wall- and interface-normal direction.

In the present chapter we give some brief notions useful for the comprehension of the thesis work presented. In section 2.1, we briefly recall some basic concepts of turbulence in Richardson's and Kolmogorov's perspective, derive the GKE and show some of the main theoretical results. This framework will be extended to turbulent enstrophy in section 2.2. The classical results, mainly concerning Homogeneous Isotropic Turbulence (HIT), will be shown by using a data set of HIT simulations at different Reynolds numbers for both the GKE and for the two-point enstrophy budget in section 2.3. These results will also serve as a reference before analysing the more complex boundary layer setup presented in chapters 4 and 5. Finally, the present

chapter will conclude by reporting some notions regarding wall turbulence and TNTI in sections 2.4 and 2.5.

## 2.1 Richardson's energy cascade and Kolmogorov's theory

The concept of the energy cascade probably has its roots in Richardson's (Richardson, 1922) phenomenological view. In particular, through the observation of clouds, Richardson came to develop his view of turbulence, which can be summarized by quoting his memorable poem:

*Big whirls have little whirls*
*that feed on their velocity,*
*And little whirls have lesser whirls*
*and so on to viscosity.*

The idea behind this phenomenological interpretation is that turbulent motions can be thought as composed by a variety of eddies of different size. The larger scale fluctuations are unstable and break up feeding smaller eddies. This process is repeated up to a scale at which the viscous stresses are sufficient to stabilise the fluid motions.

Subsequently, Kolmogorov succeeded in developing a mathematical framework that was able to incorporate this phenomenological view into a more rigorous framework. His work led to one of the only exact theories in the field of turbulence. This mathematical framework, together with some results will be briefly reported in the following subsections.

### 2.1.1 Self-similarity assumptions

A turbulent motion can be considered as composed by eddies of different sizes $\ell$, and the related velocity scales $u_\ell$. The associated scale Reynolds number can be defined as $Re_\ell = u_\ell \ell / \nu$. In general, the larger scale motions are of the order of the problem size $L_0$ and are dependent on the boundary conditions of the problem. The related velocity is of the order of the characteristic velocity of the flow considered $U_0$. Kolmogorov argued that, contrary to these large scale motions, the small scales of any turbulent flows can be thought to as universal and isotropic:

**Kolmogorov's hypothesis of local isotropy**. *At sufficiently high Reynolds number,the small-scale turbulent motions ($\ell \ll L_0$) are statistically isotropic.*

A consequence of this first hypothesis is that the directional information contained in the large anisotropic scales are gradually lost in the chaotic process of the energy cascade. In accordance with this hypothesis, Kolmogorov formulated the first similarity assumption:

**Kolmogorov's first similarity assumption**. *In every turbulent flows at sufficiently high Reynolds numbers, the small scale statistics ($\ell/L_0 \ll 1$) have an universal form that is uniquely determined by $\nu$ and $\langle\epsilon\rangle$,*

being $\epsilon$ the rate of dissipation of turbulent kinetic energy into heat. Accordingly to this similarity assumption, a unique length, time and velocity scales can be defined:

$$\eta = \left(\frac{\nu^3}{\langle\epsilon\rangle}\right)^{1/4}, \qquad \tau_\eta = \left(\frac{\nu}{\langle\epsilon\rangle}\right)^{1/2}, \qquad u_\eta = \left(\nu\langle\epsilon\rangle\right)^{1/4}. \tag{2.1}$$

These three scales constitute the Kolmogorov scales and the associated scale Reynolds number is of the order of unity: $u_\eta\eta/\nu = 1$. The ratio between the smallest and the largest scale present in the flow can be than determined with the Reynolds number:

$$\frac{L_0}{\eta} = Re^{3/4}, \qquad \frac{U_0}{u_\eta} = Re^{1/4}, \qquad \frac{\tau_0}{\tau_\eta} = Re^{1/2}. \tag{2.2}$$

Hence, as a consequence of the first similarity assumption, an increase in the Reynolds number results in the generation of a larger and larger separation between the scales of motion. As a consequence of this, we can say that, for a sufficiently high Reynolds number, there exists a range of scales such that $L_0 \gg \ell \gg \eta$. These scales will be simultaneously too large to be significantly affected by viscous phenomena, and too small to be directly affected by the boundary conditions of the problem. Kolmogorov's second similarity assumption follows:

**Kolmogorov's second similarity assumption**. *In every turbulent flow at sufficiently high Reynolds number, the statistics of the motions of scale $l$ in the range $L_0 \gg \ell \gg \eta$ have a universal form that is uniquely determined by $\epsilon$ and independent of $\nu$.*

This hypothesis introduces the concept of inertial range, in which the main physical phenomena are dominated but inertial forces that transfer energy towards smaller scales without any appreciable dissipation. This range is only determined by dissipation $\epsilon$ which is also equal to the flux of

energy, since this range can be seen as a connection between the large scales, at which energy is injected, at a rate $\epsilon \approx U_0^3/L_0$ , and the Kolmogorov scales, at which energy is dissipated at a rate of $\epsilon$. Through purely dimensional arguments and by applying Kolmogorov's second similarity assumption, it is already possible to derive a scaling law linking the characteristic scale velocity and length in the inertial range:

$$u_\ell^2 = C' \langle \epsilon \rangle^{2/3} \ell^{2/3}. \tag{2.3}$$

### 2.1.2 Generalized Kolmogorov equation

In the following, we provide a few technical details about second-order structure function and its evolution equation with the aim of better defining their features. The present subsection is taken and adapted from the appendix of Cimarelli et al. (2024b). This subsection is mostly devoted to a formal analysis of two-point statistics and of their equations, and aims to provide a clearer physical understanding of the results reported in chapters 4 and 5. To this purpose, the theoretical framework of the generalized Kolmogorov equation is also used to show how well-known results in turbulence theory are recovered.

#### Second-order structure function

By recalling the definition of the second-order structure function,

$$\langle \delta q^2 \rangle \equiv \langle \delta u_i \delta u_i \rangle \tag{2.4}$$

it is clear that the velocity increment between two points $\delta u_i \equiv u_i(x_i', t) - u_i(x_i'', t)$ is a central object, being $u_i$ the fluctuating velocity. The statistical features of the second-order structure function are better expressed by considering the two-point separation vector $r_i = x_i' - x_i''$ and the midpoint vector $x_{c_i} = (x_i' + x_i'')/2$, i.e. $\langle \delta q^2 \rangle = \langle \delta q^2 \rangle (x_{c_i}, r_i, t)$. As shown in figure 2.1, the dependence of $\langle \delta q^2 \rangle$ on the midpoint $x_{c_i}$ is related to the statistical inhomogeneity of the flow while the dependence on the separation vector $r_i$ is related to the multiscale features of the flow.

From the definition of the second-order structure function (2.4), we can write

$$\begin{aligned} \langle \delta q^2 \rangle (x_{c_i}, \boldsymbol{r}, t) = 2\langle k \rangle (\boldsymbol{x_c} + \boldsymbol{r}/2, t) + 2\langle k \rangle (\boldsymbol{x_c} - \boldsymbol{r}/2, t) \\ -2\langle u_i(\boldsymbol{x_c} + \boldsymbol{r}/2, t) u_i(\boldsymbol{x_c} - \boldsymbol{r}/2, t) \rangle \end{aligned} \tag{2.5}$$

where $k = u_i u_i/2$ is the turbulent kinetic energy. It is then clear that the second-order structure function is strictly related with the two-points correlation function,

$$R(\boldsymbol{x_c}, \boldsymbol{r}, t) \equiv \langle u_i(\boldsymbol{x_c} + \boldsymbol{r}/2, t) u_i(\boldsymbol{x_c} - \boldsymbol{r}/2, t) \rangle \tag{2.6}$$

For statistically homogeneous flows, the dependence on the mid-point position $\boldsymbol{x_c}$ vanishes and the relation between second-order structure function and two-points correlation function reduces to

$$\langle \delta q^2 \rangle(\boldsymbol{r}, t) = 4\langle k \rangle - 2R(\boldsymbol{r}, t) \tag{2.7}$$

Periodic boundary conditions can be applied in such homogeneous conditions and the kinetic energy spectrum can be also defined

$$E(\boldsymbol{k}, t) \equiv \frac{1}{(2\pi)^3} \int R(\boldsymbol{r}, t) e^{-j\boldsymbol{k}\cdot\boldsymbol{r}} d\boldsymbol{r} \tag{2.8}$$

where $j = \sqrt{-1}$ is the imaginary unit and $\boldsymbol{k}$ is the wavenumber. The above definition highlights that the second-order structure function is strictly related also to the kinetic energy spectrum as

$$\langle \delta q^2 \rangle(\boldsymbol{r}, t) = 4\langle k \rangle - 2 \int E(\boldsymbol{k}, t) e^{j\boldsymbol{k}\cdot\boldsymbol{r}} d\boldsymbol{k} \tag{2.9}$$

Equations (2.7) and (2.9) suggest that in statistically homogeneous turbulence, the three statistical observables carry the same kind of information. The main difference is indeed the support provided for the definition of scales that is the physical space $\boldsymbol{r}$ for the second-order structure function and for the two-points correlation function and the spectral space $\boldsymbol{k}$ for the kinetic energy spectrum.

Finally, we conclude this section by showing the well-known scaling law of the structure function and its analogue for the energy spectrum valid in the inertial range. By simply applying equation 2.3, it is possible to write:

$$\langle \delta q^2 \rangle = C' \langle \epsilon \rangle^{2/3} r^{2/3}, \tag{2.10}$$

or equivalently, in the spectral space:

$$E = C'' \langle \epsilon \rangle^{2/3} k^{-5/3}, \tag{2.11}$$

where $r = |\boldsymbol{r}|$ and $k = |\boldsymbol{k}|$. Equations 2.10 and 2.11 are are respectively known as the *two-third* and the *five-third* laws.

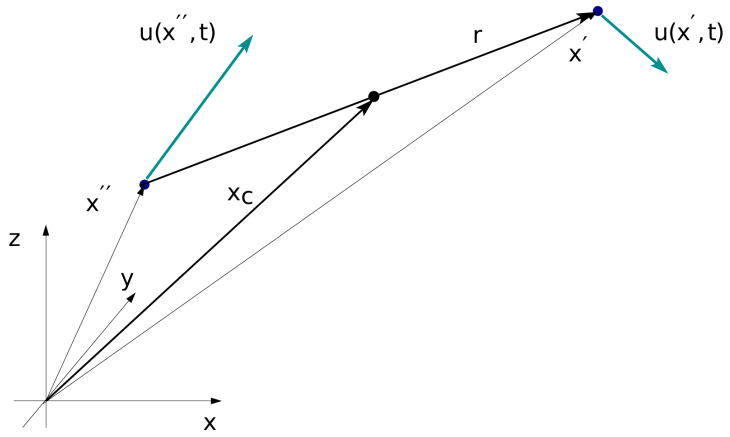


Figure 2.1: Sketch of the quantities involved in the definition of the two-point velocity increment $\delta u_i = u_i(\boldsymbol{x'}, t) - u_i(\boldsymbol{x''}, t)$. Image taken with permission of Cimarelli et al. (2024b)

### Derivation of the generalized Kolmogorov equation

The generalized Kolmogorov equation is the exact equation for the evolution of the second-order structure function $\langle \delta q^2 \rangle$. Contrary to the equation for the kinetic energy spectrum $E(\boldsymbol{k}, t)$ that can be written only for statistically homogeneous flows that feature periodic boundary conditions, the generalized Kolmogorov equation applies to any flow and, hence, also in strongly inhomogeneous and anisotropic turbulence. The exact form of the equation is due to the fact that it can be directly derived from the Navier-Stokes equations. The procedure for its derivation has been introduced by Hill (2002) without considering the Reynolds decomposition. This latter has been introduced later by Marati et al. (2004) for the derivation of the second-order structure function equation applied to the statistical symmetries of a turbulent channel.

We report here the main steps of derivation of the second-order structure function equation in its most general form by considering also the Reynolds decomposition of the flow fields. The asterisk symbol $\cdot^*$ will be used to denote total quantities, capital letters for average quantities and lower case letter for fluctuating quantities (e.g. $u_i^* = U_i + u_i$, where $u_i^*$ is the total velocity field, while $U_i = \langle u_i^* \rangle$ and $u_i$ are respectively the mean and fluctuating velocity fields, being $\langle \cdot \rangle$ the average operator). The first step is to derive the evolution equations for the fluctuating velocity increment $\delta \boldsymbol{u}$. These equations can be obtained by subtracting the Navier-Stokes equa-

tions for the velocity fluctuations written at the two points of the increment $\boldsymbol{x'}$ and $\boldsymbol{x''}$. Then, by considering that the two points $\boldsymbol{x'}$ and $\boldsymbol{x''}$ are independent variables, e.g. $\partial u_i(\boldsymbol{x'},t)/\partial x''_j = 0$, all the flow variables can be written as two-point increments. Finally, a change in the coordinate system from $(\boldsymbol{x'},\boldsymbol{x''},t)$ to $(\boldsymbol{x_c},\boldsymbol{r},t)$ can be performed by considering the following differential relations

$$\begin{cases} \dfrac{\partial}{\partial x'_i} = \dfrac{1}{2}\dfrac{\partial}{\partial x_{c_i}} + \dfrac{\partial}{\partial r_i} \\ \dfrac{\partial}{\partial x''_i} = \dfrac{1}{2}\dfrac{\partial}{\partial x_{c_i}} - \dfrac{\partial}{\partial r_i} \\ \dfrac{\partial^2}{\partial x'_i \partial x'_i} + \dfrac{\partial^2}{\partial x''_i \partial x''_i} = \dfrac{1}{2}\dfrac{\partial^2}{\partial x_{c_i}\partial x_{c_i}} + 2\dfrac{\partial^2}{\partial r_i \partial r_i} \end{cases} \tag{2.12}$$

The resulting equations for the fluctuating velocity increments read

$$\begin{aligned} &\frac{\partial \delta u_i}{\partial t} + \Big(\widetilde{u}_j + \widetilde{U}_j\Big)\frac{\partial \delta u_i}{\partial x_{c_j}} + \Big(\delta u_j + \delta U_j\Big)\frac{\partial \delta u_i}{\partial r_j} + \widetilde{u}_j \frac{\partial \delta U_i}{\partial x_{c_j}} \\ &+\delta u_j \frac{\partial \delta U_i}{\partial r_j} - \frac{\partial \delta\langle u_i u_j\rangle}{\partial x_{c_j}} = -\frac{1}{\rho}\frac{\partial \delta p}{\partial x_{c_i}} + \frac{\nu}{2}\frac{\partial^2 \delta u_i}{\partial x_{c_j}\partial x_{c_j}} + 2\nu \frac{\partial^2 \delta u_i}{\partial r_j \partial r_j} \end{aligned} \tag{2.13}$$

where we recall that $\delta\cdot$ and $\widetilde{\cdot}$ denote the two-point difference and the two-point average operators. From here on, we will refer to fluctuating velocity and pressure with the lower case letters $u_i$ and $p$, and to average velocity with upper case $U_i$. The second-order structure function equation can be finally obtained by multiplying equation (2.13) by $2\delta u_i$, by applying the average operator $\langle\cdot\rangle$ and by rearranging the viscous terms in order to highlight the dependence of the equation on the behaviour of the pseudo-dissipation $\epsilon$. The resulting final form of the generalized Kolmogorov equation reads

$$\begin{aligned} &\frac{\partial\langle\delta q^2\rangle}{\partial t} + \frac{\partial\langle\delta q^2 \delta u_j\rangle}{\partial r_j} + \frac{\partial\langle\delta q^2 \widetilde{u}_j\rangle}{\partial x_{c_j}} + \frac{\partial\langle\delta q^2\rangle \delta U_j}{\partial r_j} + \frac{\partial\langle\delta q^2\rangle \widetilde{U}_j}{\partial x_{c_j}} + \\ &\qquad 2\langle\delta u_i \delta u_j\rangle \widetilde{\left(\frac{\partial U_i}{\partial x_j}\right)} + 2\langle\delta u_i \widetilde{u}_j\rangle\, \delta\left(\frac{\partial U_i}{\partial x_j}\right) = \\ &\qquad -\frac{2}{\rho}\frac{\partial\langle\delta p \delta u_i\rangle}{\partial x_{c_i}} + 2\nu\frac{\partial^2\langle\delta q^2\rangle}{\partial r_j \partial r_j} + \frac{\nu}{2}\frac{\partial^2\langle\delta q^2\rangle}{\partial x_{c_j}\partial x_{c_j}} - 4\langle\widetilde{\epsilon}\rangle \end{aligned} \tag{2.14}$$

where the solenoidal condition of the velocity field is repeatedly applied in its derivation, i.e. $\partial\delta u_i/\partial r_i = \partial\delta u_i/\partial x_{c_i} = \partial\widetilde{u}_i/\partial r_i = \partial\widetilde{u}_i/\partial x_{c_i} = 0$. This equation represents an exact equation that statistically describes all

the degrees of freedom of turbulence by addressing the augmented space of scales and positions, $\boldsymbol{r}$ and $\boldsymbol{x}_c$ respectively. Hence, the multiscale nature of turbulence also in strongly inhomogeneous conditions is formally described by this theoretical framework.

It is useful now to highlight the conservative form of the generalized Kolmogorov equation by rewriting it as,

$$\frac{\partial \langle \delta q^2 \rangle}{\partial t} + \nabla_6 \cdot \boldsymbol{\phi} = S \tag{2.15}$$

where

$$S = -2\langle \delta u_i \delta u_j \rangle \widetilde{\left( \frac{\partial U_i}{\partial x_j} \right)} - 2\langle \delta u_i \widetilde{u}_j \rangle \, \delta \left( \frac{\partial U_i}{\partial x_j} \right) - 4\langle \widetilde{\epsilon} \rangle \tag{2.16}$$

is the source term of a 6-dimensional hyperflux $\boldsymbol{\phi}$ occurring in the compound 6-dimensional augmented space of scales $\boldsymbol{r}$ and positions $\boldsymbol{x}_c$,

$$\boldsymbol{\phi} = \begin{bmatrix} \boldsymbol{\phi_r} \\ \boldsymbol{\phi_c} \end{bmatrix} = \begin{bmatrix} \langle \delta q^2 \delta u \rangle + \langle \delta q^2 \rangle \delta U - 2\nu \dfrac{\partial \langle \delta q^2 \rangle}{\partial r_x} \\ \langle \delta q^2 \delta v \rangle + \langle \delta q^2 \rangle \delta V - 2\nu \dfrac{\partial \langle \delta q^2 \rangle}{\partial r_y} \\ \langle \delta q^2 \delta w \rangle + \langle \delta q^2 \rangle \delta W - 2\nu \dfrac{\partial \langle \delta q^2 \rangle}{\partial r_z} \\ \langle \delta q^2 \widetilde{u} \rangle + \langle \delta q^2 \rangle \widetilde{U} + \dfrac{2}{\rho} \langle \delta p \delta u \rangle - \dfrac{\nu}{2} \dfrac{\partial \langle \delta q^2 \rangle}{\partial x_c} \\ \langle \delta q^2 \widetilde{v} \rangle + \langle \delta q^2 \rangle \widetilde{V} + \dfrac{2}{\rho} \langle \delta p \delta v \rangle - \dfrac{\nu}{2} \dfrac{\partial \langle \delta q^2 \rangle}{\partial y_c} \\ \langle \delta q^2 \widetilde{w} \rangle + \langle \delta q^2 \rangle \widetilde{W} + \dfrac{2}{\rho} \langle \delta p \delta w \rangle - \dfrac{\nu}{2} \dfrac{\partial \langle \delta q^2 \rangle}{\partial z_c} \end{bmatrix} \tag{2.17}$$

and

$$\nabla_6 = \Big[ \nabla_r, \nabla_c \Big] = \left[ \frac{\partial}{\partial r_x}, \frac{\partial}{\partial r_y}, \frac{\partial}{\partial r_z}, \frac{\partial}{\partial x_c}, \frac{\partial}{\partial y_c}, \frac{\partial}{\partial z_c} \right] \tag{2.18}$$

It is then possible to interpret the generalized Kolmogorov equation as an exact statistical theoretical framework for the assessment of how kinetic energy produced at large scales is dissipated at small scales also in fully inhomogeneous conditions (Danaila et al., 2001). Indeed, by tracing back the hyperfluxes from the small scales $\boldsymbol{r}$ and regions $\boldsymbol{x}_c$ where turbulence dissipation $\epsilon$ is physically accomplished, it is possible to reconstruct the paths followed by scale energy and the large scales $\boldsymbol{r}$ and regions $\boldsymbol{x}_c$ at

which have production mechanisms inject energy. In this context, the three-dimensional field of fluxes $\boldsymbol{\phi_r}$ identifies the energy cascade process among scales while three-dimensional field of fluxes $\boldsymbol{\phi_c}$ locates the flow regions statistically involved.

It is finally worth noting that the generalized Kolmogorov equation exhibits a well-defined asymptotic behaviour at very large scales. Indeed, from equation (2.7) it is clear that by considering a separation vector $\boldsymbol{r}$ in statistical homogeneous directions such that $|\boldsymbol{r}| \gg \ell$ with $\ell$ the correlation length, the two-point correlation function vanishes $R(|\boldsymbol{r}| \gg \ell, t) = 0$ and the second-order structure function reduces to

$$\langle \delta q^2 \rangle(\boldsymbol{r}, t) = 4\langle k \rangle \tag{2.19}$$

The same reasoning can be applied to all the terms of the generalized Kolmogorov equation (Marati et al., 2004) to show that the large-scale asymptote of equation (2.14) is, within a factor 4, the single-point turbulent kinetic energy budget.

### Classical theory of turbulence

As mentioned in the previous subsections, for sufficiently high Reynolds numbers, turbulence develops scales small enough to be considered not affected by the boundary conditions of the problem. In this condition, the small scales of turbulence are assumed to recover all the statistical symmetries and can be thought as universal. In such statistical homogeneous and isotropic conditions, the generalized Kolmogorov equation (2.14) significantly simplifies. In particular, thanks to statistical homogeneity, the dependence on the mid-point vector $\boldsymbol{x}_c$ vanishes, e.g. $\langle \delta q^2 \rangle = \langle \delta q^2 \rangle(\boldsymbol{r}, t)$, and the generalized Kolmogorov equation reduces to

$$\frac{\partial \langle \delta q^2 \delta u_j \rangle}{\partial r_j} + \frac{\partial \langle \delta q^2 \rangle \delta U_j}{\partial r_j} + 2\langle \delta u_i \delta u_j \rangle \frac{\partial U_i}{\partial x_j} = 2\nu \frac{\partial^2 \langle \delta q^2 \rangle}{\partial r_j \partial r_j} - 4\langle \epsilon \rangle \tag{2.20}$$

where a statistical steady condition is also considered. Because of homogeneity, the mean velocity gradient in the production term of turbulence by mean shear has to be understood as constant, i.e. $\partial U_i / \partial x_j = const$ in homogeneous shear flows and $\partial U_i / \partial x_j = 0$ in homogeneous shear free turbulence. Equation (2.20) unequivocally highlights that the prominent feature of statistically homogeneous turbulence is the transfer of energy in the space of scales. Furthermore, by considering small scales such that $|\boldsymbol{r}| / \ell_S \ll 1$ where $\ell_S$ is the shear scale, the energy injection by mean shear can be neglected as

well as the contribution to scale transport from the mean velocity increment. In these conditions, the generalized Kolmogorov equation further reduces to

$$\frac{\partial \langle \delta q^2 \delta u_j \rangle}{\partial r_j} - 2\nu \frac{\partial^2 \langle \delta q^2 \rangle}{\partial r_j \partial r_j} = -4\langle \epsilon \rangle \tag{2.21}$$

thus showing that the small scales of homogeneous turbulence develop an equilibrium range where scale energy is transported among scales at a constant rate prescribed by the rate of energy dissipation, i.e.

$$\boldsymbol{\nabla_r} \cdot \boldsymbol{\phi_r} = -4\langle \epsilon \rangle, \tag{2.22}$$

where $\boldsymbol{\phi_r} = \langle \delta q^2 \delta u_j \rangle - 2\nu \partial \langle \delta q^2 \rangle / \partial r_j$.

The absence of effects from mean shear in this equilibrium range allows also to assume an isotropic recovery at small scales, i.e. $\langle \delta q^2 \rangle = \langle \delta q^2 \rangle(r)$ where $r = |\boldsymbol{r}|$. To better express the generalized Kolmogorov equation under statistical isotropic conditions, it is useful to recast equation (2.21) in a spherical coordinate system,

$$\frac{1}{r^2}\frac{d}{dr}\left( r^2 \langle \delta q^2 \delta u_r \rangle \right) - 2\nu \frac{1}{r^2}\frac{d}{dr}\left( r^2 \frac{d\langle \delta q^2 \rangle}{dr} \right) = -4\langle \epsilon \rangle \tag{2.23}$$

where $\delta u_r$ is the radial velocity increment (also called longitudinal velocity increment) and the terms depending on the azimuthal and polar angles cancel out due to the statistical isotropy assumption. In order to address the flux of scale energy, it is possible now to perform a spherical volume integral and the generalized Kolmogorov equation under isotropic conditions becomes

$$\langle \delta q^2 \delta u_r \rangle - 2\nu \frac{d\langle \delta q^2 \rangle}{dr} = -\frac{4}{3}\langle \epsilon \rangle r \tag{2.24}$$

thus showing that the essential feature of turbulence in statistically homogeneous isotropic conditions is the single process of flux of scale energy from large to small scales, see the sketch reported in figure 2.2. This flux is radial in the space of scales, linear with the separation $r$ and proportional to the turbulent dissipation rate $\langle \epsilon \rangle$. Notice that a similar result can be obtained also under the sole statistical homogeneity assumption as shown in Nie and Tanveer (1999).

By limiting equation 2.24 to the very small scales of the viscous range (where $\langle \delta q^2 \delta u_r \rangle \approx 0$) and by integrating in $r$, it is possible to obtain a viscous scaling of the structure function:

$$\langle \delta q^2 \rangle = \frac{1}{3\nu}\langle \epsilon \rangle r^2. \tag{2.25}$$

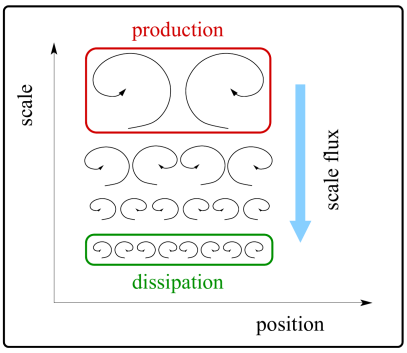


Figure 2.2: Sketch of the picture of turbulence provided by the generalized Kolmogorov equation in statistically homogeneous turbulence. The eddies are drawn only for improving the graphical readability of the sketch but are not intended to convey any insights about the flow physics provided by the generalized Kolmogorov equation. Figure taken from Cimarelli et al. (2024b).

The isotropic version of the generalized Kolmogorov equation (2.24) can finally be used to recover the famous 4/5th law (Kolmogorov, 1991). Indeed, in statistically isotropic conditions, the second- and third-order structure function tensors are completely determined by a single scalar field given by the second- and third-order moment of the longitudinal velocity increment, $\langle \delta u_r^2 \rangle$ and $\langle \delta u_r^3 \rangle$ respectively (Robertson, 1940). Accordingly, it is possible to re-express equation (2.24) as a function of longitudinal increments as

$$\frac{1}{3r^3}\frac{d}{dr}\left(r^4\langle \delta u_r^3 \rangle\right) - 2\nu\frac{d}{dr}\left[\frac{1}{r^2}\frac{d}{dr}\left(r^3\langle \delta u_r^2 \rangle\right)\right] = -\frac{4}{3}\langle \epsilon \rangle r \tag{2.26}$$

By considering now a very high Reynolds number, an inertial range of scales can be assumed where the viscous contribution can be neglected. In this range, the generalized Kolmogorov equation for isotropic turbulence expressed as a function of longitudinal increments, equation (2.26), reads

$$\langle \delta u_r^3 \rangle = -\frac{4}{5}\langle \epsilon \rangle r \tag{2.27}$$

which is the famous *four-fifth* law.

In conclusion, the generalized Kolmogorov equation provides a full description of the augmented space of turbulence $(\boldsymbol{x_c}, \boldsymbol{r}, t)$ by addressing the source and sink mechanisms and the hyperflux connecting them. By considering statistical homogeneity, the complex problem of turbulence reduces to its essential features that the generalized Kolmogorov equation recognizes in

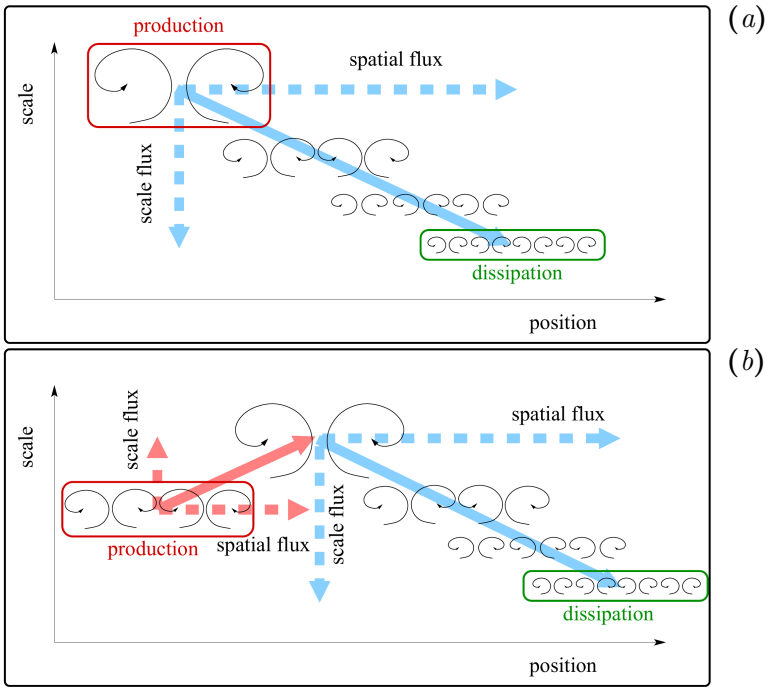


Figure 2.3: Sketch of the picture of turbulence provided by the generalized Kolmogorov equation in inhomogeneous turbulence with a forward cascade (a) and a combined reverse and forward cascade (b). The eddies are drawn only for improving the graphical readability of the sketches but are not intended to convey any insights about the flow physics provided by the generalized Kolmogorov equation. Figure taken from Cimarelli et al. (2024b).

the single process of transport of energy among scales, see equation (2.21). Hence, homogeneous turbulence develops a spectrum of scales where large and small scales are in equilibrium through a process of energy cascade in accordance with equation (2.24), see also the sketch in figure 2.2.

In the more general conditions of inhomogeneous turbulence, the formalism of the generalized Kolmogorov equation is still valid and allows again to assess the processes that occur before turbulent energy is dissipated at small scales. As unequivocally shown by the generalized Kolmogorov equation in its full form, equations (2.14) and (2.15), both the source by mean shear and dissipation by viscous mechanisms are defined in the augmented space $(\boldsymbol{x_c}, \boldsymbol{r}, t)$ and are connected by the hyperflux, sum of a spatial and a scale transport. The presence of a spatial flux greatly complicates the problem. Because of that, the rate of energy dissipation at the small scales of a given flow region is fed by turbulence production by shear occurring at the large scales of other flow regions. In other words, the large and small scales of a given region of the flow are no more in a local statistical equilibrium because of inhomogeneity.

In this context two possible scenarios are envisaged by the generalized Kolmogorov equation. The first one is sketched in figure 2.3(a) and consists in a small scale turbulent dissipation fed by a large-scale production occurring in another region of the flow through a spatial flux combined with a forward cascade. The second scenario is sketched in figure 2.3(b). Again, small-scale dissipation of a given region of the flow is fed by turbulence production occurring at the large scales of another region. However, the spatial flux is combined with both reverse and forward cascades. Qualitatively, this is the scenario observed in the inner region of wall turbulence as shown in the present work. The presence of an inverse energy cascade is supported by the generalized Kolmogorov equation only because of the presence of spatial fluxes. In fact, when dissipation acts at small scales, only the non-locality (in space) of the budget induced by spatial fluxes can allow the presence of an inverse energy cascade. This is different in flow cases where dissipation occurs at large scales, e.g. 2-D turbulence. In this case the inverse energy cascade directly feeds dissipation and hence can also occur locally in space as in homogeneous turbulence.

Let us finally notice that in the two scenarios depicted in figure 2.3(a) and (b), statistical anisotropy has not been considered. In fact, a third scenario is also supported by the generalized Kolmogorov equation that is given by the fact that both the mechanisms sketched in figure 2.3(a) and (b) can simultaneously occur in strongly anisotropic turbulence. In other words, from the turbulence production scales and regions, energy while moving in

other flow region can be continuously transferred to larger scales in some scale-directions while to small scales in the other scale-directions. This third scenario is qualitatively representative of the energy transport phenomena observed in the near-wall and outer region of wall turbulence as shown in the present work.

In conclusion, let us point out that some authors refer to equation (2.14) as the Kármán-Howarth-Monin-Hill equation. In fact, Kármán and Howarth (1938) were the first to write an equation for the second- and third-order two-point correlation for homogeneous isotropic turbulence while Monin and Yaglom (1975) were first to extend it to non-isotropic but still homogeneous conditions. Thanks to equation (2.7) and others similar, it is clear that such equations can be readily re-expressed in terms of second- and third-order structure functions thus leading to the reduced forms of the generalized Kolmogorov equation (2.21) and (2.23). On the other hand, the fully inhomogeneous anisotropic form of the generalized Kolmogorov equation has been derived for the first time by Hill (2002) directly using the formalism of the second- and third-order structure functions, in the same spirit of the original work of Kolmogorov on the theory for isotropic turbulence. Under this respect, we name equation (2.14), the generalized Kolmogorov equation.

## 2.2 Turbulent enstrophy

Turbulent enstrophy is defined as the square of vorticity fluctuations:

$$\xi = \omega_i \omega_i, \tag{2.28}$$

being vorticity the curl of the velocity $\boldsymbol{\omega} = \nabla \times \mathbf{u}$. This observable is of interest in the field of turbulence as, by its definition, it is related to some of the fundamental properties of turbulence, namely its rotational nature and the rate of dissipation of turbulent kinetic energy into heat. While the former is obvious by its very definition, the latter can be demonstrated in the following few steps. The total dissipation rate is defined as

$$\epsilon^* = 2\nu S_{ij} S_{ij} = \nu \frac{\partial u_i}{\partial x_j} \frac{\partial u_i}{\partial x_j} + \nu \frac{\partial u_i}{\partial x_j} \frac{\partial u_j}{\partial x_i} = \epsilon + \nu \frac{\partial u_i}{\partial x_j} \frac{\partial u_j}{\partial x_i}, \tag{2.29}$$

where $S_{ij} = 1/2\,(\partial u_i/\partial x_j + \partial u_j/\partial x_i)$ is the rate of deformation tensor, and $\epsilon$ is the pseudo-dissipation. The pseudo dissipation can be rearranged as

$$\begin{aligned} \epsilon = \nu \frac{\partial u_i}{\partial x_j} \frac{\partial u_i}{\partial x_j} = \nu \left(S_{ij} + \Omega_{ij}\right) \left(S_{ij} + \Omega_{ij}\right) = \\ \nu S_{ij} S_{ij} + \nu \Omega_{ij} \Omega_{ij} = \frac{\epsilon^*}{2} + \frac{\nu}{4} e_{ijk} \omega_k e_{ijk} \omega_k = \frac{\epsilon^*}{2} + \frac{\nu}{2} \omega_k \omega_k, \end{aligned} \tag{2.30}$$

being $\Omega_{ij} = 1/2\,(\partial u_i/\partial x_j - \partial u_j/\partial x_i)$ the rotation tensor. In conclusion, by using equations 2.29 and 2.30, we obtain:

$$\begin{aligned} \epsilon^* &= \nu\xi + 2\nu\frac{\partial u_i}{\partial x_j}\frac{\partial u_j}{\partial x_i}, \\ \epsilon &= \nu\xi + \nu\frac{\partial u_i}{\partial x_j}\frac{\partial u_j}{\partial x_i}, \end{aligned} \tag{2.31}$$

thus highlighting that enstrophy represents a fundamental mechanisms at the basis of dissipation. This is even more evident in statistically homogeneous flows where

$$\langle\frac{\partial u_i}{\partial x_j}\frac{\partial u_j}{\partial x_i}\rangle = \langle\frac{\partial^2 u_i u_j}{\partial x_i \partial x_j}\rangle = \frac{\partial^2\langle u_i u_j\rangle}{\partial x_i \partial x_j} = 0, \tag{2.32}$$

hence being pseudo dissipation and dissipation equal to enstrophy times viscosity on average:

$$\langle\epsilon^*\rangle = \langle\epsilon\rangle = \nu\langle\xi\rangle \tag{2.33}$$

(from the lecture notes of the course "Turbulence" held by Prof. Andrea Cimarelli). It must be pointed out that, despite being equal on average, their topology and their dynamics is not necessarily equal (Carbone and Bragg, 2020).

### 2.2.1 Two-point enstrophy budget

Identically as in equation 2.4, is is possible to define the second-order structure function related to enstrophy as:

$$\langle\delta\xi^2\rangle \equiv \langle\delta\omega_i\delta\omega_i\rangle \tag{2.34}$$

being $\omega_i$ the fluctuating vorticity and $\delta\omega_i$ its two-point increment. The same formalism and the same definitions shown in subsection 2.1.2 and in figure 2.1 are used here.

To derive the two-point budget enstrophy budget equation, we start by reporting the vorticity equation:

$$\frac{\partial\bar{\omega}_i}{\partial t} + \bar{u}_j\frac{\partial\bar{\omega}_i}{\partial x_j} = \bar{\omega}_j\frac{\partial\bar{u}_i}{\partial x_j} + \nu\frac{\partial^2\bar{\omega}_i}{\partial x_j\partial x_j}, \tag{2.35}$$

where superscript $\bar{\cdot}$ indicates total quantities. We highlight the presence of the vortex stretching term $\bar{\omega}_j\partial\bar{u}_i/\partial x_j$ which will represent a fundamental difference to what we have seen in the previous section. As before, we start

by deriving the equation for the two-point vorticity increment $\delta\omega_i$. After writing equation 2.35 in the two points $x_i'$ and $x_i''$, applying the Reynolds decomposition and considering the relations 2.12, we obtain:

$$\begin{aligned}\frac{\partial\delta\omega_i}{\partial t}+\Big(\widetilde{u}_j+\widetilde{U}_j\Big)\frac{\partial\delta\omega_i}{\partial x_{c_j}}+\Big(\delta u_j+\delta U_j\Big)\frac{\partial\delta\omega_i}{\partial r_j}+\widetilde{u}_j\frac{\partial\delta\Omega_i}{\partial x_{c_j}}+\delta u_j\frac{\partial\delta\Omega_i}{\partial r_j}\\ -\frac{\partial\delta\langle\omega_i u_j\rangle}{\partial x_{c_j}}=\Big(\widetilde{\omega}_j+\widetilde{\Omega}_j\Big)\frac{\partial\delta u_i}{\partial x_{c_j}}+\Big(\delta\omega_j+\delta\Omega_j\Big)\frac{\partial\delta u_i}{\partial r_j}+\widetilde{\omega}_j\frac{\partial\delta U_i}{\partial x_{c_j}}\\ +\delta\omega_j\frac{\partial\delta U_i}{\partial r_j}-\frac{\partial\delta\langle u_i\omega_j\rangle}{\partial x_{c_j}}+\frac{\nu}{2}\frac{\partial^2\delta\omega_i}{\partial x_{c_j}\partial x_{c_j}}+2\nu\frac{\partial^2\delta\omega_i}{\partial r_j\partial r_j}\end{aligned}\tag{2.36}$$

By multiplying equation 2.36 by $2\delta\omega_i$ and by taking the average we finally obtain the two-point enstrophy equation:

$$\begin{aligned}\frac{\partial\langle\delta\xi^2\rangle}{\partial t}+\frac{\partial\langle\delta\xi^2\delta u_j\rangle}{\partial r_j}+\frac{\partial\langle\delta\xi^2\rangle\delta U_j}{\partial r_j}+\frac{\partial\langle\delta\xi^2\widetilde{u}_j\rangle}{\partial x_{c_j}}+\frac{\partial\langle\delta\xi^2\rangle\widetilde{U}_j}{\partial x_{c_j}}+\\ 2\langle\delta\omega_i\delta u_j\rangle\widetilde{\left(\frac{\partial\Omega_i}{\partial x_j}\right)}+2\langle\delta\omega_i\widetilde{u}_j\rangle\delta\left(\frac{\partial\Omega_i}{\partial x_j}\right)=\\ 2\widetilde{\Omega}_j\langle\delta\omega_i\delta\left(\frac{\partial u_i}{\partial x_j}\right)\rangle+2\delta\Omega_j\langle\delta\omega_i\widetilde{\left(\frac{\partial u_i}{\partial x_j}\right)}\rangle+2\langle\delta\omega_i\widetilde{\omega}_j\rangle\delta\left(\frac{\partial U_i}{\partial x_j}\right)\\ +2\langle\delta\omega_i\delta\omega_j\rangle\widetilde{\left(\frac{\partial U_i}{\partial x_j}\right)}+2\langle\delta\omega_i\widetilde{\omega}_j\delta\left(\frac{\partial u_i}{\partial x_j}\right)\rangle+2\langle\delta\omega_i\delta\omega_j\widetilde{\left(\frac{\partial u_i}{\partial x_j}\right)}\rangle\\ +2\nu\frac{\partial^2\langle\delta\xi^2\rangle}{\partial r_j\partial r_j}+\frac{\nu}{2}\frac{\partial^2\langle\delta\xi^2\rangle}{\partial x_{c_j}\partial x_{c_j}}-4\langle\widetilde{\epsilon_\xi}\rangle\end{aligned}\tag{2.37}$$

Compared to the generalized Kolmogorov equation 2.14, this equation contains an additional source term, constituted by the vortex stretching. The other terms and their interpretation remain consistent with the terms in the GKE. On the left-hand side we reported respectively the time variation, the inertial transport among scales and in the physical space (in which the pressure contribution is now missing) through both the average and the fluctuating velocity fields and the production terms by mean vorticity gradient. On the right-hand side, we reported the vortex stretching term, transport due to diffusion both in the scales and in the physical space and finally the enstrophy destruction term, defined as

$$\epsilon_\xi=\nu\frac{\partial\omega_i}{\partial x_j}\frac{\partial\omega_i}{\partial x_j}\tag{2.38}$$

that acts as a sink of enstrophy by smoothing out the vorticity gradients. While the turbulent kinetic energy dissipation has a more familiar physical interpretation, as it converts kinetic energy into heat (i.e. from a coherent component of the molecular motion to a completely disorganised one), the destruction of enstrophy may be less familiar. Similarly to the dissipation of energy, this term arises from the homogenising effect of the diffusion process that tends to make the field uniform. In the case of vorticity, this translates in the dampening of the local peaks. In a simplified system with no vorticity flux from the boundaries, the total vorticity content is constant, while the enstrophy content can be increased through the generation of local accumulations of vorticity against which the homogenising effect of diffusion is opposed. In a nutshell, this term, removes the "energy" contained by the vorticity "signal" in the domain volume $V$ ($\int_V |\boldsymbol{\omega}|^2 \, dV$) increasing the entropy of the system, as well dissipation does it for the velocity field.

Equation 2.37 can be expressed in terms of a net source and divergence of fluxes:

$$\frac{\partial \langle \delta\xi^2 \rangle}{\partial t} + \nabla_6 \cdot \boldsymbol{\phi}_{\boldsymbol{\xi}} = S_\xi \tag{2.39}$$

where

$$\begin{aligned} S_\xi = -2\langle \delta\omega_i \delta u_j \rangle \widetilde{\left(\frac{\partial \Omega_i}{\partial x_j}\right)} - 2\langle \delta\omega_i \widetilde{u}_j \rangle \delta\left(\frac{\partial \Omega_i}{\partial x_j}\right) + 2\widetilde{\Omega}_j \langle \delta\omega_i \delta\left(\frac{\partial u_i}{\partial x_j}\right) \rangle \\ + 2\delta\Omega_j \langle \delta\omega_i \widetilde{\left(\frac{\partial u_i}{\partial x_j}\right)} \rangle + 2\langle \delta\omega_i \widetilde{\omega}_j \rangle \delta\left(\frac{\partial U_i}{\partial x_j}\right) - 4\langle \widetilde{\epsilon}_\xi \rangle \end{aligned} \tag{2.40}$$

is the source term, and

$$\boldsymbol{\phi}_{\boldsymbol{\xi}} = \begin{bmatrix} \boldsymbol{\phi}_{\boldsymbol{\xi}_r} \\ \boldsymbol{\phi}_{\boldsymbol{\xi}_c} \end{bmatrix} = \begin{bmatrix} \langle \delta\xi^2 \delta u \rangle + \langle \delta\xi^2 \rangle \delta U - 2\nu \dfrac{\partial \langle \delta\xi^2 \rangle}{\partial r_x} \\ \langle \delta\xi^2 \delta v \rangle + \langle \delta\xi^2 \rangle \delta V - 2\nu \dfrac{\partial \langle \delta\xi^2 \rangle}{\partial r_y} \\ \langle \delta\xi^2 \delta w \rangle + \langle \delta\xi^2 \rangle \delta W - 2\nu \dfrac{\partial \langle \delta\xi^2 \rangle}{\partial r_z} \\ \langle \delta\xi^2 \widetilde{u} \rangle + \langle \delta\xi^2 \rangle \widetilde{U} - \dfrac{\nu}{2} \dfrac{\partial \langle \delta\xi^2 \rangle}{\partial x_c} \\ \langle \delta\xi^2 \widetilde{v} \rangle + \langle \delta\xi^2 \rangle \widetilde{V} - \dfrac{\nu}{2} \dfrac{\partial \langle \delta\xi^2 \rangle}{\partial y_c} \\ \langle \delta\xi^2 \widetilde{w} \rangle + \langle \delta\xi^2 \rangle \widetilde{W} - \dfrac{\nu}{2} \dfrac{\partial \langle \delta\xi^2 \rangle}{\partial z_c} \end{bmatrix} \tag{2.41}$$

are the fluxes of enstrophy in the compound space $(\boldsymbol{r}, \boldsymbol{x_c})$.

As for the GKE, at large scales, each term of the two-point enstrophy budget will approach twice the value of the corresponding single-point term. In homogeneous isotropic conditions, the large-scale asymptotic of the structure function will be

$$\langle \delta\xi^2 \rangle = 2\langle \epsilon \rangle. \tag{2.42}$$

### 2.2.2 Two-point enstrophy in homogeneous isotropic turbulence

In the present subsection, we apply equation 2.37 to the homogeneous isotropic case in order to obtain some reference scaling laws as previously done in section 2.1.2 for the GKE. In statistically steady homogeneous and isotropic conditions, equation 2.37 reads

$$\begin{aligned} \frac{\partial \langle \delta\xi^2 \delta u_j \rangle}{\partial r_j} - 2\nu \frac{\partial^2 \langle \delta\xi^2 \rangle}{\partial r_j \partial r_j} = \\ 2\langle \delta\omega_i \widetilde{\omega}_j \delta \left( \frac{\partial u_i}{\partial x_j} \right) \rangle + 2\langle \delta\omega_i \delta\omega_j \widetilde{\left( \frac{\partial u_i}{\partial x_j} \right)} \rangle - 4\langle \epsilon_\xi \rangle \end{aligned} \tag{2.43}$$

By rewriting this equation in a spherical coordinate system, we obtain

$$\begin{aligned} \frac{1}{r^2}\frac{d}{dr}\left( r^2 \langle \delta\xi^2 \delta u_r \rangle \right) - 2\nu \frac{1}{r^2}\frac{d}{dr}\left( r^2 \frac{d\langle \delta\xi^2 \rangle}{dr} \right) = \\ 2\langle \delta\omega_i \widetilde{\omega}_j \delta \left( \frac{\partial u_i}{\partial x_j} \right) \rangle + 2\langle \delta\omega_i \delta\omega_j \widetilde{\left( \frac{\partial u_i}{\partial x_j} \right)} \rangle - 4\langle \epsilon_\xi \rangle \end{aligned} \tag{2.44}$$

with $r = |\mathbf{r}|$ as before. The vortex stretching terms have been left in the original Cartesian formulation, as we could not obtain simplifications from their spherical formulation, which would considerably complicate the writing without bringing benefits. It is obvious, however, that the vortex stretching contribution in homogeneous isotropic stationary conditions is only statistically dependent on $r$, despite its analytical formulation not being trivial. By performing the integral over a spherical volume, we obtain a formulation highlighting the fluxes of enstrophy:

$$\langle \delta\xi^2 \delta u_r \rangle - 2\nu \frac{d\langle \delta\xi^2 \rangle}{dr} = \frac{1}{4\pi r^2} \int_{\mathcal{B}_r} VS r^2 \sin(\theta) dr d\theta d\psi - \frac{4}{3}\langle \epsilon_\xi \rangle r \tag{2.45}$$

where $VS$ refers to the vortex stretching terms, $\mathcal{B}_r$ is the spherical volume of radius $r$ and $\theta$ and $\psi$ are respectively the polar and azimuthal angles. The

present equations (2.44 and 2.45) are identical to the one obtained for the second-order structure function of velocity (equation 2.23) except for the source contribution given by the vortex stretching, which does not vanish in HIT conditions. Indeed, the vortex stretching mechanism is connected to the energy cascade itself, which by definition is active in the inertial range. Hence, it can never be neglected except in the viscous range. This will be more clearly visualized in the following subsection 2.3.

By limiting equation 2.44, to very small scales, we obtain the viscous scaling of the enstrophy structure function:

$$\langle \delta\xi^2 \rangle = \frac{1}{3\nu}\langle \epsilon_\xi \rangle r^2 \tag{2.46}$$

Finally, it should be mentioned that, by means of estimates, in Davidson et al. (2008) the authors derive a scaling for the inertial enstrophy flux in the inertial range to be $\sim \langle\epsilon\rangle/r^2$. We can adapt this conclusion to our framework as in the following. From equation 2.3, we may approximate $\delta u_r \sim \langle\epsilon\rangle^{1/3} r^{1/3}$ and, analogously, $\delta\omega_r \sim \langle\epsilon\rangle^{1/3} r^{-2/3}$. From these estimates, it follows the inertial flux of enstrophy in the inertial subrange to be approximatively:

$$\langle \delta\xi^2 \delta u_r \rangle \sim \langle\epsilon\rangle \langle \frac{\delta u_r^3}{r^2} \rangle \sim \langle\epsilon\rangle r^{-1}, \qquad \text{for } \eta \ll r \ll L_0 \tag{2.47}$$

Similarly, by applying the small-scale asymptotic, we can derive an estimated scaling of the inertial enstrophy transport in the viscous range. In particular, by exploiting equation 2.46, and the relation for the second-order longitudinal velocity increments in the viscous range

$$\langle \delta u_\parallel^2 \rangle = \frac{1}{15\nu}\langle\epsilon\rangle r^2 \tag{2.48}$$

we may obtain the naïve estimate

$$\langle \delta\xi^2 \delta u_r \rangle \sim \frac{\langle \epsilon_\xi \rangle}{3\nu} \sqrt{\frac{\langle\epsilon\rangle}{15\nu}} r^3 \sim r^3 \tag{2.49}$$

by using the rough approximation $\delta u_r \sim \sqrt{(\langle\epsilon\rangle/15\nu)}r$ from equation 2.48.

In conclusion, the framework at the basis of the GKE was extended to enstrophy in order to expand the study of its dynamics also in the space of scales as well as in physical space. The present framework provides access to the entire compound space of scales and physical space through an exact mathematical formulation with no limits of applicability (such as the requirement of periodic boundary conditions for spectral budgets). The two-point enstrophy budget, as shown in the following chapters, will provide an

alternative perspective on topics such as the confinement effects in the proximity of a solid wall and a turbulent/non-turbulent interface. It will also allow a deeper insight into the dynamics of enstrophy generation, and thus related to how dissipation originates.

## 2.3 Essential features of turbulence

In the present section we will make use of data of statistically steady homogeneous isotropic Direct Numerical Simulations (DNS) at different Reynolds numbers in order to show and discuss the main theoretical results from the previous sections 2.1 and 2.2. Furthermore, the present section is meant to provide a reference of what should be expected in the most fundamental and simplified flow paradigm able to embrace the features of 3D turbulence before analysing the more complex flow settings of the temporal boundary layer.

The simulations used are those presented in Ghira et al. (2022) for which we sincerely thank the authors, and in particular Professor Carlos da Silva for the support and the help. In particular, our analysis is limited to the three simulations with a Taylor-based Reynolds number of $Re_\lambda \approx (140, 240, 400)$. The direct numerical simulations of statistically stationary homogeneous isotropic turbulence are carried out with tri-periodic boundary conditions and a forcing scheme described in Alvelius (1999). The cubic domain is discretized in a number of collocation points of $N^3 = 512^3$, $N^3 = 1024^3$ and $N^3 = 2048^3$ respectively, evenly distributed among the three directions. The resulting resolution is $k_{max}\eta \geq 2.0$ for all simulations. For further details we refer the reader to Ghira et al. (2022).

### 2.3.1 Structure functions

We start by showing in figure 2.4 the shape of the structure functions of both turbulent kinetic energy $\langle \delta q^2 \rangle$ and turbulent enstrophy $\langle \delta \xi^2 \rangle$ at the three Reynolds number considered. The theoretical scaling laws for the viscous and inertial ranges are reported as dashed lines together with the profiles. As already pointed out, it is not possible to observe a purely inertial transport-dominated range in the enstrophy structure function in figure 2.4(b), hence, only the viscous scaling $\langle \delta \xi^2 \rangle = \langle \epsilon_\xi \rangle r^2 / 3\nu$ is reported. All profiles are made dimensionless with Kolmogorov scales. As expected, the viscous scaling appears to approximate very well the curves at very small scales for all Reynolds numbers. In particular, this scaling appears to constitute a reasonable approximation for $\langle \delta q^2 \rangle$ up to $r \approx 5\eta$, while the profile

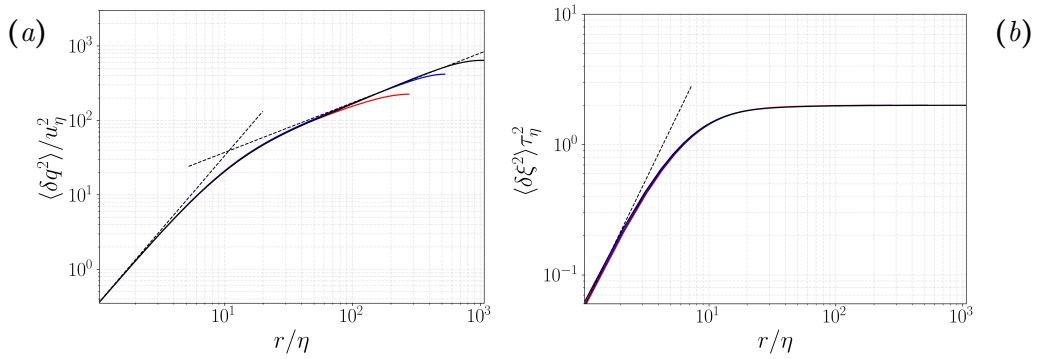


Figure 2.4: Second-order structure functions in HIT of energy $\langle \delta q^2 \rangle$ (a) and of enstrophy $\langle \delta \xi^2 \rangle$ (b) at Taylor-based Reynolds numbers of $Re_\lambda \approx 140$ (solid red lines), $Re_\lambda \approx 240$ (solid blue lines) and $Re_\lambda \approx 400$ (solid black lines). In both (a) and (b) the viscous scaling laws are reported in dotted black lines starting from the origin of the graphs. In (a) also the inertial scaling law for $\langle \delta q^2 \rangle$ is reported in black dotted line. All the curves are made dimensionless by using Kolmogorov scales.

of $\langle \delta \xi^2 \rangle$ starts to deviate from its viscous scaling already at $r \approx 3\eta$. In figure 2.4(a) it is possible to note the widening of the validity range of the inertial scaling $\langle \delta q^2 \rangle \sim \langle \epsilon \rangle^{2/3} r^{2/3}$ as the Reynolds number increases. At the highest Reynolds number reported $Re_\lambda \approx 400$, it is possible to observe a full decade of scale separation in this range. On the contrary, the enstrophy structure function is already saturated at those scales, reaching the asymptotic value $\langle \delta \xi^2 \rangle / \langle \epsilon \rangle = 2$. Enstrophy is related to velocity gradients, hence being, in a sense, a "small-scale quantity". Since small-scales are thought to be universal and independent on the large-scale problem-dependent motions, it is not surprising that its structure function collapses at all the considered Reynold numbers (figure 2.4(b)).

### 2.3.2 Two-point budgets

Following the analysis of the structure functions, we move on to analyse the budget that governs their dynamics. In figure 2.5, the terms of the budget equations 2.23 and 2.44 are reported respectively. In the well-known budget of $\langle \delta q^2 \rangle$, in figure 2.5(a), it is possible to observe the profile of diffusive and inertial transports in the space of the scales and the dissipation that, in equation 2.23, represents a constant value. In statistically steady conditions, the two transports plus the forcing term (active at large scales and not shown as it depends on arbitrary choices and is beyond the scope of

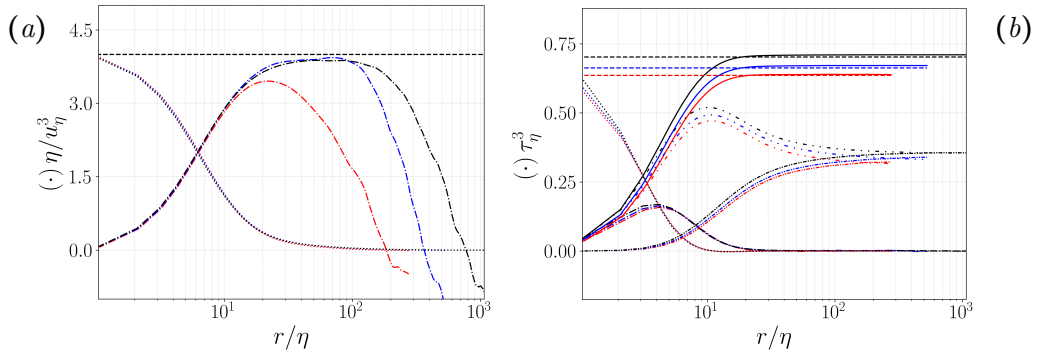


Figure 2.5: Budgets of $\langle \delta q^2 \rangle$ (a) and $\langle \delta \xi^2 \rangle$ (b) at Taylor-based Reynolds numbers of $Re_\lambda \approx 140$ (red lines), $Re_\lambda \approx 240$ (blue lines) and $Re_\lambda \approx 400$ (black lines). (a) Dissipation $4\langle \epsilon \rangle$ (dashed lines), diffusive transport (dotted lines) and inertial transport (dash-dotted lines). (b) Enstrophy destruction $4\langle \epsilon_\xi \rangle$ (dashed lines), diffusive transport (dotted lines), inertial transport (dash-dotted lines) and vortex stretching (solid lines). The two vortex stretching contributes are also reported: $2\langle \delta\omega_i \widetilde{\omega}_j \delta\,(\partial u_i/\partial x_j)\rangle$ (dash-dash-dotted lines) and $2\langle \delta\omega_i \delta\omega_j \widetilde{(\partial u_i/\partial x_j)}\rangle$ (loosely dash-dash-dotted lines). All the curves are made dimensionless by using Kolmogorov scales.

this chapter) sum up to the dissipation and perfectly balance at all scales. While the diffusive transport nicely collapses for all the Reynolds numbers (being active at small-scales), the inertial transport shows a wider and wider range of activity as the Reynolds number increases, connecting the regions of injection of energy to the region where diffusive phenomena are relevant.

A lesser-known budget, on the other hand, is the $\langle \delta \xi^2 \rangle$ budget reported in figure 2.5(b). Its constituent terms (equation 2.44) all show a shape, relevance and range of activity that is not affected by the increase of the Reynolds number. The cause of the non-perfect collapse of the curves will be investigated in future works to establish whether it is a lack of convergence or an actual Reynolds number dependence.

At first glance, it is possible to note that the budget is dominated either by vortex stretching or diffusive transport at all scales. The inertial transport of enstrophy shows a good collapse at all Reynolds numbers, without increasing its relevance as the separation of scales increases. Indeed, this observation should not surprise us. The vortex stretching mechanism (acting as a source in the enstrophy budget) is connected to the energy cascade process, so it is reasonable to expect it to be active from the scales at which the inertial transport of energy begins to be dominant, which can be confirmed by comparing figure 2.5(a) and (b). By definition, at scales smaller

than these, viscosity starts to be relevant, and with it also the diffusive transport. These observations imply that, independently on the Reynolds number, there cannot be a region in which the inertial transport of enstrophy is dominant with respect to both vortex stretching and diffusive transport. In figure 2.5(b), we separately report the two vortex stretching contributions $2\langle\delta\omega_i\widetilde{\omega}_j\delta\left(\partial u_i/\partial x_j\right)\rangle$ and $2\langle\delta\omega_i\delta\omega_j\widetilde{(\partial u_i/\partial x_j)}\rangle$. The first contribution can be expressed as

$$2\langle\delta\omega_i\widetilde{\omega}_j\delta\left(\frac{\partial u_i}{\partial x_j}\right)\rangle = 2\langle\delta\omega_i\widetilde{\omega}_j\frac{\partial\delta u_i}{\partial x_{c_j}}\rangle. \tag{2.50}$$

The operator $\widetilde{\cdot}$ (applied to the vorticity $\omega_j$) has an effect similar to a low-pass filter, being more influenced by the scales larger than the separation length $r$ considered. Furthermore, this term contains the gradient of the velocity increment with respect to the midpoint $\left(\partial\delta u_i/\partial x_{c_j}\right)$. Since we know that the term $\delta u_i$ is, in a sense, more closely related to a change in $\boldsymbol{r}$ than to a change in $\boldsymbol{x_c}$, it is not surprising that its trend is not peaked at a specific scale, but that is slowly increasing until reaching the single-point asymptotic value. On the other hand, the second contribution can be expressed as

$$2\langle\delta\omega_i\delta\omega_j\widetilde{\left(\frac{\partial u_i}{\partial x_j}\right)}\rangle = 2\langle\delta\omega_i\delta\omega_j\frac{\partial\delta u_i}{\partial r_j}\rangle \tag{2.51}$$

and is the vortex stretching contribution given by the velocity increment gradients in the space of scales. The two-point increment operator $\delta\cdot$ has the effect of highlighting motions with a scale similar to the separation length $r$ considered. Hence, the peak exhibited around $r \approx 10\eta$ can be interpreted as a high vortex stretching activity at these scales.

Finally, it is possible to notice that the scales at which the inertial transport of enstrophy is active are similar to those at which the diffusive transport of $\langle\delta q^2\rangle$ is active and that the diffusive transport of enstrophy decays much faster than the one of energy. It appears that the "inertial" dynamics of enstrophy is active at scales that are viscosity dominated for the velocity field, which may be surprising. We conjecture that the inertial enstrophy transport observed at such small scales (in the range of $1 \lesssim r/\eta \lesssim 10$) is not to be interpreted as a fully turbulent cascade process caused by the inertial interactions of the velocity field. Rather, it could be the result of a stirring process of surfaces at constant $\xi$ that, under the effect of the shear of the velocity field, come close together. This scenario resembles a Batchelor-like process which (in scalar fields with a Schmidt number $Sc > 1$) allows the generation of scales smaller than the one contained in the velocity field itself. In this process, the uniform velocity shear performs a stirring of the scalar

iso-surfaces, allowing the generation of scales smaller than the Kolmogorov scale $\eta$ (i.e. the scale below which the velocity field is linear) (Batchelor, 1959).

### 2.3.3 Inertial fluxes

In concluding the present section, we report the inertial fluxes of energy and enstrophy ($\langle \delta q^2 \delta u_r \rangle$ and $\langle \delta \xi^2 \delta u_r \rangle$) in figure 2.6.

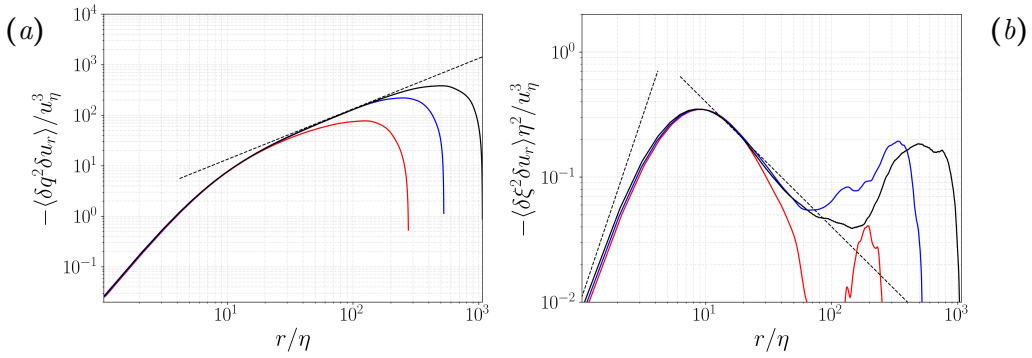


Figure 2.6: Inertial fluxes of $\langle \delta q^2 \rangle$ (a) and $\langle \delta \xi^2 \rangle$ (b) at Taylor-based Reynolds numbers of $Re_\lambda \approx 140$ (red lines), $Re_\lambda \approx 240$ (blue lines) and $Re_\lambda \approx 400$ (black lines). In (a) the theoretical scaling law of $\langle \delta q^2 \delta u_r \rangle = -4/3 \langle \epsilon \rangle r$ is reported in dashed black line. In (b) the estimates $\langle \delta \xi^2 \delta u_r \rangle \sim r^3$ (left) and $\langle \delta \xi^2 \delta u_r \rangle = -\langle \epsilon \rangle / r$ (right) are reported in dashed black lines. All curves are made dimensionless by using Kolmogorov units.

The scaling of the inertial flux $-\langle \delta q^2 \delta u_r \rangle = 4/3 \langle \epsilon \rangle r$ is obtained by simply neglecting the diffusive transport in equation 2.24, since in the inertial range, by definition, both viscous phenomena and production mechanisms (constituted by the forcing, in the present set-up) are negligible. Consequently, this scaling is found to be valid from scales $r \gtrsim 40\eta$ up to the scales at which energy injection has a direct effect. On the other hand, the scaling of the inertial enstrophy flux $-\langle \delta \xi^2 \delta u_r \rangle \approx \langle \epsilon \rangle / r$ is obtained by means of estimates. Nevertheless, it shows a good accordance with the data (figure 2.6(b)), approximating the slope of the two highest Reynolds curves in the inertial range. This result is in good agreement with what is observed in Baj et al. (2022). Both scaling laws appear to be approached as the Reynolds number increases, with the simulation at the highest Reynolds number $Re_\lambda \approx 400$ showing a good range of validity.

## 2.4 Wall-bounded flows

The presence of a solid boundary strongly modifies the classical picture of turbulence described in previous sections. The strong inhomogeneity and anisotropy imposed by the presence of a wall and of a mean shear challenges the development of a complete theory able to explain and predict the interplay between the elementary phenomena governing the flow. In the family of wall turbulent flows it is common to identify different regions based on their features. One of the categorisations distinguishes a near-wall region, a bulk region and an overlap region in between. In the near-wall region, the production of turbulent fluctuations exceeds their dissipation rate. The excess is transported towards the wall and towards the bulk region, where is finally dissipated. The overlap region lying between these two layers constitutes a region of local equilibrium between production and dissipation. The near-wall layer is certainly crucial to the dynamics of attached shear flows: it is dominated by intense interacting structures (Townsend, 1976; Robinson, 1991) and is the seat of the highest rate of turbulent energy production and of the highest turbulent intensities. In this region, turbulence is sustained by a self-sustaining and autonomous cycle (Jiménez and Pinelli, 1999). However, for high Reynolds numbers, also the outer overlap layer is thought to become relevant (see Smits et al. (2011) for a detailed review) being the site of self-sustaining mechanisms of large flow structures following mixed inner/outer scaling (Mizuno and Jiménez, 2013).

The strong inhomogeneity not only causes the phenomena mentioned above, but also affects the energy cascade mechanism itself. In fact, in wall turbulence, the classic energy cascade (dependent only on the scalar parameter $\langle\epsilon\rangle$) is replaced by anisotropic and inhomogeneous turbulence production and spatial fluxes. Such processes are strongly scale and position dependent and lead to a geometrically complex redistribution of energy where reverse energy cascade processes from small to large scales (Piomelli et al., 1991; Domaradzki et al., 1994; Härtel et al., 1994; Dunn and Morrison, 2005) play a fundamental role as shown in Cimarelli et al. (2013, 2016). Several fundamental features of wall turbulence have been unveiled by applying the generalized Kolmogorov equation to channel flows, see e.g. Danaila et al. (2001); Marati et al. (2004); Cimarelli et al. (2013, 2015b, 2016); Hamba (2018, 2019); Gatti et al. (2020); Zimmerman et al. (2022); Apostolidis et al. (2023)

Despite the relevance of the results obtained, when dealing with boundary layers, wall turbulence is characterized also by entrainment phenomena at the turbulent/non-turbulent interface (da Silva et al., 2014) whose phys-

ical features cannot be addressed in channel flows. Such phenomena make the study of boundary layers of a more general relevance for industrial and geophysical problems. However, the spatial inhomogeneity in the streamwise direction renders boundary layers more challenging for their study in comparison with streamwise-homogeneous channels especially when dealing with the generalized Kolmogorov equation. It should be noted that the Fourier transform is not applicable in the streamwise direction due to the inhomogeneity in such direction, thus strongly limiting also the use of the formalism given by the spectral energy budget often used in channel flows as a spectral counterpart of the generalized Kolmogorov equation, see e.g. Mizuno (2016); Cho et al. (2018); Lee and Moser (2019); Wang et al. (2021). A method to circumvent all these issues is to consider a temporally evolving boundary layer Kozul et al. (2016, 2020); Zhang et al. (2018, 2023), which has been shown to present statistical features very similar to those of the spatially evolving boundary layer.

The scenario outlined above sees energy and momentum as central quantities. However, it is not the only possibility. In fact, a picture based on vorticity is at least an equally interesting perspective. Vorticity is generated at the wall, due to the no-slip condition that allows the wall to generate tangential stresses, and is immediately injected in the fluid domain through diffusion. This injection of vorticity into the domain is called the "boundary vorticity flux". This flux in the near-wall region is in the opposite direction to the momentum flux (Eyink, 2008; Bechlars and Sandberg, 2017; Kumar et al., 2023). In particular, Lighthill (1963) introduced the idea that vorticity is generated at the wall through tangential pressure gradients (and eventual accelerations of the wall), causing a wall-normal vorticity flux in the fluid domain. Subsequently, this concept has been extended to curved walls by Lyman (1990). Lighthill and Lyman proposed two different formulations of the boundary vorticity flux, whose formulation cannot be unambiguously determined, although Lyman's interpretation is the most accepted at present (see Morton (1984); Wu and Wu (1993a, 1996, 1993b); Eyink (2008); Terrington et al. (2021) for a complete review). These two formulations of the boundary vorticity flux have recently been extended to enstrophy, thus to the boundary enstrophy flux, in Terrington et al. (2023).

Furthermore, vorticity dynamics also plays a role in the energy cascade process. Indeed, by applying the filtering formalism (as in Germano (1992)), it is possible to express the kinetic energy cascade rate in terms of the subgrid stresses and of the velocity field gradient, which in turn can be decomposed into a symmetrical (pure strain) and an anti-symmetrical (pure rotation) component (see Meneveau (2011) and Johnson and Wilczek (2024)

for a detailed review). In Johnson (2020) and Johnson (2021), the author evaluate the magnitude of the two contributions, finding that, in homogeneous isotropic conditions, strain-rate self-amplification accounts for a bit more than half of the intensity of the energy cascade, with vortex stretching accounting for the remaining part. These characteristics make vorticity statistics interesting as they can both give an insight into the topology of the structures involved in wall turbulence (as in Bechlars and Sandberg (2017); Kumar et al. (2023)) and a different view into areas where the energy cascade process is profoundly modified.

In the following, we briefly outline some of the notions that will be used throughout the thesis. In particular, we mention the different regions of a wall-turbulent flow, providing a few basic relations, and some of the features of the turbulent/non-turbulent interface which characterises the outer region of the boundary layer.

### 2.4.1 Flow regions

Many of the studies on wall turbulence are conducted on three canonical flows, which, in their simplicity, allow the possibility of capturing many of the features of wall turbulence. These paradigmatic flows are the channel flow, the pipe flow, and the boundary layer. In all these flows, it is possible to distinguish an internal dynamic (near the wall), and an external dynamic (far from the wall).

The mean velocity profile in the inner layer, as first postulated by Prandtl (1925), is independent of outer quantities such as, for the boundary layer, the external velocity $U_0$ and the boundary layer thickness $\delta$, but is only dependent on friction units. For high Reynolds numbers, the inner layer can be defined as the region $z/\delta \ll 1$, e.g. $z/\delta < 0.1$ (Pope, 2000). From the streamwise momentum flux equation it can be derived that universal friction velocity and friction length scales can be defined as:

$$u_\tau = \sqrt{\frac{\tau_w}{\rho}}, \qquad \ell_\nu = \frac{\nu}{u_\tau}, \tag{2.52}$$

where $\rho$ is the density of the fluid, $\nu$ is the kinematic viscosity and the wall shear stress:

$$\tau_w = \mu \frac{dU}{dz}, \tag{2.53}$$

being $\mu = \rho\nu$ the dynamic viscosity and $dU/dz$ the mean velocity gradient in the wall-normal direction $z$. The resulting non-dimensional velocities and

lengths are denoted with the superscript $\cdot^+$:

$$u^+ = \frac{u}{u_\tau}, \qquad z^+ = \frac{z}{\ell_\nu}. \tag{2.54}$$

It is now possible to define the friction Reynolds number:

$$Re_\tau = \frac{\delta u_\tau}{\nu}, \tag{2.55}$$

where $\delta$ corresponds to the boundary layer thickness, or equivalently, the half-width of the channel for the channel flow or the internal radius for the pipe flow.

In the inner layer it is possible to distinguish the viscous sublayer ($z^+ < 5$) where the Reynolds stresses are negligible with respect to the viscous stresses and the buffer layer ($5 < z^+ < 30$). In the viscous sublayer, for small $z^+$, by applying the Taylor-series expansion to the "law of the wall" (Pope, 2000) it is possible to obtain:

$$U^+ = z^+, \tag{2.56}$$

which is found to be a reasonable approximation up to $z^+ < 5$.

The outer layer, on the other hand, can be defined as the region in which the direct effects of viscosity on the mean profile are negligible, hence for $z^+ \gg 1$, e.g. $z^+ > 100$ as reported in figure 2.7. For high Reynolds numbers, an overlap region between $100 < z^+ < 0.1Re_\tau$ emerges (being $z^+ = 0.1Re_\tau$ equivalent to $z/\delta = 0.1$). This region is called the overlap layer and is a region of the flow in which both the inner and outer asymptotic are satisfied (meaning that both viscous effects and the dependence on the wall distance can be neglected). Many results and models concern this range of distances from the wall, which are of crucial importance for reduced order models. We briefly report some of them in the following.

The first relation that we report is the famous log-law

$$U^+ = \frac{1}{\kappa} \ln z^+ + B, \tag{2.57}$$

where $B$ is a constant and $\kappa$ is the von Kármán constant. The second result applicable in the overlap layer regards the turbulent shear stresses:

$$-\langle uw \rangle^+ = 1. \tag{2.58}$$

An interesting aspect that can be observed in the overlap layer is that the production and dissipation of turbulent kinetic energy almost balance each

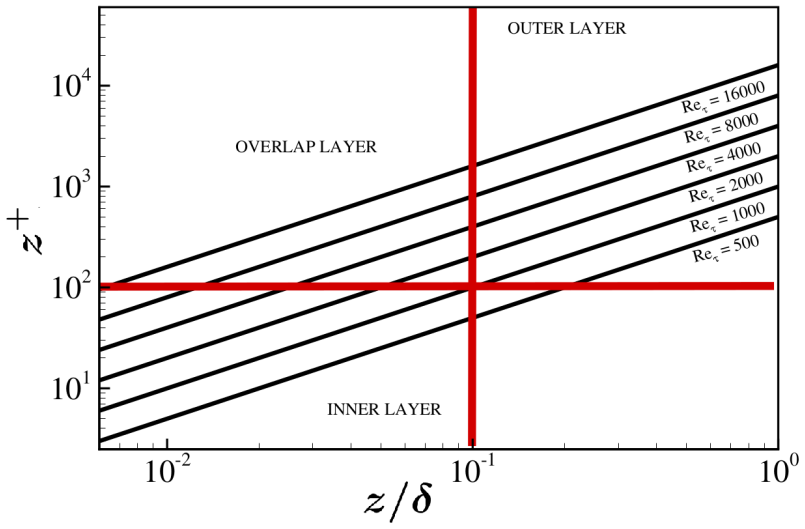


Figure 2.7: Inner, outer and overlap layers in wall turbulence for different Reynolds numbers. The conditions $z/h \ll 1$ and $z^+ \gg 1$ for the existence of the overlap layer are settled to $z/\delta < 0.1$ and $z^+ > 100$ and denoted with the red vertical and horizontal lines, respectively. Image taken and adapted from the lecture notes of the course "Turbulence" held by Prof. Andrea Cimarelli.

other out $-\langle uw \rangle dU/dz \approx \langle \epsilon \rangle = u_\tau^3/(\kappa z)$. For this reason, the overlap layer is also referred to as the "equilibrium layer". Through this observation and by applying theoretical arguments, it is possible to derive a scaling law for the Kolmogorov scale in the overlap layer, that in inner units reads:

$$\eta^+ = (\kappa z^+)^{1/4}, \tag{2.59}$$

indicating that the dissipative small scales increase in size as we move away from the wall. On the other hand, it is also possible to derive a scaling law for a scale that is linked to the energy-containing eddies, the shear-scale $\ell_S$ (Marati et al., 2004). In fact, by exploiting the equilibrium assumption and the scaling laws $|\delta \boldsymbol{u}| \sim |\boldsymbol{r}|(dU/dz)$ (velocity increment induced by shear) and $|\delta \boldsymbol{u}| \sim \langle \epsilon \rangle^{1/3} |\boldsymbol{r}|^{1/3}$ (inertial cascade scaling), it is possible to obtain the cross-over scale between the production-dominated and cascade-dominated eddies $\ell_S$. This scale is found to vary with the wall distance as:

$$\ell_S^+ = \kappa z^+. \tag{2.60}$$

Hence, despite the fact that both $\eta^+$ and $\ell_s^+$ increase with the distance from

the wall, the scale of the energy-containing eddies $\ell_s^+$ grows faster than the dissipative scale, which also increases the separation of scales and enables the presence of an inertial range in the overlap layer.

The most widely accepted phenomenological interpretation of what is observed in the overlap layer is certainly Townsend's attached eddy hypothesis (Townsend, 1951, 1961, 1976). We refer the reader to Marusic and Monty (2019) for an exhaustive review of the subject. The attached eddy hypothesis applies to inviscid, asymptotically high–Reynolds number wall-bounded flows. From this hypothesis derives the attached eddy model (Townsend, 1976), subsequently refined by Perry and Chong (1982). These models are based on the idea that the overlap layer is populated by a hierarchy of structures attached to the wall that are similar in size to their distance from it $\ell \sim z$. Therefore, the velocity at a wall-distance of $z$, will be influenced by the velocities of the attached eddies of size $\ell > z$. These eddies transfer their energy to smaller scales (detached eddies) at a rate $\langle \epsilon_\ell \rangle$. As explained in Nikora (1999), this effect, combined with the equilibrium assumption $-\langle uw \rangle dU/dz \approx \langle \epsilon \rangle \sim u_\tau^3/z \sim u_\tau^3 k$ lead to the following. The energy dissipation at a certain distance $z$ can be considered as the sum of the contributions of all the superimposed cascades with rate $\langle \epsilon_\ell \rangle$. Hence, starting with the largest scale present in the flow, corresponding to $k \sim 1/\delta$, the flux $\langle \epsilon \rangle$ increases with the wavenumber $k$ until it reaches $1/z$ and then stabilizes to $\langle \epsilon_\ell \rangle$. This fact leads to the following scalings:

$$E_{ii}(k_i) \sim \langle \epsilon(k_i) \rangle^{2/3} k_i^{-5/3} \sim u_\tau^2 k_i^{-1}, \qquad \text{for } (1/\delta) \leq k_i \leq 1/z \tag{2.61}$$

and the conventional Kolmogorov scaling for the direct cascade of detached motions:

$$E_{ii}(k_i) \sim \langle \epsilon(k_i) \rangle^{2/3} k_i^{-5/3} \sim \langle \epsilon_\ell(k_i) \rangle^{2/3} k_i^{-5/3}, \qquad \text{for } k_i \geq 1/z. \tag{2.62}$$

The above scaling relations (equations 2.61 and 2.62) only hold in the streamwise and longitudinal directions ($i = x, y$).

## 2.5 Turbulent/non-turbulent interface

The outer region of the boundary layer is governed by the turbulent entrainment phenomenon, which is a process that naturally occurs when a turbulent region faces a non-turbulent one from one or more sides, or more generally, it can take place between regions with different turbulent intensities. Through the turbulent entrainment, these two regions exchange

mass, momentum, and scalars, determining the growth, spreading and mixing of the flow considered. Taylor first hypothesised that the entrainment velocity is constant and proportional to a characteristic velocity of the flow $\langle u_e \rangle = \gamma U_0$, where $\langle u_e \rangle$ is the mean velocity of the fluid towards the interface and $\gamma$ is the entrainment coefficient. In boundary layers, this process is univocally related to drag. In fact, from the von Kármán integral equation we obtain $C_f = d\theta/dx$ (for spatially evolving boundary layers), where $C_f$ is the friction coefficient and $\theta$ is the momentum thickness, whose rate of change is determined by the entrainment occurring at the edge of the boundary layer. More precisely, the entrainment process takes place across the Turbulent/Non-Turbulent Interface (TNTI)(see da Silva et al. (2014) for a detailed review). Given its relevance for a wide range of applications, the TNTI, first examined by Corrsin and Kistler (1955), has been thoroughly studied and characterized in jets (Westerweel et al., 2005; da Silva and Taveira, 2010), wakes (Bisset et al., 2002; Zhou and Vassilicos, 2017), turbulent boundary layers (Borrell and Jiménez, 2016; Zhang et al., 2018, 2023), shear layers (Watanabe et al., 2015) and other flow configurations. The most distinctive feature characterizing either sides of a TNTI is vorticity (Corrsin and Kistler, 1955), which is the most natural metric to use in defining this interface. Through the vorticity equation it is possible to obtain:

$$\int_{\partial V(t)} \omega_i u_e \, dS = - \int_{\partial V(t)} \nu \frac{\partial \omega_i}{\partial x_j} \hat{n}_j \, dS \tag{2.63}$$

indicating that the increase in turbulent volume $V(t)$ due to entrainment is accomplished by viscous diffusion through the volume boundary $\partial V(t)$, being $\hat{n}_j$ the normal to it. This result is to be expected since the only way in which an initially irrotational particle can acquire vorticity is through a viscous process, dictating the presence of a viscous layer (named the "viscous superlayer") in between the turbulent and the non-turbulent regions. Below this laminar layer of thickness on the order of a few Kolmogorov scales $\eta$, a region of high turbulent intensity can be observed, called the "turbulent sublayer". The thickness of this layer is larger than the one of the viscous superlayer and has been measured in several flows, exhibiting a thickness on the order of one Taylor microscale $\lambda$ (Ruban and Vonatsos, 2008) or from 10 to 20 Kolmogorov scales $\eta$ (see Silva et al. (2018); Zecchetto and da Silva (2021) and references therein). However, the debate on the scaling units of this layer is still open. Although the entrainment process is ultimately completed by diffusion, the turbulent motions underneath the TNTI certainly have a great influence on it. Indeed, such turbulent motions impose both the gradients at the interface and its surface area, which together are the

only two factors that prescribe the diffusion rate. From a local perspective, the processes of diffusion and turbulent stirring can be seen as having two opposing effects on the gradients and thus contrast each other. Molecular diffusion causes homogenization of the considered field, thus eroding the gradients and the effectiveness of the diffusion itself. On the contrary, the turbulent stirring induced by the fluctuating velocity field sustains the gradients by distorting and pushing toward each other the iso-concentration surfaces (Sreenivasan, 2019). Analogously, the concurrent effect of turbulent motions and diffusion also imposes the area $S_\ell$ over which diffusion acts. In fact, the TNTI has the topology of a fractal surface (as well as other iso-surfaces in a turbulent flow (Sreenivasan et al., 1989)) with a theoretical dimension $D \approx 7/3$ with an upper cut-off coinciding with the largest scale present in the flow $L_0$ and a lower cut-off dictated by the smallest scale allowed by diffusion $\ell$ (i.e. the Kolmogorov scale for the velocity field $\ell = \eta$, and Batchelor scale for a scalar field $\ell = \eta_\theta$):

$$S_\ell = S_0 \left( \frac{\ell}{L_0} \right)^{2-D} \tag{2.64}$$

where $S_0$ is a reference area.

The turbulent stirring is usually distinguished in large-scale engulfment and small-scale nibbling (Mathew and Basu, 2002; Westerweel et al., 2005; Westerweel et al., 2009; Watanabe et al., 2015; Borrell and Jiménez, 2016; Jahanbakhshi and Madnia, 2016). The process of entrainment is initiated by the large-scale coherent structures of turbulence by engulfment and is then further processed by nibbling mechanisms at smaller and smaller scales produced by the turbulent cascade where, finally, molecular diffusion completes the turbulent entrainment and mixing (Cimarelli and Boga, 2021). It is then evident that turbulent mixing is a spatially evolving cascade process involving the full spectrum of scales (Sreenivasan, 1996; Schumacher and Sreenivasan, 2005; Schumacher et al., 2005; Cimarelli et al., 2015a, 2021) and different flow regions. More specifically, at the TNTI it is possible to observe the simultaneous presence of forward cascade processes for the normal-to-the-interface scales and reverse cascade processes for the parallel-to-the-interface scales. This has been observed both using classical statistics (Cimarelli et al., 2015a, 2021) and through local approaches by means of conditional averages (Watanabe et al., 2020; Zhou and Vassilicos, 2020).

# Chapter 3

# Temporal boundary layer

In the present chapter, we describe the flow configuration on which most of the analyses contained in this thesis work are carried out, the Turbulent Temporal Boundary Layer (TTBL). In addition, some of the main topics concerning wall turbulence are briefly investigated. With respect to the investigated themes, the TTBL has shown to qualitatively have the same features as the spatially developing boundary layer. The results presented in this chapter have been published in Cimarelli et al. (2024a).

## 3.1 Flow settings

The TTBL consists of an initially stationary fluid with a solid wall at the bottom ($z = 0$) moving with constant velocity $U_w$. Differently from the more classical spatially developing boundary layer, this flow evolves in time, presenting spatial homogeneity both in the spanwise ($y$) and in the streamwise directions ($x$). This simulation set-up has already been used in previous works (Kozul et al., 2016, 2020; Zhang et al., 2018, 2023), showing qualitatively similar features as the spatially evolving temporal boundary layer. In figure 3.1, an instantaneous snapshot showing the topology of the flow is reported.

The initial condition set for the streamwise velocity has been chosen so that it mimics the wake of a wall-mounted trip wire (widely used to trigger transition to turbulence in wind tunnel experiments):

$$u_d^*(x_d, y_d, z_d, t_d = 0) = (1 + c)\,\frac{U_w}{2}\left[1 + \tanh\left(\frac{D - z_d}{2h}\right)\right], \tag{3.1}$$

where $D$ is the diameter of the wire, while $h = 54\nu/U_w$ is the momentum thickness associated with the shear layer imposed. A white noise of intensity $0.1U_w$ (such that $c(x_d, y_d, z_d) \in [-0.05, 0.05]$) is superimposed to the initial condition in order to achieve a faster transition. The Reynolds number based on the tripping thickness is set to $Re_D = U_w D/\nu = 500$. In the above initial conditions, the subscript "$d$" ($\cdot_d$) is used to denote dimensional quantities.

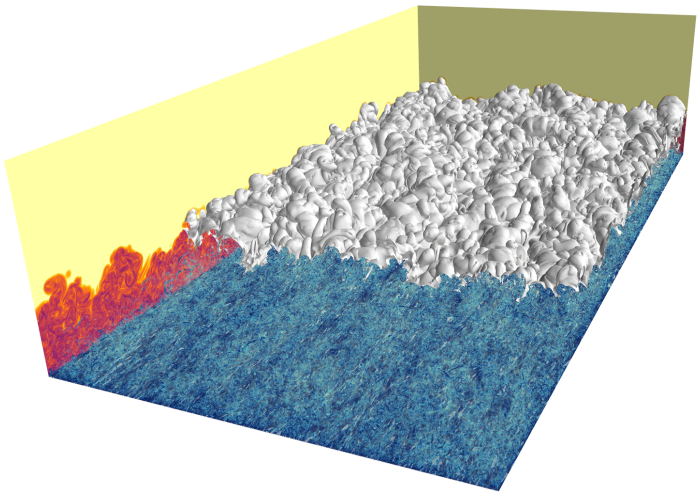

Figure 3.1: Instantaneous snapshot of the enstrophy field $\xi = \omega_i\omega_i$ of the temporal boundary layer at $Re_\tau = 1500$. Respectively slices in logarithmic scale in the background (from yellow, indicating low values, to purple, indicating higher values), portion of isosurface of enstrophy $\xi = 1.4 \cdot 10^{-6}\langle\xi\rangle|_w$ (grey) and volume rendering of enstrophy (from transparent yellow, indicating low values, to opaque blue, indicating higher values). Figure taken from Cimarelli et al. (2024b).

In the rest of the paper, equations and quantities, unless otherwise specified, are expressed in dimensionless form by using $D$ and $U_w$. We recall that the asterisk $(\cdot^*)$ denotes total quantities.

In the streamwise and spanwise directions, periodic boundary conditions are imposed. In the wall-normal direction, a Dirichlet boundary condition for the velocity is used at the wall, by imposing $u^*(x, y, z = 0) = 1$ and $v^*(x, y, z = 0) = w^*(x, y, z = 0) = 0$, while at the top of the domain $(L_z)$, a free-slip impermeable condition $w^*(x, y, z = L_z) = 0$ and $(\partial u^*/\partial z)|_{L_z} = (\partial v^*/\partial z)|_{L_z} = 0$ is used. In Figure 3.2, the temporal evolution of the flow is shown by reporting slices of modulus of instantaneous spanwise vorticity $|\omega_y^*|$ at different time instants corresponding to different values of friction Reynolds number $Re_\tau$.

The simulations have been carried out using the DNS code CaNS (Costa, 2018), that employs a standard pressure-projection method and a staggered second-order finite-difference scheme for the spatial discretization. Time integration is carried out using a mixed approach. In particular, the viscous terms in the wall-normal direction are integrated implicitly through the use of a Crank–Nicholson scheme, while all the other terms are integrated explic-

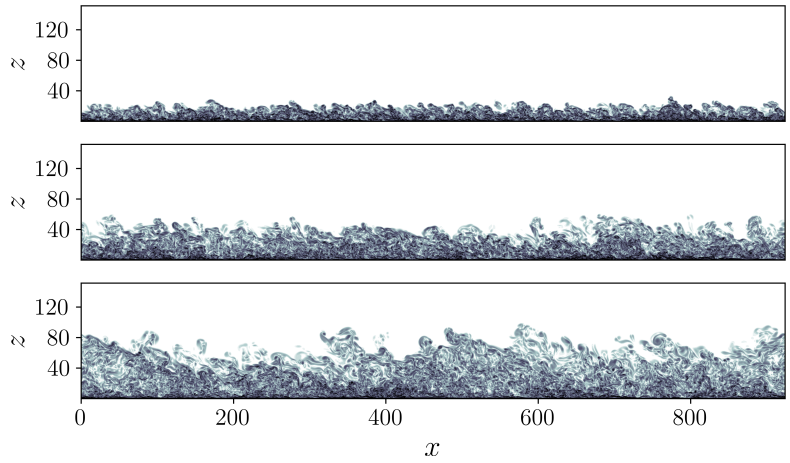


Figure 3.2: Instantaneous contours of modulus of span-wise vorticity $|\omega_y^*|$ at three different time instants corresponding (from top to bottom) to $Re_\tau = 500$, 1000 and 1500. Darker colour indicates a greater intensity.

itly by using a three-step Runge–Kutta method with a CFL = 0.95. The domain size in the vertical direction is chosen in order to have a final boundary layer thickness that is 1/3 of the domain height in order to avoid confinement effects, see again Kozul et al. (2016). On the other hand, the wall-parallel dimensions of the numerical domain are chosen in order to be able to accommodate the long and wide structures classically known to occur in wall turbulence. The resulting domain size is $(L_x, L_y, L_z) = (924, 462, 220)\,D$, discretized by using a number of grid points $(N_x, N_y, N_z) = (3072, 3072, 768)$ that leads to a spatial resolution in the spatially homogeneous directions of $(\Delta x^+, \Delta y^+) = (5.8, 2.9)$ at the final Reynolds number reached by the simulations. The grid is chosen in order to have a good resolution also at the time instant in which the viscous length is minimum. This instant occurs in the early stage of the simulation (as shown in figure 3.3(a) from the peak in the friction coefficient $C_f$), and even at this stage the resolution is $(\Delta x^+, \Delta y^+, \Delta z_w^+) = (8.7, 4.4, 0.13)$, being $\Delta z_w^+$ the resolution in the wall-normal direction at the wall. The grid is homogeneous in $x$ and $y$ directions and is stretched in the wall-normal direction using a standard error function clustering with a stretching parameter $\alpha_z = 2.25$ (reference in chapter 2 in Orlandi (2000)). Additional information are reported in table 3.1.

In order to improve the statistical convergence of the results, four independent simulations have been carried out by changing the seed of the

Table 3.1: Domain size and spatial resolution evaluated at three time instants corresponding to $Re_\tau = 500$, 1000 and 1500. $\Delta z_\delta$ is the wall-normal resolution at $z = \delta$, being $\delta$ the boundary layer thickness.

| $Re_\tau$ | $(L_x, L_y, L_z)/\delta$ | $\Delta x^+$ | $\Delta y^+$ | $\Delta z_w^+$ | $\Delta z_\delta^+$ | $\Delta z_\delta/\eta$ |
|---|---|---|---|---|---|---|
| 500 | $42.5, 19.6, 10.1$ | 6.7 | 3.4 | 0.10 | 4.2 | 0.66 |
| 1000 | $18.5, 9.3, 4.4$ | 6.1 | 3.0 | 0.09 | 7.1 | 0.95 |
| 1500 | $11.9, 5.9, 2.8$ | 5.8 | 2.9 | 0.09 | 9.2 | 1.13 |

pseudo-random noise $c$ in the initial condition (equation 3.1). Averages quantities are indicated with $\langle\cdot\rangle$ and are computed by spatial averaging in the wall-parallel homogeneous directions ($x$ and $y$) and by ensemble averaging between the four independent realizations of the flow. The standard Reynolds decomposition is adopted and denoted as $u_i^* = U_i + u_i$, where $u_i^*$ is the total velocity field, while $U_i = \langle u_i^* \rangle$ and $u_i$ are respectively the mean and fluctuating velocity fields.

## 3.2 Main flow features

The flow configuration of the temporal boundary layer has been less thoroughly investigated in the literature with respect to the more classical spatially evolving boundary layer and most of the works on the TTBL are relatively recent (see again Kozul et al. (2016, 2020); Zhang et al. (2018, 2023)). For this reason we start our analysis by characterizing this flow and by addressing some basic topics commonly pursued in boundary layers.

As a first step, we start by analysing the evolution of some basic integral quantities as the friction coefficient $C_f$ and the friction Reynolds number $Re_\tau$. In figure 3.3 (a), the temporal evolution of these two quantities is reported as a function of the momentum thickness Reynolds number $Re_\theta = U_w\theta/\nu$ together with the classical scaling of the zero pressure gradient turbulent boundary layer. The friction coefficient appears to follow the classical relation $C_f \sim 0.024 Re_\theta^{-1/4}$ that has been extensively verified in the spatially evolving turbulent boundary layer through both DNS and experimental investigations (Schlichting and Kestin (1961); Schlatter et al. (2010), to provide some examples). The scaling of the friction Reynolds number $Re_\tau \sim Re_\theta^{7/8}$ is also found to be in good agreement with the theory. In our simulations the proportionality factor between these two quantities is measured to be 0.93, which is quite similar to the fitting $Re_\tau \approx 1.13 Re_\theta^{0.843}$ obtained in Schlatter and Örlü (2010) for the spatial boundary layer. In fig-

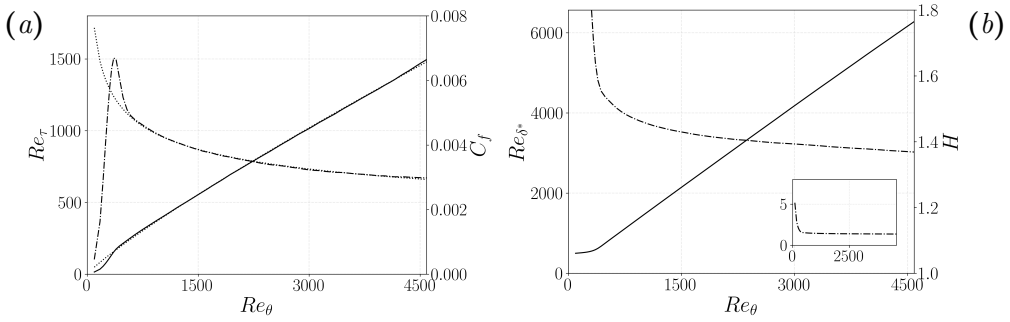


Figure 3.3: (a) Evolution of the friction Reynolds number $Re_\tau$ (solid line) and of the friction coefficient $C_f$ (dash-dotted line) as a function of the Reynolds number based on the momentum thickness $Re_\theta$ . The two respective fitting laws have been reported in dotted line. (b) Evolution of the Reynolds number based on the displacement thickness $Re_{\delta^*}$ (solid line), and of the shape factor $H$ (dash-dotted line). In the inset, the shape factor is shown in a different scale.

ure 3.3(b), the evolution of the shape factor $H = \delta^*/\theta$ and of the Reynolds number based on the displacement thickness $Re_{\delta^*} = U_w\delta^*/\nu$ are reported. Also the trend of $H$ as function of $Re_\theta$ is again in good agreement with the results of the spatial boundary layer found in the literature (Monkewitz et al., 2007). Equivalently, the trend of $Re_{\delta^*}$ is reported, being the shape factor $H = Re_{\delta^*}/Re_\theta$ equal to the slope of this curve.

We now proceed to analyze the mean velocity profiles at three values of $Re_\tau$, shown in figure 3.4(a). The diagnostic function $\Xi(z) = z^+\partial U^+/\partial z^+$ is also reported, in order to better visualize the value of the von Kármán constant $\kappa$ in the overlap region. In order to recover the classical view of wall turbulence, figure 3.4(a) we reported the velocity difference with respect to the velocity of the wall, being $U_w$ non-null. In the viscous sublayer, up to $z^+ \approx 5$, the linear relation $u^+ = z^+$ provides a good approximation. Another fundamental law in wall turbulence is the relation $u^+ = 1/\kappa \ln z^+ + B$, valid in the overlap region. From the diagnostic function, it appears that the Reynolds number is not high enough to show a properly extended plateau region (corresponding to a purely logarithmic curve), but the logarithmic law is found to approximate reasonably well the lower part of the overlap layer, for $40 < z^+ < 0.1Re_\tau$, using the fitting values of $\kappa = 0.436$ and $B = 5.75$. It should be pointed out that, by using the values obtained by Marusic et al. (2010) on high Reynolds numbers data ($\kappa = 0.384$ and $B = 4.173$), we obtain a reasonable fitting in the outer overlap region of

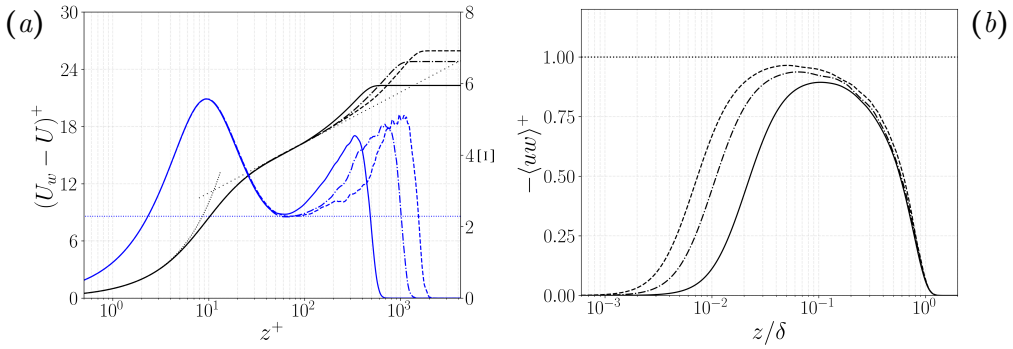


Figure 3.4: (a) Mean velocity profiles $(U_w - U)$ (black lines) and relative diagnostic function $\Xi$ (blue lines) at different time instants corresponding to friction Reynolds number of $Re_\tau = 500$ (solid lines), $Re_\tau = 1000$ (dash-dotted lines) and 1500 (dashed lines). The linear and logarithmic behaviour are reported in dotted lines. (b) Profiles of Reynolds shear stresses compared with $u_\tau^2$ (dotted line) at $Re_\tau = 500$ (solid line), $Re_\tau = 1000$ (dash-dotted line) and 1500 (dashed line).

profile at the highest $Re_\tau$ in the present results. In particular, these values are found to better approximate the interval $120 < z^+ < 0.16Re_\tau$. Another consequence of the separation of the scales of motions involved, can be seen in the profile of the Reynolds shear stresses reported in figure 3.4(b), that, for high Reynolds numbers should reach the asymptotic limit $-\langle uw \rangle^+ = 1$.

One of the important topics under debate in the wall-turbulence context regards the anomalous inner scaling of the turbulent fluctuations. In figure 3.5(a), the turbulence intensity in its three components is reported at different Reynolds numbers. The highest turbulent fluctuations can be observed in the buffer layer. In particular, the predominant component is constituted by the streamwise velocity fluctuations. The main subject of debate regards the inner scaling of these components of the Reynolds stresses. In particular, a Reynolds number dependence is observed in these near-wall quantities, despite the universality verified in the mean flow, once rescaled in inner units with the kinematic viscosity $\nu$ and the wall shear stress $\tau_w$ (i.e. with $u_\tau$ for velocities and $\nu/u_\tau$ for lengths). In fact, as shonw in figure 3.5(b), an increase is observed in the intensities of the streamwise and spanwise turbulent fluctuations as the Reynolds number increases. Mainly, two scaling laws were proposed in order to correct the trend of the streamwise

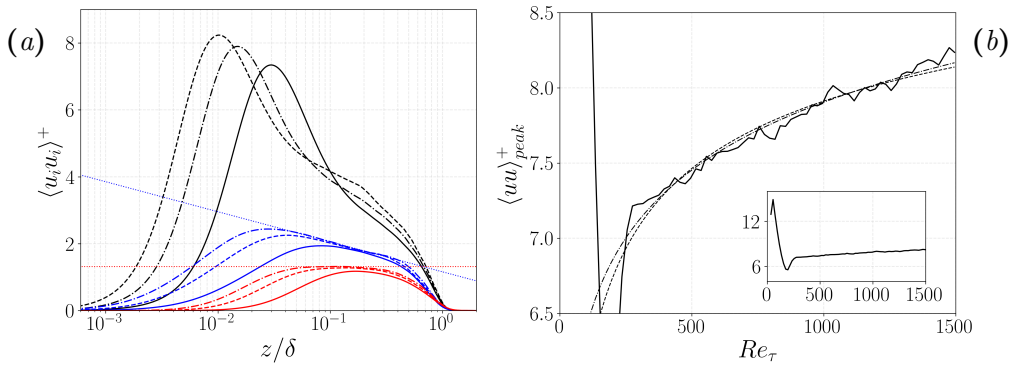


Figure 3.5: (a) Turbulence intensities $\langle uu \rangle$ (black lines), $\langle vv \rangle$ (blue lines) and $\langle ww \rangle$ (red lines), at three different time instants corresponding to friction Reynolds number of $Re_\tau = 500$ (solid lines), $Re_\tau = 1000$ (dash-dotted lines) and 1500 (dashed lines). The fitting laws are reported in dotted lines. (b) Evolution of the streamwise turbulence intensity inner peak value (solid line) as a function of the friction Reynolds number. The scaling laws from equation 3.2 are reported in dash-dotted line (logarithmic law) and in dotted line (power law). In the inset, the same quantity is reported in a different scale.

turbulence intensity peak $\langle uu \rangle^+_{peak}$:

$$\begin{aligned} \langle u^2 \rangle^+_{peak} &\sim A \ln (Re_\tau) + B, \\ \langle u^2 \rangle^+_{peak} &\sim \alpha \left( 1/4 - \beta Re_\tau^{-1/4} \right). \end{aligned} \tag{3.2}$$

The first proposed scaling results from the inner-outer interaction between near-wall and outer eddies (Marusic et al., 2017), while the second scaling reported is based on the constraint provided to dissipation by the maximum asymptotic value of turbulence production (Chen and Sreenivasan, 2021). These two scaling laws present a similar behaviour for low and intermediate Reynolds numbers, but their trend start to deviate more significantly at high Reynolds numbers. The present data, can be reasonably fitted with both the two scaling laws (figure 3.5(b)), since the Reynolds numbers involved are not high. The parameters used are respectively $A = 0.65$ and $B = 3.40$ for the logarithmic law and $\alpha = 41.1$ and $\beta = 0.32$ for the power law. This measured values are roughly consistent with those found in the literature for other more classical wall-bounded flows: being $A = 0.63$, $B = 3.80$, $\alpha = 46$ and $\beta = 0.42$.

Another feature of the turbulent intensities profiles that deserves attention, is their trend in the overlap layer. According to Townsend's original

work (Townsend, 1976), the overlap layer can be viewed as an equilibrium layer, in which the shear stress is constant and equal to $\rho u_\tau$, and where turbulence production and dissipation almost balance. This layer is thought to be populated by a hierarchy of self-similar eddies attached to the wall. As a consequence, the characteristic lengths of these eddies must proportional to the distance from the wall. The so-called attached eddy model (Marusic and Monty, 2019) is based on these arguments. This model appears capable of giving a physical explanation to several statistical features of wall turbulence while also providing quantitative predictions in the overlap layer. Among these predictions, the attached eddy model provide the scaling laws for the three turbulence intensities:

$$\begin{aligned} \langle u^2 \rangle^+ &\sim B_1 - A_1 \ln\left(z/\delta\right), \\ \langle v^2 \rangle^+ &\sim B_2 - A_2 \ln\left(z/\delta\right), \\ \langle w^2 \rangle^+ &\sim B_3. \end{aligned} \tag{3.3}$$

Both experiments and numerical simulations at high Reynolds numbers have shown a good agreement with these laws (for a more extensive overview see Marusic and Monty (2019) and references contained therein). As shown in figure 3.5(a), the data from the present temporal boundary layer simulations are also in good accordance, although the limited Reynolds number, made exception for the law of $\langle uu \rangle^+$. The values of the constants measured in the present results are respectively $B_2 = 1.16$, $A_2 = 0.39$ and $B_3 = 1.32$. From figure 3.5(a), a logarithmic region may appear to be present also in the profile of $\langle uu \rangle^+$, but its range of extension is inconsistent with the overlap layer region. In order to observe a fully developed logarithmic behaviour in the profile of $\langle uu \rangle^+$, a much higher Reynolds number is required. Another important prediction resulting from the attached eddy model concerns the scaling law for the turbulent spectra in the overlap layer. In fact, the superposition of Kolmogorov's like energy cascade, triggered by eddies whose size is proportional to the wall distance within an equilibrium layer where production follows the law of the wall and balances dissipation, leads to the following scaling of the energy spectra (as shown in Nikora (1999)):

$$\begin{aligned} E_{uu}\left(k_x\right) &\sim u_\tau^2 k_x^{-1} \qquad \text{for} \qquad \frac{1}{\delta} < k_x < \frac{1}{z}, \\ E_{uu}\left(k_x\right) &\sim \left(\frac{u_\tau^3}{\kappa z}\right)^{2/3} k_x^{-5/3} \qquad \text{for} \qquad k_x > \frac{1}{z}, \end{aligned} \tag{3.4}$$

where $E_{uu}$ is the energy spectrum of streamwise velocity fluctuations and $k_x$ is the streamwise wavenumber. Therefore, for scales smaller than the local

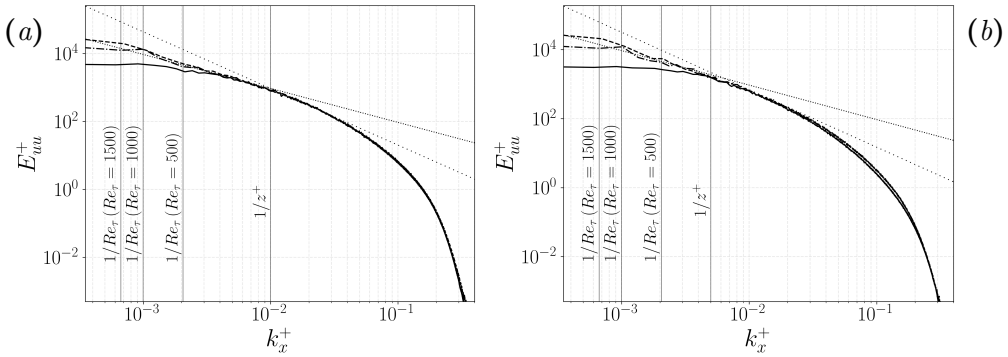


Figure 3.6: Longitudinal energy spectra of streamwise velocity fluctuations $E_{uu}$ in the streamwise wavenumber $k_x$ evaluated in the overlap layer at (a) $z^+ = 100$ and (b) $z^+ = 200$ for three different friction numbers $Re_\tau = 500$ (solid lines), $Re_\tau = 1000$ (dash-dotted lines) and $Re_\tau = 1500$ (dashed lines). The scaling laws $k_x^{-1}$ (dotted lines) and $k_x^{-5/3}$ (loosely dotted lines) are reported together with the respective cross-over scales $1/z$ and $1/\delta$ (vertical solid lines).

wall distance (i.e. detached eddies), a classical energy cascade with the scaling $k_x^{-5/3}$ is expected, while for scales of the same order or larger than the wall distance, a $k_x^{-1}$ scaling is expected. In figure 3.6, the streamwise energy spectra in the streamwise wavenumber obtained by the present data is reported and compared with the scalings predicted by the attached eddy model at two different wall distances in the overlap layer. In the two higher Reynolds number cases, in which the separation of scales is sufficiently high, it is possible to observe a good agreement with this model. The cross-over scale between the two scaling laws is also found to be of the order of the wall distance, corresponding to a wavenumber $k_x = 1/z$.

# Chapter 4

# Turbulent kinetic energy

In the present chapter, we address the issues of energy transfer and production applied to the previously described Turbulent Temporal Boundary Layer (TTBL) setup. In section 4.1, the view provided by the single-point budget of Turbulent Kinetic Energy (TKE) is presented. This view is then expanded to the space of scales via the GKE in section 4.2. In this section, the results are presented on some subspaces of the compound space offered by the GKE, allowing for more macroscopic or more detailed views depending on the purpose. The data of a channel flow at equal friction Reynold number ($Re_\tau = 1500$) are exploited to highlight the effect of the presence of the TNTI in the TTBL. The results contained in the present chapter have been published on Cimarelli et al. (2024a,b)

## 4.1 Single-point budget

Before addressing the Generalized Kolmogorov Equation (GKE), we start by analyzing the single-point budget of turbulent kinetic energy $k = u_i u_i/2$. These budget will be useful to have a general picture of the different regions of the flow before investigating the scale-by-scale behaviour. For the symmetries of the temporal boundary layer, the turbulent kinetic energy budget equation reads:

$$\begin{gathered}\frac{\partial\langle k\rangle}{\partial t} = T + T_p + D + P - \langle\epsilon\rangle, \\ T = -\frac{\partial\langle kw\rangle}{\partial z}, \qquad T_p = -\frac{1}{\rho}\frac{\partial\langle pw\rangle}{\partial z}, \qquad D = \nu\frac{\partial^2\langle k\rangle}{\partial z^2}, \\ P = \langle uw\rangle\frac{\partial U}{\partial z}, \qquad \langle\epsilon\rangle = \nu\langle\frac{\partial u_i}{\partial x_j}\frac{\partial u_i}{\partial x_j}\rangle.\end{gathered} \tag{4.1}$$

$T_p$ is the pressure transport term, $T$ and $D$ are respectively the turbulent and diffusive transport terms, $P$ is the production and $\langle\epsilon\rangle$ is the dissipation. The behaviour of the different terms is reported in figure 4.1. At a first glance, it is possible to notice that transport terms appear to be relevant

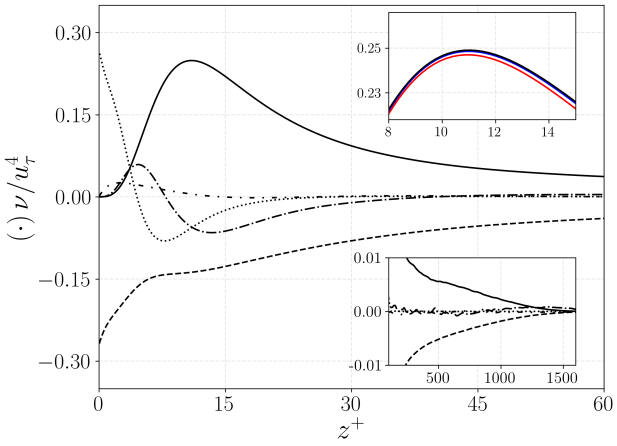


Figure 4.1: Turbulent kinetic energy budget in viscous units at a friction Reynolds number $Re_\tau = 1500$. Turbulent production $P$ is reported in solid lines, turbulent transport $T$ in dash-dotted lines, diffusive transport $D$ in dotted lines, pressure transport $T_p$ in loosely dash-dotted lines and dissipation $-\langle\epsilon\rangle$ in dashed lines. In the bottom inset the budget terms are reported on a larger scale to show the outer region. In the top inset the production $P$ peak at different Reynolds numbers is reported, $Re_\tau = 500$ (solid red line), 1000 (solid blue line), 1500 (solid black line).

only in the near-wall region, while the outer region appears to be in a local equilibrium between turbulent production and dissipation, as shown in the lower inset. The region very close to the wall is dominated by diffusive transport and dissipation, while turbulent production appear to become relevant for $z^+ > 5$. In the upper inset of figure 4.1, the peak of production at different Reynolds numbers is shown. As the Reynolds number increases, the value of this peak should asymptotically reach the value of $1/4$ at a wall distance of $z^+ = 11$ (Laadhari, 2002). The two highest Reynolds numbers shown, $Re_\tau = 1000$ and $Re_\tau = 1500$, seem to approach this limit as expected.

In order to obtain a more concise and easy-to-understand picture of what is shown in figure 4.1, it is possible to rewrite equation 4.1 in term of a net source $s$ and of the divergence of fluxes $\psi$. In the temporal boundary layer

flow configuration, this equation reads:

$$\begin{aligned} \frac{\partial \psi}{\partial z} &= s, \\ s &= -\frac{\partial \langle k \rangle}{\partial t} - \langle uw \rangle \frac{\partial U}{\partial z} - \langle \epsilon \rangle, \\ \psi &= \langle kw \rangle + \frac{1}{\rho} \langle pw \rangle - \nu \frac{\partial \langle k \rangle}{\partial z}. \end{aligned} \tag{4.2}$$

In figure 4.2, the net source $s$ and the fluxes $\psi$ are reported at different friction Reynolds numbers. From this first macroscopic view, it is already possible to identify two regions of great importance for wall turbulence. The

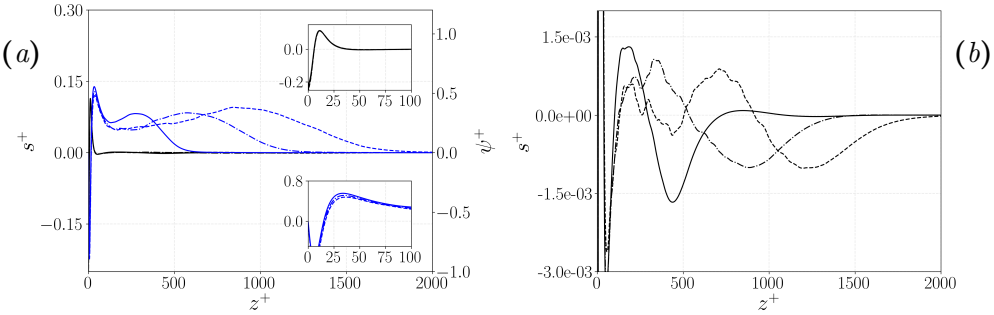


Figure 4.2: (a) Extended source $s^+$ (black lines) and spatial flux $\psi^+$ (blue lines) of turbulent kinetic energy for three different evolution times corresponding to $Re_\tau = 500$ (solid), 1000 (dash-dotted) and 1500 (dashed). The two insets report an enlarged view of the near-wall behaviour. (b) Enlarged view of the second-outer source of turbulent kinetic energy. Figure taken and adapted from Cimarelli et al. (2024a)

source term $s$ identifies the buffer layer region (approximately $5 < z^+ < 60$), where turbulent net production is positive, and a viscous sublayer ($z^+ < 5$) that acts as the main sink of turbulent kinetic energy. As expected from equation 4.2, the spatial flux show a flex point in the peak location of the source term (located in $z^+ = 11$, at a value of $s^+_{max} = 0.11$, as in accordance with Cimarelli et al. (2015b)). From the proximity of this flex point, the flux diverges, exhibiting also a change in sign. In fact, from this region of high production, the flux feeds both the viscous sublayer and the outer region. The flux reaches a peak around $z^+ = 35$ from where it start decreasing, as the net source becomes negative. By taking a look at the net source on an enlarged scale, as shown in figure 4.2(b), it is possible to observe a slightly positive peak, meaning that what appeared to be an equilibrium layer in figure 4.1 actually constitutes a slightly positive outer energy source.

Although weaker in intensity with respect to the inner one, this source is expected to become dominant at high Reynolds numbers. In fact, its mixed scaling in inner/outer units, makes its contribution increase as the Reynolds number increases. In the present results we measure its extension to be approximately $100 < z^+ < 0.55Re_\tau$. Accordingly, the spatial flux in this region is energized by the outer source and increases reaching its maximum near the end of the outer source extension, i.e. $z^+ \approx 0.55Re_\tau$. The value of the outer peak in the flux also increases as the Reynolds number increases, as a result of the increasing energy introduced by the outer source. Energy is finally released and dissipated at $z^+ > 0.55Re_\tau$. At the same time, the increasing contribution given by the outer energy source, also limits the spatial fluxes coming from the near-wall region toward the outer region. The result of this can be seen in the lower inset in figure 4.2(a), where the decrease of the inner peak of the flux with $Re_\tau$ is shown. As conjectured in Cimarelli et al. (2015b), the repulsion effect of the outer source that acts as a confinement for the near-wall dynamics, could have a connection with the anomalous scaling with $Re_\tau$ observed in the inner peak of turbulence intensities show in figure 3.5(b).

It is possible to notice that the spatial flux is still active at wall distances higher than the mean interface position, i.e. $z^+ > Re_\tau$. This is due to the presence of potential fluctuations in the irrotational region (Zecchetto et al., 2024). These fluctuations are the result of non-local phenomena of displacement of otherwise quiescent fluid performed by the large-scale structures populating the turbulent core of the boundary layer (Cimarelli et al., 2021). Accordingly, the fluctuations of the external region are non-turbulent and irrotational in nature and the spatial flux feeding them is non-diffusive, $\psi \approx \langle kw \rangle + \langle pw \rangle / \rho$.

The picture depicted by the turbulent kinetic energy budget illustrated above conforms well with the results observed in other more classical flow configurations, such as channel and pipe flows (see e.g. Bernardini et al. (2014); Lee and Moser (2015); Pirozzoli et al. (2021)).

## 4.2 Two-point budget

After the brief description that led us to identify the different regions of the flow and its main features, we can go into greater depth by investigating the processes of energy transfer and production in the space of scales in addition to the physical space. To this aim, we must employ a tool that allows us to capture the multiscale nature of the processes involved. In this perspec-

tive, the use of two-point statistics is demanding. Several works in the past have shown that the generalized Kolmogorov equation (Hill, 2002) represents a sufficiently general statistical formalism to address the multidimensional cascade processes of turbulence from its production to its dissipation. Examples of its application in wall turbulence are Danaila et al. (2001); Marati et al. (2004); Cimarelli et al. (2013, 2016); Chiarini et al. (2022); Yao et al. (2022); Zimmerman et al. (2022), in thermally driven turbulence are Rincon (2006); Togni et al. (2015), in separated and reattaching flows are Mollicone et al. (2018); Gatti et al. (2020) and in turbulent jets and wakes are Burattini et al. (2005); Gomes-Fernandes et al. (2015); Portela et al. (2017); Cimarelli et al. (2021).

As described in chapter 2, the generalized Kolmogorov equation is written in terms of the second-order structure function of the fluctuating velocity field

$$\langle \delta q^2 \rangle = \langle \delta u_i \delta u_i \rangle, \tag{4.3}$$

where $\delta u_i = u_i\left(x', t\right) - u_i\left(x'', t\right)$ is the increment of the fluctuating velocity. Hereafter, we will often refer to the second-order structure function as the scale energy even if such an interpretation is somewhat arguable especially in inhomogeneous flows for large separations, see the discussion in Cimarelli et al. (2016) and the possible alternative expression derived in Hamba (2018). Here, we develop the formalism for the symmetries of a temporal evolving turbulent boundary layer. In these settings, the generalized Kolmogorov equation, in symbolic form reads

$$\begin{gathered}
\frac{\partial \langle \delta q^2 \rangle}{\partial t} = T_r + D_r + T_c + \Pi - E, \\
T_r = -\frac{\partial \langle \delta q^2 \rangle \delta U}{\partial r_x} - \frac{\partial \langle \delta q^2 \delta u_i \rangle}{\partial r_i}, \qquad D_r = 2\nu \frac{\partial^2 \langle \delta q^2 \rangle}{\partial r_i \partial r_i}, \\
T_c = -\frac{\partial \langle \delta q^2 \widetilde{w} \rangle}{\partial z_c} - \frac{2}{\rho} \frac{\partial \langle \delta p \delta w \rangle}{\partial z_c} + \frac{\nu}{2} \frac{\partial^2 \langle \delta q^2 \rangle}{\partial {z_c}^2}, \\
\Pi = -2 \langle \delta u \delta w \rangle \widetilde{\left( \frac{\partial U}{\partial z} \right)} - 2 \langle \delta u \widetilde{w} \rangle \delta \left( \frac{\partial U}{\partial z} \right), \qquad E = 4 \langle \widetilde{\epsilon} \rangle
\end{gathered} \tag{4.4}$$

where $U = U(z,t)$ is the mean streamwise velocity, $\boldsymbol{r} = \boldsymbol{x'} - \boldsymbol{x''}$ is the two-point separation vector, $\boldsymbol{x_c} = (\boldsymbol{x'} + \boldsymbol{x''})/2$ is the position vector of the mid-point and $\widetilde{\cdot}$ denotes the two-point average. Finally,

$$\langle \epsilon \rangle = \nu \langle \frac{\partial u_i}{\partial x_j} \frac{\partial u_i}{\partial x_j} \rangle \tag{4.5}$$

is the turbulent pseudo-dissipation. $T_r$ and $D_r$ are the scale-energy exchanges among different scales respectively due to inertial and viscous diffusion mechanisms, $T_c$ is the scale-energy exchange among different wall distances and $\Pi$ and $4\langle\widetilde{\epsilon}\rangle$ are the source and sink terms of turbulence related with production due to mean shear and turbulent dissipation, respectively.

To highlight its conservative form, equation (4.4) can also be rewritten as

$$\frac{\partial\langle\delta q^2\rangle}{\partial t} + \boldsymbol{\nabla_4}\cdot\boldsymbol{\phi} = S, \tag{4.6}$$

thus emphasizing that the Kolmogorov equation represents an exact and formally precise formalism for the study of the hyperflux of scale energy in the compound space of scales through the three-dimensional flux

$$\phi_{r_i} = \partial\langle\delta q^2\delta u_i\rangle + \langle\delta q^2\delta U\rangle\delta_{i1} - 2\nu\frac{\partial\langle\delta q^2\rangle}{\partial r_i} \tag{4.7}$$

and physical space through the one-dimensional flux

$$\phi_{c_z} = \langle\delta q^2\widetilde{w}\rangle + \frac{2}{\rho}\langle\delta p\delta w\rangle - \frac{\nu}{2}\frac{\partial\langle\delta q^2\rangle}{\partial z_c} \tag{4.8}$$

from the production to the dissipation regions of the augmented space of turbulence identified by the source term

$$S = -2\langle\delta u\delta w\rangle\widetilde{\left(\frac{\partial U}{\partial z}\right)} - 2\langle\delta u\,\widetilde{w}\rangle\,\delta\left(\frac{\partial U}{\partial z}\right) - 4\langle\widetilde{\epsilon}\rangle\ . \tag{4.9}$$

In the following subsections we will only consider the data at the highest Reynolds number reached in the present simulations (i.e. $Re_\tau = 1500$). We will begin our analysis by investigating the 3D compound space constituted by the streamwise and spanwise separation lengths $r_x, r_y$ for the space of scales and by the wall distance $z_c$ for the physical space at $r_z = 0$ in subsection 4.2.1. In subsection 4.2.2, the analysis will proceed by taking a deeper insight in the simplified 2-D subspace constituted by the $r_y, z_c$ space, which is thought to be to some degree characterizing for canonical wall turbulent flows. In this subsection, data from a channel flow at the same Reynolds number ($Re_\tau = 1500$ from Cimarelli et al. (2015b)) will be exploited in order to better study the effect of the presence of a free Turbulent/Non-Turbulent Interface (TNTI) and to be able to compare how the multiscale phenomena change in the region of the TNTI itself with respect to the centreline of the channel. Finally, the analysis will be concluded in subsection 4.2.3 with a more quantitative view of the multiscale phenomena observed by further limiting the analysis to profiles in the $r_y$ scale at some selected wall distances.

### 4.2.1 Paths of scale energy and sources in the $(r_x, r_y, z_c)$ compound space

In the 3D subspace constituted by $(r_x, r_y, z_c)$, equation 4.6 can be rewritten in the form

$$\left.\frac{\partial \phi_{r_\pi}}{\partial r_\pi}\right|_{r_z=0} + \left.\frac{\partial \phi_{c_z}}{\partial z_c}\right|_{r_z=0} = \zeta_{r_z=0}, \tag{4.10}$$

where $\pi = x, y$ denotes the statistically homogeneous streamwise and spanwise directions and $\zeta_{r_z=0}$ is the extended source term that together with production and dissipation takes into account also the time variation of the local scale-energy content and the scale-energy exchange with the $r_z \neq 0$-space,

$$\zeta_{r_z=0} = -\left.\frac{\partial \langle \delta q^2 \rangle}{\partial t}\right|_{r_z=0} - 2\langle \delta u \delta w \rangle \left.\left(\frac{\partial U}{\partial z}\right)\right|_{r_z=0} - 4\langle \epsilon \rangle - \left.\frac{\partial \phi_{r_z}}{\partial r_z}\right|_{r_z=0}, \tag{4.11}$$

being $\phi_{r_z} = \langle \delta q^2 \delta w \rangle - 2\nu \partial \langle \delta q^2 \rangle / \partial r_z$. In this space, the streamwise scale transport due to the mean velocity field is zero $\partial \langle \delta q^2 \delta U \rangle / \partial r_x$ since $\delta U = 0$ for $r_z = 0$. Analogously, the turbulence production due to the mean shear increment is zero, $-2\langle \delta u \widetilde{w} \rangle \delta \left(\partial U / \partial z\right) = 0$, being $\delta \left(\partial U / \partial z\right) = 0$ for $r_z = 0$. Equation 4.10 highlights that the generalized Kolmogorov equation represents an exact and formally precise formalism for the study of the cascade processes in the space of wall-parallel scales through the flux

$$\phi_{r_\pi} = \langle \delta q^2 \delta u_\pi \rangle - 2\nu \frac{\partial \langle \delta q^2 \rangle}{\partial r_\pi} \tag{4.12}$$

and the flux of scale energy between different flow regions through the spatial flux

$$\phi_{c_z} = \langle \delta q^2 \widetilde{w} \rangle + \frac{2}{\rho} \langle \delta p \delta w \rangle - \frac{\nu}{2} \frac{\partial \langle \delta q^2 \rangle}{\partial z_c} \tag{4.13}$$

from the production to the dissipation regions. In figure 4.3(a), the near-wall behaviour of the cascade and spatial fluxes of scale energy are reported. The fluxes are indicated with the streamlines and are coloured with the extended source term $\zeta$ that, as shown in equation 4.15 denotes the amount of scale-energy locally drained and released. From here on, we will make use of the concept of forward/reverse energy cascade to denote whether the fluxes in the space of scales are going towards smaller ($\phi_{r_{x,z}} < 0$) or larger scales ($\phi_{r_{x,z}} > 0$) respectively. Analogously, we will make use of the terms descending/ascending to indicate the spatial fluxes going towards or away from the wall ($\phi_{c_z} < 0$ and $\phi_{c_z} > 0$ respectively). The field of

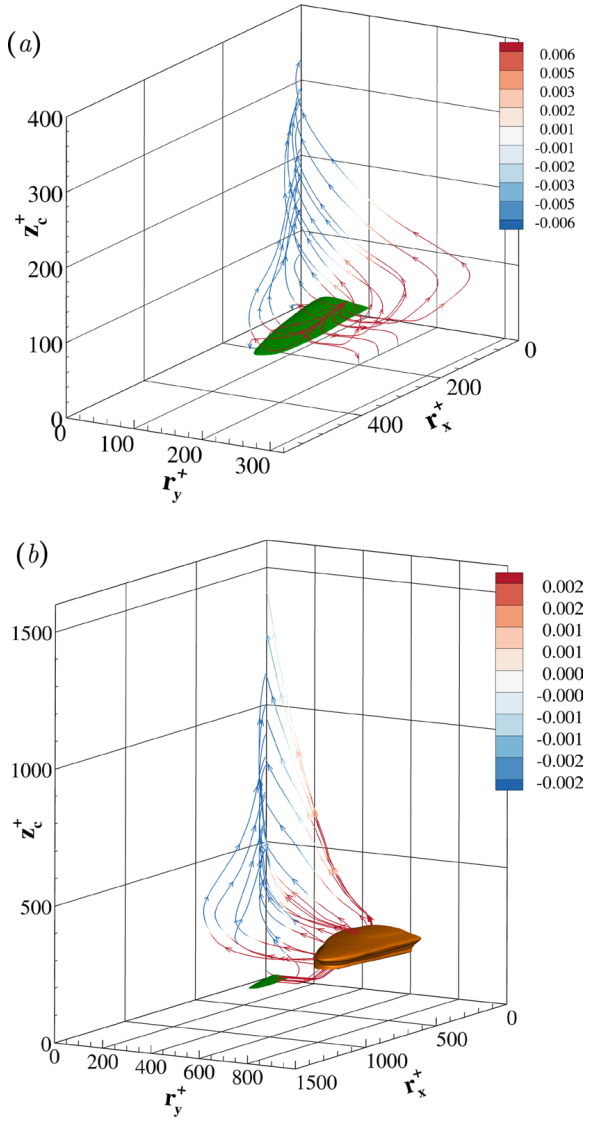


Figure 4.3: Source and fluxes of scale energy in the near-wall (a) and outer (b) regions of the turbulent boundary layer at $Re_\tau = 1500$. The scale-energy paths $(\phi_{r_x}, \phi_{r_y}, \phi_{c_z})$ are coloured with $\zeta^+$ and the scale-energy source $S^+ = 0.46$ and $S^+ = 0.01$ are reported with a green and orange iso-surface, respectively. Figure taken from Cimarelli et al. (2024a)

fluxes takes origin from a singularity point $\left(r_x^+, r_y^+, z_c^+\right) = (0, 70, 16)$ located well within the near-wall scale-energy source region (green iso-surface). The fluxes are energized by the near-wall source (see the streamlines colour) and

diverges feeding both longer and wider fluctuations before bending towards the wall and towards the bulk of the flow. By considering the branch of fluxes towards the bulk, a spiraling behaviour consisting of spatially ascending reverse and forward cascades is observed in agreement with results first reported in Cimarelli et al. (2013) for channel flows and confirmed by Yao et al. (2022) for boundary layers undergoing bypass transition. The behaviour consists of reverse cascades intercepting longer and wider structures away from the wall followed by a forward cascade feeding the small-scale range at still higher wall distances where scale energy is eventually dissipated. By extending the analysis to larger scales and higher wall distances, it is possible to clearly see the presence of an outer scale-energy source. As shown in figure 4.3(b), the field of fluxes feeding the $z_c$-distributed small-scale dissipative sink in the outer region of the flow are strongly influenced by the outer source of scale energy (orange iso-surface). In particular, the field of fluxes emerging from the near-wall region is found to be energized by the outer source (see the streamlines color) and within it further diverges feeding even longer and wider structures before eventually converging towards smaller scales. Compared with the near-wall source peak located at $\left(r_x^+, r_y^+, z_c^+\right) = (0, 40, 11)$ with intensity $S_{inn}^+ = 0.73$, the peak value of the outer source is weaker $S_{inn}^+ = 0.014$ and involves significantly larger scales $\left(r_x^+, r_y^+, z_c^+\right) = (0, 0.26Re_\tau, 0.1Re_\tau)$.

In the framework of wall-bounded flows, the peculiarity of boundary layers is the presence of entrainment phenomena at the edge of the boundary layer itself. The field of fluxes that feeds this region of the flow is shown in figure 4.4. Similar to the family of fluxes feeding the $z_c$-distributed dissipative range of small scales of the outer region, the branch of fluxes feeding the interface is energized by the outer scale-energy source (see the streamlines colour). Again a divergent pattern of the flux streamline is observed towards longer and wider structures but, in this case, it is not followed by convergence towards the small scales. Instead, the field of fluxes is almost aligned with the $z_c$-direction with a small but non-negligible reverse cascade both in the streamwise and spanwise scales. In other words, the turbulent core of the boundary layer is found to sustain a variety of large wall-parallel structures at the boundary layer interface region. Interestingly, this phenomenology is fully consistent with recent findings on the TNTI of free shear flows reported in Cimarelli et al. (2015a); Zhou and Vassilicos (2020); Cimarelli et al. (2021).

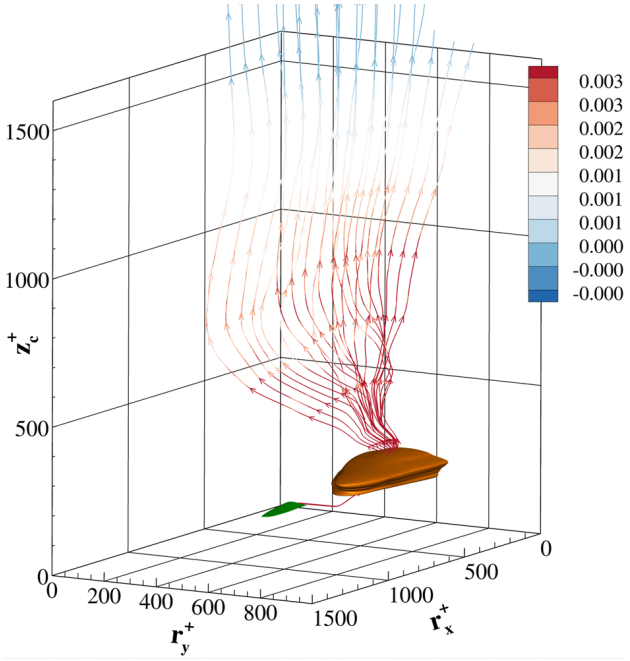


Figure 4.4: Branch of scale-energy fluxes towards the interface dissipative sink of the turbulent boundary layer at $Re_\tau = 1500$. The scale-energy paths $(\phi_{r_x}, \phi_{r_y}, \phi_{c_z})$ are coloured with $\zeta^+$ and the scale-energy source $S^+ = 0.46$ and $S^+ = 0.01$ are reported with a green and orange iso-surface, respectively. Figure taken from Cimarelli et al. (2024a)

### 4.2.2 Effect of the TNTI in the $(r_y, z_c)$ compound space

Although the dynamic shown in the previous subsection has 3D characteristics, much of the information reported can also be deduced by looking at the sole $(r_y, z_c)$ subspace, which qualitatively shows the same main features of the fluxes and is able to capture the two source regions. These source regions, in fact, show a peak of activity in the $r_x = 0$ plane and appear elongated in the $r_x$ scales. For this reason we will now limit our analysis to the subspace $(r_y, z_c)\,|_{r_x,z=0}$. This simplification will allow us an easier to understand and more quantitative analysis, for example of some scaling quantities related to the reverse energy transfer. The analysis will now proceed taking a closer look to the effect of the presence of a free TNTI when compared to a bounded flow such as the channel flow and of the phenomena that are observed in the vicinity of the TNTI region itself.

The DNS channel flow data used as a comparison have already been used for studies of wall turbulence in Cimarelli et al. (2015b), to which the reader

is referred for further details on the main flow features and on the numerics. As a brief summary of the DNS set-up, the channel flow simulation at the friction Reynolds number at $Re_\tau = 1500$ has been performed using a pseudospectral code based on Fourier expansions in the homogeneous directions and Chebyshev polynomials in the wall-normal direction. Time is advanced using a mixed Runge–Kutta and Crank–Nicolson scheme, while the nonlinear terms are calculated in physical space with aliasing errors removed by the 3/2-rule. Full details of the algorithm can be found in Chevalier et al. (2007). The domain size is $(L_x, L_y, L_z) = (37.7, 10.5, 2)\,\delta$ in the streamwise ($x$), spanwise ($y$) and wall-normal ($z$) directions, respectively. The number of modes used for the spatial discretization is $(N_x, N_y, N_z) = (6144, 3456, 577)$ thus leading to a physical space resolution $(\Delta x^+, \Delta y^+) = (9.2, 4.5)$ in the spatially homogeneous directions and $\left(\Delta z_w^+, \Delta z_\delta^+\right) = (0.02, 8)$ in the wall-normal direction, respectively at the wall and at the channel centreline $z = \delta$. The channel flow exhibit the same homogeneities of the TTBL, with the addition of a reflection symmetry around the centreline and of the stationarity $\partial\langle\cdot\rangle/\partial t = 0$. For this reason all the equations derived for the TTBL equally apply to the channel flow with these two additional simplifications.

By further restricting equation 4.10 to the case $r_x = 0$, we obtain

$$\left.\frac{\partial \phi_{r_y}}{\partial r_y}\right|_{r_{x,z}=0} + \left.\frac{\partial \phi_{c_z}}{\partial z_c}\right|_{r_{x,z}=0} = \zeta_{r_{x,z}=0}, \tag{4.14}$$

where

$$\begin{aligned}\zeta_{r_{x,z}=0} = -\left.\frac{\partial\langle\delta q^2\rangle}{\partial t}\right|_{r_{x,z}=0} - 2\langle\delta u \delta w\rangle \left.\left(\frac{\partial U}{\partial z}\right)\right|_{r_{x,z}=0} \\ -4\langle\epsilon\rangle - \left.\frac{\partial \phi_{r_x}}{\partial r_x}\right|_{r_{x,z}=0} - \left.\frac{\partial \phi_{r_z}}{\partial r_z}\right|_{r_{x,z}=0},\end{aligned} \tag{4.15}$$

is the extended source term taking into account the scale-energy exchange with the $r_x \neq 0$ and $r_z \neq 0$ dimensions through the terms $-\partial\phi_{r_x}/\partial r_x|_{r_{x,z}=0}$ and $-\partial\phi_{r_z}/\partial r_z|_{r_{x,z}=0}$ respectively. Notice that in the case of the temporal boundary layer, a gate of scale-energy exchange is also open for the time dimension being $\partial\langle\delta q^2\rangle/\partial t|_{r_{x,z}=0} \neq 0$. To simplify the notation, $|_{r_{x,z}=0}$ will be dropped in what follows. Analogously to the previous subsection, we will refer to the concept of forward/reverse cascade to denote fluxes in the spanwise space of scales towards smaller and larger scales $r_y$, i.e. $\phi_{r_y} < 0$ and $\phi_{r_y} > 0$, respectively. In figure 4.5, the source term $S$ and the fluxes $\left(\phi_{r_y}, \phi_{z_c}\right)$ are reported in the space of spanwise scales and wall distances $(r_y, z_c)$ for both the TTBL, in figure 4.5(a), and the channel flow, in figure

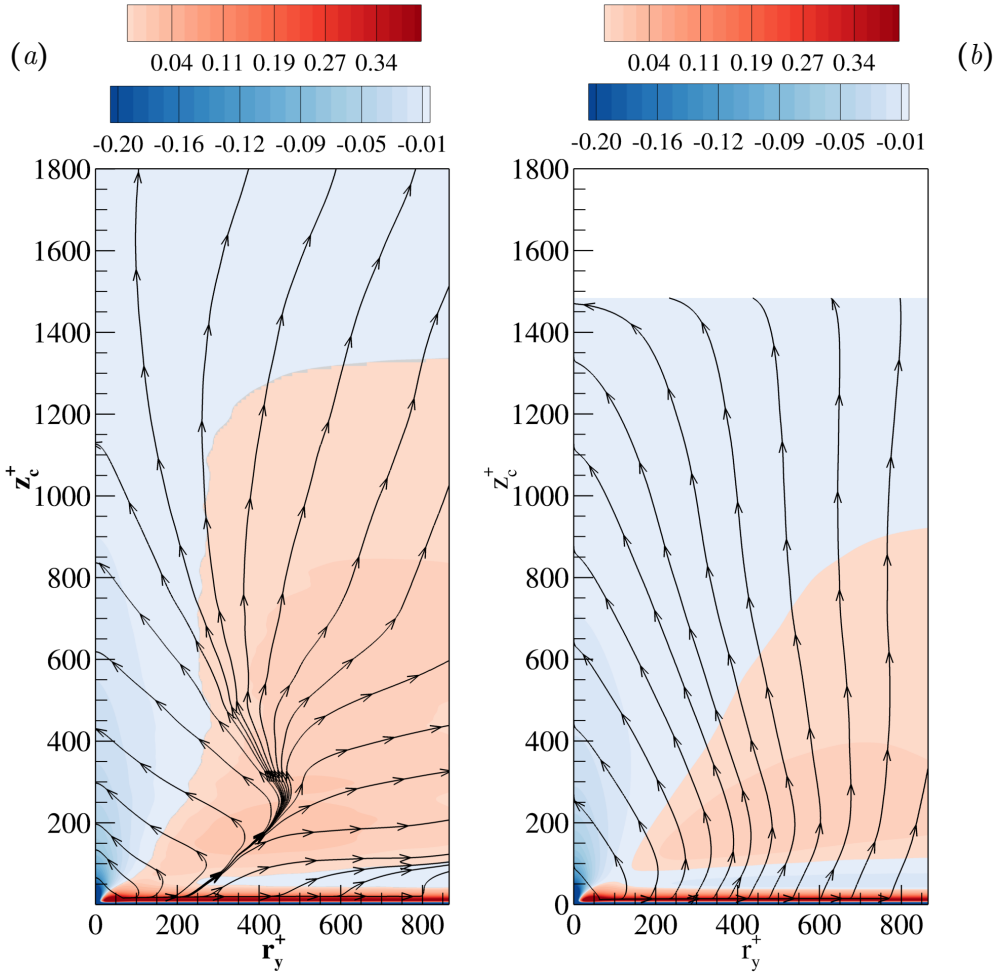


Figure 4.5: Fluxes of scale energy (black lines with arrows) in the compound space of spanwise scales and wall distances $(\phi^+_{r_y}, \phi^+_{c_z})(0, r_y^+, 0, z_c^+)$ and isocontours of the scale energy source $S^+(0, r_y^+, 0, z_c^+)$ for the turbulent boundary layer (a) and the turbulent channel (b) at $Re_\tau = 1500$. Figure taken from Cimarelli et al. (2024a).

4.5(b). The source term is reported as isocontours ranging from negative values (indicating a sink of scale-energy, in blue colours) to positive values (indicating a source, in red colours), while the fluxes are visualized through the streamlines. Streamlines tilted towards the right or towards the left indicate a reverse or forward energy cascade in the spanwise scales respectively. The overall picture conforms with a near-wall turbulence production

region that feeds through spatial fluxes and forward/reverse cascade processes the entire flow field. As shown by the isocontours of the source term $S$ reported in figure 4.5, the buffer layer region, in the range of spanwise scales $20 < r_y^+ < 80$, is the site of the most intense sourcing mechanisms of turbulence (see figure 4.6(a,b) for the near-wall close-up). From this source

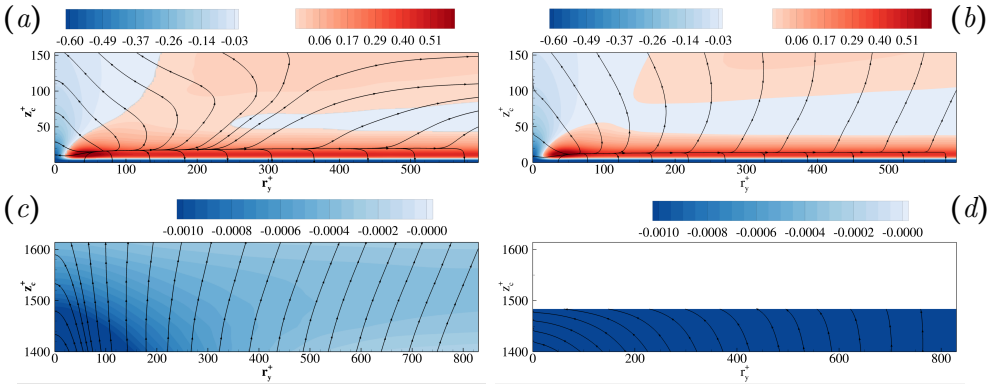


Figure 4.6: Near-wall (a,b) and outer (c,d) zoom of the fluxes of scale energy (black lines with arrows) in the compound space of spanwise scales and wall distances $(\phi^+_{r_y}, \phi^+_{c_z})(0, r_y^+, 0, z_c^+)$ and isocontours of the scale energy source $S^+(0, r_y^+, 0, z_c^+)$ for the turbulent boundary layer (a,c) and the turbulent channel (b,d) at $Re_\tau = 1500$.

region, scale energy is radiated to feed both the wall and the outer regions where it is finally dissipated. As shown by Cimarelli et al. (2013), a distinguishing feature of wall turbulence is that scale energy is transferred first towards larger scales before bending to small scales where it is eventually dissipated. Hence, reverse energy cascade processes take place that pose strong difficulties for theories in wall turbulence and for its modelling. In fact, energy emerges from small scales near the wall to drive the large-scale quasi-coherent motions of the outer regions (Jiménez and Pinelli, 1999). The latter undergo instability and by bursting generate smaller turbulent motions where scale energy is eventually removed by viscous dissipation. Hence, small and large scales are in equilibrium only by considering a non-local and multidimensional coupling based on reverse and forward cascades between scales and spatial fluxes between different flow regions. In figure 4.5, it is possible to notice the $r_x = 0$ cross-section of the outer source region already highlighted in figure 4.3. The presence of this outer scale-energy source, as shown in Cimarelli et al. (2015b), exhibits statistical features that agree with the hypothesis of an overlap layer dominated by self-similar structures attached to the wall. Such an increasingly relevant outer produc-

tion cycle is then conjectured to be at the basis of the anomalous scaling of near-wall quantities (Marusic et al., 2017; Chen and Sreenivasan, 2021). The underlying physical mechanism is the repulsion of the fluxes emerging from the near-wall region (Cimarelli et al., 2015b).

The multidimensional scenario of wall turbulence described so far is shared by both turbulent boundary layer and channel flow thus suggesting that the spatially evolving forward and reverse energy cascade is a robust phenomenological feature of wall turbulence overall. The specific features related to the presence of entrainment mechanisms in the turbulent/non-turbulent interface region of boundary layers are addressed in the following.

**Source of scale energy**

By starting the analysis from the near-wall region, we observe that the sourcing mechanisms of turbulence are essentially the same for channel and boundary layer as shown by the isocontours reported in figure 4.6(a,b). In particular, the peak activity is located at $\left(r_y^+, z_c^+\right) = (40, 11)$ with an intensity $S = 0.73$ for both flow configurations. Conversely, the turbulent entrainment at the interface affects the source mechanisms of the overlap and outer regions of the flow. It consists in an enhancement and shift towards smaller scales and wall distances of the sourcing mechanisms of the overlap layer. In particular, we measure that the peak value of the source term in the overlap layer is located at $\left(r_y^+, z_c^+\right) = (400, 158) = (0.26Re_\tau, 0.1Re_\tau)$ with an intensity $S^+ = 0.014$ for the boundary layer and at $\left(r_y^+, z_c^+\right) = (442, 192) = (0.3Re_\tau, 0.128Re_\tau)$ with an intensity $S^+ = 0.0086$ for the channel. The location of the outer peak of the source term is reported using both inner and outer units since the underlying flow structures are found to agree with the self-similar scaling of attached eddies (Cimarelli et al., 2015b; Marusic and Monty, 2019). The enhancement of the intensity of the outer self-sustaining mechanisms in the settings of turbulent boundary layers is at the basis of a more significant protrusion of the positive values of $S$ towards the outer region, see figure 4.5. In particular, we measure that the production mechanisms of turbulence exceed dissipation up to $z_c^+ \approx 1300$ in the turbulent boundary layer compared with $z_c^+ \approx 900$ in the channel. Interestingly, a change in topology of the source term is observed also in the transitional region between the buffer and overlap layers. It consists in a net separation of the near-wall and overlap source mechanisms by a sink layer $S < 0$ that in the case of channel flows extend at all scales while for boundary layers a bridge of positive source between the buffer and overlap self-sustaining mechanisms is found for intermediate scales $100 < r_y^+ < 250$.

### Field of fluxes

In analogy of the source term, also the field of fluxes of scale energy $\left(\phi_{r_y}, \phi_{z_c}\right)$ in the near-wall region is found to be substantially the same for the two flow configurations. As shown in figure 4.6(a,b), the field of fluxes takes its origin from the peak region of the scale-energy source and diverges, locally feeding smaller and larger scales before bending towards the wall and the outer region. The wall layer and the $z_c$-distributed range of small scales represent the two sink regions attracting the field of fluxes in wall turbulence. The two branches of fluxes that connect the peak of scale energy source to these two sink regions will be analysed separately in the following.

***Branch of fluxes towards the dissipative sink at the wall***

By considering first the branch of fluxes moving towards the wall, it is possible to observe that after an initial reverse energy cascade the field of fluxes bends towards the wall with a rapidly vanishing scale-space flux. In particular, the near-wall asymptotic behaviour is

$$(\phi_{r_y}, \phi_{z_c}) \sim (0, 1)\, z_c \qquad \text{for } \; z_c \to 0 \tag{4.16}$$

since the near-wall scaling is such that $\delta u, \delta v \sim z_c$, $\delta w \sim z_c^2$ and $\delta p \sim \delta p_w$, see the appendix in Cimarelli et al. (2013). Hence, the viscous sublayer of both boundary layers and channels is characterized by a dissipative sink fed by a field of fluxes aligned with the wall-normal direction that are homogeneously distributed at all scales. As shown by means of the scale-by-scale budgets in section 4.2.3, this behaviour conforms with a viscous sublayer where the dissipative mechanisms are characterized by a variety of horizontal scales imposed by the variety of scales of the overlying turbulent dynamics with only the wall-normal scales recovering the classical role of dissipation at small scales.

***Branch of fluxes toward the $z_c$-distributed dissipative sink at small scales***

By considering now the branch of fluxes feeding the outer regions of the flow, we remark again that both forward and reverse cascade processes are present. The cross-over scale $\ell_b$ between these two phenomena, defined by $\phi_{r_y}(\ell_b, z_c) = 0$, is reported in figure 4.7. In agreement with the idea that the large-scale motion attached to the wall is the flow pattern mostly intercepted by the fluxes ascending from the near-wall region, the cross-over scale $\ell_b$ is found to follow a linear scaling with the wall distance

$$\ell_b^+ \approx 40 + 2.3 z_c^+. \tag{4.17}$$

It is widely recognized that coherent structures are associated with strong events of energy transfer (Piomelli et al., 1996; Hamba, 2019; Chan et al., 2021; Wang et al., 2021; Chiarini et al., 2022). In the inner region of wall-bounded turbulent flows these structures are thought to be self-similar (Marusic and Monty, 2019) and to form a self-sustaining process (Jiménez and Pinelli, 1999; Panton, 2001). The picture consists of pair of streamwise vortices that create longer and wider streamwise velocity streaks. In turn, the low-speed streamwise velocity streaks while growing become unstable and burst thus creating smaller and smaller detached eddies. As shown in Cimarelli et al. (2013, 2016), the spatially ascending reverse and forward cascades conform with this scenario. In particular, from the turbulence production processes associated with streamwise vortices the combined reverse cascade and spatial flux agrees with the generation of longer and wider streaks ascending from the wall. On the other hand, the subsequent combination of forward cascade and spatial flux agrees with the generation of detached eddies at progressively higher wall distance from the burst of the streaks itself. Note that more recent studies of turbulent structures highlight that coherent motions can also be generated by shear at any wall distance and that by growing become attached to the wall (Lozano-Durán and Jiménez, 2014). Also this phenomenon finds support in the generalized Kolmogorov equation through the positive value of the source term in the overlap layer, see again figure 4.5. The source term energizes the field of fluxes in the overlap layer thus supporting the idea that coherent motions can be also locally generated by shear. The self-similar scaling 4.17 gives further support to all these phenomenological interpretations of the scale-by-scale energy exchange described by the generalized Kolmogorov equation. This self-similar scaling holds in the overlap layer of both boundary layer and channel, the only difference being the extension of its validity that for channels is for $z_c^+ < 180 = 0.12Re_\tau$ while for boundary layers is $z_c^+ < 120 = 0.08Re_\tau$.

By entering the outer region of the flow, this self-similarity of the flow structures is lost and, consequently, the crossover scale b stops its growth. This is the region where channels and boundary layers mostly differ from each other. In particular, in a turbulent channel the crossover scale saturates by oscillating around the value $\ell_b^+ \approx 700 = 0.46Re_\tau$ and goes to infinity at the channel centreline, see again figure 4.7. Hence, the outer flow structures involved in the reverse energy cascade in channels scale with the channel height rather than the distance from the wall. However, as shown in figure 4.5(b), the intensity of the reverse energy flux is very weak thus suggesting that the outer region of channels is barely influenced by reverse energy cascade processes. Accordingly, the outer region can be thought as

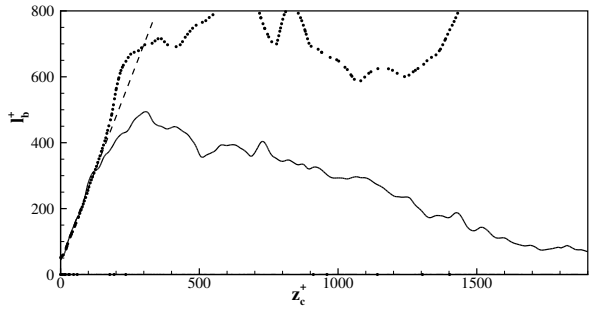


Figure 4.7: Crossover scale $\ell_b^+(z_c^+)$ as a function of the wall distance in the turbulent boundary layer (solid line) and turbulent channel (dotted line). The dashed line reports the self-similar scaling 4.17. Figure taken from Cimarelli et al. (2024b).

the region of the channels where a Richardson energy cascade scenario is recovered when generalized by taking into account spatial fluxes. The generalized Richardson energy cascade consists in spatially ascending cascade processes that transfer energy from the energy containing scales identified by the crossover scale $\ell_b$ at a certain distance from the wall to the small scales of higher wall distances where it is finally dissipated. Since $\ell_b \to \infty$ for $z_c^+ \to Re_\tau$, we also have that the core region of the channel is uniquely characterized by a forward cascade towards small scales. Notice that the small-scale asymptotic behaviour of fluxes both for channels and boundary layers is

$$(\phi_{r_y}, \phi_{z_c}) = (1, 0)|\boldsymbol{r}| \qquad \text{for } |\boldsymbol{r}| \to 0 \tag{4.18}$$

and is dominated by the viscous scale-space flux since $\delta u_i \sim |\boldsymbol{r}|$ and $\delta p \sim |\boldsymbol{r}|$, see the appendix in Cimarelli et al. (2013). Hence, the fluxes become asymptotically normal to the $z_c$-axis by approaching the dissipative range of small scales.

Contrary to channel flows, in the outer region of boundary layers the cross-over scale $\ell_b$ decreases monotonically with the wall distance, see again figure 4.7. This behaviour is confirmed by the scale-energy paths shown in figure 4.5(a). The monotonic decrease of $\ell_b$ is such that we can expect that for sufficiently high wall distances the cross-over scale reduces to the Kolmogorov scale, $\ell_b \to \eta$, and, hence, all the scales of the interface region are expected to undergo a reverse energy cascade. This scenario is confirmed by the zoom of the scale-energy paths reported in figure 4.6(c). The range of scales of forward cascade gets progressively smaller for increasing wall distance contrary to channels where forward cascades dominate the entire

range of scales. This behaviour of the interface region of boundary layers conforms with the scale-by-scale phenomenology of the interface of shear-less flows and jets reported in Cimarelli et al. (2015a, 2021) and Zhou and Vassilicos (2020). It consists in a physics of turbulence confined to two dimensions, where reverse cascade processes from the turbulent core feed long and wide flow interface structures thus sustaining the turbulent entrainment and the propagation of the turbulent front. A forward cascade survives only in the normal to the interface direction. Hence, the scenario conforms with long and wide interface structures where dissipation is accomplished by normal to the interface gradients over a very thin layer of the order of the Kolmogorov scale. As better shown by the scale-by-scale budgets reported in subsection 4.2.3, this phenomenology is consistent with what is found to characterize the interface region of boundary layers. Notice that such mechanisms have similarities with the almost 2-D dissipative processes of the viscous sublayer analysed so far.

Coming back to the overall behaviour of the outer region of boundary layers, it is worth noting that the reverse energy cascade is far more intense than in channels, see again figure 4.5(a). Hence, analogously to the buffer and overlap layers, the reverse cascade is recognized to play a fundamental role also for the outer flow dynamics contrary to channels where we have already shown to be essentially ineffective, see figure 4.5(b) for comparison. To note that such an enhancement of the reverse energy cascade with respect to channels is found to occur also within the inner region, in the overlap layer, compare again figure 4.5(a,b). An accompanying feature of this stronger influence of the reverse energy cascade in boundary layers, is a rather different topology of the scale-energy fluxes with respect to channels also from the overlap layer region. By comparing figure 4.5(a,b), it is possible to observe that the field of fluxes in boundary layers exhibits a diverging pattern contrary to the almost uniform topology of the fluxes in channels. We remind the reader that in accordance with 4.14, we have

$$\boldsymbol{\nabla_\pi} \cdot \boldsymbol{\phi_\pi} = \zeta \tag{4.19}$$

with $\boldsymbol{\nabla_\pi} = (\partial/\partial r_y, \partial/\partial z_c)$ and $\boldsymbol{\phi_\pi} = (\phi_{r_y}, \phi_{z_c})$. Hence, the divergence of the fluxes is given by the extended source term. The behaviour of the extended source term (not shown for brevity) resembles the one of the source term, $\zeta \approx S$. As a consequence, the divergence of the fluxes almost follows the behaviour of the source term $S$ that, as shown in the previous paragraph, exhibits some differences between channels and boundary layers. However, such differences are not as significant as those observed in the pattern taken by the field of fluxes. The reason is the most effective action of the source

term on the pattern of fluxes rather than on their intensity. Let us try to grasp the essential aspects by rewriting equation (4.19) in a curvilinear coordinate system adapted to the flux vector field,

$$\frac{1}{h_\tau}\frac{\partial \phi_\tau}{\partial \tau} + \frac{\phi_\tau}{\jmath}\frac{\partial h_n}{\partial \tau} = \zeta \tag{4.20}$$

where $\tau$ and $n$ denote the tangential and normal directions to the field of fluxes, $\jmath = h_\tau h_n$ is the Jacobian while $h_\tau = \sqrt{(\partial r_y/\partial \tau)^2 + (\partial z_c/\partial \tau)^2}$ and $h_n = \sqrt{(\partial r_y/\partial n)^2 + (\partial z_c/\partial n)^2}$ are the scale factors. From (4.20) it is evident how the divergence of the field of fluxes $\zeta$ takes the combined effect of a change of the flux intensity $\phi_\tau$ and of an opening/closing of the field pattern $h_n$. Evidently the former prevails on the latter in channel flows while in boundary layers the opposite occurs thus leading to a more divergent pattern of the field of fluxes. The associated enhancement of reverse/forward cascade in boundary layers is such that a divergence line appears in the overlap layer, see again figure 4.5(a). The dynamical relevance of this divergence line is such that all the scales populating the outer flow region, say for $z_c^+ > 400 = 0.26Re_\tau$, are fed by fluxes that trace back to this line. As for the cross-over scale $\ell_b$, the divergence line intercepts scales linearly increasing with the wall distance thus suggesting again self-similar attached eddies as underlying flow structures. In particular, we measure $r_y^+ \approx 200 + 1.2z_c^+$.

### 4.2.3 Scale-by-scale budgets

In the present section, a more quantitative view of the multi-scale processes of wall-bounded turbulence with and without interfaces is provided by means of the generalized Kolmogorov equation evaluated at fixed wall distances and as a function of the sole spanwise scale, i.e. by fixing $r_x = r_z = 0$. The analysis will not address the field of fluxes but the overall transport terms in the space of scales and wall distances as described by equation (4.4).

#### Buffer layer

By starting the analysis from the buffer layer, it is possible to see from figure 4.8(a) that the dynamics of the near-wall production region in boundary layers and channels is essentially the same, in accordance with the previous analysis in subsection 4.2.2. It consists in a turbulence production that dominates the budget by largely exceeding the amount of dissipation,

$\Pi - E > 0$, i.e. the buffer layer is a net energy source region of turbulence. As already noted in Cimarelli and De Angelis (2012), a distinguishing feature of wall turbulence is that the peak of turbulence production is not located at the large scales but amid the spectrum of scales, $r_y^+ = 40$, thus leading to overwhelming difficulties for turbulence models (Cimarelli and De Angelis, 2014). The clear matching of scales suggests a strong connection of the production peak with quasi-streamwise vortices. The scale-energy excess of this region, $\Pi - E > 0$, is eventually drained by inertial scale-space transport $T_r < 0$ and by spatial transport $T_c < 0$ to feed both larger and smaller scales (through forward and reverse cascades) of the other regions of the flow (through spatial fluxes).

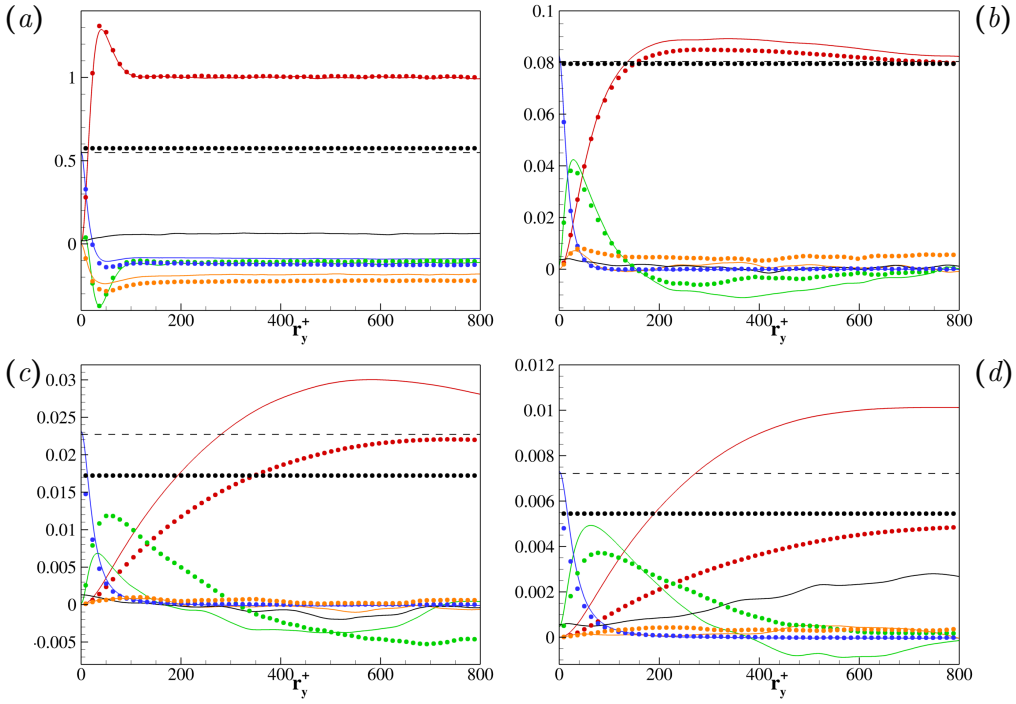


Figure 4.8: Scale-by-scale budgets of wall turbulence evaluated at different wall distances $z_c^+ = 11$ (a), $z_c^+ = 114$ (b), $z_c^+ = 450$ (c), $z_c^+ = 1000$ (d) reported as a function of the spanwise scale $r_y^+$ for $r_x = r_z = 0$. Data from the turbulent boundary layer are reported with lines while those from the turbulent channel are reported with symbols. Different colours are used for the different terms of the generalized Kolmogorov equation (4.4): $\Pi$ (red), $T_r$ (green), $D_r$ (blue), $T_c$ (orange), $E$ (black, dashed line) and $\partial\langle\delta q^2\rangle/\partial t$ (black, solid line). Figure taken from Cimarelli et al. (2024b)

### Overlap layer

Also the overlap layer is found to be substantially unaltered between channel and boundary layer as shown in figure 4.8(b). In accordance with the equilibrium assumption of the overlap layer, production and dissipation almost balance each other $\Pi - E \approx 0$ and consequently the role of spatial fluxes is almost negligible $T_c \approx 0$. An exception to this equilibrium assumption is given by the range of intermediately large scales where a net source, although weak compared the one in the buffer layer, is present. Such range of production scales is at the basis of the outer scale-energy source already described in subsection 4.2.2 and is responsible for the sustainment of the reverse energy cascade processes of these region of the flow. Accordingly, the inertial scale-space flux is negative $T_r < 0$ thus draining energy to feed reverse cascade processes. This phenomenon is more intense in boundary layers in accordance with the enhancement of the outer scale-energy source and of the reverse cascade phenomena previously discussed in subsection 4.2.2.

Note that the shift to larger scales of the turbulence production processes by increasing the wall distance allows for a larger separation of scales with respect to the scale-space diffusion $D_r$. Hence, a small inertial sub-range takes place in the overlap layer where the inertial scale-space flux sustains turbulence $T_r > 0$. The emergence of an inertial subrange of scales can be addressed by considering the behaviour of the cross-over scales between production-dominated, cascade-dominated and viscosity-dominated scales,

$$T_r(\ell_p, z_c) = \Pi, \qquad T_r(\ell_\nu, z_c) = D_r. \tag{4.21}$$

Accordingly, the inertial subrange is defined as the range of scale $\ell_\nu < r_y < \ell_p$. As shown in figure 4.9, both scales increases with the wall distance but the steeper increase of the turbulence production scale $\ell_p$ allows for the development of an increasingly large inertial subrange. Such scenario can be formalized using scaling arguments typical of the overlap region. In this region of the flow, turbulence production can be estimated as $u_\tau^3/(\kappa z)$. By invoking the equilibrium assumption, turbulent dissipation can be equivalently written as $\langle \epsilon \rangle = u_\tau^3/(\kappa z)$. By substituting this behaviour into the definition of the Kolmogorov scale, we have the following scaling for the smallest turbulent scales

$$\eta^+ \sim (\kappa z^+)^{1/4}. \tag{4.22}$$

On the other, the estimate for the scaling of the large-production scales can be obtained by comparing the velocity increments induced by shear $|\delta \boldsymbol{u}| \sim$

$|\boldsymbol{r}|(\partial U/\partial z)$ from those related to the inertial cascade $|\delta \boldsymbol{u}| \sim \langle\epsilon\rangle^{1/3}|\boldsymbol{r}|^{1/3}$. The result is the so-called shear scale $\ell_S = \sqrt{\langle\epsilon\rangle/(\partial U/\partial z)^3}$, see Marati et al. (2004). By using again the scaling of shear and dissipation in the overlap region, $\partial U/\partial z \sim u_\tau/(\kappa z)$ and $\langle\epsilon\rangle = u_\tau^3/(\kappa z)$, we have that the shear scale linearly increases with the wall distance

$$\ell_S^+ \sim \kappa z^+. \tag{4.23}$$

As shown in figure 4.9, these self-similar scaling are found to be a robust formalism quantitatively describing the behaviour of the inertial subrange in the overlap layer of wall turbulence. Notice that while the production scale is directly described by the shear scale, $\ell_p \approx \ell_S$, the viscous cut-off scale of the energy cascade $\ell_\nu$ is found to be larger than the Kolmogorov scale, $\ell_\nu \approx 6.5\eta$ thus suggesting that the extension of the viscous subrange of turbulence is of the order of 6.5 Kolmogorov scales. In closing this section, let us notice that such self-similar scaling are followed within the overlap layer for $z_c^+ < 300 = 0.2Re_\tau$ then the production scale $\ell_p$ is found to almost saturate its growth in the outer region. It is then evident that the generation of a larger separation of scales for the development of a sufficiently large inertial subrange in the outer region of the flow is realized by an increase of the extension of the overlap layer $z_c^+ = 0.2Re_\tau$ that in turn is given by an increase of the friction Reynolds number.

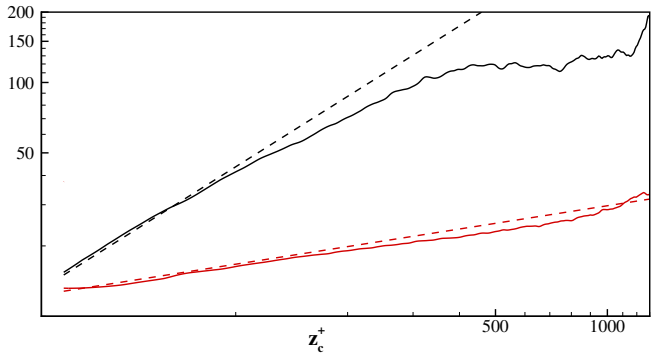


Figure 4.9: Inertial and viscous cross-over scales, $\ell_p^+(z_c^+)$ (black line) and $\ell_\nu^+(z_c^+)$ (red line), as a function of the wall distance in the turbulent boundary layer. The dashed lines report the self-similar scaling $\ell_p^+ = \kappa\, z_c^+$ and $\ell_\nu^+ = 6.5\,(\kappa\, z_c^+)^{1/4}$. Figure taken from Cimarelli et al. (2024b).

### Outer layer

The main differences between boundary layer and channel become evident when considering the outer flow region shown in figure 4.8(c,d). In accordance with the previous analysis in section 4.2.2, it consists in an enhancement of the turbulence production mechanisms and of the reverse energy cascade processes in boundary layers with respect to channels. In particular, the enhancement of production is such that an excess of scale energy $\Pi - E > 0$ is observed also at $z_c^+ = 1000 = 0.66Re_\tau$ in the case of boundary layers. On the other hand, the enhancement of the reverse energy cascade is such that a significant large scale sink $T_r < 0$ is observed also at $z_c^+ = 1000 = 0.66Re_\tau$ in the case of boundary layers. It is worth noting the already mentioned increase of scale separation that enables the appearance of a increasingly large inertial subrange in between production and scale-space diffusion where the inertial scale-space transport dominates the budget $T_r > 0$. Another important aspect related with the increasing of the wall distance $z_c$ is the increase of non-equilibrium effects in temporal boundary layers. In particular, for $z_c^+ = 1000 = 0.66Re_\tau$ the non-equilibrium term significantly takes part on the budget by draining a significant portion of scale energy to sustain the temporal growth of the boundary layer, i.e. $\partial\langle\delta q^2\rangle/\partial t > 0$. The scale energy drained to sustain the propagation of turbulence is made available locally by production processes since the spatial transport term is almost negligible $T_c \approx 0$. The opposite scenario occurs in the interface region as shown in the following section.

### Interface layer

The scale-by-scale budget at the mean interface position of the boundary layer and at the channel centre is reported in figure 4.10(a). As already mentioned, turbulence in this region of the flow is sustained by transport processes both in the space of scales and physical space, $T_r > 0$ and $T_c > 0$, being the production processes significantly smaller in boundary layers, $\Pi < T_c < T_r$ and, for symmetry reasons, null in channel, $\Pi = 0$. Analogously to the external part of the outer layer, the scale energy provided by the transport terms and by the local production in boundary layer, significantly exceed the local dissipation $T_r + T_c + P > E$ thus sustaining the propagation of the turbulent interface that in the case of temporally evolving flows is given by the non-equilibrium term, i.e.

$$\frac{\partial\langle\delta q^2\rangle}{\partial t} \approx T_r + T_c + P - E > 0 \tag{4.24}$$

The scale-space distribution of the processes involved is such that the wide flow structures are those generated first during the boundary layer growth. It is then of relevance to address the nature of the transport phenomena involved in turbulent entrainment.

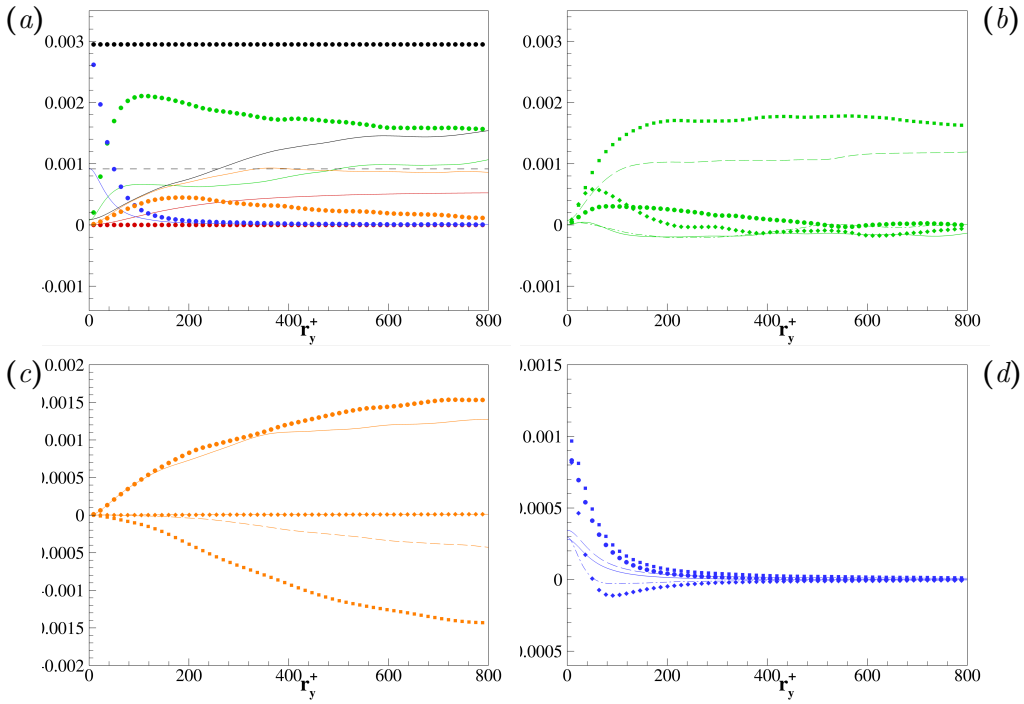


Figure 4.10: Scale-by-scale budget of wall turbulence evaluated at $z_c^+ = 1500$ (centre of the channel and mean interface position of the boundary layer) reported as a function of the spanwise scale $r_y^+$ for $r_x = r_z = 0$. Data from the turbulent boundary layer are reported with lines while those from the turbulent channel are reported with symbols. Different colours are used for the different terms of the generalized Kolmogorov equation (4.4): $\Pi$ (red), $T_r$ (green), $D_r$ (blue), $T_c$ (orange), $E$ (black, dashed line) and $\partial\langle\delta q^2\rangle/\partial t$ (black, solid line). The overall budget is reported in (a). The contributions to $T_r$ are shown in (b) where $-\partial\langle\delta q^2\delta u\rangle/\partial r_x$ (solid line and circle), $-\partial\langle\delta q^2\delta v\rangle/\partial r_y$ (dashed-dotted line and diamond), $-\partial\langle\delta q^2\delta w\rangle/\partial r_z$ (dashed line and square). The contributions to $T_c$ are shown in (c) where $-\partial\langle\delta q^2\widetilde{w}\rangle/\partial z_c$ (solid line and circle), $-(2/\rho)\partial\langle\delta p\delta w\rangle/\partial z_c$ (dashed line and square), $(\nu/2)\partial^2\langle\delta q^2\rangle/\partial {z_c}^2$ (dashed-dotted line and diamond). The contributions to $D_r$ are shown in (d) where $2\nu\partial^2\langle\delta q^2\rangle/\partial r_x^2$ (solid line and circle), $2\nu\partial^2\langle\delta q^2\rangle/\partial r_y^2$ (dashed-dotted line and diamond), $2\nu\partial^2\langle\delta q^2\rangle/\partial r_z^2$ (dashed line and square). Figure taken from Cimarelli et al. (2024b).

As shown figure 4.10(c), the spatial transport providing scale energy at the mean interface position is mainly due to turbulent transport phenomena. Indeed, pressure transport is found to drain scale energy from this region while the viscous transport is almost negligible. Hence, the scale energy provided from below by spatial transport in the boundary layer can be modelled as

$$T_c \approx -\frac{\partial\langle\delta q^2\widetilde{w}\rangle}{\partial z_c} - \frac{2}{\rho}\frac{\partial\langle\delta p\delta w\rangle}{\partial z_c} \tag{4.25}$$

Notice that the amount of scale energy drained by the pressure transport is found to be released in the very external flow region of the boundary layer (not shown) where the balance reduces to

$$\frac{\partial\langle\delta q^2\rangle}{\partial t} \approx -\frac{2}{\rho}\frac{\partial\langle\delta p\delta w\rangle}{\partial z_c} > 0, \qquad \text{for } z_c^+ > 1.3Re_\tau \tag{4.26}$$

since the scale-space transport phenomena and hence dissipation are almost null there in accordance with the irrotational and non-turbulent nature of the fluctuations populating the external flow region. This behaviour fully agrees with that observed in the external region of free-shear flows as shown in Cimarelli et al. (2021). Hence, this behaviour of the pressure transport phenomena is a peculiar feature of turbulent interfaces in general. As a matter of fact, the pressure transport at the channel centre is found to play a less relevant role and, hence, the spatial transport is found to be determined solely by the turbulent transport, i.e. $T_c \approx \partial\langle\delta q^2\widetilde{w}\rangle/\partial z_c > 0$.

By considering now the behaviour of the scale-space transport at the mean interface position, it is important to remind that the analysis of the field fluxes reported in section 4.2.2 revealed that the most energized scales of the interface region are the large ones. This is a result of the combined action of spatial fluxes with reverse cascades, with the latter involving almost all the range of scales of the interface region. The almost absence of forward cascade mechanisms in the space of spanwise scales gives rise to very important questions. How is dissipation accomplished in the interface region? What are the turbulence phenomena involved? To address these issues in figure 4.10(b), the scale space transport term is split in its contributions related with the cascade processes in the $r_x$, $r_y$ and $r_z$ scales. It is evident that the transport in the scales parallel to the mean interface $(r_x, r_y)$ is weak compared to that in the scales normal to the mean interface $r_z$, hence

$$T_r \approx -\frac{\partial\langle\delta q^2\delta w\rangle}{\partial r_z} > 0 \tag{4.27}$$

By recalling that the scale-by-scale budget is reported for $r_z = 0$ this result tell us that a significant forward cascade is occurring in the $r_z$ space that is almost homogeneous in the $r_y$ space. Hence, in this region, a forward cascade across the scales normal to the mean interface is experienced by a variety of motions with different spanwise scales, from narrow to wide. On the contrary, scale-space transport in the spanwise scales is negative, highlighting a draining of scale energy to feed wider motions near the interface. Also the scale-space transport in the streamwise scales is negative highlighting that a forward cascade towards the $r_x = 0$ scales is absent at the mean interface and supporting the existence of a reverse cascade towards the $r_x \neq 0$ scales. These observations are consistent with the picture of a propagating turbulent front where wide and long interface structures are generated by spatially ascending reverse cascade processes whose thickness is reduced by spatially ascending forward cascade mechanisms in the normal to the interface scales. In this scenario, dissipation is accomplished by vertical friction phenomena in a very thin interfacial layer over long and wide interface structures. To note that such mechanisms of dissipation share strong similarities with those commonly studied in 2-D turbulence (Boffetta and Ecke, 2012). This phenomenology has been observed also in free-shear flows by Cimarelli et al. (2015a, 2021); Zhou and Vassilicos (2020) thus possibly suggesting that the underlying physics is a robust and peculiar feature of turbulent interfaces in general. As a matter of fact, the behaviour of the scale-space transport at the channel centre is completely different and conforms with a forward cascade in the entire three-dimensional space of scales $(r_x, r_y, r_z)$ being the contributions to $T_r$ all positive. Hence, the channel centre is characterized by the generation of progressively smaller eddies that are eventually dissipated by classical small-scale viscous phenomena.

**Viscous sublayer**

The phenomena observed in the interface region have been found to have some similarities with the cascade and dissipation processes classically occurring in 2-D turbulence (Boffetta and Ecke, 2012). Wall turbulence is characterized by another region where 2-D turbulence effects are present, the viscous sublayer. Indeed, in this region of the flow the impermeability condition of the wall constrains the flow dynamics to two dimensions. Despite the flow dynamics in this region of the flow do not differ between channels and boundary layers, we will analyse it in order to highlight the similarities and the differences with respect to the scale-by-scale processes of the interface region. The main difference of the viscous sublayer from the

interface region is given by the fact that in the former the two-dimensional behaviour of turbulence is imposed by the wall constraint while in the latter by the dynamics of the interface. A second difference is also given by the fact that the no-slip condition of the wall makes the viscous sublayer dominated by viscous mechanisms contrary to the interface region where also inertial processes are dominant.

To better understand the scale-by-scale behaviour of the viscous sublayer with respect to the one at the interface, we perform a near-wall asymptotic analysis similar to the one reported in Cimarelli et al. (2013). The near-wall scaling of velocity and pressure is such that $\delta u, \delta v \sim z_c$, $\delta w, \widetilde{w} \sim z_c^2$ and $\delta p \sim \delta p_w$ where $\delta p_w$ is a characteristic pressure increment at the wall. By considering these two useful relationships (Hill, 2002)

$$\frac{\partial}{\partial r_i} = \frac{1}{2}\left(\frac{\partial}{\partial x_i'} - \frac{\partial}{\partial x_i''}\right) \qquad \frac{\partial}{\partial x_{c_i}} = \left(\frac{\partial}{\partial x_i'} + \frac{\partial}{\partial x_i''}\right) \tag{4.28}$$

we can write the near-wall asymptotic behaviour of the terms of the generalized Kolmogorov equation that for $r_z = 0$ reads

$$\begin{aligned}
&\frac{\partial\langle\delta q^2\rangle}{\partial t} \sim z_c^2, \qquad 2\langle\delta u\delta w\rangle\widetilde{\left(\frac{\partial U}{\partial z}\right)} \sim z_c^3, \qquad 4\langle\widetilde{\epsilon}\rangle \approx 4\nu\langle\frac{\partial u_i}{\partial z}\frac{\partial u_i}{\partial z}\rangle,\\
&\frac{\partial\langle\delta q^2\delta u_i\rangle}{\partial r_i} \sim z_c^3, \qquad 2\nu\frac{\partial^2\langle\delta q^2\rangle}{\partial r_\pi \partial r_\pi} \sim z_c^2,\\
&2\nu\frac{\partial^2\langle\delta q^2\rangle}{\partial r_z \partial r_z} \approx 2\nu\langle\frac{\partial u_i}{\partial z}\frac{\partial u_i}{\partial z}\rangle + 2\nu\langle\frac{\partial u_i'}{\partial z'}\frac{\partial u_i''}{\partial z''}\rangle, \qquad \frac{\partial\langle\delta q^2\widetilde{w}\rangle}{\partial z_c} \sim z_c^3,\\
&\frac{2}{\rho}\frac{\partial\langle\delta p\delta w\rangle}{\partial z_c} \sim z_c^2, \qquad \frac{\nu}{2}\frac{\partial^2\langle\delta q^2\rangle}{\partial z_c \partial z_c} \approx 2\nu\langle\frac{\partial u_i}{\partial z}\frac{\partial u_i}{\partial z}\rangle - 2\nu\langle\frac{\partial u_i'}{\partial z'}\frac{\partial u_i''}{\partial z''}\rangle,
\end{aligned} \tag{4.29}$$

where $\pi = x, y$ denotes the wall-parallel directions. Hence, we have that both production and scale-space transport rapidly vanish approaching the wall

$$\Pi \sim z_c^3, \qquad T_r \sim z_c^3 \tag{4.30}$$

and the budget reduces to a balance of spatial transport and scale-space diffusion with dissipation,

$$T_c + D_r - E \sim 0, \tag{4.31}$$

where $D_r$ is determined by the scale-space diffusion in the wall-normal scales, $D_r = 2\nu\partial^2\langle\delta q^2\rangle/\partial r_z^2$, while $T_c$ by the viscous diffusion, $T_c = (\nu/2)\partial^2\langle\delta q^2\rangle/\partial {z_c}^2$. In particular, the asymptotic scaling suggests that in the limit of large scales

$T_c = D_r = E/2$ while at small scales $T_c = 0$ and $D_r = E$. As shown in figure 4.11, these asymptotic scaling are found to fully describe the scale-by-scale behaviour of the viscous sublayer.

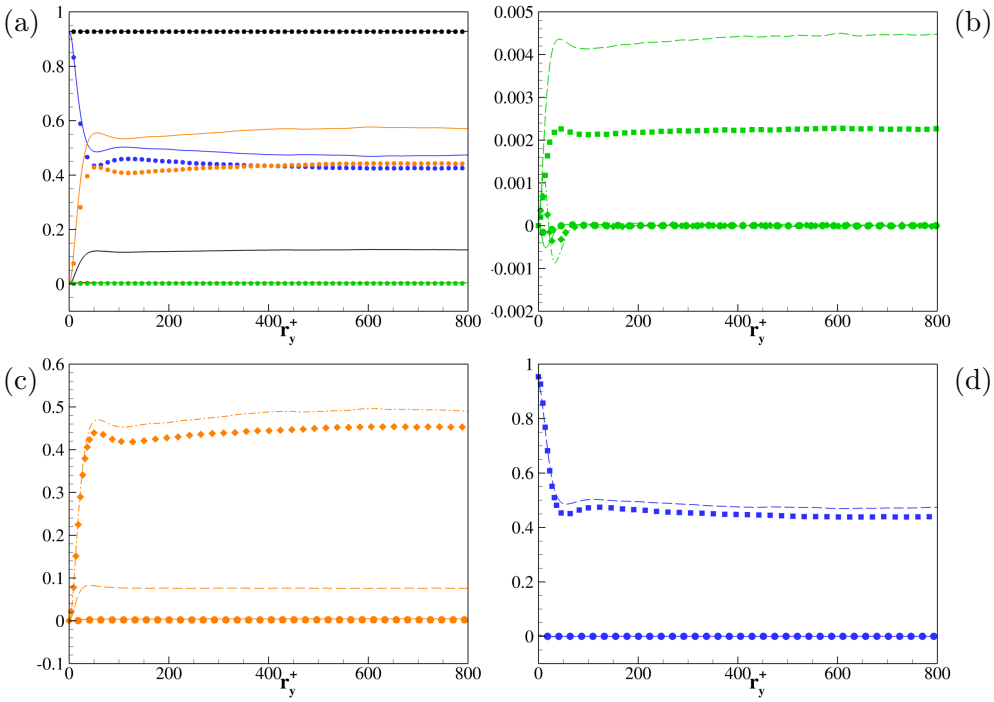


Figure 4.11: Scale-by-scale budget of wall turbulence evaluated in the viscous sublayer $z_c^+ = 1$ reported as a function of the spanwise scale $r_y^+$ for $r_x = r_z = 0$. Data from the turbulent boundary layer are reported with lines while those from the turbulent channel are reported with symbols. Different colors are used for the different terms of the generalized Kolmogorov equation (4.4): $\Pi$ (red), $T_r$ (green), $D_r$ (blue), $T_c$ (orange), $E$ (black, dashed line) and $\partial\langle\delta q^2\rangle/\partial t$ (black, solid line). The overall budget is reported in (a). The contributions to $T_r$ are shown in (b) where $-\partial\langle\delta q^2\delta u\rangle/\partial r_x$ (solid line and circle), $-\partial\langle\delta q^2\delta v\rangle/\partial r_y$ (dashed-dotted line and diamond), $-\partial\langle\delta q^2\delta w\rangle/\partial r_z$ (dashed line and square). The contributions to $T_c$ are shown in (c) where $-\partial\langle\delta q^2\widetilde{w}\rangle/\partial z_c$ (solid line and circle), $-(2/\rho)\partial\langle\delta p\delta w\rangle/\partial z_c$ (dashed line and square), $(\nu/2)\partial^2\langle\delta q^2\rangle/\partial {z_c}^2$ (dashed-dotted line and diamond). The contributions to $D_r$ are shown in (d) where $2\nu\partial^2\langle\delta q^2\rangle/\partial r_x^2$ (solid line and circle), $2\nu\partial^2\langle\delta q^2\rangle/\partial r_y^2$ (dashed-dotted line and diamond), $2\nu\partial^2\langle\delta q^2\rangle/\partial r_z^2$ (dashed line and square). Figure taken from Cimarelli et al. (2024b).

In accordance with the near-wall asymptotic scaling and the scale-by-scale budget shown in figure 4.11, the wall region is characterized by a

spatially descending forward cascade in the sole space of wall-normal scales. Hence, dissipation is accomplished by wall-normal velocity gradients occurring in a very thin layer over a wide range of horizontal scales in analogy with the 2-D phenomenology observed for the interface region. The main difference is the physical nature of the two transports occurring in physical and scale space that in the viscous sublayer is given by viscous diffusion phenomena

$$T_c \approx \frac{\nu}{2}\frac{\partial^2\langle\delta q^2\rangle}{\partial z_c \partial z_c}, \qquad D_r \approx 2\nu\frac{\partial^2\langle\delta q^2\rangle}{\partial r_z \partial r_z}, \qquad T_r \approx 0 \tag{4.32}$$

while in the interface layer by inertial turbulence mechanisms

$$T_c \approx -\frac{\partial\langle\delta q^2\widetilde{w}\rangle}{\partial z_c}, \qquad D_r \approx 0, \qquad T_r \approx -\frac{\partial\langle\delta q^2\delta w\rangle}{\partial r_z}. \tag{4.33}$$

# Chapter 5

# Turbulent enstrophy

We now move to analyse enstrophy in the temporal boundary layer in order to try to obtain a deeper insight about the confinement effects observed in the previous chapter 4. In section 5.1, the characteristics of single-point enstrophy and the budget that establishes its dynamics is investigated. Subsequently, the second section 5.2 deals with its distribution and its dynamics in the compound space of both scales and physical space.

## 5.1 Single-point budget

Turbulent enstrophy, defined as $\xi = \omega_i \omega_i$, is an observable closely related to the very nature of turbulence, given its close connection with dissipation and with its rotational nature. Its mean profile is shown in figure 5.1(a) where it is also compared with pseudo-dissipation $\langle \epsilon \rangle$, showing only a small discrepancy in a region between the viscous sublayer and the buffer layer. By applying equation 2.31 and 2.32 to the symmetries of the temporal boundary layer, we obtain:

$$\langle \epsilon \rangle = \nu \langle \xi \rangle + \nu \frac{\partial^2 \langle ww \rangle}{\partial z^2}. \tag{5.1}$$

Hence, the difference between the two terms is equal to the curvature of the term $\langle ww \rangle$ multiplied by viscosity.

We start the analysis by investigating the single-point enstrophy budget and its contributions $\langle \omega_x \omega_x \rangle$, $\langle \omega_y \omega_y \rangle$ and $\langle \omega_z \omega_z \rangle$ in order to obtain additional information on the confinement effect given by the wall and by the TNTI. For the symmetries of the temporal boundary layer, the turbulent enstrophy

budget equation reads:

$$\begin{gathered}\frac{\partial\langle\xi\rangle}{\partial t} = T_\xi + D_\xi + P_\xi + VS - \langle\epsilon_\xi\rangle, \\ T_\xi = -\frac{\partial\langle\xi w\rangle}{\partial z}, \qquad D_\xi = \nu\frac{\partial^2\langle\xi\rangle}{\partial z^2}, \qquad P_\xi = -2\langle\omega_y w\rangle\frac{\partial\Omega_y}{\partial z}, \\ VS = 2\langle\omega_x\omega_z\rangle\frac{\partial U}{\partial z} + 2\Omega_y\langle\omega_i\frac{\partial u_i}{\partial y}\rangle + 2\langle\omega_i\omega_j\frac{\partial u_i}{\partial x_j}\rangle, \\ \langle\epsilon_\xi\rangle = 2\nu\langle\frac{\partial\omega_i}{\partial x_j}\frac{\partial\omega_i}{\partial x_j}\rangle,\end{gathered} \tag{5.2}$$

being $T_\xi$ and $D_\xi$ the turbulent and viscous transport of enstrophy. $P_\xi$ is its production by mean vorticity gradient, $VS$ is the vortex stretching term that acts as a source by amplifying the vorticity through velocity gradients and $\epsilon_\xi$ the enstrophy destruction by vorticity gradients. The behaviour of the different terms is reported in figure 5.1(b). The dynamics of enstrophy

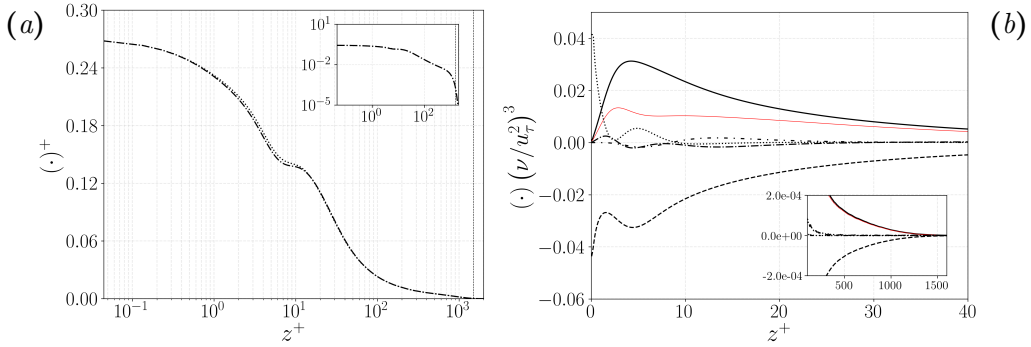


Figure 5.1: (a) Turbulent enstrophy $\langle\omega_i\omega_i\rangle$ (dash-dotted lines) compared to turbulent pseudo-dissipation $\langle\epsilon\rangle$ (dotted lines). The two terms are reported in logarithmic scale in the inset in order to better visualise the outer region. The vertical dotted line indicates the mean interface region. (b) Turbulent enstrophy budget: vortex stretching $VS$ is reported in solid lines, turbulent transport $T_\xi$ in dash-dotted lines, diffusive transport $D_\xi$ in dotted lines, production by mean vorticity gradient $P_\xi$ in loosely dash-dotted lines and enstrophy destruction $-\langle\epsilon_\xi\rangle$ in dashed lines. The $VS$ contribution $2\langle\omega_i\omega_j\partial u_i/\partial x_j\rangle$ is reported in red solid lines. In the inset the budget terms are reported on a larger scale to show the outer region. All curves are reported in viscous units and refer to the friction Reynolds number $Re_\tau = 1500$.

appear to be more concentrated in the near-wall region with respect to the one of the TKE (in figure 4.1) and its turbulent transport appears to

be more moderate in intensity. This can be explained by the fact that enstrophy is a "small-scale quantity", being related to velocity gradients, and does not correlate well with large-scale velocity fluctuations, which instead are the motions that more effectively accomplish the turbulent transport. Transport by diffusion is predominant only very close to the wall, while in almost all the rest of the domain, the enstrophy budget can be reasonably approximated with just production by vortex stretching and destruction via vorticity gradients. In particular, for $z^+ \gtrsim 40$, only the purely fluctuating contribution $2\langle\omega_i\omega_j\partial u_i/\partial x_j\rangle$ to vortex stretching appears to be relevant. This is even more pronounced in the outer region, reported in the inset in figure 5.1(b). This concept can be referred to as a spatial locality. Hence, in the outer region ($z^+ \gtrsim 40$), the budget equation 5.2 may be approximated as:

$$\langle\omega_i\omega_j\frac{\partial u_i}{\partial x_j}\rangle \approx -\nu\langle\frac{\partial\omega_i}{\partial x_j}\frac{\partial\omega_i}{\partial x_j}\rangle. \tag{5.3}$$

Therefore, in order to understand the dynamics of enstrophy (linked to the generation of dissipation), it is interesting to study the local distribution, generation and destruction of enstrophy, which we will focus on in the following.

### 5.1.1 Confinement effects

Vorticity, can only be generated by shear forces, which, in the presented flow settings, can only be introduced by the wall. In particular, the solid wall, whose normal is parallel to the $z$-direction, can only introduce streamwise $\langle\omega_x\omega_x\rangle$ and spanwise $\langle\omega_y\omega_y\rangle$ enstrophy contributions. Enstrophy is then transported away from the wall, initially by pure diffusion (since $w \sim z^2$) and then also via convective turbulent transport. Finally, the *VS* term, which in addition to pure stretching is also responsible for vortex tilting, accomplish the amplification and redistribution of the vorticity between its various components. In order to distinguish the various mechanisms described, we can start by analysing the three different contributions to enstrophy (hereafter named $\xi_x = \omega_x\omega_x$, $\xi_y = \omega_y\omega_y$ and $\xi_z = \omega_z\omega_z$). In figure 5.2, we report the three contributions normalized over the total turbulent enstrophy $\xi_{x_i}/\xi$, in order to better highlight the anisotropy level (in isotropic conditions $\langle\xi_x\rangle/\langle\xi\rangle = \langle\xi_y\rangle/\langle\xi\rangle = \langle\xi_z\rangle/\langle\xi\rangle = 1/3$). Furthermore, this allows a clear view of the enstrophy distribution among its components at all the wall distances, despite the enstrophy intensity changes of order of magnitudes while moving away from the wall. The picture that emerges can be interpreted as follows. In the viscous sublayer, the dynamics appear to

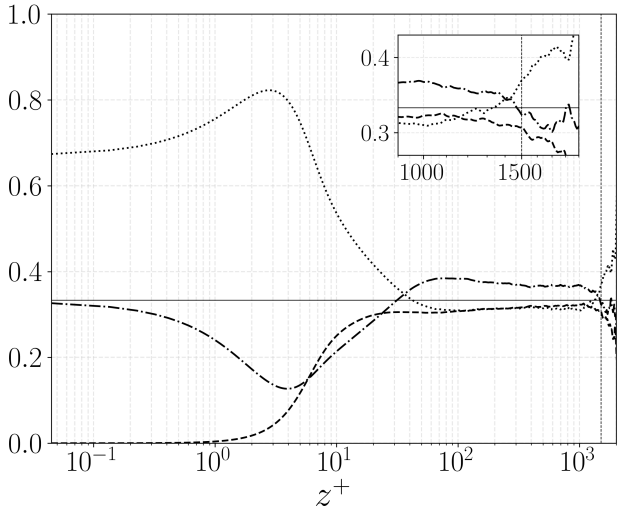


Figure 5.2: Distribution of the enstrophy content among its three contributions: streamwise $\langle \xi_x \rangle / \langle \xi \rangle$ (dash-dotted line), spanwise $\langle \xi_y \rangle / \langle \xi \rangle$ (dotted line) and wall-normal $\langle \xi_z \rangle / \langle \xi \rangle$ (dashed line). The reference value of 1/3, corresponding to equal distribution is reported as a solid line, while the vertical densely dotted vertical line indicates the mean interface position $z^+ = Re_\tau = 1500$. In the inset, an enlargement is reported to better highlight the interface region.

be dominated by the generation and transport by diffusion (figure 5.1(b)) of enstrophy through wall-normal gradients, caused by the presence of the wall. In fact, spanwise enstrophy $\langle \xi_y \rangle$, generated by streamwise near-wall velocity fluctuations, appears to be predominant, with streamwise enstrophy $\langle \xi_x \rangle$ being the only other non-negligible contribution. On the other hand, wall-normal enstrophy contribution $\langle \xi_z \rangle$ is negligible, being the only contribution to enstrophy not including $z$-derivatives of the velocity. From the buffer layer to just before the interface region, the streamwise vorticity is slightly more intense than the spanwise and the wall-normal, which are comparable in intensity. This may be due to the fact that, in the boundary layer, the turbulent motions tend to be elongated in the streamwise direction $x$, causing more moderate velocity gradients in this direction. As a result, the only enstrophy contribution that does not contain velocity gradients in $x$ (i.e. $\langle \xi_x \rangle$) is the most intense one. Near the TNTI region, it is possible to observe scenario similar to the one observed in the viscous sublayer, albeit more moderate in intensity. In fact, as shown in the inset of figure 5.2, spanwise vorticity is once again dominant, with wall-normal vorticity being

the lowest among the three contributions. This scenario is in accordance with the idea that, near the TNTI, as in the near-wall region, the flow tends to generate long and wide structures that dissipate energy through sharp gradients in the wall- and interface-normal direction.

By writing an equation for each of the three contributions of enstrophy, for the temporal boundary layer configuration we obtain:

$$\begin{aligned}
\frac{\partial\langle\xi_x\rangle}{\partial t} &= T_{\xi_x} + D_{\xi_x} + VS_x - \langle\epsilon_{\xi_x}\rangle,\\
T_{\xi_x} = -\frac{\partial\langle\omega_x\omega_x w\rangle}{\partial z}, &\qquad D_{\xi_x} = \nu\frac{\partial^2\langle\omega_x\omega_x\rangle}{\partial z^2},\\
VS_x = 2\langle\omega_x\omega_z\rangle\frac{\partial U}{\partial z} + 2\Omega_y\langle\omega_x\frac{\partial u}{\partial y}\rangle &+ 2\langle\omega_x\omega_j\frac{\partial u}{\partial x_j}\rangle,\\
\langle\epsilon_{\xi_x}\rangle &= 2\nu\langle\frac{\partial\omega_x}{\partial x_j}\frac{\partial\omega_x}{\partial x_j}\rangle,
\end{aligned} \tag{5.4}$$

$$\begin{aligned}
\frac{\partial\langle\xi_y\rangle}{\partial t} &= T_{\xi_y} + D_{\xi_y} + P_{\xi_y} + VS_y - \langle\epsilon_{\xi_y}\rangle,\\
T_{\xi_y} = -\frac{\partial\langle\omega_y\omega_y w\rangle}{\partial z}, &\qquad D_{\xi_y} = \nu\frac{\partial^2\langle\omega_y\omega_y\rangle}{\partial z^2},\\
P_{\xi_y} = -2\langle\omega_y w\rangle\frac{\partial\Omega_y}{\partial z}, &\qquad VS_y = 2\Omega_y\langle\omega_y\frac{\partial v}{\partial y}\rangle + 2\langle\omega_y\omega_j\frac{\partial v}{\partial x_j}\rangle,\\
\langle\epsilon_{\xi_y}\rangle &= 2\nu\langle\frac{\partial\omega_y}{\partial x_j}\frac{\partial\omega_y}{\partial x_j}\rangle
\end{aligned} \tag{5.5}$$

and

$$\begin{aligned}
\frac{\partial\langle\xi_z\rangle}{\partial t} &= T_{\xi_z} + D_{\xi_z} + VS_z - \langle\epsilon_{\xi_z}\rangle,\\
T_{\xi_z} = -\frac{\partial\langle\omega_z\omega_z w\rangle}{\partial z}, &\qquad D_{\xi_z} = \nu\frac{\partial^2\langle\omega_z\omega_z\rangle}{\partial z^2},\\
VS_z = 2\Omega_y\langle\omega_z\frac{\partial w}{\partial y}\rangle + 2\langle\omega_z\omega_j\frac{\partial w}{\partial x_j}\rangle, &\qquad \langle\epsilon_{\xi_z}\rangle = 2\nu\langle\frac{\partial\omega_z}{\partial x_j}\frac{\partial\omega_z}{\partial x_j}\rangle.
\end{aligned} \tag{5.6}$$

In particular, since the dominant terms in the turbulent enstrophy budget (figure 5.1(b)) appear to be its amplification by vortex stretching $VS$ and its destruction by vorticity gradients $\epsilon_\xi$, we will take a closer look to the decomposition of these two components of the budget in their contribution $VS_x$, $VS_y$, $VS_z$ and $\langle\epsilon_{\xi_x}\rangle$, $\langle\epsilon_{\xi_y}\rangle$ and $\langle\epsilon_{\xi_z}\rangle$. In figure 5.3(a) and (b), we report the distribution of the contributions normalized over the total $VS$ and $\langle\epsilon_\xi\rangle$ respectively. For the sake of clarity we do not show all the separate contributions, but only the most relevant terms, reported in red. In

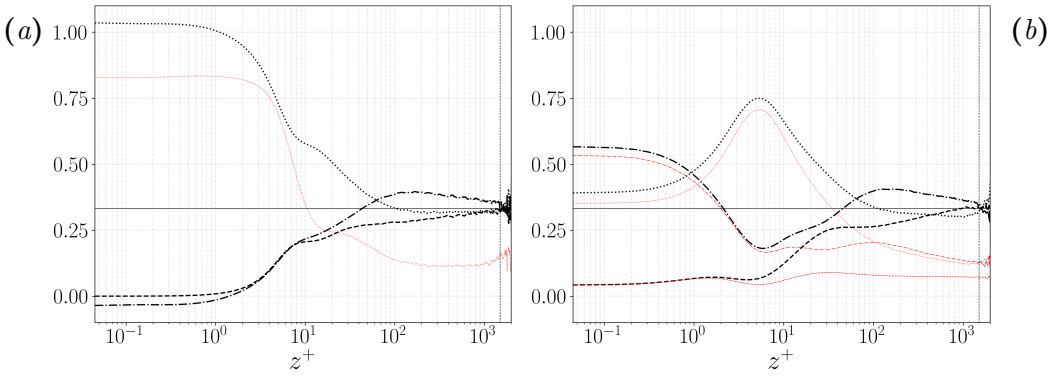


Figure 5.3: Distribution among the vortex stretching contributions $VS_x$ (dash-dotted line), $VS_y$ (dotted line) and $VS_z$ (dashed line) (a) and enstrophy destruction contributions $\langle \epsilon_{\xi_x} \rangle$ (dash-dotted line), $\langle \epsilon_{\xi_y} \rangle$ (dotted line) and $\langle \epsilon_{\xi_z} \rangle$ (dashed line) (b). In (a) the term $2\Omega_y \langle \omega_y \frac{\partial v}{\partial y} \rangle + 2\langle \omega_y \omega_y \frac{\partial v}{\partial y} \rangle$ is reported in dashed red line. In (b) the terms $2\nu\langle(\partial\omega_x/\partial z)^2\rangle$ (dash-dotted), $2\nu\langle(\partial\omega_y/\partial z)^2\rangle$ (dotted) and $2\nu\langle(\partial\omega_z/\partial z)^2\rangle$ (dashed) are reported in red lines. The reference value of 1/3, corresponding to equal distribution are reported as black solid lines, while the vertical densely dotted vertical lines indicate the mean interface position $z^+ = Re_\tau = 1500$.

the viscous sublayer, the only active vortex stretching term is the one amplifying spanwise vorticity, mainly by "pure" stretching of the mean and fluctuating spanwise vorticity $2\Omega_y \langle \omega_y \frac{\partial v}{\partial y} \rangle + 2\langle \omega_y \omega_y \frac{\partial v}{\partial y} \rangle$, reported in red in figure 5.3(a). On the other hand, the streamwise vorticity generated at the wall, on average, is not amplified locally, but is just transported by diffusion and dissipated locally, mainly by wall-normal gradients (as shown in figure 5.3(b) in red dash-dotted line). For this reason, we can consider that the fully 3-D dynamics of turbulence is only recovered from outside of the viscous sublayer onward. From the overlap layer onwards, the vortex stretching distribution among its contributions recover a similar trend to the one observed in the enstrophy contributions itself, suggesting a recovery of isotropy of the dynamics in the limits of the intrinsic anisotropies given by the shear. In figure 5.3(b), the rate of destruction of the three enstrophy contributions $\langle \epsilon_{\xi_x} \rangle$, $\langle \epsilon_{\xi_y} \rangle$ and $\langle \epsilon_{\xi_z} \rangle$ is reported. It is immediately possible to notice that in the near-wall region, most of the enstrophy destruction is accomplished by gradients in the wall-normal direction (reported in red). Despite the lower value of streamwise enstrophy contribution $\langle \xi_x \rangle$ with respect to the spanwise one $\langle \xi_y \rangle$ in the very near-wall region (figure 5.2), its destruction rate appears to be higher. In between the viscous sublayer and the buffer layer,

these two contributions to enstrophy destruction swap, recovering the trend of enstrophy distribution itself, observed in figure 5.2, again indicating a recovery of a fully 3-D dynamics.

In conclusion, turbulent enstrophy has shown a local dynamic mainly composed by production and destruction except for the very near-wall region, where the diffusive transport is relevant. By looking at its composition between the three contributions $\langle\omega_x\omega_x\rangle$, $\langle\omega_y\omega_y\rangle$ and $\langle\omega_z\omega_z\rangle$, it is possible to observe some confinement effects in the proximity of the wall and near the TNTI region as both of these regions have shown a predominance of spanwise vorticity. In particular, the near-wall dynamics appear to be dominated by the vortex stretching of spanwise vorticity, while in the bulk region, from after the buffer layer, the fully 3-D dynamic is quickly recovered.

## 5.2 Two-point budget

We can now proceed in analysing enstrophy and its dynamics by also expanding its behaviour in the space of scales. In order to achieve this, we apply the framework presented in section 2.2 to the temporal boundary layer. We start by recalling the second-order structure function of the fluctuating vorticity

$$\langle\delta\xi^2\rangle = \langle\delta\omega_i\delta\omega_i\rangle, \tag{5.7}$$

where $\delta\omega_i = \omega_i(x',t) - \omega_i(x'',t)$ is the increment of the vorticity fluctuations. By applying equation 2.37 to the flow configuration of the temporal

boundary layer, we obtain

$$\begin{gathered}
\frac{\partial\langle\delta\xi^2\rangle}{\partial t} = T_{r_\xi} + D_{r_\xi} + T_{c_\xi} + VS_{\delta\xi} + \Pi_{\delta\xi} - E_{\delta\xi}, \\
T_{r_\xi} = -\frac{\partial\langle\delta\xi^2\rangle\delta U}{\partial r_x} - \frac{\partial\langle\delta\xi^2\delta u_j\rangle}{\partial r_j}, \qquad D_{r_\xi} = 2\nu\frac{\partial^2\langle\delta\xi^2\rangle}{\partial r_j\partial r_j}, \\
T_{c_\xi} = -\frac{\partial\langle\delta\xi^2\widetilde{w}\rangle}{\partial z_c} + \frac{\nu}{2}\frac{\partial^2\langle\delta\xi^2\rangle}{\partial z_c^2}, \\
VS_{\delta\xi} = 2\widetilde{\Omega}_y\langle\delta\omega_i\delta\left(\frac{\partial u_i}{\partial y}\right)\rangle + 2\delta\Omega_y\langle\delta\omega_i\widetilde{\left(\frac{\partial u_i}{\partial y}\right)}\rangle + 2\langle\delta\omega_x\widetilde{\omega}_z\rangle\delta\left(\frac{\partial U}{\partial z}\right) \\
+2\langle\delta\omega_x\delta\omega_z\rangle\widetilde{\left(\frac{\partial U}{\partial z}\right)} + 2\langle\delta\omega_i\widetilde{\omega}_j\delta\left(\frac{\partial u_i}{\partial x_j}\right)\rangle + 2\langle\delta\omega_i\delta\omega_j\widetilde{\left(\frac{\partial u_i}{\partial x_j}\right)}\rangle, \\
\Pi_{\delta\xi} = -2\langle\delta\omega_y\widetilde{w}\rangle\delta\left(\frac{\partial\Omega_y}{\partial z}\right) - 2\langle\delta\omega_y\delta w\rangle\widetilde{\left(\frac{\partial\Omega_y}{\partial z}\right)}, \\
E_{\delta\xi} = 4\langle\widetilde{\epsilon}_\xi\rangle.
\end{gathered} \tag{5.8}$$

As before, $\widetilde{\omega}_i = 1/2\left(\omega_i\left(x',t\right) + \omega_i\left(x'',t\right)\right)$ is the two-point average of the vorticity and $\Omega_y$ is the mean spanwise vorticity. Equation 5.8 closely resembles the generalized Kolmogorov equation 4.4 except for the missing transport contribution due to pressure and for the additional production term constituted by the vortex stretching. $T_{r_\xi}$ and $D_{r_\xi}$ are the inertial and diffusive transport terms in the space of scales respectively, $T_{c_\xi}$ is the transport in the physical space, $\Pi_{\delta\xi}$ and $VS_{\delta\xi}$ are production terms by mean vorticity gradient and by vortex stretching and $E_{\delta\xi} = 4\langle\widetilde{\epsilon}_\xi\rangle$ is the enstrophy destruction, with

$$\langle\epsilon_\xi\rangle = 4\nu\langle\frac{\partial\omega_i}{\partial x_j}\frac{\partial\omega_i}{\partial x_j}\rangle. \tag{5.9}$$

This equation can be rewritten once again in its conservative form, highlighting the source terms and the fluxes. Similarly to equation 4.6, we get

$$\frac{\partial\langle\delta\xi^2\rangle}{\partial t} + \boldsymbol{\nabla_4}\cdot\boldsymbol{\phi_\xi} = S_\xi. \tag{5.10}$$

As in equation 4.6, the fluxes in the compound space constituted by $(r_x, r_y, r_z)$ for the space of scales and by $z_c$ in the physical space are

$$\phi_{\xi_{r_i}} = \partial\langle\delta\xi^2\delta u_i\rangle + \langle\delta\xi^2\delta U\rangle\delta_{i1} - 2\nu\frac{\partial\langle\delta\xi^2\rangle}{\partial r_i} \tag{5.11}$$

and

$$\phi_{\xi_{c_z}} = \langle \delta\xi^2 \widetilde{w} \rangle - \frac{\nu}{2} \frac{\partial \langle \delta\xi^2 \rangle}{\partial z_c} \tag{5.12}$$

respectively. The net source term reads

$$S_\xi = \Pi_{\delta\xi} + VS_{\delta\xi} - E_{\delta\xi}. \tag{5.13}$$

The results are organized as follows. In subsection 5.2.1, the two-point enstrophy is decomposed into three contributions $\langle \delta\omega_x^2 \rangle$,$\langle \delta\omega_y^2 \rangle$ and $\langle \delta\omega_z^2 \rangle$. The results are reported in the $(r_y, r_x)|_{r_z=0}$ space at different wall distances $z_c$. We then proceed to analyse the budget terms grouped by net source and fluxes, first in compound space $(r_x, r_y, z_c)|_{r_z=0}$ in section 5.2.2 and then in the subspaces $(r_y, z_c)|_{r_x,r_z=0}$ and $(r_y, z_c)|_{r_x,r_z=0}$ in section 5.2.3. Finally, the chapter is concluded with a more detailed view, showing the individual terms of the scale-by-scale budgets in the spanwise scales $r_y$ at different wall-distances $z_c$.

### 5.2.1 Structure function

Before addressing the terms of the two-point enstrophy budget equation, we start the analysis by showing how the enstrophy structure function $\langle \delta\xi^2 \rangle$ is distributed among its three contributions $\langle \delta\xi_x^2 \rangle = \langle \delta\omega_x \delta\omega_x \rangle$, $\langle \delta\xi_y^2 \rangle = \langle \delta\omega_y \delta\omega_y \rangle$ and $\langle \delta\xi_z^2 \rangle = \langle \delta\omega_z \delta\omega_z \rangle$. Our analysis is limited to the subspace $r_z = 0$ and, for the sake of clarity, we only show these distributions in the $(r_y, r_x)$ plane at some wall distances $z_c$ that are representative of the behaviour in the main regions of the flow.

Starting with the very near-wall region, we report the distribution of enstrophy at a wall distance of $z_c^+ = 0.5$ in figure 5.4. We recall that at such a wall distance, in the single-point view (figure 5.2), $\langle \xi_y \rangle$ is the dominant contribution, followed by $\langle \xi_x \rangle$, about half its intensity and $\langle \xi_z \rangle$ which is negligible compared to the first two. The distribution of enstrophy in the wall-parallel scales, is very reminiscent of the footprint given by the structures lying at higher wall distances. In particular, in figure 5.4(a), it can be observed a peak of the streamwise enstrophy contribution $\langle \delta\xi_x^2 \rangle$ at spanwise scales $r_y$ that are compatible with the dimension of the quasi-streamwise vortices populating the buffer layer (i.e. $r_y \approx 50$). This peak may be due to the spanwise velocity $v$ induced by those vortices in the very near-wall region, that in turn generate a streamwise vorticity by no-slip condition, through $\partial v/\partial z|_w$ gradients. Analogously, in figure 5.4(b), it is possible to observe the footprint of the streamwise velocity fluctuation, namely the streaks. In fact, these very large structures, elongated in the

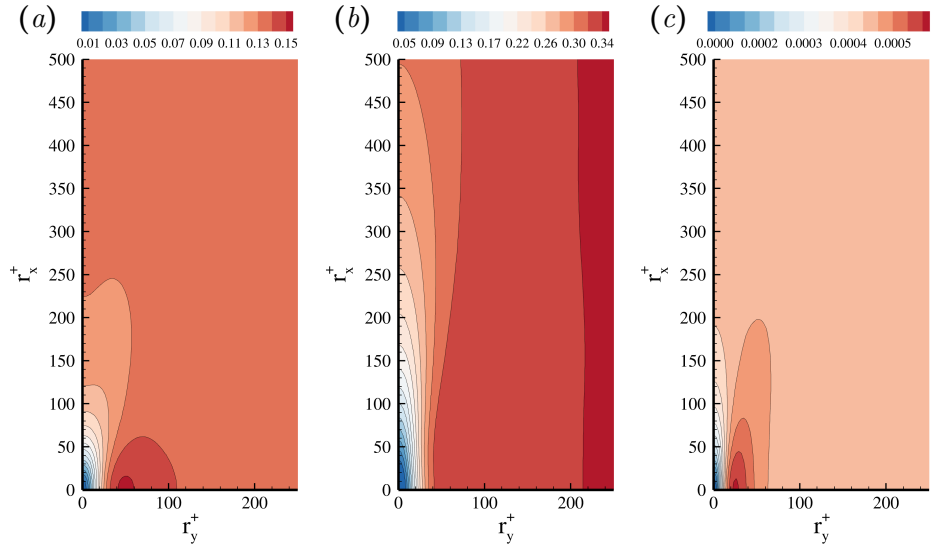


Figure 5.4: Second-order structure functions of streamwise $\langle \delta\xi_x^2 \rangle^+$ (a), spanwise $\langle \delta\xi_y^2 \rangle^+$ (b) and wall-normal $\langle \delta\xi_z^2 \rangle^+$ (c) enstrophy contributions in viscous units at a wall-distance of $z_c^+ = 0.5$.

$r_x$ scales, give rise to a similarly elongated spanwise vorticity near to the wall (mainly by $\partial u/\partial z|_w$). Finally, the wall-normal vorticity component, depicted through $\langle \delta\xi_z^2 \rangle$ in figure 5.4(c), exhibit a much lower intensity (as already pointed out in section 5.1) and a peak at spanwise separation lengths $r_y$ comparable, albeit smaller, to the one observed in $\langle \delta\xi_x^2 \rangle$. This feature may be the footprint of a region present in the buffer layer that will be commented on in the following. Throughout the extension of the viscous sublayer, the situation is consistent with what observed in figure 5.4, with an increasing intensity of $\langle \xi_z^2 \rangle$.

Transitioning to the buffer layer, a different scenario emerges. In particular, the streamwise enstrophy contribution at $z_c^+ = 11$, reported in figure 5.5(a), begins to recall the shape that would be expected in an isotropic scenario, i.e. slightly elongated along the $r_x$ axis (since the separation length in $r_x$ is a longitudinal increment for $\delta\omega_x$). We briefly recall that, in an isotropic scenario, one should expect to observe a slightly elongated longitudinal structure function with respect to the transverse ones. In the present case, this translates in $\langle \delta\xi_x^2 \rangle$ being slightly elongated in $r_x$, $\langle \delta\xi_y^2 \rangle$ slightly elongated in $r_y$ and $\langle \delta\xi_z^2 \rangle$ radially distributed in the $(r_x, r_y)$ plane (and elongated in the $r_z$ scales, which are not visible here). The impossibility of

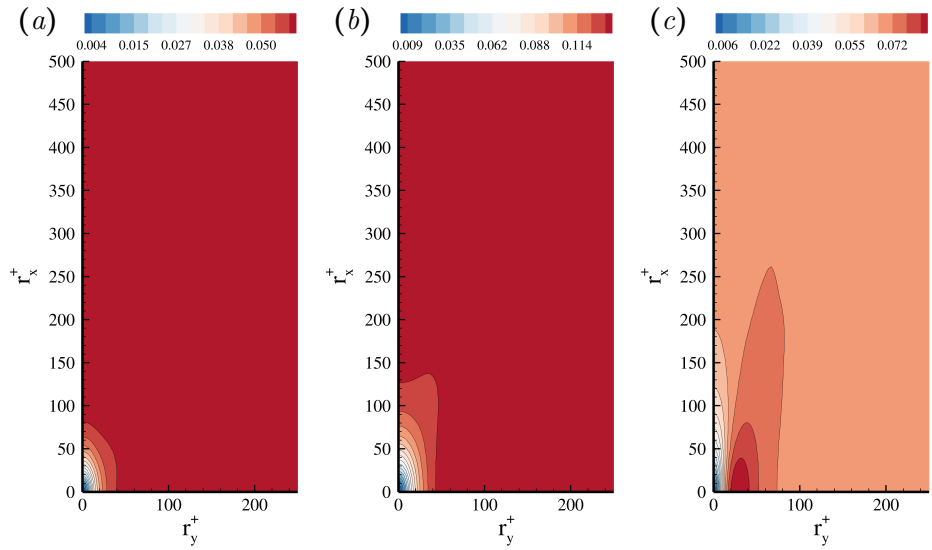


Figure 5.5: Second-order structure functions of streamwise $\langle \delta\xi_x^2 \rangle^+$ (a), spanwise $\langle \delta\xi_y^2 \rangle^+$ (b) and wall-normal $\langle \delta\xi_z^2 \rangle^+$ (c) enstrophy contributions in viscous units at a wall-distance of $z_c^+ = 11$.

identifying a characteristic scale by looking at the streamwise enstrophy contribution $\langle \delta\xi_x^2 \rangle$ at this wall distance, where we know that quasi-streamwise vortices are present, may indicate that most of the enstrophy is contained in disorganized motions, thus saturating the structure function, making their contribution not visible over the already high enstrophy content of the other chaotic motions. On the other side, the spanwise enstrophy contribution, in figure 5.5(b), still shows an elongated shape in the transverse separation lengths $r_x$ (i.e. being far from the isotropic case). The effect of the longitudinal velocity fluctuations appears to be still dominant at this wall distance. Finally, the peak of wall-normal vorticity $\langle \delta\xi_z^2 \rangle$ depicted in figure 5.4(c) is still present in the buffer layer, in figure 5.5(c), with a much stronger intensity. The mechanism causing this seems to be the only one visible both locally, where it takes place, and close to the wall, where it leaves its footprint. In fact, the mechanisms that we know to be active in the buffer layer, such as the quasi-streamwise vortices and the streaks, have so far been visible mainly very close to the wall and not directly in the region where they are most intense. To try to provide an explanation of what is observed, we report in figure 5.6 the isosurface representing this high $\langle \delta\xi_z^2 \rangle$ value together with the high values of the different contributions to the vortex stretching.

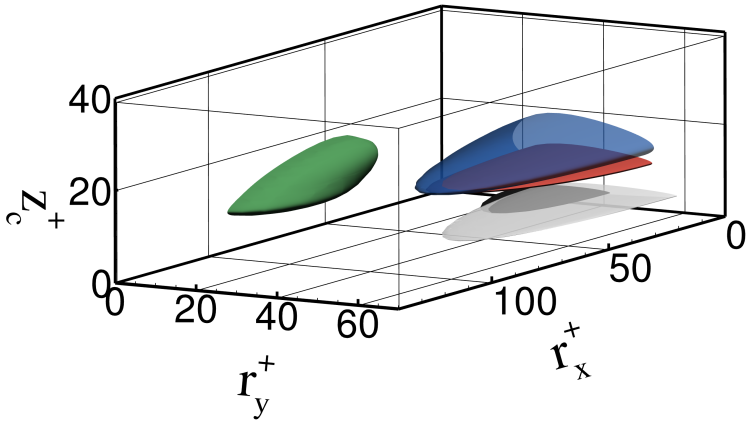


Figure 5.6: Isosurfaces of $\langle \delta\xi_z^2 \rangle^+ = 0.08$ (transparent blue), $2\Omega_y^+ \langle \delta\omega_i \delta \left( \frac{\partial u_i}{\partial y} \right) \rangle^+ = 0.05$ (transparent white), $2\langle \delta\omega_x \delta\omega_z \rangle^+ \frac{\partial U^+}{\partial z^+} = 0.028$ (red), $2\langle \delta\omega_i \widetilde{\omega}_j \delta \left( \partial u_i / \partial x_j \right) \rangle^+ = 0.017$ (black) and $2\langle \delta\omega_i \delta\omega_j (\widetilde{\partial u_i / \partial x_j}) \rangle^+ = 0.0156$ (green) in the near-wall region.

The $\Pi_{\delta\xi}$ production term is not reported as its maximum value $\Pi_{\delta\xi}^+ = 0.0044$ (located in the buffer layer), is found to be smaller by one order of magnitude than all the vortex stretching contributions. In particular, the $\langle \delta\xi_z^2 \rangle$ isosurface, in transparent blue, appears to be located near the region of maximum activity of the term $2\langle \delta\omega_x \delta\omega_z \rangle \partial U / \partial z$, while all the other three vortex stretching contributions (in equation 5.14 and in the label of figure 5.6) act either very near the wall, at similar wall-parallel scales, or in a completely different region. This term links the mean gradient $\partial U / \partial z$ and the correlation between the streamwise and wall-normal vorticity components $\delta\omega_x$ and $\delta\omega_z$. We therefore presume that the peak in $\langle \delta\xi_z^2 \rangle$ located in the buffer layer may be due to the tilting of the quasi-streamwise vortices, which, acquiring a wall normal vorticity component, become the main vorticity contribute in the $z$-direction, since this vorticity component is small in this flow region. Furthermore, this term represents the largest contribution to the enstrophy generation in the buffer layer, indicating that, possibly, dissipation in the buffer layer is generated mainly by mechanisms linked to the tilting of quasi-streamwise vorticity. On the other hand, the other main coherent structures appear to generate dissipation mainly through their footprint at the wall, and not locally at the wall distance at which they exhibit their maximum energy content.

As we move toward the outer region, passing through the overlap layer,

we can observe a gradual recovery of isotropy in all vorticity components. As shown in figure 5.7, the distribution of enstrophy among its three contributions is exactly as expected in an isotropic case. In fact, its intensity is evenly distributed among all $\langle \delta\xi^2_{x_i} \rangle$ and the shape is slightly elongated in the longitudinal direction of the structure function considered. It is also worth noting the increase in the size of the scales involved as we move away from the wall, as expected.

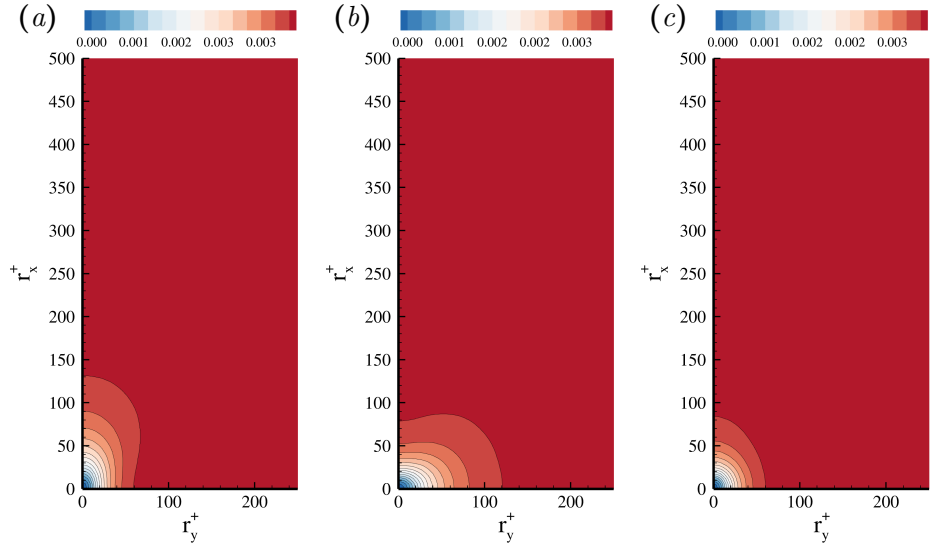


Figure 5.7: Second-order structure functions of streamwise $\langle \delta\xi^2_x \rangle^+$ (a), spanwise $\langle \delta\xi^2_y \rangle^+$ (b) and wall-normal $\langle \delta\xi^2_z \rangle^+$ (c) enstrophy contributions in viscous units at a wall-distance of $z_c^+ = 450$.

Finally, in figure 5.8 we report the enstrophy distribution at the mean interface location $z^+ = Re_\tau = 1500$. In this region, the isotropy that was recovered by the flow in the outer region, is again unbalanced, albeit less intensively. In fact, it is possible to notice that $\langle \delta\xi^2_y \rangle$ is spread over a wider range of scales with respect to $\langle \delta\xi^2_x \rangle$ and with a slightly higher intensity. This observation is in accordance with the idea of long (in $r_x$) and wide (in $r_y$) structures that dissipate energy through sharp gradients in the interface-normal direction. In addition to being a less intense phenomenon than the confinement given by the solid wall, it must be said that the statistical tool we are exploiting makes use of the classical averages (as opposed to the conditional averages), hence failing to follow the corrugated surface of the instantaneous TNTI. Consequently, the observed effect is mitigated since we

are calculating statistics in a plane parallel to the wall intersecting both protruding bulges containing both turbulent motions and non-turbulent zones (see figure 3.1). Furthermore, it must be noted that, given the intricate nature of the TNTI, the direction normal to it can strongly differ with respect to the wall-normal direction. Nevertheless, the framework used, despite its inability to follow the intricate instantaneous isosurfaces characteristic of a turbulent flow, is able to identify the overall effect of the fundamental mechanisms and place it in a sound mathematical context.

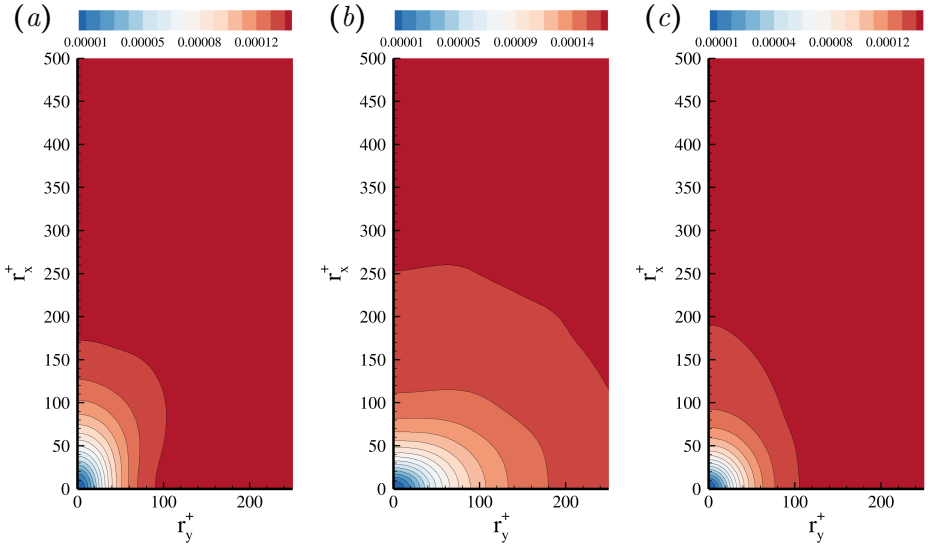


Figure 5.8: Second-order structure functions of streamwise $\langle \delta\xi_x^2 \rangle^+$ (a), spanwise $\langle \delta\xi_y^2 \rangle^+$ (b) and wall-normal $\langle \delta\xi_z^2 \rangle^+$ (c) enstrophy contributions in viscous units at a wall-distance of $z_c^+ = Re_\tau = 1500$.

### 5.2.2 Sources and paths in the $(r_x, r_y, z_c)$ compound space

In starting this subsection, we report the budget equation 5.8 applied to the case $r_z = 0$ that will be analysed in the following. By imposing $r_z = 0$, the two-point increments and averages of the average quantities simplify to $\delta\langle\cdot\rangle = 0$ and $\widetilde{\langle\cdot\rangle} = \langle\cdot\rangle$ respectively. Consequently, the terms in equation 5.8

reduce to:

$$
\begin{aligned}
T_{r_\xi} &= -\frac{\partial\langle\delta\xi^2\delta u_j\rangle}{\partial r_j}, \qquad D_{r_\xi} = 2\nu\frac{\partial^2\langle\delta\xi^2\rangle}{\partial r_j\partial r_j},\\
T_{c_\xi} &= -\frac{\partial\langle\delta\xi^2\widetilde{w}\rangle}{\partial z_c} + \frac{\nu}{2}\frac{\partial^2\langle\delta\xi^2\rangle}{\partial z_c^2},\\
VS_{\delta\xi} &= 2\Omega_y\langle\delta\omega_i\delta\left(\frac{\partial u_i}{\partial y}\right)\rangle + 2\langle\delta\omega_x\delta\omega_z\rangle\frac{\partial U}{\partial z}\\
&+2\langle\delta\omega_i\widetilde{\omega}_j\delta\left(\frac{\partial u_i}{\partial x_j}\right)\rangle + 2\langle\delta\omega_i\delta\omega_j\widetilde{\left(\frac{\partial u_i}{\partial x_j}\right)}\rangle,\\
\Pi_{\delta\xi} &= -2\langle\delta\omega_y\delta w\rangle\frac{\partial\Omega_y}{\partial z},\\
E_{\delta\xi} &= 4\langle\epsilon_\xi\rangle.
\end{aligned}
\tag{5.14}
$$

As in chapter 4, we can express the budget as an extended source term and the divergence of fluxes in the $(r_x, r_y, z_c)\,|_{r_z=0}$ subspace:

$$
\left.\frac{\partial\phi_{\xi_{r_\pi}}}{\partial r_\pi}\right|_{r_z=0} + \left.\frac{\partial\phi_{\xi_{c_z}}}{\partial z_c}\right|_{r_z=0} = \mathcal{S}_{r_z=0}, \tag{5.15}
$$

being

$$
\phi_{\xi_{r_\pi}} = \langle\delta\xi^2\delta u_\pi\rangle - 2\nu\frac{\partial\langle\delta\xi^2\rangle}{\partial r_\pi} \tag{5.16}
$$

the flux in the space of wall-parallel scales, and

$$
\phi_{\xi_{c_z}} = \langle\delta\xi^2\widetilde{w}\rangle - \frac{\nu}{2}\frac{\partial\langle\delta\xi^2\rangle}{\partial z_c} \tag{5.17}
$$

the flux in the physical space, consisting of the wall distance. Again, $\pi = x, y$ denotes the statistically homogeneous streamwise and spanwise directions and $\mathcal{S}_{r_z=0}$ is the extended source term, which in addition to the production by mean vorticity gradient, to vortex stretching and to the enstrophy destruction, takes into account the enstrophy exchange with the $r_z \neq 0$-space,

$$
\mathcal{S}_{r_z=0} = -\left.\frac{\partial\langle\delta\xi^2\rangle}{\partial t}\right|_{r_z=0} + \Pi_{\delta\xi}|_{r_z=0} + VS_{\delta\xi}|_{r_z=0} - 4\nu\langle\epsilon_\xi\rangle - \left.\frac{\partial\phi_{\xi_{r_z}}}{\partial r_z}\right|_{r_z=0}, \tag{5.18}
$$

being $\phi_{\xi_{r_z}} = \langle\delta\xi^2\delta w\rangle - 2\nu\partial\langle\delta\xi^2\rangle/\partial r_z$.

In figure 5.9, sources and sinks of enstrophy are reported through isosurfaces, while fluxes are represented by streamlines. Red isosurfaces represent a positive source of enstrophy, while blue and grey isosurfaces represent sinks

of enstrophy with different intensities. In particular, it is possible to identify two intense source regions ($S_\xi > 0$) in the near-wall region. As better shown in figure 5.10, both isosurfaces are located in the buffer layer, which, even without considering these two peaks, is the region with the highest net enstrophy production rate. These isosurfaces are elongated in the $r_x$ direction and are centred in the $r_y = 0$ and $r_x = 0$ planes respectively, with the most intense being the one originating on the $r_x = 0$ plane. The maximum value reached by the source term in this region is $S_\xi^+ = 0.0088$, located in $\left(r_x^+, r_y^+, z_c^+\right) = (0, 43, 12)$. The second source region shows a similar intensity $S_\xi^+ = 0.0083$, at the same distance from the wall, centred in $\left(r_x^+, r_y^+, z_c^+\right) = (145, 0, 12)$. Although the buffer layer represents the main net amplifier of enstrophy, it should be remembered that all enstrophy fluxes start from the wall and, while ascending, are deflected and amplified by the vortex stretching and production mechanisms. On the contrary, we recall that in the turbulent kinetic energy, production is embedded in the flow system, which therefore shows a singularity point located in the buffer layer from which the fluxes originate. The enstrophy fluxes starting from the wall are initially purely diffusive and, as they move away from the wall, begin to acquire an increasing convective contribution given by turbulence. At the same time, the wall is also the region in which the rate of enstrophy destruction is the highest, as shown by the solid blue isosurface in figures 5.9 and 5.10. A portion of enstrophy destruction is also accomplished at all wall distances, at small wall-parallel scales, depicted by the grey isosurface in transparency. The latter extends across the entire thickness of the boundary layer and appears to be fed mainly by fluxes diverging from the source region with origin in the $r_x = 0$ plane. The fluxes originating near the $r_x = 0$ plane, appear to split in two groups. The first group of fluxes, generated at a scale smaller than a certain threshold (shown in more details in the next subsection) end up destroying enstrophy at small scales while moving away from the wall in a slightly helical ascent. In contrast, the second group, constituted by fluxes that are generated at scales larger than this threshold, ascend vertically with a slight deviation towards larger spanwise scales. As it can be noted from the enlargement reported in figure 5.10, these fluxes show an initially predominant vertical component and, in the proximity of the source region, diverge toward larger and smaller spanwise scales $r_y$. On the other hand, the fluxes lying on the $r_y = 0$ plane present an initially strong direct enstrophy cascade in the streamwise scales $r_x$. Hence, the source region lying on the $r_y = 0$ plane mainly acts as a repulsion towards lower and higher wall distances in the physical space.

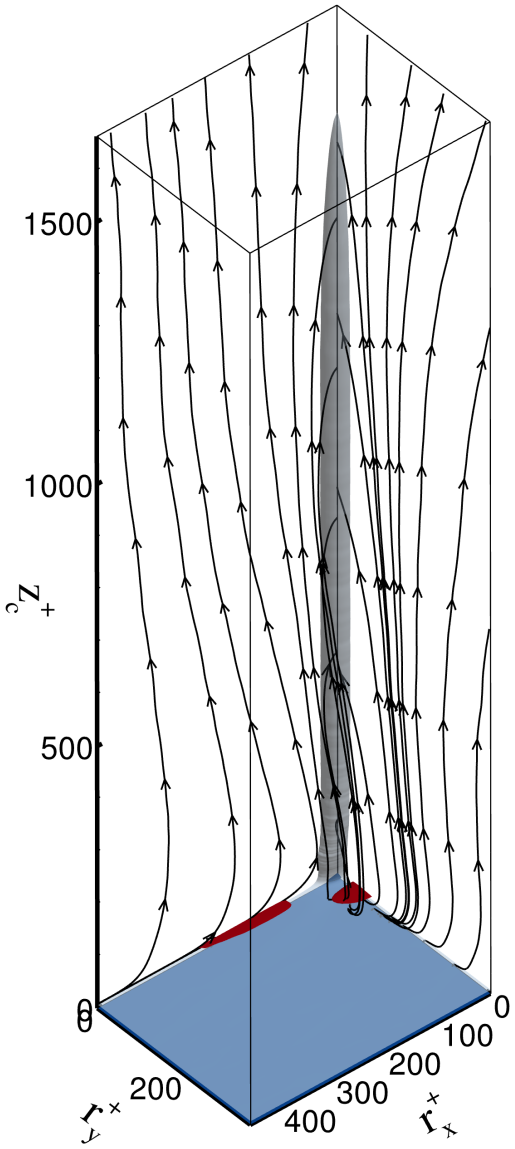


Figure 5.9: Sources and fluxes of scale-enstrophy. Isosurfaces of positive net source of enstrophy $S_\xi^+ = 0.008$ (red) and negative net source $S_\xi^+ = -0.05$ (solid blue) and $S_\xi^+ = -5 \times 10^{-6}$ (transparent grey). The fluxes are reported as black lines and arrows.

Finally, it is possible to note the presence of a spanwise scale $r_y$ that discriminates between the two different behaviours observed in the vicinity

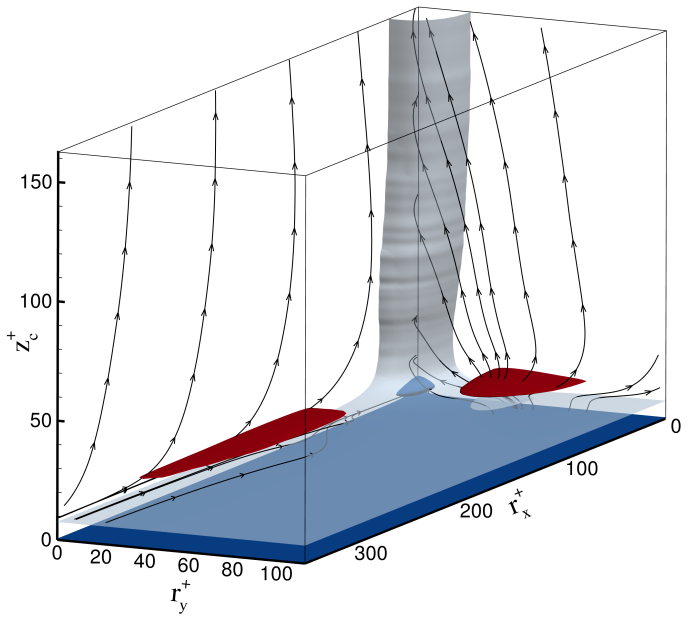


Figure 5.10: Sources and fluxes of scale-enstrophy in the near-wall region. Isosurfaces of positive net source of enstrophy $S_\xi^+ = 0.008$ (red) and negative net source $S_\xi^+ = -0.05$ (solid blue) and $S_\xi^+ = -5 \times 10^{-6}$ (transparent grey). The fluxes are reported as black lines and arrows.

of the two planes $r_x = 0$ and $r_y = 0$ respectively. In figure 5.11, the fluxes arising from the wall are shown. The fluxes generated at a scale $r_y^+ \lesssim 55$ end up being confined below the buffer layer due to the repulsion exerted by the source region lying on the $r_y = 0$ plane. These fluxes continue their direct cascade in the streamwise scales and end up dying on the $z_c$-axis. The dynamics of enstrophy generated at $r_y^+ \lesssim 55$ scales can be considered as local, since, after being generated at the wall and diffused in the viscous sublayer, it undergoes a simple and spatially local direct enstrophy cascade. On the other hand, the fluxes generated at a spanwise scale $r_y^+ \gtrsim 55$, manage to get through the buffer layer, feeding the outer region of the flow. The isosurface of enstrophy destruction in figure 5.11, is coloured by the intensity of the structure function $\langle \delta\xi^2 \rangle$, highlighting that the enstrophy that remains confined under the buffer layer is quite low in intensity and may be generated by local small-scale velocity fluctuations. On the other hand, the high enstrophy content generated at the wall by the footprint of the structures populating the buffer layer and the overlap layer, manage to

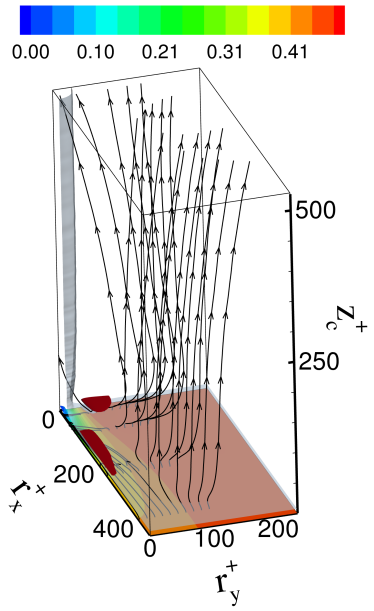


Figure 5.11: Sources and fluxes of scale-enstrophy highlighting the presence of a diving spanwise scale. Isosurfaces of positive net source of enstrophy $S_\xi^+ = 0.008$ are reported in red. The main sink of enstrophy $S_\xi^+ = -0.05$ is coloured by intensity of $\langle \delta\xi^2 \rangle^+$ and the weaker sink $S_\xi^+ = -5 \times 10^{-6}$ is reported in transparent grey. The fluxes are reported as black lines and arrows.

reach the outer region, probably since its characteristic scale is coherent with the dimension of the turbulent motions that most effectively accomplish the spatial transport, thus efficiently correlating with them. In this way, the large structures $r_y^+ \gtrsim 55$ that populate the outer region not only show their footprint at the wall (which represent the dominant enstrophy feature in the viscous sublayer), but also interact with the wall itself. This view seems to be consistent with the picture depicted by the "wall cycle" described in Jiménez and Pinelli (1999), where the mechanism of generation of secondary streamwise vorticity at the wall subsequently transferred towards the buffer layer is firstly described.

The presence of a scale qualitatively separating the two behaviours, that is in first approximation constant with respect to $r_x$ such that $r_y^+ \approx 55$, makes the study of the separate $(r_y, z_c)$ and $(r_x, z_c)$ dynamics worthwhile. For this reason, we proceed in the following section by investigating these two dynamics, with particular focus on the $(r_y, z_c)$ dynamics, which appears

to be more rich and more representative of the phenomena occurring.

### 5.2.3 Sources and fluxes in the $(r_y, z_c)$ and $(r_x, z_c)$ compound space

In order to simplify the interpretation of what we saw in the previous section, we will now focus on the topology of sources and fluxes in the planes $r_z = r_x = 0$ and $r_z = r_y = 0$, which we will henceforth refer to as the $(r_y, z_c)$ and $(r_x, z_c)$ subspaces. In figure 5.12(a) and (b), the source term $S_\xi^+$ and the field of fluxes are reported on these two planes respectively. From a first macroscopic view, it is possible to observe some differences. In particular, the fluxes on the $(r_y, z_c)$ plane, undergo an initial reverse enstrophy transfer towards larger spanwise scales $r_y$ as they ascend until they pass the high production zone located in the buffer layer, better shown in the enlargement reported in figure 5.13(a). It is then possible to identify two groups of fluxes. The first one, originating at the wall at spanwise scales $r_y^+ \lesssim 110$, undergo a direct enstrophy cascade while moving away from the wall and ends up dissipating at small scales. On the other hand, the second group of fluxes, generated at scales $r_y^+ \gtrsim 110$, ascends almost vertically after passing the buffer layer and slightly deviates towards larger scales while approaching the interface region.

The fluxes lying on the $(r_x, z_c)$ plane, on the other hand, present a very strong direct cascade component towards small $r_x$ scales in the buffer layer (figure 5.12(b) and 5.13(b)). As they move towards smaller scales, the fluxes are energised by the source term that extends up to $r_x^+ \approx 50$ and acts as a repulsion by accelerating them (increasing $\phi_{\xi_{r_x}}$ and by deflecting them towards the wall and away from it). Since the enstrophy fluxes always start at the wall and with an initially vertical direction, the fluxes deflected towards smaller wall distances with respect to the buffer layer do not end up at the wall, but they reach the $r_x = 0$ axis. To note that the fluxes entering the domain from the right (i.e. large $r_x$ scales), in the enlargement shown in figure 5.13(b), are not generated in the buffer layer, but are simply generated at the wall at large streamwise scales which do not fit in the plot. In particular, it is found that all the streamlines that reach the $z_c$-axis at a wall distance $z_c^+ > 3$(diverging from the buffer layer as they approach small $r_x$ scales), are generated at the wall around a streamwise scale $r_x^+ \approx 710$. At the same time, the fluxes that are ascending starting from the wall at scales smaller than $r_x^+ \approx 710$, reported in figure 5.13(b), are strongly affected by the repulsion of the buffer layer source and immediately bend towards smaller scales, ending up dissipating at small scales.

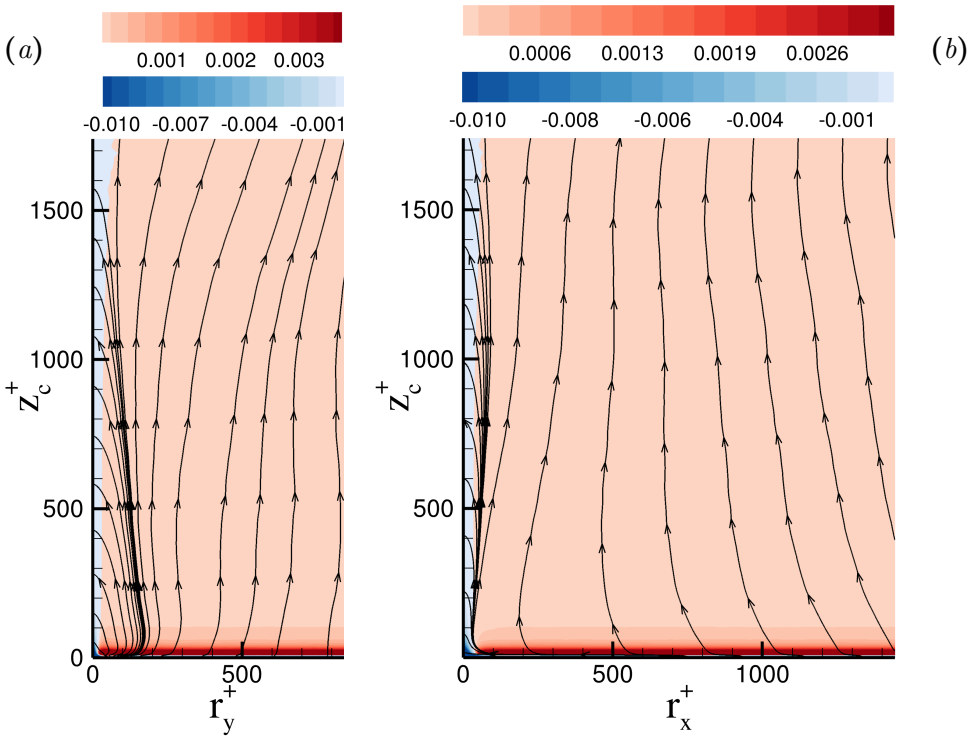


Figure 5.12: Sources $S^+$ and fluxes $\boldsymbol{\phi}^+$ of scale-enstrophy in the subspaces $(r_y^+, z_c^+)|_{r_z, r_x=0}$ (a) and $(r_x^+, z_c^+)|_{r_z, r_y=0}$ (b). Negative values of $S^+ < 0$ are reported on scale of blues, while positive values $S^+ > 0$ on scale of reds. The fluxes $((\phi_{r_y}^+, \phi_{c_z}^+)(r_y^+, z_c^+)$ in (a) and $(\phi_{r_x}^+, \phi_{c_z}^+)(r_x^+, z_c^+)$ in (b)) are reported as black lines and arrows.

As for the turbulent kinetic energy in chapter 4, the spanwise dynamic provides a richer and more indicative picture, with also the presence of reverse enstrophy transfer phenomena. In figure 5.13(a), it is possible to note the $(r_y, z_c)$ cross-section of the high production region observed in figure 5.10. This source region strongly deflects the ascending fluxes and its topology is such that the fluxes originated at the wall at a spanwise scale $r_y^+ \lesssim 50$ undergo a direct enstrophy cascade while moving away from the wall, while those generated at a $r_y^+ \gtrsim 50$ grow in size while ascending and begin a direct cascade only at higher distances from the wall. Again, this picture is consistent with the idea that quasi-streamwise vortices generate a secondary streamwise vorticity $\omega_x$ by inducing a spanwise velocity $v$ near the wall as

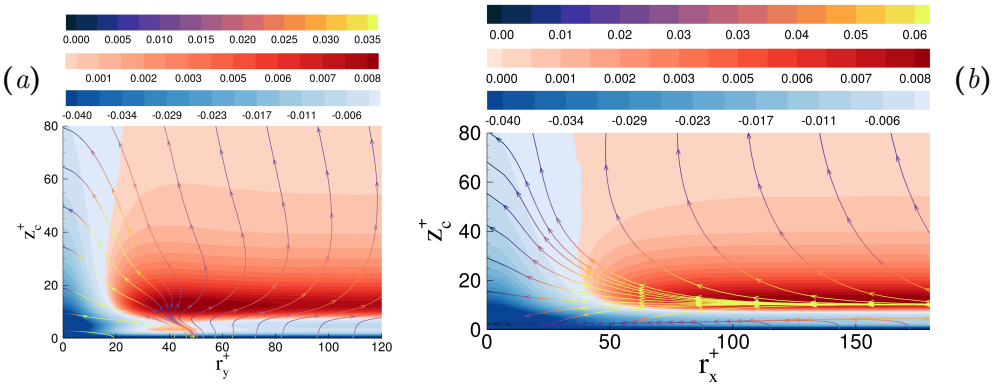


Figure 5.13: Sources $S^+$ and fluxes $\boldsymbol{\phi}^+$ of scale-enstrophy in the near-wall region reported in the subspaces $(r_y^+, z_c^+)|_{r_z,r_x=0}$ (a) and $(r_x^+, z_c^+)|_{r_z,r_y=0}$ (b). Negative values of $S^+ < 0$ are reported on scale of blues, while positive values $S^+ > 0$ on scale of reds. The fluxes $((\phi_{r_y}^+, \phi_{c_z}^+)(r_y^+, z_c^+)$ in (a) and $(\phi_{r_x}^+, \phi_{c_z}^+)(r_x^+, z_c^+)$ in (b)) are represented by lines and arrows and are coloured by the intensity of fluxes, $\sqrt{\phi_{r_y}^2 + \phi_{c_z}^2}^+$ in (a) and $\sqrt{\phi_{r_x}^2 + \phi_{c_z}^2}^+$ in (b).

in the "wall cycle" described in Jiménez and Pinelli (1999). This vorticity is subsequently transported away from the wall towards the buffer layer.

Analogously as in section 4.2.2, we can define a cross-over scale $\ell_{\xi_b}$ such that $\phi_{\xi_{r_y}}(\ell_{\xi_b}, z_c) = 0$ that separates the direct and the reverse enstrophy transfer. Despite the different topology of the fluxes $\phi_\xi|_{r_z,r_x=0}$ and $\phi|_{r_z,r_x=0}$, this cross-over scale is found to scale linearly and in a very similar way to that exhibited by the analogous $l_b$ (separating the direct and reverse energy transfer). The scaling of these two quantities is reported in figure 5.14. The cross-over scales are compared with the injection scale of energy (defined as the scale $\ell_{\Pi_{max}}$ such that $\Pi(\ell_{\Pi_{max}}, z_c) = \max(\Pi(r_y, z_c))$) and are found to scale similarly up to $z_c^+ \approx 200$. This similarity indicates that the split energy cascade observed in the dynamics of the scale-energy, presumably due to the presence of the attached eddies is also present in the enstrophy. This may be interpreted as follows. The process of a direct energy cascade, connected to the detached eddies breakage, leads to the generation of finer scales, both in terms of energy and in term of enstrophy. On the other hand, the reverse $r_y$ energy transfer, linked to the growth of the attached eddies as

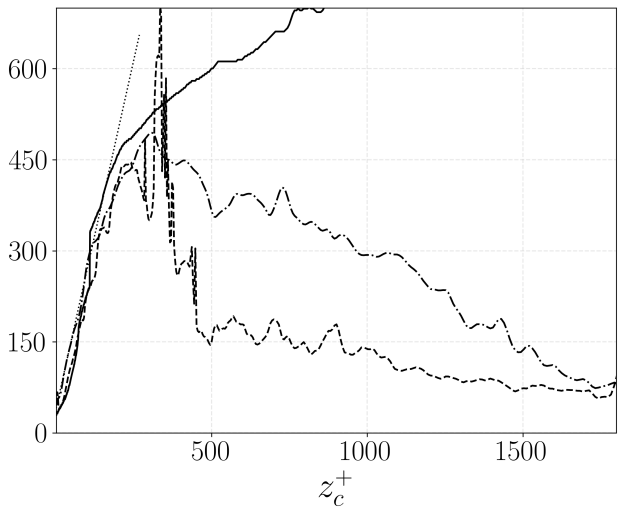


Figure 5.14: Crossover scales of scale-enstrophy $\ell^+_{\xi_b}(z_c^+)$ (dashed line) and scale-energy $\ell^+_b(z_c^+)$ (dash-dotted line) as a function of the wall distance. The energy injection scale $\ell_{\Pi_{max}}$ is reported in solid line. The dotted line reports the self-similar scaling 4.17.

we move towards higher wall distances, also leads to the generation of more relaxed velocity gradients composing enstrophy. In this respect, enstrophy seems to behave as a tracer of turbulent energy that, in a sense, mimics its behaviour.

### 5.2.4 Scale-by-scale budgets

We conclude the present chapter by analysing the scale-by-scale spanwise budgets that can provide us with a more quantitative and precise view of what has been described above. As for the analysis of the enstrophy structure function in section 5.2.1, we limit the analysis to few wall-distances that are representative of the flow region in which they are located.

#### Very near-wall region

We start our analysis with the very near-wall region. In figure 5.15(a), the enstrophy budget in the spanwise scales $r_y$ at a wall distance $z_c^+ = 0.5$ is reported. As expected at such a wall distance, the dominant mechanisms are the viscous ones. In fact, the main contributions to the budget in this location are the diffusive transports both among scales and in the physical space. However, the vortex stretching term is already active with

a non-negligible intensity. From figure 5.15(b), where the vortex stretching term is decomposed in its four contributions, it appears that the main contribution responsible for this comes from the term $2\Omega_y\langle\delta\omega_i\delta\left(\partial u_i/\partial y\right)\rangle$, which can be interpreted as the stretching and tilting of the mean vorticity $\Omega_y$. In particular, this term exhibits a peak at scales compatible with the quasi-streamwise vorticies living in the buffer layer, suggesting that this effect could be caused by the stretching of $\Omega_y$ due to the spanwise velocities with alternating sign induced near the wall by the counter rotating quasi-streamwise vortices, corresponding to the $2\Omega_y\langle\delta\omega_y\delta\left(\partial v/\partial y\right)\rangle$ term. On the contrary, the term $2\langle\delta\omega_x\delta\omega_z\rangle\partial U/\partial z$, appears to be negative with a similar shape but with a lower intensity. This anti-correlation may be explained by comparing it term-by-term with the first contribution. In fact, near the wall we may expect $2\Omega_y\langle\delta\omega_x\delta\left(\partial u/\partial y\right)\rangle$ to be the only other relevant component of $2\Omega_y\langle\delta\omega_i\delta\left(\partial u_i/\partial y\right)\rangle$. If this is true, it can be deduced that $2\Omega_y\langle\delta\omega_x\delta\left(\partial u/\partial y\right)\rangle \approx -2\langle\delta\omega_x\delta\omega_z\rangle\partial U/\partial z$, since $\Omega_y = \partial U/\partial z$, and $\delta\omega_z = \delta\left(\partial v/\partial x - \partial u/\partial y\right) \approx -\partial u/\partial y$ near the wall. In correspondence with the mild peak observed in the vortex stretching at $r_y^+ \approx 40$, it is possible to observe a valley in the diffusive scale transport which takes charge of draining the scale-enstrophy injected by transporting it towards smaller scales. As shown in figure 5.15(c), this transport is mainly constituted by the transport across wall-normal scales $r_z$, reaffirming that, at such wall distances, enstrophy is transported toward smaller $r_z$ scales, corresponding to sharp wall-normal gradients. Thus, in the very-near wall region, the budget may be approximated as:

$$-2\nu\frac{\partial^2\langle\delta\xi^2\rangle}{\partial r_z^2} - \frac{\nu}{2}\frac{\partial^2\langle\delta\xi^2\rangle}{\partial z_c^2} = 2\Omega_y\langle\delta\omega_i\delta\left(\frac{\partial u_i}{\partial y}\right)\rangle - 4\langle\epsilon_\xi\rangle. \tag{5.19}$$

Finally, we report the inertial transport of enstrophy in figure 5.15(d), which, despite being negligible in intensity, shows features which are to some degree similar to those observed in the interface region, again emphasising the similarities of the phenomena occurring in these two regions. In particular, the spanwise transport $\partial\langle\delta\xi^2\delta v\rangle/\partial r_y$ shows a typical pattern of a direct enstrophy cascade, draining enstrophy from the injection scale and introducing it at smaller scales. This term corresponds to the longitudinal component of the inertial transport and, like the longitudinal diffusive transport $2\nu\partial^2\langle\delta\xi^2\rangle/\partial r_y^2$, has a negative peak near the injection scale. On the other hand, the wall-normal inertial transport $\partial\langle\delta\xi^2\delta w\rangle/\partial r_z$ appears to inject enstrophy at all $r_y$ scales, indicating that also the inertial transport in the wall-normal scales is performing a direct enstrophy transfer.

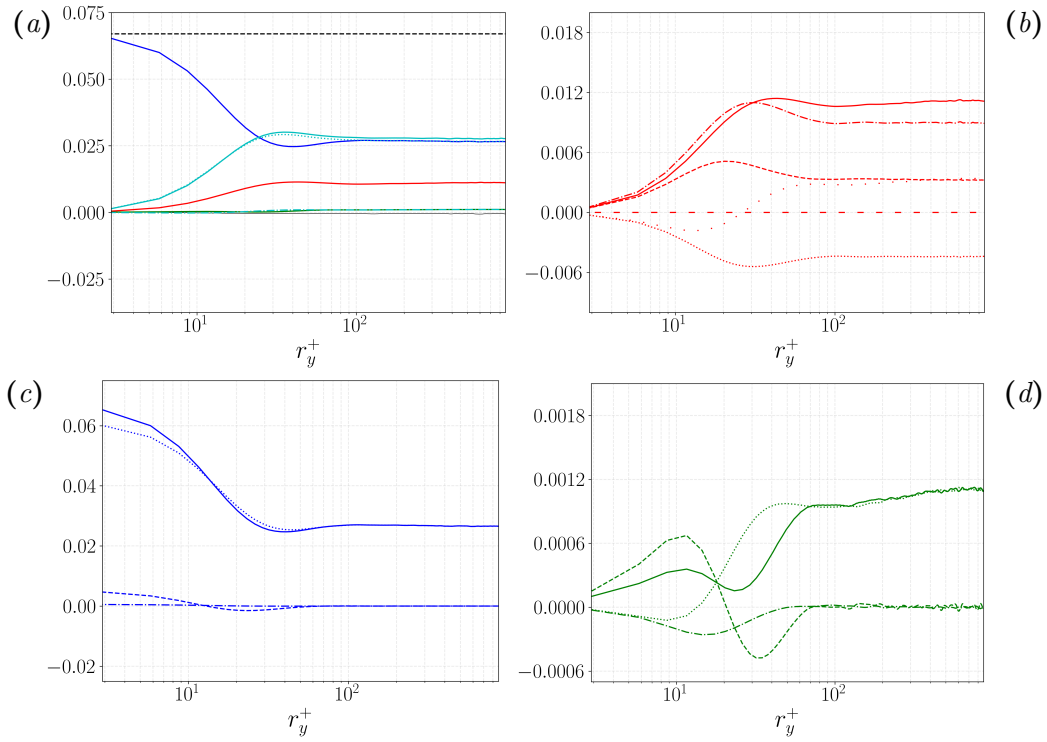


Figure 5.15: Scale-by-scale budget of turbulent enstrophy in the spanwise scales $r_y^+$ evaluated at $z_c^+ = 0.5$. The complete budget is reported in (a). The terms of equation 5.14 are represented with different colours: $T^+_{r_\xi}$ (green), $D^+_{r_\xi}$ (blue), $T^+_{c_\xi}$ (cyan dash-dotted line for the turbulent transport and cyan dotted line for the diffusive one), $VS^+_{\delta\xi} + \Pi^+_{\delta\xi}$ (red), $E^+_{\delta\xi}$ (dashed black line) and $\partial\langle\delta\xi^2\rangle/\partial t$ computed as residue (thin solid black line). The source terms are reported in (b): total $VS^+_{\delta\xi} + \Pi^+_{\delta\xi}$ (solid line), $2\Omega^+_y\langle\delta\omega_i\delta\left(\partial u_i/\partial y\right)\rangle^+$ (dash-dotted line), $2\langle\delta\omega_x\delta\omega_z\rangle^+\partial U^+/\partial z^+$ (dotted line), $2\langle\delta\omega_i\widetilde{\omega}_j\delta\left(\partial u_i/\partial x_j\right)\rangle^+$ (dashed line), $2\langle\delta\omega_i\delta\omega_j(\widetilde{\partial u_i/\partial x_j})\rangle^+$ (loosely dotted line) and $\Pi^+_{\delta\xi}$ (loosely dashed line). Diffusive transport among scales is reported in (c): total $D^+_{r_\xi}$ (solid line), $2\nu(\partial^2\langle\delta\xi^2\rangle/\partial r_x^2)^+$ (dash-dotted line), $2\nu(\partial^2\langle\delta\xi^2\rangle/\partial r_y^2)^+$ (dashed line) and $2\nu(\partial^2\langle\delta\xi^2\rangle/\partial r_z^2)^+$ (dotted line). Inertial transport among scales is reported in (d): total $T^+_{r_\xi}$ (solid line), $-(\partial\langle\delta\xi^2\delta u\rangle/\partial r_x)^+$ (dash-dotted line), $-(\partial\langle\delta\xi^2\delta v\rangle/\partial r_y)^+$ (dashed line) and $-(\partial\langle\delta\xi^2\delta w\rangle/\partial r_z)^+$ (dotted line).

### Buffer layer

In the buffer layer, the overall budget (reported in figure 5.16(a) at a wall distance of $z_c^+ = 11$) quickly recovers the macroscopic characteristics

observed in the HIT case shown in chapter 2, but with some differences. Among these differences, we can observe that in this region the budget results in an overall net source of enstrophy. We can also observe a peak in the vortex stretching at $r_y^+ \approx 40$, with the resulting negative valley in the inertial transport draining scale-enstrophy from the injection scale. By examining the composition of the various terms, the differences with respect to HIT are more evident. The vortex stretching term, depicted in figure 5.16(b), is dominated by the $2\langle\delta\omega_x\delta\omega_z\rangle\partial U/\partial z$ term. As already pointed out in section 5.2.1, this term may be interpreted as the vortex tilting given by the mean velocity gradient, that appears to be the most relevant contribution acting in the buffer layer. Apparently, the production of enstrophy (hence dissipation) in the buffer layer is sustained by the combined effect of the mean velocity shear and of vorticity tilted at an angle, hence retaining both a streamwise and a vertical component. The diffusive scale transport, shown in figure 5.16(c), appears to be still dominated by the transport across wall-normal scales. Finally, in figure 5.16(d), the inertial transport contributions are shown. As already mentioned, the local minimum in the inertial transport is found to correspond with the enstrophy injection scale $r_y^+ \approx 40$. The presence of a slight negative turbulent transport in the single-point budget, constrains the inertial transport to recover that value at large scales. In particular, $\partial\langle\delta\xi^2\delta u_i\rangle/\partial r_i = \partial\langle\delta\xi^2\delta w\rangle/\partial r_z = \partial\langle\delta\xi^2\widetilde{w}\rangle/\partial z_c = \partial\langle\xi w\rangle/\partial z$, at $r_y$ large enough for the two points $\boldsymbol{x'}$ and $\boldsymbol{x''}$ to be decorrelated.

As a first approximation, we may express the budget in the spanwise scales (at $r_x = r_z = 0$) as:

$$\begin{aligned}\frac{\partial\langle\delta\xi^2\rangle}{\partial t} + \frac{\partial\langle\delta\xi^2\delta u_j\rangle}{\partial r_j} - 2\nu\frac{\partial^2\langle\delta\xi^2\rangle}{\partial r_z^2} = 2\langle\delta\omega_x\delta\omega_z\rangle\frac{\partial U}{\partial z} \\ +2\langle\delta\omega_i\widetilde{\omega}_j\delta\left(\frac{\partial u_i}{\partial x_j}\right)\rangle + 2\langle\delta\omega_i\delta\omega_j\widetilde{\left(\frac{\partial u_i}{\partial x_j}\right)}\rangle - 4\langle\epsilon_\xi\rangle.\end{aligned} \tag{5.20}$$

This equation resembles the budget in the isotropic homogeneous case (equation 2.43) with the additional $2\langle\delta\omega_x\delta\omega_z\rangle\frac{\partial U}{\partial z}$ contribution to vortex stretching and with the simplification that diffusive scale transport is mainly active in the $r_z$ scales.

### Outer region

Moving from the buffer layer to the outer region, the flow fully recovers the scenario observed in homogeneous isotropic turbulence, with the only exception being a positive net source of enstrophy. In figure 5.17, this scenario

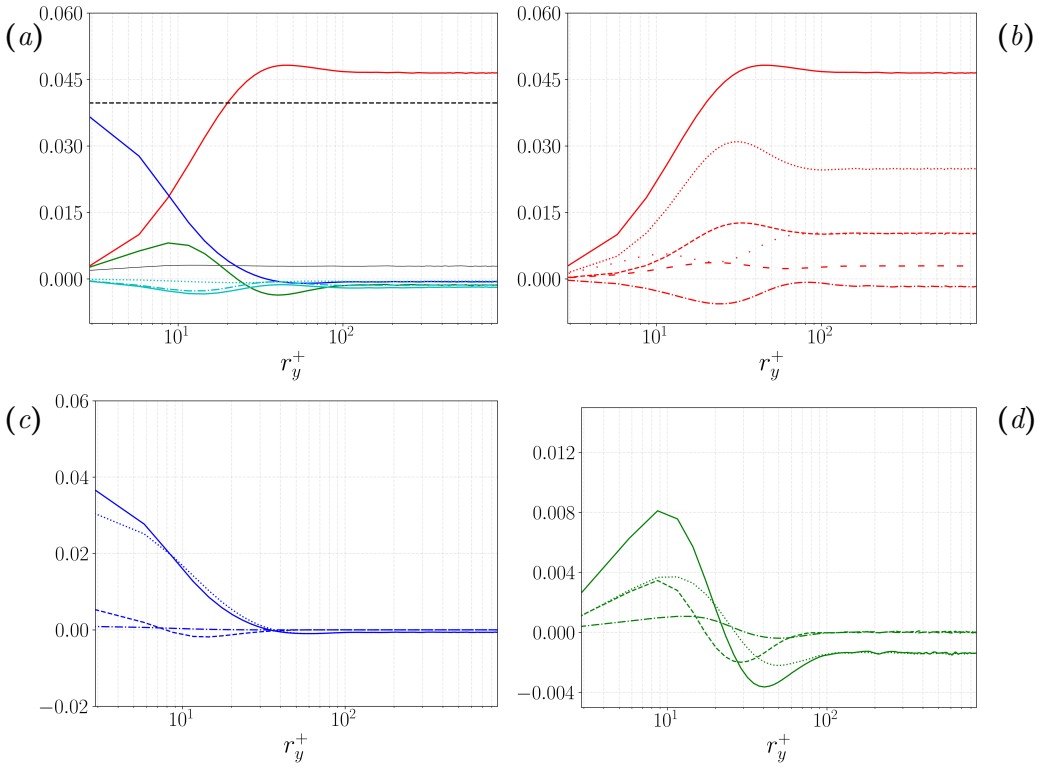


Figure 5.16: Scale-by-scale budget of turbulent enstrophy in the spanwise scales $r_y^+$ evaluated at $z_c^+ = 11$. The complete budget is reported in (a). The terms of equation 5.14 are represented with different colours: $T^+_{r_\xi}$ (green), $D^+_{r_\xi}$ (blue), $T^+_{c_\xi}$ (cyan dash-dotted line for the turbulent transport and cyan dotted line for the diffusive one), $VS^+_{\delta\xi} + \Pi^+_{\delta\xi}$ (red), $E^+_{\delta\xi}$ (dashed black line) and $\partial\langle\delta\xi^2\rangle/\partial t$ computed as residue (thin solid black line). The source terms are reported in (b): total $VS^+_{\delta\xi} + \Pi^+_{\delta\xi}$ (solid line), $2\Omega_y^+\langle\delta\omega_i\delta\left(\partial u_i/\partial y\right)\rangle^+$ (dash-dotted line), $2\langle\delta\omega_x\delta\omega_z\rangle^+\partial U^+/\partial z^+$ (dotted line), $2\langle\delta\omega_i\widetilde{\omega}_j\delta\left(\partial u_i/\partial x_j\right)\rangle^+$ (dashed line), $2\langle\delta\omega_i\delta\omega_j\widetilde{(\partial u_i/\partial x_j)}\rangle^+$ (loosely dotted line) and $\Pi^+_{\delta\xi}$ (loosely dashed line). Diffusive transport among scales is reported in (c): total $D^+_{r_\xi}$ (solid line), $2\nu(\partial^2\langle\delta\xi^2\rangle/\partial r_x^2)^+$ (dash-dotted line), $2\nu(\partial^2\langle\delta\xi^2\rangle/\partial r_y^2)^+$ (dashed line) and $2\nu(\partial^2\langle\delta\xi^2\rangle/\partial r_z^2)^+$ (dotted line). Inertial transport among scales is reported in (d): total $T^+_{r_\xi}$ (solid line), $-(\partial\langle\delta\xi^2\delta u\rangle/\partial r_x)^+$ (dash-dotted line), $-(\partial\langle\delta\xi^2\delta v\rangle/\partial r_y)^+$ (dashed line) and $-(\partial\langle\delta\xi^2\delta w\rangle/\partial r_z)^+$ (dotted line).

is depicted at a wall distance $z_c^+ = 450$. The vortex stretching composition, reported in figure 5.17(b), is identical to the one observed in figure 2.5(b), with the only relevant contributions being the fully fluctuating com-

ponents $2\langle\delta\omega_i\widetilde{\omega}_j\delta\left(\partial u_i/\partial x_j\right)\rangle$ and $2\langle\delta\omega_i\delta\omega_j\widetilde{(\partial u_i/\partial x_j)}\rangle$. The diffusive scale transport also appears to be evenly split between the three components. As expected in isotropic conditions, only a different behaviour of the $r_y$ transport is observed, since it represent the transport among the longitudinal scales. The only qualitative difference with respect to the homogeneous isotropic case lies in the inertial scale transport distribution. In fact, its distribution among the transversal scales $r_x$ and $r_z$ appears different, with the wall-normal transport (in $r_z$) being more active, and the streamwise one (in $r_x$) being negligible. Thus, the enstrophy budget in the outer region of the boundary layer can be approximated with the unsteady homogeneous isotropic one:

$$\begin{aligned}\frac{\partial\langle\delta\xi^2\rangle}{\partial t}+\frac{\partial\langle\delta\xi^2\delta u_j\rangle}{\partial r_j}-2\nu\frac{\partial^2\langle\delta\xi^2\rangle}{\partial r_j\partial r_j}=\\ +2\langle\delta\omega_i\widetilde{\omega}_j\delta\left(\frac{\partial u_i}{\partial x_j}\right)\rangle+2\langle\delta\omega_i\delta\omega_j\widetilde{\left(\frac{\partial u_i}{\partial x_j}\right)}\rangle-4\langle\epsilon_\xi\rangle.\end{aligned}\tag{5.21}$$

**Interface region**

In conclusion, the interface region, whose budget is reported in figure 5.18(a), also shows a good similarity with the homogeneous isotropic case, with a main difference being the presence of a non-negligible spatial transport at large scales. This transport is due to the temporal growth of the boundary layer, which, as expected, is mainly accomplished by large scales through turbulent transport (Cimarelli and Boga, 2021). The distribution of the vortex stretching contributions shown in figure 5.18(b) appears qualitatively equal to the homogeneous isotropic case, as well as the diffusive scale transport in figure 5.18(c). Finally, the inertial transport among wall-normal scales (dotted line in figure 5.18(d)), appears to be the major inertial transport contribution at all scales, indicating that the enstrophy cascade in the wall-normal direction is more intense with respect to those in the wall-parallel scales. This observation is in good agreement with the physical interpretation of interface region described so far as it provides a further indication in support of the idea that enstrophy, and thus dissipation, increasingly relies on wall-normal gradients as it is transported towards the TNTI region.

In the TNTI region, the budget may be approximated as an unsteady

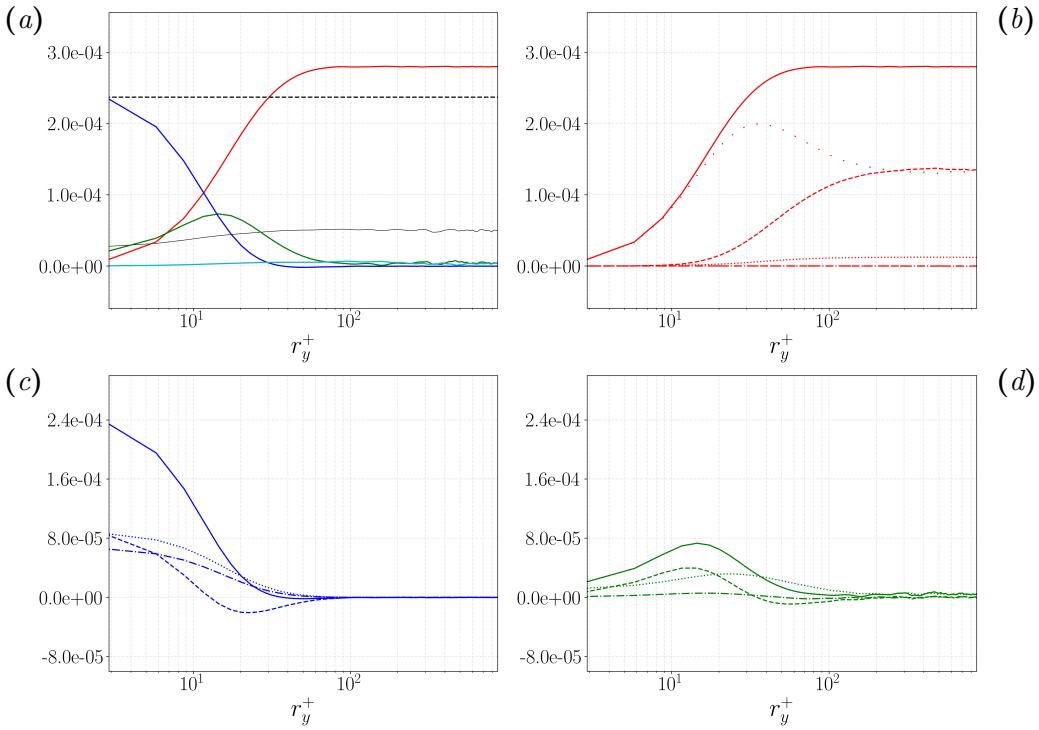


Figure 5.17: Scale-by-scale budget of turbulent enstrophy in the spanwise scales $r_y^+$ evaluated at $z_c^+ = 450$. The complete budget is reported in (a). The terms of equation 5.14 are represented with different colours: $T^+_{r_\xi}$ (green), $D^+_{r_\xi}$ (blue), $T^+_{c_\xi}$ (cyan dash-dotted line for the turbulent transport and cyan dotted line for the diffusive one), $VS^+_{\delta\xi} + \Pi^+_{\delta\xi}$ (red), $E^+_{\delta\xi}$ (dashed black line) and $\partial\langle\delta\xi^2\rangle/\partial t$ computed as residue (thin solid black line). The source terms are reported in (b): total $VS^+_{\delta\xi} + \Pi^+_{\delta\xi}$ (solid line), $2\Omega_y^+\langle\delta\omega_i\delta\left(\partial u_i/\partial y\right)\rangle^+$ (dash-dotted line), $2\langle\delta\omega_x\delta\omega_z\rangle^+\partial U^+/\partial z^+$ (dotted line), $2\langle\delta\omega_i\widetilde{\omega}_j\delta\left(\partial u_i/\partial x_j\right)\rangle^+$ (dashed line), $2\langle\delta\omega_i\delta\omega_j\widetilde{(\partial u_i/\partial x_j)}\rangle^+$ (loosely dotted line) and $\Pi^+_{\delta\xi}$ (loosely dashed line). Diffusive transport among scales is reported in (c): total $D^+_{r_\xi}$ (solid line), $2\nu(\partial^2\langle\delta\xi^2\rangle/\partial r_x^2)^+$ (dash-dotted line), $2\nu(\partial^2\langle\delta\xi^2\rangle/\partial r_y^2)^+$ (dashed line) and $2\nu(\partial^2\langle\delta\xi^2\rangle/\partial r_z^2)^+$ (dotted line). Inertial transport among scales is reported in (d): total $T^+_{r_\xi}$ (solid line), $-(\partial\langle\delta\xi^2\delta u\rangle/\partial r_x)^+$ (dash-dotted line), $-(\partial\langle\delta\xi^2\delta v\rangle/\partial r_y)^+$ (dashed line) and $-(\partial\langle\delta\xi^2\delta w\rangle/\partial r_z)^+$ (dotted line).

isotropic case with the addition of spatial transport:

$$\frac{\partial\langle\delta\xi^2\rangle}{\partial t} + \frac{\partial\langle\delta\xi^2\delta u_j\rangle}{\partial r_j} + \frac{\partial\langle\delta\xi^2\widetilde{w}\rangle}{\partial z_c} - 2\nu\frac{\partial^2\langle\delta\xi^2\rangle}{\partial r_j\partial r_j} = \\ +2\langle\delta\omega_i\widetilde{\omega}_j\delta\left(\frac{\partial u_i}{\partial x_j}\right)\rangle + 2\langle\delta\omega_i\delta\omega_j\widetilde{\left(\frac{\partial u_i}{\partial x_j}\right)}\rangle - 4\langle\epsilon_\xi\rangle. \tag{5.22}$$

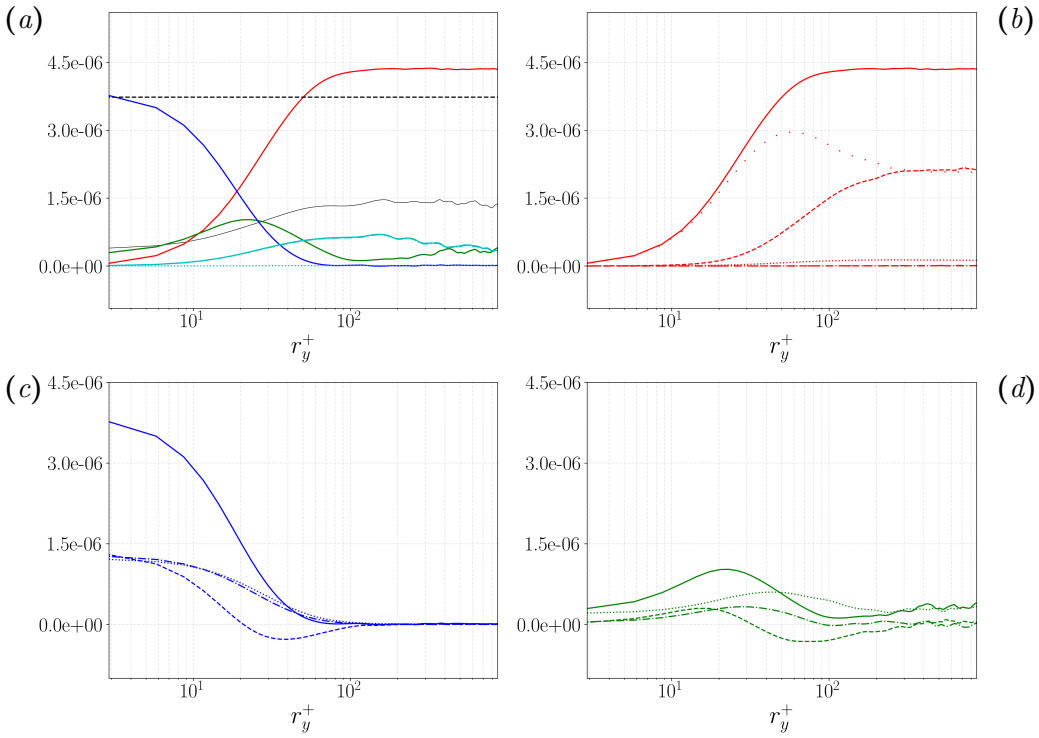


Figure 5.18: Scale-by-scale budget of turbulent enstrophy in the spanwise scales $r_y^+$ evaluated at $z_c^+ = Re_\tau = 1500$. The complete budget is reported in (a). The terms of equation 5.14 are represented with different colours: $T^+_{r_\xi}$ (green), $D^+_{r_\xi}$ (blue), $T^+_{c_\xi}$ (cyan dash-dotted line for the turbulent transport and cyan dotted line for the diffusive one), $VS^+_{\delta\xi} + \Pi^+_{\delta\xi}$ (red), $E^+_{\delta\xi}$ (dashed black line) and $\partial\langle\delta\xi^2\rangle/\partial t$ computed as residue (thin solid black line). The source terms are reported in (b): total $VS^+_{\delta\xi} + \Pi^+_{\delta\xi}$ (solid line), $2\Omega_y^+ \langle\delta\omega_i\delta\left(\partial u_i/\partial y\right)\rangle^+$ (dash-dotted line), $2\langle\delta\omega_x\delta\omega_z\rangle^+\partial U^+/\partial z^+$ (dotted line), $2\langle\delta\omega_i\widetilde{\omega}_j\delta\left(\partial u_i/\partial x_j\right)\rangle^+$ (dashed line), $2\langle\delta\omega_i\delta\omega_j(\widetilde{\partial u_i/\partial x_j})\rangle^+$ (loosely dotted line) and $\Pi^+_{\delta\xi}$ (loosely dashed line). Diffusive transport among scales is reported in (c): total $D^+_{r_\xi}$ (solid line), $2\nu(\partial^2\langle\delta\xi^2\rangle/\partial r_x^2)^+$ (dash-dotted line), $2\nu(\partial^2\langle\delta\xi^2\rangle/\partial r_y^2)^+$ (dashed line) and $2\nu(\partial^2\langle\delta\xi^2\rangle/\partial r_z^2)^+$ (dotted line). Inertial transport among scales is reported in (d): total $T^+_{r_\xi}$ (solid line), $-(\partial\langle\delta\xi^2\delta u\rangle/\partial r_x)^+$ (dash-dotted line), $-(\partial\langle\delta\xi^2\delta v\rangle/\partial r_y)^+$ (dashed line) and $-(\partial\langle\delta\xi^2\delta w\rangle/\partial r_z)^+$ (dotted line).

In conclusion, the TNTI and the very near-wall regions are the only ones where the spatial transport has been found to be non-negligible.

# Chapter 6

# Conclusions

Some of the most groundbreaking results in the field of turbulence research date back to Kolmogorov's seminal intuitions. Particularly successful were Kolmogorov's assumptions concerning the universality of small scale motions in flows with a sufficiently high Reynolds number. These assumptions, extensively tested, made it possible to separate the dynamic of the large-scale motions, dependent from the boundary conditions of the problem considered, from the small-scale dynamic. Kolmogorov's pioneering work also led to the derivation of some of the only exacts results in turbulence, which are valid under the assumptions of homogeneity and isotropy. The theoretical framework he used was expanded over the years to allow its application to more general flow configurations, until reaching the general formulation of the Generalized Kolmogorov Equation (GKE) (Hill, 2002), applicable to fully inhomogeneous, anisotropic and unsteady flows. This equation constitutes an exact framework to study the multi-scale nature of turbulent flows as it expands the momentum balance equation to the compound space of both scales and physical space, allowing the access to the full dynamics constituted by production and transfer mechanisms among different regions of the flow and among scales of different dimensions.

In the present thesis work, we apply the framework of the generalized Kolmogorov equation to the study of the dynamics of a turbulent boundary layer, with particular focus on the confinement effects given by the presence of the solid wall, and given by the presence of a Turbulent/Non-Turbulent Interface (TNTI), over which the turbulent entrainment phenomenon occurs. The framework provided by the GKE is then expanded to study the dynamics of turbulent enstrophy. The latter represents an interesting observable to gain a deeper insight in the confined dynamics and in the reverse energy transfer phenomena observed in the near-wall and TNTI regions. Enstrophy is in fact related to energy dissipation and also to the energy cascade phenomenon through the vortex stretching term.

**Homogeneous isotropic turbulence**

In chapter 2, after a brief presentation of the theoretical framework, we apply the energy and enstrophy two-point budget equations to direct numerical simulations of statistically steady, homogeneous and isotropic turbulence at different Reynolds numbers, up to $Re_\lambda \approx 400$. This first step allowed us to set a reference (mainly for the lesser known two-point enstrophy budget) before diving in the complex dynamic exhibited by the boundary layer. During this preliminary analysis it was possible to note that, unlike energy, enstrophy cannot have a range in which its budget is dominated by the inertial transport. In fact, the vortex stretching mechanism, acting as a source of enstrophy, is very active until the scales at which diffusion is relevant, given its connection with the energy cascade process. Indeed, the inertial enstrophy transport has shown a region of activity at scales that correspond to a viscosity dominated regime in the energy budget. Therefore, this transport is not to be understood as turbulent transport, but rather as performed by a homogeneous shear. We conjecture that this may be caused by a "Batchelor-like" process (Batchelor, 1959), allowing the generation of scales smaller than those present in the velocity field itself.

**Temporal boundary layer**

The analysis of the temporal boundary layer, up to a friction Reynolds number $Re_\tau = 1500$, begins in chapter 3 with the presentation of the flow settings and the characterisation of its main features. In this chapter, some of the most commonly investigated features in boundary layers are addressed. The temporal boundary layer showed characteristics in good accordance with those of the more common spatially evolving boundary layers, proving to be a good candidate for the study of the main features of wall turbulence and of the TNTI, while retaining the statistical homogeneity in both the streamwise and spanwise directions. These homogeneities simplify the set-up and reduce the dimensionality of the two-point budgets by one dimension. After this necessary assessment, the analysis proceeds by investigating the multiscale phenomena, respectively addressing the turbulent kinetic energy and the turbulent enstrophy dynamics in chapters 4 and 5 respectively.

**Generalized Kolmogorov equation**

The picture emerging from the GKE applied to the temporal boundary layer depicts the presence of a peak of scale-energy source in the buffer layer from which the field of fluxes diverges to feed the two dissipative sinks of the

flow, the viscous sublayer at the wall and the $z_c$-distributed range of small scales. The branch of fluxes feeding the dissipative sink at the wall starts from the singularity point in the buffer layer and exhibits an in-plane forward and reverse energy cascade before bending towards the wall. By approaching the wall, the fluxes become progressively aligned with the wall-normal direction. Indeed, the cascade mechanisms in the space of wall-parallel scales rapidly vanish with the wall distance and only a cascade towards progressively smaller wall-normal scales survives. Accordingly, the high rates of dissipation in the viscous sublayer are realized by the vertical shearing in a very thin layer of motions mainly confined along two directions covering a wide range of wall-parallel scales, i.e. the near-wall footprint of the variety in size of eddies populating the entire boundary layer. On the other hand, the branch of fluxes feeding the $z_c$-distributed small scale dissipative sink form spatially ascending reverse energy cascades through self-similar eddies growing in size with the wall distance. This pattern is followed by spatially ascending forward cascades through detached eddies thus reaching sufficiently small scales where eventually scale energy is dissipated. Hence, small scales in wall turbulence are found to be in equilibrium with large scales only when spatial fluxes induced by the inhomogeneity of the flow are taken into account. In other words, a generalized Richardson energy cascade takes place where large scales are in equilibrium with small scales at higher wall distances trough a combined forward cascade and spatial flux.

The results obtained on the boundary layer are then compared with those of a turbulent channel at the same friction Reynolds number $Re_\tau = 1500$, allowing to evaluate the effect of the presence of the TNTI. The turbulence process of entrainment in the boundary layer is found to modify but not to completely alter the described scenario. In particular, the main difference exhibited by the boundary layer with respect to channel flow consists in an increase of the intensity of the reverse energy cascade processes. In fact, their role is found to become relevant also in the outer region contrary to channels where they are almost irrelevant from a dynamical point of view. An additional repercussion of the increased reverse energy cascade intensity in the boundary layer consists in the appearance of a divergence line of fluxes in the overlap layer representing a specific set of self-similar eddies growing with the wall distance. Their relevance is given by the fact that all the fluxes feeding the outer region of the flow are found to pass through this set of "attached eddies".

The process of turbulent entrainment in the boundary layer is found to markedly modify the dynamics as we approach the interface region, with respect to the centreline of the channel. In fact, the latter is characterized

by a local forward energy cascade, as expected due to symmetry reasons. On the contrary, the TNTI region is found to be characterized by a reverse energy cascade that, although weak, involves the almost entire range of wall-parallel scales. Hence, the propagation of the turbulent front and the intensity of turbulent entrainment are sustained by a spatially ascending reverse cascade in the wall-parallel directions, with a simultaneous direct energy cascade in the wall-normal scales. This behaviour of the fluxes denotes that the boundary layer growth is sustained at the TNTI region by means of ascending large scale motions that become longer and wider while approaching the interface and squeeze in the wall-normal direction, thus sustaining sharp vertical gradients, through which dissipation and diffusion are sustained. This picture shows clear similarities with what was observed in the viscous sublayer.

**Single- and two-point enstrophy budgets**

The insight gained from the turbulent enstrophy statistics seems to confirm this interpretation. Already from the single-point statistics, by decomposing the individual enstrophy contributions, it was possible to see a completely confined dynamic in the near-wall region, characterized by a prevalent spanwise vorticity component, amplified by pure stretching. The fully 3-D dynamics appears to be recovered after the viscous sublayer, reaching a more isotropic scenario in the overlap region. Once again, the spanwise vorticity component begins to gain relevance as we approach the TNTI region, indicating the emergence of a confinement effect, as the one observed in the near-wall region.

Through two-point statistics it was possible to observe that the structures populating the buffer layer and the outer region have an effect on enstrophy mainly through their footprint at the wall rather than through an action localised at the wall-distance at which they reside. In fact, vorticity is generated at the wall with patterns that clearly recall the streaks (visible in $\langle \delta\omega_y^2 \rangle$) and the quasi-streamwise vortices (visible in $\langle \omega_x^2 \rangle$). Enstrophy is transported from the wall towards the rest of the domain through fluxes that are initially vertical and purely diffusive. It is observed that the behaviour of these fluxes is very different depending on the spanwise scale at which they are generated. In particular, fluxes of enstrophy generated at a spanwise scale $r_y^+ \lesssim 55$ undergo a strong direct enstrophy cascade in the streamwise direction without being able to reach the outer region above the buffer layer. In fact, the buffer layer is shown to be the seat of the most intense positive net source of enstrophy, hence acting as a repulsion

for the fluxes. The dynamics of the branch of fluxes generated at $r_y^+ \lesssim 55$ is completely local and regards the enstrophy generated at a scale too small to effectively correlate with the turbulent motions that more efficiently accomplish the turbulent transport. These scales are also found to be the ones with a lower enstrophy content. On the other hand, the enstrophy generated at a spanwise scale $r_y^+ \gtrsim 55$ is able to reach and feed the outer region of the boundary layer, ascending through the positive source region in the buffer layer (which causes a reverse enstrophy transfer in the spanwise scales). This view is consistent with the "wall-cycle" described in Jiménez and Pinelli (1999). While in the near-wall region, the enstrophy dynamics is dominated by the pure stretching of spanwise vorticity through spanwise velocity fluctuations induced by the quasi-streamwise vortices, the buffer layer appears to be dominated by the vortex tilting due to the mean velocity gradient $2\langle\delta\omega_x\delta\omega_z\rangle\partial U/\partial z$. This phenomenon appears to be the only one that is active locally where the coherent structures reside. We therefore deduce that this is the main phenomenon of enstrophy (hence dissipation) production to which coherent structures contribute with a local action rather than a footprint at the wall. The outer region of the boundary layer exhibits an isotropic behaviour of enstrophy, that is lost as we approach the TNTI region. In this region, in fact, the distribution of enstrophy is again uneven, with the spanwise contribution increasing its relevance and being distributed among large wall-parallel scales. Accordingly, a mild reverse wall-parallel enstrophy transfer, combined with a direct wall-normal one is observed, again highlighting the anisotropy of the TNTI region, characterized by dissipation occurring over a range of wide wall-parallel scales with sharp gradients normal to it.

# Appendix

# Appendix A

# Dynamical experiments

One of the topics debated in the context of wall turbulence concerns the dynamic interaction between the inner and outer cycles, acting respectively in the buffer layer and in the overlap layer. These two cycles are thought to be autonomous and self-sustaining (Jiménez and Pinelli, 1999) and the effect of their combined action determines the overall momentum and heat exchange. Many of the studies conducted in the field of turbulence research (including the analyses presented in the previous chapters 3, 4 and 5) deal with flow realization snapshots, thus losing possible information about the dynamic causality of the phenomena that naturally occur over time. In order to try to overcome this limitation, we propose an approach that aims at dynamically establish the separate role of these two layers through the temporal evolution of passive scalars transported by artificially modified velocity fields. In particular, three passive scalars are respectively evolved under the separate action of the complete velocity field (for reference) and of two velocity fields in which the near-wall and the outer cycles are alternatively suppressed. The choice of addressing the scalar field evolution is crucial to decouple the effect of the two layers, otherwise concealed by the non-linearity of the flow evolution. This approach has already shown interesting results when applied to the study of the role of large and small scales in the entrainment process in a temporal planar jet in Cimarelli and Boga (2021).

The application of this approach to study the role of the inner and outer cycles in the temporal boundary layer was tested through preliminary simulations presented in Boga et al. (2024). The methodology is presented in section A.1, while the results are reported and discussed in section A.2. The results of an alternative approach, intended to show the robustness of the method used, are reported in section A.3. The appendix is concluded with final remarks in section A.4.

## A.1 Simulations and experimental set-up

In the following section we present the methodology used to carry out the experiments, starting with the presentation of the chosen flow configuration, the description of the experimental set-up and a final brief section regarding the filtering operation used in the experiments.

### A.1.1 Flow settings

The flow selected for the numerical experiments is a temporal boundary layer, already presented in chapter 3 to which we refer the reader for further details. The setup of the simulation is the same as the one adopted in the previous chapters, with the addition of the passive scalar field. Furthermore, since the topics analysed here are less demanding in terms of resolution compared to the dynamics of enstrophy addressed in chapter 5, a coarser grid has been used.

The scalar concentration at the wall is fixed and equal to $\Theta_w$, while the fluid in the domain has an initially null scalar concentration. The initial scalar profile is analogous to the one used for the velocity 3.1,

$$\theta_d^*(x_d, y_d, z_d, t_d = 0) = \frac{\Theta_w}{2}\left[1 + \tanh\left(\frac{D - z_d}{2h_\theta}\right)\right] \tag{A.1}$$

with $h_\theta = 54\alpha/\Theta_w$ and $\alpha$ being the scalar diffusivity. The Schmidt number is set to $Sc = \nu/\alpha = 1$. As in section 3, the asterisk is used to denote dimensional quantities. Analogously, unless otherwise specified, scalar quantities are expressed in dimensionless form by using $\Theta_w$.

Consistently with the previous chapters, the standard Reynolds decomposition is adopted also for the scalar field and denoted as $\theta^* = \Theta + \theta$, where $\theta^*$ is the total scalar field, while $\Theta = \langle\theta^*\rangle$ and $\theta$ are respectively the mean and fluctuating scalar fields.

Periodic boundary conditions are applied in the streamwise and spanwise directions also for the scalar field. The domain extension is unchanged $(L_x, L_y, L_z) = (924, 462, 220)\,D$ discretised with $(N_x, N_y, N_z) = (1536, 1536, 576)$ points. The resulting resolution in terms of friction units is reported in table A.1.

The code and numerical schemes used are the same as those used for the simulations in section 3.1, to which we refer the reader. The mixed time integration described above is applied also for the scalar field. The diffusive terms are integrated implicitly while all others explicitly with a three-step Runge–Kutta method with a $CFL = 0.7$. We verified that, despite the lower

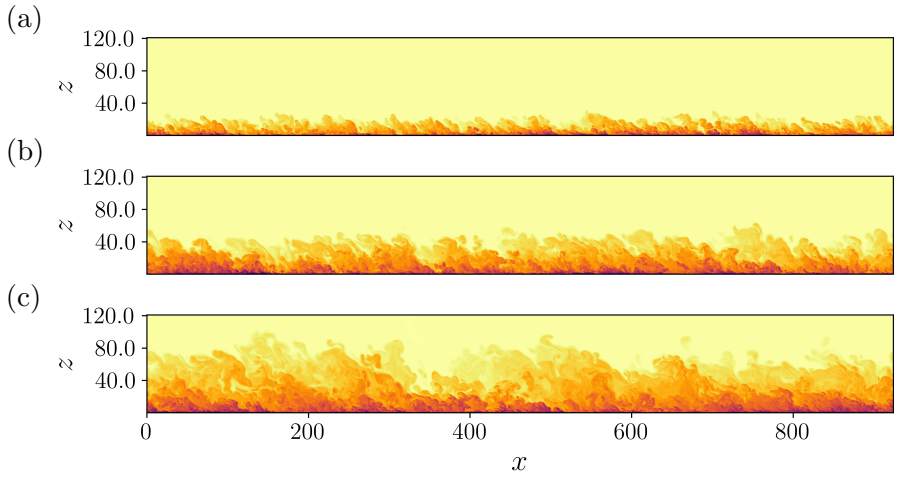


Figure A.1: Sections of the scalar field $\theta^*$ at different time instants corresponding respectively to (a) $Re_\tau = 500$, (b) $Re_\tau = 1000$ and (c) $Re_\tau = 1500$. The scalar concentration increases from light to dark colours. Figure taken from Boga et al. (2024).

Table A.1: Grid resolution in friction units for three different time instants corresponding to three different friction Reynolds numbers. The subscript $\cdot_{|w}$ and $\cdot_{|\delta}$ indicates a quantity measured respectively at the wall ($z = 0$) and at $z = \delta$.

| $Re_\tau$ | $\Delta x^+$ | $\Delta y^+$ | $\Delta z_w^+$ | $\Delta z_\delta^+$ |
|---|---|---|---|---|
| 500 | 13.6 | 6.8 | 0.14 | 5.7 |
| 1000 | 12.3 | 6.2 | 0.13 | 9.5 |
| 1500 | 11.6 | 5.8 | 0.12 | 12.1 |

resolution used, the classical statistics obtained are reliable when compared to those obtained in chapter 3.

### A.1.2 Numerical experiments

As mentioned above, the present work aims to dynamically establish the role played by the inner and outer cycles by analysing the evolution of two additional passive scalars transported by two modified velocity fields where the near-wall and outer cycles are alternatively suppressed. The two modified velocity fields are obtained through a filtering operation performed at runtime. It is important to underline that the filtering operation is not directly applied to the scalar fields, but it is only used to obtain the two modified velocity fields transporting the two alternative scalars. These ve-

locity fields are not integrated over time but are obtained at each time-step from the total velocity. The resulting set of equations is:

$$\begin{cases} \dfrac{\partial u_i^*}{\partial x_i} = 0 \\ \dfrac{\partial u_i^*}{\partial t} + \dfrac{\partial u_i^* u_j^*}{\partial x_j} = -\dfrac{\partial p}{\partial x_i} + \dfrac{1}{Re}\dfrac{\partial^2 u_i^*}{\partial x_j \partial x_j} \\ \dfrac{\partial \theta^*}{\partial t} + \dfrac{\partial \theta^* u_j^*}{\partial x_j} = \dfrac{1}{ReSc}\dfrac{\partial^2 \theta^*}{\partial x_j \partial x_j} \\ \dfrac{\partial \theta_{out}^*}{\partial t} + \dfrac{\partial \theta_{out}^* u_j^{*out}}{\partial x_j} = \dfrac{1}{ReSc}\dfrac{\partial^2 \theta_{out}^*}{\partial x_j \partial x_j} \\ \dfrac{\partial \theta_{inn}^*}{\partial t} + \dfrac{\partial \theta_{inn}^* u_j^{*inn}}{\partial x_j} = \dfrac{1}{ReSc}\dfrac{\partial^2 \theta_{inn}^*}{\partial x_j \partial x_j} \end{cases} \tag{A.2}$$

where $\theta^*$ is the passive scalar transported by the complete velocity field $u_i^*$, $\theta_{out}^*$ is the scalar transported by the velocity field retaining the sole outer cycle $u_i^{*out}$ and $\theta_{inn}^*$ is the scalar field transported by the velocity field retaining the sole inner cycle $u_i^{*inn}$. A schematic representation of the method adopted is reported in figure A.2.

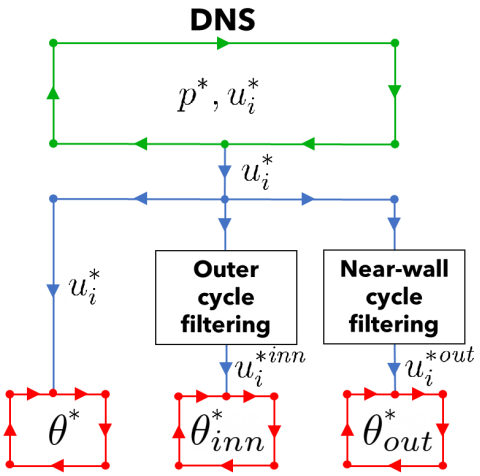


Figure A.2: Schematic representation of the procedure implemented for the numerical experiments.

The initial condition for the two scalar fields $\theta_{out}^*$ and $\theta_{inn}^*$ is taken from the reference case $\theta^*$ at a time instant corresponding to $Re_\tau = 500$.

### A.1.3 Filtering

Two different filtering approaches have been tested. For the sake of clarity, in the present subsection we only describe the first approach, the results of which are presented in subsection A.2. The description and the results of the second approach, based on a filtering operation applied only to sub-portions of the domain, are reported in section A.3. The filter used in both approaches is a 2-D Gaussian filter applied in the homogeneous directions $x$ and $y$,

$$\bar{u}_i^*(x,y,z,t) = \int_{-\infty}^{+\infty}\int_{-\infty}^{+\infty} u_i^*(x+r_x, y+r_y, z, t)\, G(r_x, r_y)\, dr_x dr_y, \quad \text{(A.3)}$$

$$G(r_x, r_y) = \frac{1}{2\pi\Delta_x\Delta_y} e^{-\frac{1}{2}\left(\frac{r_x^2}{\Delta_x^2}+\frac{r_y^2}{\Delta_y^2}\right)} \quad \text{(A.4)}$$

where $\bar{u}_i^*$ is the resulting filtered velocity and $\Delta_x$ and $\Delta_y$ are the characteristic lengths of the filter in the streamwise and spanwise directions. The velocity field retaining the sole outer cycle is defined as $u_i^{*out} = \bar{u}_i^*$ and, hence, it contains only the large-scale motions, which are those mainly contributing to the outer cycle dynamics. On the other hand, the velocity field retaining the sole inner cycle $u_i^{*inn}$ is defined as $u_i^{*inn} = u_i^* - \bar{u}_i^* + U_i$, and hence, it contains only the small-scale motions that are dominant in the near-wall cycle, being large-scale motions merely an imprinting from the outer flow. The action of the average velocity $U_i(z,t)$ is added explicitly, since $\langle u_i^* - \bar{u}_i^* \rangle = 0$. The filter lengths are chosen on the basis of the premultiplied spectra shown in figure A.3 and are respectively set to $\Delta_x^+ = 600$ and $\Delta_y^+ = 100$. The portions of the spectra filtered out in the spanwise direction to obtain $u_i^{*inn}$ and $u_i^{*out}$ are shown in shaded grey in figure A.3(a) and (b), respectively measured in the buffer layer and in the outer region. Note that the shaded grey areas shown in figure A.3 are merely indicative since the Gaussian filter does not prescribe a sharp cut-off scale in spectral space.

## A.2 Results

Let us start analysing the scalar field topology at the final friction Reynolds number $Re_\tau = 1500$ reached during the experiments. In figure A.4 the instantaneous scalar contours are shown on a wall-normal $(x,z)$ section. The trace of the large engulfing scales is clearly visible in $\theta_{out}^*$ and, at first glance, the thickness of the boundary layer seems comparable to that of the reference case $\theta^*$. Concurrently, the effect of the lack of the small scales

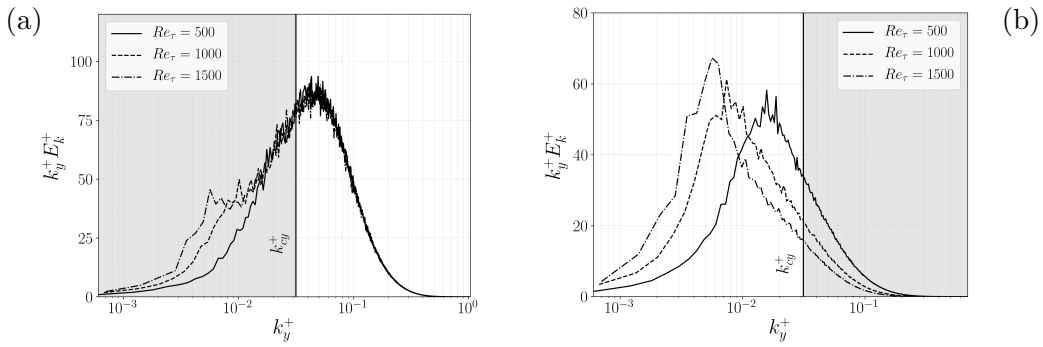


Figure A.3: Premultiplied spectra of the turbulent kinetic energy $E_k$ in the spanwise wavenumber $k_y$ respectively (a) in the buffer layer at $z^+ = 20$ and (b) in the outer region at $z = 0.3\delta$. The shaded areas are indicative of the filtered regions of the spectra (a) in $u^{*inn}$ and (b) in $u^{*out}$, being $k_{cy}^+ = 2\pi/\Delta_y^+$ the wavenumber corresponding to the spanwise filter length in inner units. Figure taken from Boga et al. (2024).

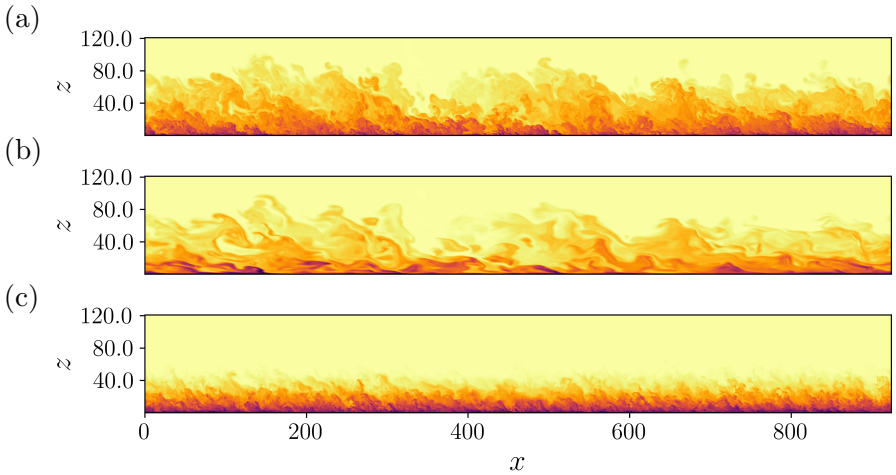


Figure A.4: Sections of the scalar fields of the three experiments at the same time instant, corresponding to $Re_\tau = 1500$. Respectively (a) $\theta^*$, (b) $\theta^*_{out}$ and (c) $\theta^*_{inn}$. The reference case (a) is duplicated here in order to simplify the comparison. Figure taken from Boga et al. (2024).

can be seen in the presence of large unmixed regions. On the contrary, the field $\theta^*_{inn}$ appears to be more mixed and exhibits a slower growth rate, which can be attributed to the lack of large-scale engulfment events.

We now proceed to analyse the data from a statistical point of view, starting with the temporal evolution of two integral quantities, namely the

Stanton number

$$St = -\frac{1}{ReSc}\left.\frac{\partial \Theta}{\partial z}\right|_w \tag{A.5}$$

and the boundary layer thickness based on the scalar concentration $\delta_\theta$, defined such that $\Theta(\delta_\theta) = 0.01\Theta_w$, reported in figure A.5(a) and (b) respectively.

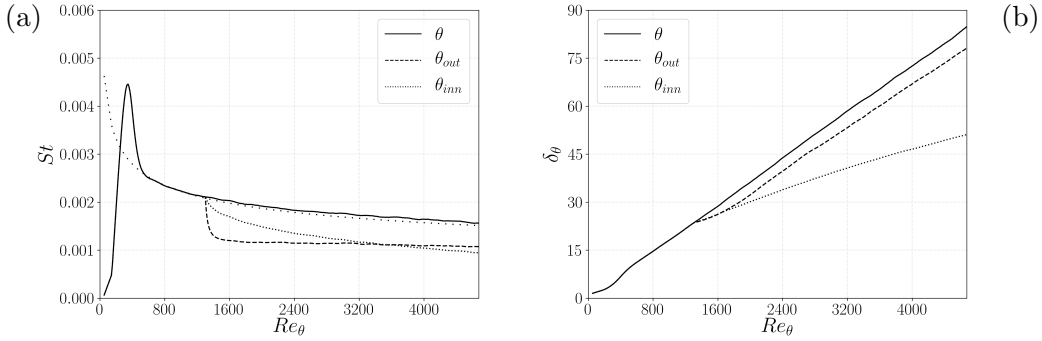


Figure A.5: (a) Temporal evolution of the Stanton number and its theoretical law $St = 0.0125 Re_\theta^{-1/4}$ in loosely dotted line and (b) temporal evolution of the boundary layer thickness based on the scalar concentration $\delta_\theta$. Figure taken from Boga et al. (2024).

The Stanton number $St$ (reported in figure A.5(a)) shows a significant reduction in both the experiments when compared to the reference case. In particular, the scalar field $\theta^*_{out}$ exhibits an abrupt decrease in the wall scalar transfer as soon as the experiment starts, settling immediately afterwards. On the contrary, the field $\theta^*_{inn}$ shows a gradual and sustained decrease in $St$. Indeed, the decrease in scalar transfer at the wall observed in the field $\theta^*_{out}$ may be explained as the direct effect of the suppression of the main turbulent motions involved in the near-wall cycle. This hypothesis is supported by the fact that the probability density function of $\theta^*_{out}$ in the viscous sublayer (reported in figure A.6(a)) shows a lower anisotropy level (visualized as a limited extension of the left tail). This more symmetrical profile compared to the reference case indicates that, by suppressing the near-wall cycle, we also suppressed the high-intensity scalar fluctuations near the wall. On the other hand, the field $\theta^*_{inn}$ preserves the scales directly contributing to the wall scalar transfer. In this case, the reduction in $St$ can be attributed to the increase in the mean scalar concentration caused by the suppression of the outer cycle. In fact, the suppression of the outer cycle leads to a reduction in scalar flux, which acts as a bottleneck on the near-wall region. This idea is supported by the fact that the field $\theta^*_{inn}$ shows a probability density function

in the viscous sublayer (figure A.6(a)) with a shape qualitatively similar to that of the reference case $\theta^*$, but shifted towards higher scalar values. This similarity suggests a similar physics of the scalar fluctuations, but with a gradual saturation due to the reduced scalar flux sustained by the outer cycle. This dynamic is consistent with the gradual reduction in $St$ observed in figure A.5(a).

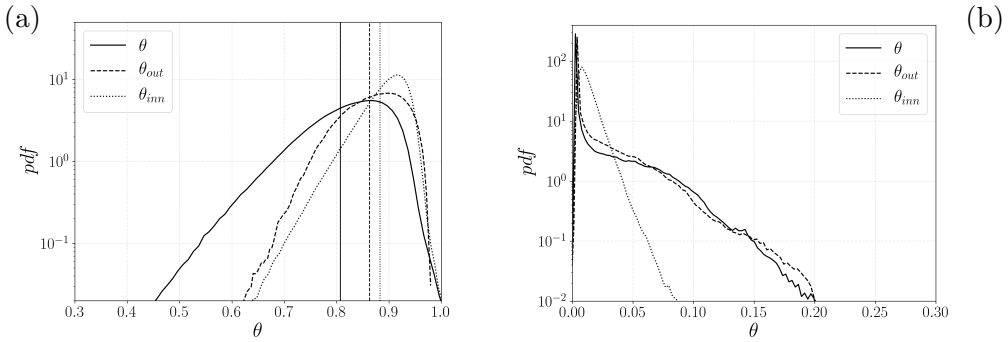


Figure A.6: Probability density function of $\theta^*$ (a) at $z^+ = 5$ and (b) at $z = \delta_\theta$ at the final $Re_\tau = 1500$. The vertical lines in (a) indicate the respective mean values of the scalars. Figure taken from Boga et al. (2024).

We now consider the temporal evolution of the boundary layer thickness $\delta_\theta$ reported in figure A.5(b). After an initial readjustment, the trend of $\delta_{\theta_{out}}$ resumes a growth rate similar to that of the reference $\delta_\theta$. This almost unaltered growth rate can be explained through the following two considerations. The first is that large-scale anisotropic motions that mainly contribute to the entrainment process (Cimarelli and Boga, 2021) are preserved in $u_i^{*out}$, whose trace can be seen in the right tail of the $\theta^*_{out}$ pdf reported in figure A.6(b). The second consideration regards the measured observable $\delta_\theta$. In fact, the position of the mean interface is not very sensitive to the threshold used. For this reason, the reduction in the scalar concentration flux supplied by the inner region in $\theta^*_{out}$ has little influence on the evolution of this observable. On the contrary, the suppression of the large anisotropic motions in $u_i^{*inn}$ directly acts on the entrainment process at the interface of the boundary layer, resulting in a slower growth rate of $\delta_{\theta_{inn}}$. Similar results have been obtained when analysing the entrainment process in turbulent jets with an approach similar to the one presented here (Cimarelli and Boga, 2021).

For a deeper understanding of the dynamics observed so far, we now move to examine the mean profiles and the variances of the scalar fields

(a)

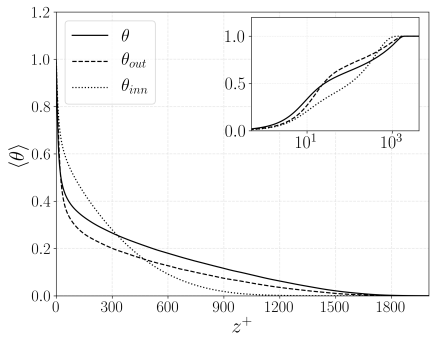


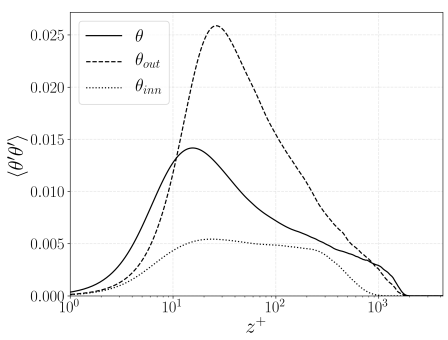


(b)

Figure A.7: (a) Mean scalar profiles, respectively $\Theta$ in the main panel and $1-\Theta$ in semi-logarithmic axes in the inset panel and (b) variances at $Re_\tau = 1500$. Figure taken from Boga et al. (2024).

reported in figure A.7. Both profiles $\Theta_{out}$ and $\Theta_{inn}$ show a higher scalar concentration in the near-wall region, for $z^+ < 20$. This is in accordance with the reduction observed in the $St$ for the two reasons explained above, namely: the reduced scalar flux towards the outer region caused by the suppression of the inner cycle in $\theta^*_{out}$ and the blockage effect caused by the suppression of the outer cycle in $\theta^*_{inn}$ (that will be shown in figure A.8). Despite a different distribution of the scalar concentration $\Theta_{out}$, a region resembling a logarithmic behaviour can still be observed as shown in the inset of figure A.7(a). The lower scalar flux supplied by the near-wall region does not seem to influence the outer dynamics of $\theta^*_{out}$. On the other hand, $\theta^*_{inn}$ presents a qualitatively different profile. The suppression of the outer cycle, with the associated reduction of the mean scalar flux, results in a high scalar concentration region extending from the near-wall up to a good portion of the outer region.

In order to quantify the reduction of the fluxes, we introduce the following equation:

$$St = \langle\theta w\rangle - \frac{1}{ReSc}\frac{\partial\Theta}{\partial z} + \beta \quad \text{with} \quad \beta = \frac{d}{dt}\int_0^z \Theta dz \tag{A.6}$$

obtained by integrating in the wall-normal direction the equation for the mean scalar concentration. To note that, for $z \gg \delta_\theta$ the above equation simply reads

$$St = \beta\,(z \to \infty) \tag{A.7}$$

where $\beta\,(z \to \infty)$ is the rate of entrainment of scalar concentration. The terms of equation (A.6) of the two experiments are shown and compared with

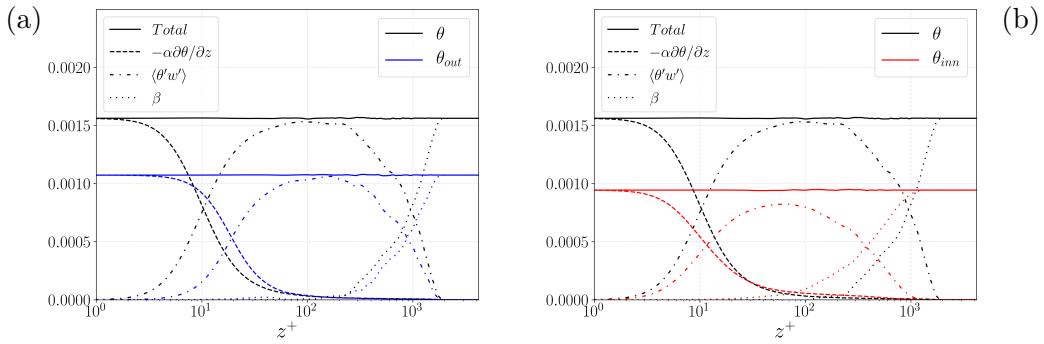


Figure A.8: Mean fluxes of (a) $\theta^*_{out}$ and (b) $\theta^*_{inn}$ compared with $\theta^*$ at $Re_\tau = 1500$. Figure taken from Boga et al. (2024).

the reference case in figure A.8. At first glance, one can see a macroscopic similarity in the shape of the fluxes with a global reduction in accordance with the reduction observed in the $St$. Taking a closer look to the turbulent flux, it can be seen that $\langle\theta_{out}w_{out}\rangle$ appears to be more active at a higher distance from the wall, while $\langle\theta_{inn}w_{inn}\rangle$ appears to be more active closer to the wall, as expected. Since $\langle\theta w\rangle$ and $\beta$ must sum up to $St$ in the outer region (where $-1/(ReSc)\partial\Theta/\partial z$ is negligible), these different profiles of $\langle\theta w\rangle$ determine also the shape of $\beta$. The high activity of $\langle\theta_{out}w_{out}\rangle$ in the outer region results in a steep profile of $\beta_{out}$, meaning that the scalar flux is mainly sustained by the entrainment process occurring away from the wall and near the interface. On the contrary, the lower activity of $\langle\theta_{inn}w_{inn}\rangle$ in the outer region results in a less steep profile of $\beta_{inn}$, suggesting that the main scalar flux is sustained by the homogenization in the core of the boundary layer, thus by the mixing effect of the small quasi-isotropic scales. Despite the similarity between the mean profiles $\Theta_{out}$ and $\Theta$, their variances, reported in figure A.7(b), present different characteristics. In particular, $\langle\theta_{out}\theta_{out}\rangle$ exhibits a more pronounced peak located at a greater distance from the wall with respect to $\langle\theta\theta\rangle$. This difference can be attributed to the presence of large unmixed regions initiated by the large-scale anisotropic motions and left unmixed by the absence of the small mixing scales. Conversely, the profile of $\langle\theta_{inn}\theta_{inn}\rangle$ resembles the reference profile, although it appears to be damped, indicating a more uniform field. Both $\langle\theta_{out}\theta_{out}\rangle$ and $\langle\theta_{inn}\theta_{inn}\rangle$ present lower values in the near-wall region with respect to the reference case.

In order to take a closer look into the dynamics of the scalar fluctuations

we introduce the scalar variance budget equation:

$$\frac{\partial\langle\theta\theta\rangle}{\partial t} + \frac{\partial}{\partial z}\left(\Phi_u + \Phi_\alpha\right) = \Pi_\theta - \epsilon_\theta, \tag{A.8}$$

where the turbulent production $\Pi_\theta$ and dissipation $\epsilon_\theta$ terms are defined as:

$$\Pi_\theta = -2\langle\theta w\rangle\frac{\partial\Theta}{\partial z} \quad \text{and} \quad \epsilon_\theta = \frac{2}{ReSc}\langle\frac{\partial\theta}{\partial x_j}\frac{\partial\theta}{\partial x_j}\rangle \tag{A.9}$$

and the turbulent $\Phi_u$ and diffusive $\Phi_\alpha$ fluxes as:

$$\Phi_u = \langle\theta\theta w\rangle \quad \text{and} \quad \Phi_\alpha = -\frac{1}{ReSc}\frac{\partial\langle\theta\theta\rangle}{\partial z} \tag{A.10}$$

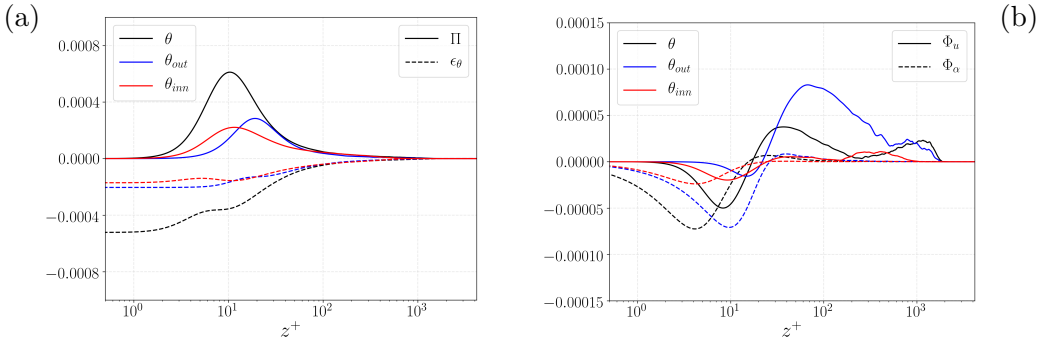


Figure A.9: Scalar variance (a) production $\Pi_\theta$, dissipation $\epsilon_\theta$ and (b) turbulent and diffusive fluxes $\Phi_u$ and $\Phi_\alpha$ at $Re_\tau = 1500$. Figure taken from Boga et al. (2024).

The picture shown by the scalar variance budget in figure A.9 can be interpreted as follows. Both the scalar variance production and the turbulent flux towards the near-wall region are strongly reduced in $\theta^*_{out}$, thus justifying the lower scalar variance observed in the near-wall region. In addition to this reduction, a shift to higher wall distances can also be observed, reinforcing the idea that large-scale motions are not directly active in the near-wall region, beside the imprinting they give on the flow and the modulation with which they act on the small scales. The diffusive flux and the dissipation adapt themselves to this scenario. On the other hand, the inner dynamics of $\theta^*_{inn}$ appear qualitatively similar to the reference case, even if lower in intensity. This is in accordance with the idea that the inner cycle finds itself in a condition bounded by the outer dynamics but remains qualitatively unaltered. In particular, the suppression of the outer cycle limits the turbulent flux of fluctuations directed toward the wall, and the increase of the mean scalar value limits the possibility of a large variance because of the intrinsic limitation $\theta^* \leq 1$.

## A.3 Effects of the filtering procedure

In order to show the robustness of the present results on the type of filtering procedure adopted, we show in the present section the results obtained through a different filtering approach. This second approach tested uses the filtering operation only in sub-portions of the domain to obtain the two modified velocity fields. The field $u_i^{*out}$ is obtained by lowpass filtering the near-wall region ($z^+ < 60 = z_f^+$) in order to suppress the inner cycle and leave the outer cycle motions unaltered. On the other hand, $u_i^{*inn}$ is obtained by lowpass filtering the outer region ($z^+ > 60 = z_f^+$) and leaving the velocity in the near-wall region unchanged. The filter lengths vary

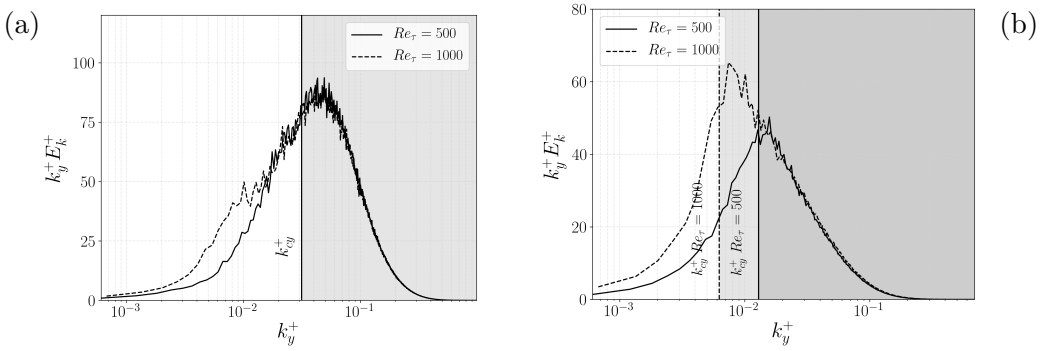


Figure A.10: Premultiplied spectra of the turbulent kinetic energy $E_k$ in the spanwise wavenumber $k_y$ respectively (a) in the buffer layer at $z^+ = 20$ and (b) in the outer region at $z^+ = 200$. The shaded areas indicate the filtered regions of the spectra (a) in $u_{out}$ and (b) in $u_{inn}$, being $k_{cy}^+ = 2\pi/\Delta_y^+$ the wavenumber corresponding to the spanwise filter length in inner units. In (b), $k_{cy}^+$ is reported at the initial $Re_\tau = 500$ and final $Re_\tau = 1000$.

gradually among the two regions through the use of a smoothing function $\widetilde{\Delta_i} = \Delta_i 0.5(1 \pm \tanh(z_f/(2h_\Delta))(1 - z/z_f))$ with $\Delta_i$ being the reference Gaussian filter lengths used in the streamwise and spanwise directions. In both experiments the width of the hyperbolic tangent is set to $h_\Delta = 0.2$. In the experiment $\theta_{out}^*$ (where the inner cycle is suppressed) $\Delta_i$ is expressed in inner units, while in the experiment $\theta_{inn}^*$ (where the outer cycle is suppressed), $\Delta_i$ is expressed in outer units. The filter lengths are chosen to remove most of the energy content in the region where they are applied. By looking at the premultiplied spectra, they have been respectively set to $\Delta_x^+ = 600$ and $\Delta_y^+ = 100$ for $u_i^{*out}$, and $\Delta_x = 1.5\delta$ and $\Delta_y = 0.5\delta$ for $u_i^{*inn}$. In order to ensure $u_i^{inn}$ and $u_i^{*out}$ to be divergence free, the pressure projection method is

applied to the two velocity fields after the filtering operation. The portions of the spectra filtered out in the spanwise direction to obtain $u_i^{*inn}$ and $u_i^{*out}$ are shown in shaded grey in figure A.10(a) and (b), respectively measured in the buffer layer and in the outer region.

This second approach has been tested on a smaller domain, with a lower resolution and up to a friction Reynolds number of $Re_\tau = 1000$. The results reported should be interpreted only as qualitative and aimed at validating what is presented in section A.2. The domain extension is $(L_x, L_y, L_z) = (600, 300, 150)D$ discretized in $(N_x, N_y, N_z) = (512, 512, 384)$ points leading to the spatial resolution parameters reported in table A.2. All other parameters and numerical schemes used are as in section A.1.1.

Table A.2: Grid resolution in friction units for two time instants corresponding to different friction Reynolds numbers. The subscript $\cdot_{|w}$ and $\cdot_{|\delta}$ indicates a quantity measured respectively at the wall ($z = 0$) and at $z = \delta$.

| $Re_\tau$ | $\Delta x^+$ | $\Delta y^+$ | $\Delta z_w^+$ | $\Delta z_\delta^+$ |
|---|---|---|---|---|
| 500 | 26.7 | 13.4 | 0.14 | 7.9 |
| 1000 | 23.8 | 11.9 | 0.13 | 12.5 |

We now proceed to present the results of the experiments. All the figures reported are maintained as in section A.2 in order to have a clear comparison between the two. In figure A.11, the instantaneous scalar contours are shown on a wall-normal section. The scalar fields of the two experiments $\theta_{out}^*$ and $\theta_{inn}^*$ show a very different topology compared to those obtained with the approach presented in section A.2 (figure A.4). In particular, $\theta_{out}^*$ looks macroscopically similar to the reference $\theta^*$, with a rescaling toward lower scalar values. By taking a closer look, in the near-wall region (which is difficult to distinguish) it is possible to note substantial differences resulting from the absence of small-scale motions. On the contrary, the field $\theta_{inn}^*$ appears completely different with respect to the reference case due to the application of the filtering operation with large filter lengths ($\Delta_x = 1.5\delta$ and $\Delta_y = 0.5\delta$). Despite this topological difference, we will show that the statistics of interest for this work and the main conclusions obtained in section A.2 remain consistent.

As shown in figures A.12(a) and A.5(a), the Stanton number evolutions resulting from the two approaches are qualitatively similar. Accordingly, also the pdf profiles measured in the viscous sublayer reported in figures A.13(a) and A.6(a) describe a similar scenario. A similarity can also be found in the temporal evolution of the boundary layer thickness as shown in

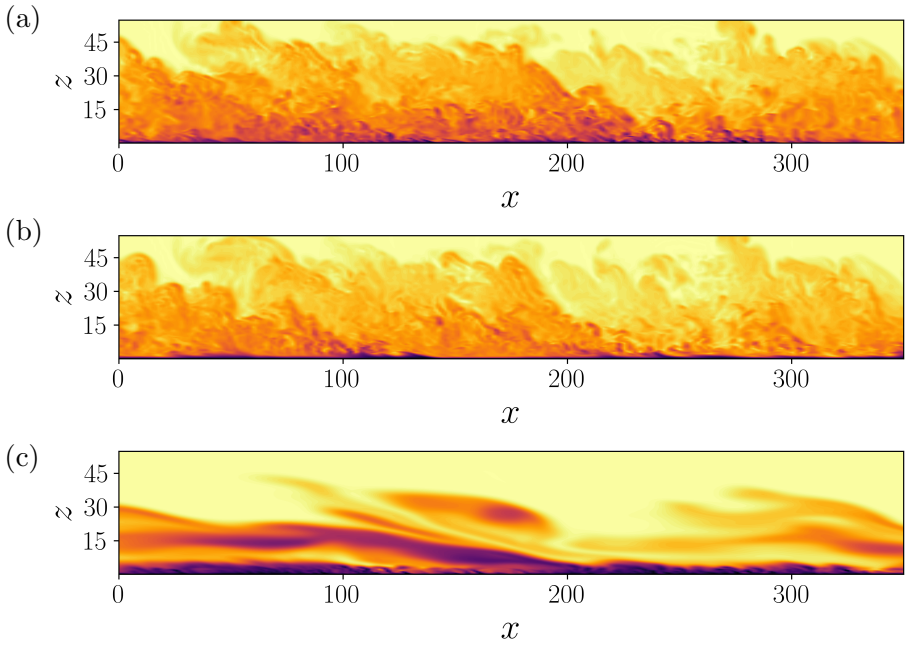


Figure A.11: Sections of the scalar fields of the three experiments at the same time instant, corresponding to $Re_\tau = 1000$. Respectively (a) $\theta^*$, (b) $\theta^*_{out}$ and (c) $\theta^*_{inn}$. The reference case (a) is duplicated here in order to simplify comparisons.

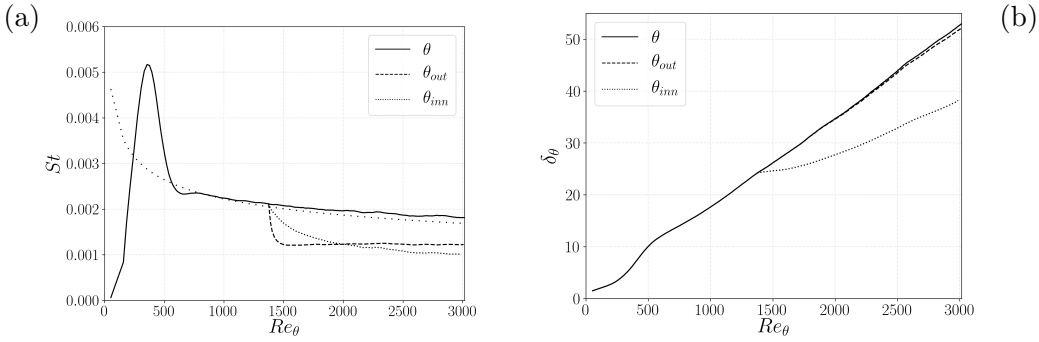


Figure A.12: (a) Temporal evolution of the Stanton number and its theoretical law $St = 0.0125 Re_\theta^{-1/4}$ in loosely dotted line and (b) temporal evolution of the boundary layer thickness based on the scalar concentration $\delta_\theta$.

figures A.12(b) and A.5(b) and in the respective pdf profiles measured at the

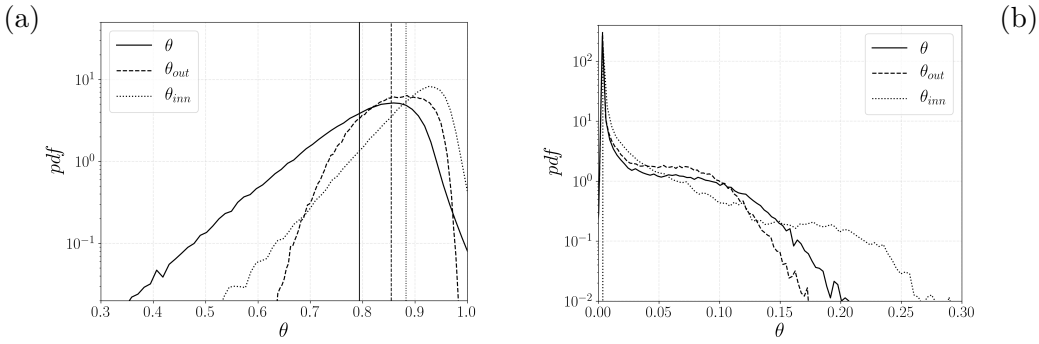


Figure A.13: Probability density function of $\theta^*$ (a) at $z^+ = 5$ and (b) at $z = \delta_\theta$ at the final $Re_\tau = 1000$. The vertical lines in (a) indicate the respective mean values of the scalars.

mean scalar interface (figures A.13(b) and A.6(b)). One notable difference is in the pdf distribution of $\theta^*_{inn}$ (dotted line). The presence of an extended right tail in the pdf of $\theta^*_{inn}$ in figure A.13(b) is caused by the intersection between the plane located at the mean scalar interface position and the protruding bulges generated by the large anisotropic fluctuations. These bulges contain a wide range of scalar values and remain unmixed due to the absence of the small scales. The extension of this tail is more pronounced than in the first approach because of the larger filter lengths used. A minor change can also be observed in the evolution of $\delta_{\theta_{inn}}$ (reported in figure A.12(b)) which is nearly identical to that of the reference case $\delta_\theta$. In the present approach, in fact, the velocity field in the outer region is not modified ($u_i^{*inn} = u_i^*$) and the small difference between $\delta_{\theta_{inn}}$ and $\delta_\theta$ is only the result of the lower scalar concentration flux coming from the inner cycle. This effect is comparable to a threshold change in the definition of the mean interface position, which is therefore negligible.

The mean profiles reported in figure A.14 show a behaviour in accordance with the one observed in figure A.7, while the scalar variances describe a scenario opposite to the one observed in section A.2 and in accordance with what is shown in figure A.11. The highly unmixed outer region of $\theta^*_{inn}$ causes a peak in $\langle \theta_{inn}\theta_{inn} \rangle$ that has a great impact on the scalar variance fluxes, as we will see.

The mean fluxes reported in figure A.15 are in good accordance with what is observed in figure A.8.

Finally, the scalar variance budgets show some macroscopic differences due to the more intrusive nature of the approach presented in this section.

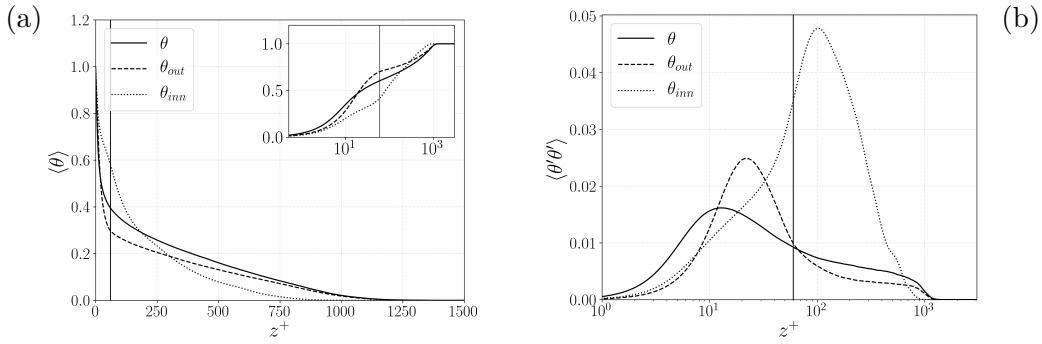


Figure A.14: (a) Mean scalar profiles and (b) variances at $Re_\tau = 1000$. The solid vertical line is located at $z_c^+ = 60$.

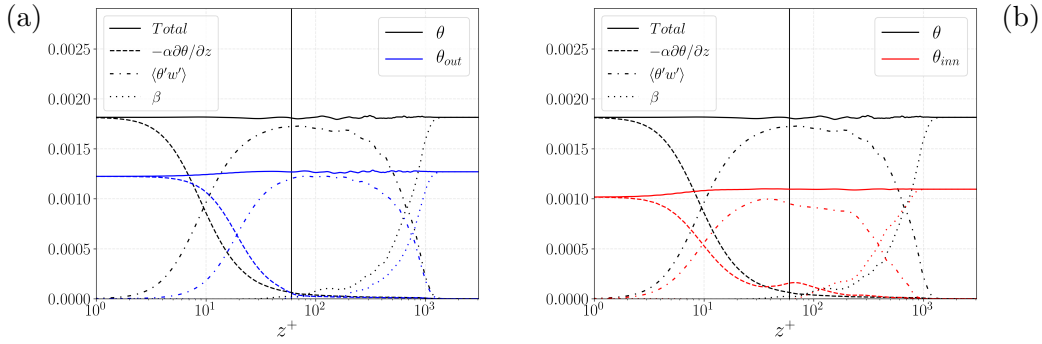


Figure A.15: Mean fluxes of (a) $\theta_{out}$ and (b) $\theta_{inn}$ compared with $\theta$ at $Re_\tau = 1000$. The solid vertical line is located at $z_c^+ = 60$.

However, if we limit our analysis far enough from the region directly affected by the filtering operation (i.e. $z^+ \ll 60$ for $\theta^*_{inn}$ and $z^+ \gg 60$ for $\theta^*_{out}$) we can note that the main conclusions drawn in section A.2 find support in these graphs.

In conclusion, despite the topological differences shown by the corresponding scalar fields of the two presented approaches, the results obtained lead to the same considerations. Confirmation of this can be found in the similarities between the evolution of the integral quantities, in the mean profiles, in the turbulent fluxes of both the mean scalar concentration and its variance and the production and dissipation of the fluctuations (if confined in the regions of interest, namely the inner region for $\theta^*_{inn}$ and the outer region for $\theta^*_{out}$).

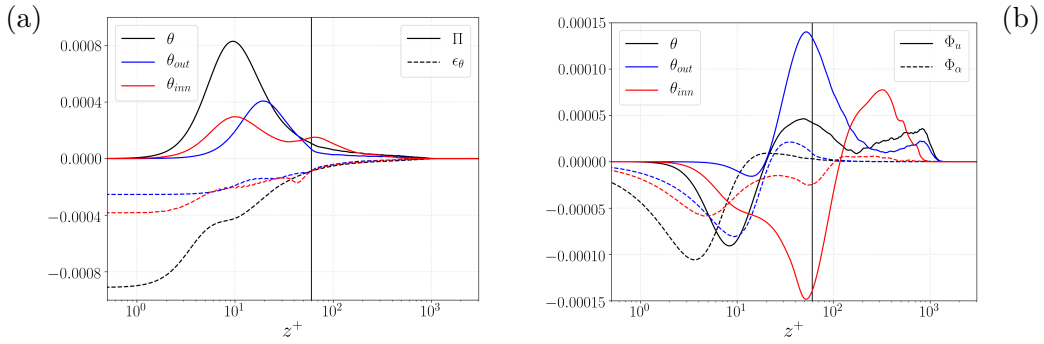


Figure A.16: Scalar variance (a) production $\Pi$, dissipation $\epsilon_\theta$ and (b) turbulent and diffusive fluxes $\Phi_u$ and $\Phi_\alpha$ at $Re_\tau = 1000$. The solid vertical line is located at $z_c^+ = 60$.

## A.4 Concluding remarks

An attempt to decouple the dynamics of the inner and outer cycles in the flow configuration of a temporally evolving boundary layer is carried out. The attempt is based on studying the evolution of two additional passive scalars driven by two modified velocity fields. The use of the two scalar fields is the key point that allows us to separate the two effects, as it allows us to study a field on which no direct manipulation has been applied. The velocity fields used to transport these two additional scalars are obtained at each timestep by manipulating the total velocity $u_i^*$ in order to retain only features of the inner ($u_i^{*inn}$) and outer ($u_i^{*out}$) cycles respectively. More specifically, the two velocity fields are obtained by suppressing scales that are mostly contributing to the inner or outer cycle activities based on their dimension.

The outer cycle dynamics observed through $\theta_{out}^*$ show many similarities with the reference case $\theta^*$. In both approaches tested, it seems possible to identify a logarithmic-like region in the mean profile $\Theta_{out}$. Furthermore, the growth rate of the scalar boundary layer thickness $\delta_{\theta_{out}}$ is unaltered, indicating that the entrainment process at the boundary layer interface is not very sensitive to the near-wall region dynamics. At the same time, in the region directly affected in this experiment (i.e. the inner region), the effect of inner cycle suppression can be observed. In this region, both a reduction in the scalar transfer at the wall (caused by the damping of the scalar fluctuations) and a reduction of turbulent production and transport mechanisms occur. In particular, the reduction of the mean scalar flux in the near-wall region also implies a reduction in the whole domain due to the

conservation law. Summarising, by suppressing the small scales, the outer cycle appears to maintain its dynamics unaltered and simply rescales the scalar flux according to what is supplied by the flux coming from the inner cycle. From a modelling perspective, this conclusion may be relevant for reduced-order approaches such as wall-modelled LES and RANS.

The inner cycle, on the other hand, is confined on both sides, facing the wall at its lower boundary and the outer cycle on the other side. The suppression of the outer cycle appears to have the effect of a bottleneck for the inner cycle. This interpretation is supported by the fact that the pdf of $\theta^*_{inn}$ in the near-wall region shows a similar distribution but with a shift towards higher values (reason for the gradual reduction of the Stanton number). Other symptoms of an almost unchanged dynamic can be found in the production and turbulent transport mechanisms in the near-wall region. Despite appearing rescaled, these profiles show a very similar shape to the reference case $\theta^*$. In the outer region of $\theta^*_{inn}$, the suppression of large anisotropic scales has the effect of reducing the rate of entrainment and the generation of a more homogeneous scalar field.

In conclusion, both the inner and outer cycles appear to have quite independent dynamics, with the difference being that, the outer cycle simply rescales to lower scalar values depending on what is supplied from the inner cycle, facing a free region on its top bound. On the other hand, the inner cycle dynamics is confined to operate in between the wall and the outer cycle, whose suppression can act as a bound, limiting the inner cycle to operate in a narrower and narrower range of scalar values due to the intrinsic limitation $\theta^* \leq 1$.

# Appendix B

# On floating point precision in computational fluid dynamics using OpenFOAM

Before starting my PhD, I got interested in topics concerning supercomputing. This interest started during my work experience at the High-Performance Computing (HPC) centre at CINECA. Some of the topics covered include the impact of using reduced computational accuracy on performance using the OpenFOAM code. The causes of the observed results have been explained by means of an ad hoc theoretical model. These activities were finalised during my first year of PhD. The present appendix contains the main results regarding this topic, taken from Brogi et al. (2024).

## B.1 Introduction

An increasingly wider community is choosing the open source software OpenFOAM (2022a,b) as a flexible tool to perform numerical simulation in continuum mechanics including fluid dynamics, solid mechanics and electromagnetics. OpenFOAM's modular structure allows end users to easily build new solvers and developers to add new features, constantly enlarging the range of possible applications of interest for both the academy and industry (Di Paolo et al., 2021; Rauter et al., 2021). However, made an exception for a recent coordinated effort (www.exafoam.eu), relatively less attention has been paid by OpenFOAM developers to computational performances. In particular, aspects such as its parallel efficiency on massively parallel machines remain challenging (Axtmann and Rist, 2016). Individual research groups have managed to resolve implementation bottlenecks and improve the performance of OpenFOAM, (see Bná et al. (2020) and references therein) but, often the lack of generality of their implementations has prevented their direct inclusion in the official OpenFOAM distributions.

Tailored optimization strategies are indeed required for any application

to exploit the computational power of current and next-generation supercomputing systems (e.g. Folch et al. (2023)). Modern HPC machines typically achieve their full computational power using heterogeneous hardware (e.g. CPU-GPU) and a huge number (up to millions) of computing units. Optimizing and reducing data movement, including memory access and I/O, is therefore a basic requirement to reach peak performances. The strong imbalance between the computational power and memory bandwidth still remains a major issue and it has not been attenuated by the latest technological trends. Performing arithmetic operations remains indeed several orders of magnitude faster than accessing data in memory, or performing communications between different computational nodes of a cluster machine. From this perspective, most of the real applications, including OpenFOAM, are and will become more and more memory-bound (Abdelfattah et al., 2021; Succi et al., 2019).

Changing algorithms can help to significantly improve the communication-to-computation ratio (i.e. the operational intensity) of an application but it may be a challenging and time consuming exercise, especially for complex general-purpose codes such as OpenFOAM. Reducing floating point precision arithmetic is instead often a simple but effective way of cutting down data movement and increasing the computational speed for most applications. On modern CPUs, performing operations in single precision (32-bit) is twice as fast as in double precision (64-bit), since the amount of data moved in memory is halved and arithmetic operations are twice as fast as double precision (Baboulin et al., 2009). When considering less conventional hardware such as NVIDIA GPU Tensor Cores the computational gain becomes even more attractive. These architectures in fact support half precision arithmetic with dedicated functional units (accelerators) in the hardware that makes low precision much faster than higher precision (Haidar et al., 2018). With this hardware, half precision arithmetic has a theoretical speedup of 16× instead of the expected 4×, with respect to double precision (Abdelfattah et al., 2019). Moreover, the use of low-precision arithmetic may also be an effective way to reduce power and energy consumption (Sakamoto et al., 2020), one of the main factors to be considered in using and designing current and next-generation high-performance computing machines. In reduced precision, energy saving is mainly due to the overall shortening of the execution time Sakamoto et al. (2020), which is in turn related to the combined effect of the lower cost per arithmetic operation and decreased memory communication. However, using low floating point precision is not always possible. Traditionally, CFD codes work with double precision since for complex fluid problems linear algebra solvers may

not converge or not provide the solution with the required degree of accuracy. Several studies have proposed using mixed precision algorithms to unleash the power of multi-precision hardware without sacrificing accuracy or numerical stability (Abdelfattah et al. (2021) for a review).

In OpenFOAM, a mixed precision feature has been released with version v1906. It is implemented in its complex framework following a rather simple idea: all the code is compiled in single precision except for the linear algebra solvers, which work in double precision. The reduced memory consumption alleviates the bandwidth bottleneck of OpenFOAM, thus increasing the computational speed of almost any application. However, to our knowledge, there are no systematic studies on the use of reduced precision computations in CFD applications in the literature, making an exception for more specific case studies such as the recent work on fluid the lattice Boltzmann method based fluid solvers (Lehmann et al., 2022). Let us also note that in OpenFOAM, the fluid governing equations are discretized using the finite volume method (Ferziger et al., 2002) and the fluid solvers have in general low order of accuracy in space and time (below or up to the second order). From this perspective, therefore, it is interesting to understand whether a precision reduction (from single to double) significantly impacts the accuracy and stability of such low-order solvers.

In this work, we analyse and discuss the impact of floating point precision reduction (single and mixed with respect to double) on real CFD applications using OpenFOAM. In particular, we consider two important aspects such as the convergence and accuracy of computed solutions, the computational performance on both CPU and hybrid CPU-GPU hardware as well as the parallel efficiency of CFD applications. With the aid of theoretical and experimental analysis, we describe how precision reduction affects the individual parts of the applications that are commonly present in CFD solvers. To try to keep our results as much as possible of general interest, both incompressible and compressible solvers have been selected for testing, since they may represent the basis for any more complex solver to be built on (e.g. multiphase solvers). The quality of computed solutions (accuracy and convergence) of these solvers are tested considering important flow phenomena in laminar and turbulent flow regimes as well as the presence of shock wave discontinuities. Performance gain and change in the scaling behaviour of applications on parallel machines due to precision reduction are also considered. A theoretical model for the strong scaling of applications is also developed, which allows us to explain and better understand the changes observed with reduced floating point precision and different hardware specifics. Finally, we demonstrate how significant can be the effect

of mixed precision on computational performance, with a speedup of 2.4×, when considering the hybrid CPU-GPU implementation of OpenFOAM that has been recently made available to users. Let us also note that, in this work, we do not directly discuss power and energy consumption aspects for which the interested reader is referred to one of the few dedicated works (e.g. (Sakamoto et al., 2020)). However, any improvement in the computational performance in reduced precision may be related to a shortening of the computational time and hence, decreased energy consumption.

## B.2 Impact of precision reduction on the quality of computed solutions

Most CFD solver algorithms, such as those implemented in OpenFOAM, can be divided into two main steps: the assembly of a matrix that results from the discretization (Finite Volumes, in OpenFOAM) of the governing partial differential equations, and the solution of the linear algebra system that brings to the numerical solution of the equations. When OpenFOAM is compiled in single/double precision means that all floating point numbers, hence for both the matrix assembly and the linear algebra solver, are in single/double precision. When using a mixed precision built of OpenFOAM, all floating point numbers are in single precision for the matrix assembly but are converted in double precision before solving the linear algebra. Here we analyse the impact of reduced floating-point precision (single and mixed) on two important aspects of CFD applications: the accuracy and convergence of computed solutions. Given the large number of CFD applications available in OpenFOAM, we limit our study to solvers for single-phase incompressible and compressible flows. It is well known in fact that these solvers face different computational challenges and represent the ground for almost any more complex solver (e.g. multiphase). Here, and in the rest of the paper, we use OpenFOAM v1912 for our tests, if not otherwise stated. The classical `icoFOAM` (incompressible) and `rhoPimpleFOAM` (compressible) solvers have been selected to solve radically different benchmarks: the laminar 3D lid-driven cavity, the decay of isotropic turbulence, the shock tube and the starting compressible jet. The lid driven cavity is a well known benchmark for incompressible solvers (Shankar and Deshpande, 2000), especially when considering the laminar steady state regime. The isotropic turbulence benchmark (Pirozzoli and Grasso, 2004) is also a standard test and it is well suited to evaluate the effect of reduced precision on numerical simulations with turbulence, here in the weakly compressible regime.

The Sod shock tube test (Sod, 1978) is instead used to understand whether discontinuous solutions are affected by floating point precision representation. The fully compressible dynamic of a starting jet (high Mach and high Reynolds number) is used to test the behaviour of the numerical solver with reduced precision for transient compressible problems. Finally, as an example of a complex real-case application, we consider the simulation of a compressible, multiphase turbulent volcanic plume with the OpenFOAM-based solver `ASHEE` (Cerminara et al., 2016).

### B.2.1 Lid-driven cavity

In this benchmark, an incompressible fluid is initially at rest in a cubic cavity. A tangential velocity is imposed on the top boundary and no-slip conditions (wall) are enforced on all the other boundaries. The flow regime in the cavity depends only on the dimensionless Reynolds number ($\mathrm{Re} = UL/\nu$, with $U$, the velocity of the moving lid, L the length of the cavity and $\nu$ the kinematic viscosity). The interested reader may refer to Shankar and Deshpande (2000) for a complete review. Here we consider the laminar steady state regime for two different Reynolds numbers ($\mathrm{Re} = 100, 1000$). For this benchmark, we used the incompressible `icoFOAM` (v1912) solver compiled in single, mixed and double precision. We refer the reader to Appendix E of the original paper (Brogi et al., 2024) for details of the simulation setup (boundary conditions and numerical schemes).

All the simulations converge to physical solutions (figure B.1) and regardless of the precision, they are consistent with a well-known reference study (Ku et al., 1987). In particular, our results demonstrate that the single precision is sufficient for the fluid solver to provide accurate velocity profiles along the cavity centerlines (figure B.1), with a mesh size of $100^3$. We then also tested the order of accuracy, that is how the accuracy of the numerical solution varies with increasing mesh size, in both single and double precision for $\mathrm{Re} = 100$. Our test shows that the order of accuracy is rather low, less than 1 for all variables (Appendix B.C, figure BA4, table B.4). However, the convergence is almost the same in double and single precision. In other words, it seems that precision reduction has no effect on grid convergence, at least for such a low-order fluid solver.

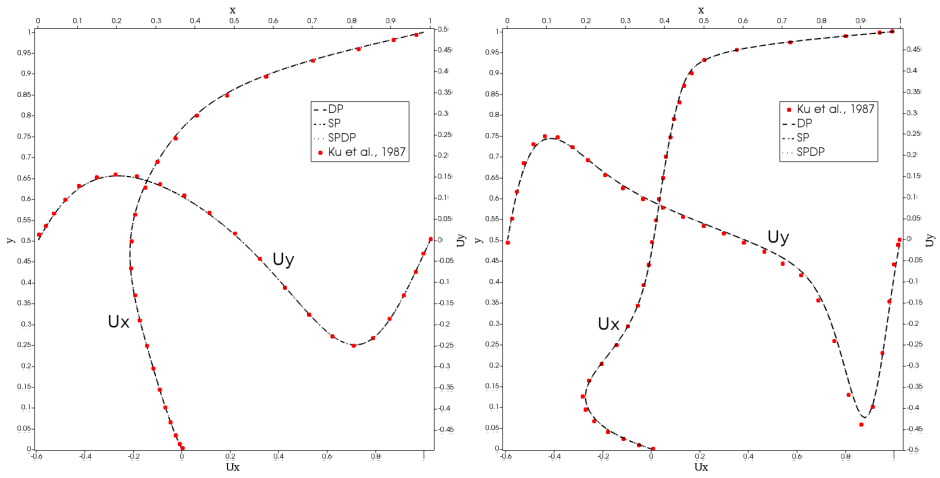


(a) Re = 100. (b) Re = 1000.

Figure B.1: Lid-driven cavity benchmark solved with `icoFOAM` solver, using a mesh size of $100^3$ cells, in single (SP), double (DP) and mixed precision (SPDP). Velocity profiles of $U_x$ along y-axis centreline (left vertical axis) and $U_y$ along x-axis centreline (top horizontal axis) are compared with those extracted from the figures of Ku et al. (1987). Figure taken from Brogi et al. (2024).

### B.2.2 Compressible decaying homogeneous and isotropic turbulence

Turbulence is one of the main non-linear complexities of fluid dynamics. For a comprehensive review of such an important topic, the interested reader may refer, among many other classical textbooks, to Pope (2000). In brief, turbulent flows are characterized by a wide range of spatial and temporal scales, due to the presence of large eddies (defining the integral scale $L$) that continuously break into smaller and smaller eddies, until the dissipation scale is reached. This is the smallest scale and is called the Kolmogorov micro-scale $\eta$. The ratio between the integral and the dissipation scale grows with the Reynolds number $L/\eta \propto \mathrm{Re}^{\frac{3}{4}}$. A simulation that is able to capture all the scales (from the largest integral one, down to the smallest dissipation scale) is called Direct Numerical Simulation (DNS). When the flow is far from boundaries, the typical behaviour of turbulence is described by the energy cascade of the kinetic energy spectrum. When it is impossible to resolve all the relevant scales, one of the possibilities is to use the Large Eddy Simulations (LES) method, to take into account of the energy cascade in

the sub-grid terms. A general description of the physical, mathematical and numerical problem can be found in (Blaisdell et al., 1991; Wang and Maxey, 1993; Garnier et al., 1999; Pope, 2000; Honein and Moin, 2004; Pirozzoli and Grasso, 2004; Lesieur et al., 2005; Liao et al., 2009; Bernardini and Pirozzoli, 2009; Bernardini, 2014; Bernardini et al., 2021) and in references therein. Homogeneous and isotropic decaying turbulence is a classic benchmark used to test the capabilities of numerical codes to solve turbulence far from boundaries. Here, we are following the same procedure described by Cerminara et al. (2016); Cerminara (2016), by using the `ASHEE` code in its single-phase and mixed-precision configuration. The objective is to compare the mixed-precision solution with the double-precision one, having already validated the latter with the eight-order scheme by Pirozzoli and Grasso (2004). Double precision is often needed in problems facing turbulence, to solve as accurately as possible the non-linear advection terms present in the Navier-Stokes equations. Indeed, these terms tend to grow with the spatial scale, becoming larger than the (mainly linear) dissipation terms. For this reason, double precision becomes even more important in LES, where the smallest scale is much larger than the dissipation scale and its contribution is taken into account using non-linear sub-grid scale turbulence viscosity terms (Lesieur et al., 2005).

The DNS test is performed using a mesh size of $256^3$ cells in a cubic box with side $L = 2\pi$ and periodic boundary conditions. In this way, boundary effects can be neglected. The initial spectrum is the same described in Section 5.2 of Cerminara (2016), so that the root-mean-square Mach number is $\mathrm{Ma}_{\mathrm{rms}} = 0.2$, the initial Taylor microscale is $\lambda = 0.5$, the eddy turnover time is $\tau_{\mathrm{e}} = 3.66$, the Reynolds number based on the Taylor micro-scale is $\mathrm{Re}_\lambda = 116$, and the maximum wave-number is $k_{\mathrm{max}} = 127$. In this way, its product with the Kolmogorov micro-scale $\eta = 0.023$ is large enough to have a proper DNS. The same initial condition is mapped into a $32^3$ mesh to perform a LES to be compared with the previous DNS results. LES are executed by using the Moin's model (Cerminara et al., 2016; Cerminara, 2016). We refer the reader to Appendix E of the original paper (Brogi et al., 2024) for details of the simulation setup (boundary conditions and numerical schemes). The comparison has been performed by using both mixed and double precision. In single precision, the fluid solver does not necessarily converge. For instance, the LES with mesh size $64^3$ is unstable (due to the divergence of linear algebra for the energy equation), but it is stable for mesh size $32^3$.For the smaller mesh size (larger cells) numerical dissipation may be more effective in killing numerical noise that triggers the instability. Therefore, in general, the fluid solver in single precision is

more sensitive to the numerical noise at the high frequency that is caused by the smallest turbulent scales that are near or smaller than the cell size. In figure B.2, we report the spectrum of the kinetic energy for the DNS and LES simulations in double and mixed precision. Mixed precision works pretty well for this test case, with minor influence on the solution: the relative error with respect to the double precision case is $6.0 \cdot 10^{-7}$, and $7.2 \cdot 10^{-7}$, for the DNS and LES, respectively. 90% of the error is contained in the region $k < 10$, and $k < 5$, respectively for DNS and LES. By using a different LES sub-grid model, the effect of precision can have a larger impact. For example, by using the dynamic WALE model (Cerminara et al., 2016; Cerminara, 2016), the relative discrepancy increases to $1.4 \cdot 10^{-4}$. Finally, also for this test case, we analyzed the convergence of the error with the increasing mesh size. The error for the kinetic energy spectrum is computed for each mesh size with respect to the results obtained with a large mesh ($256^3$). The order of accuracy, also for this test case, is quite low but very similar in mixed and double precision (Appendix B.C, figure BA5, table B.4).

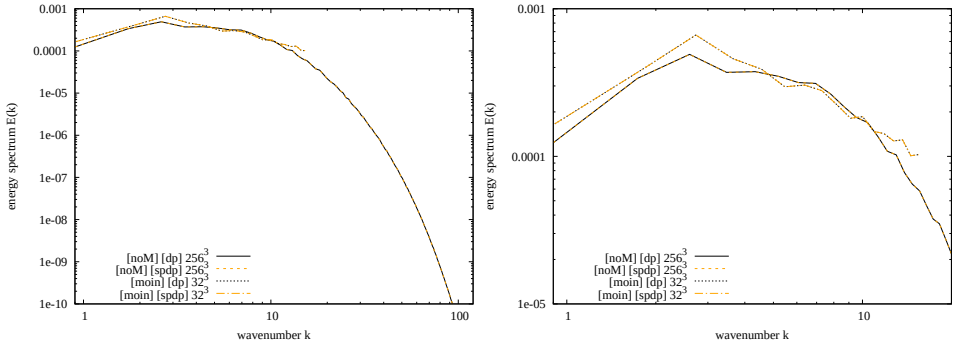


Figure B.2: Kinetic energy spectrum of the DNS (noM) and of the LES (moin) in double precision (dp) and mixed precision (spdp), after $t = 5.5\tau_e$. The right panel is just a zoom in the region resolved by the LES. Figure taken from Brogi et al. (2024).

### B.2.3 Starting compressible square jet

A high-speed injection of a warm gas (330 K) into a static atmosphere with a slightly lower temperature (300 K) is considered. For simplicity, the jet fluid enters the atmospheric box through a square inlet (0.0635 m) resolved with a homogeneous structured mesh (no grid stretching). Given the low gas viscosity ($1.8 \times 10^{-5}$ Pa s) and high velocity (364 m/s) of the in-

jected fluid, the jet flow is unsteady and compressible, characterized by high Mach number ($> 1$ locally) and Reynolds number. Non-linear instabilities in the jet shear layer (such as Kelvin-Helmholtz instabilities), eddies, and pressure waves contribute to the formation of a turbulent buoyant plume in these conditions. As the jet enters the atmospheric box it forms a vortex and pushes the static air outwards, producing an intense pressure wave that propagates radially (figure B.3). In our setup, the simulation is stopped when the first transient reaches the boundary of the computational domain and hence before the turbulent plume develops. The solver `rhoPimpleFOAM` for compressible laminar and turbulent flow is used for this test case. An LES approach combined with a one-equation eddy viscosity model (Yoshizawa, 1986) is used to allow the solver to deal with the unresolved scales of the turbulent flow. For testing, velocity and pressure probes are placed along the jet centerline, in the jet shear layer and far from the flow field in the atmosphere to record pressure waves. We refer the reader to Appendix E of the original paper (Brogi et al., 2024) for details of the simulation setup (boundary conditions and numerical schemes).

Single precision for this test case is not sufficient for linear algebra to converge. Therefore, no numerical solution is available with this precision. Mixed and double precision runs instead converge to physical solutions that result to be very similar. In particular, for a test case with a coarse mesh, the time series of pressure and velocity for all probes overlap almost completely (figure B.4). When considering a test case with a refined mesh (double number of cells in the jet diameter), double precision and mixed precision start to be different. The differences are particularly evident in those parts of the recorded signals where high-frequency content is present on all fluid variables (e.g. $Uy$ in figure B.4b). The system sensitivity to tiny differences in the initial conditions may explain the changes observed in the numerical solutions with reduced precision and refined mesh. The impact of mixed precision on the accuracy of computed solutions can be evaluated by considering the statistical quantities of the fluid variables only (see section B.2.2).

### B.2.4 Mixed precision in a real use-case: the simulation of a volcanic plume

Moving to a geophysical scale problem, we present a numerical simulation of the evolution of an explosive volcanic eruption in a still atmosphere. Volcanic plumes are characterized by high Reynolds and Mach numbers. The multiphase gas-particle mixture injected into the atmosphere by these kinds of fascinating and catastrophic events is typically very hot (above

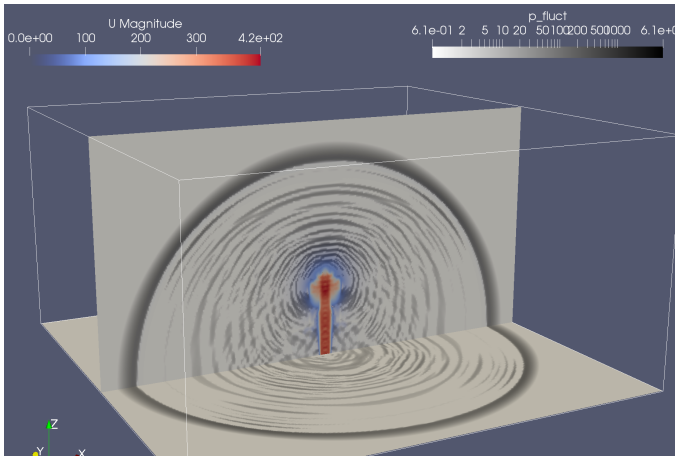


Figure B.3: Screenshot of LES simulation of the supersonic starting jet using `rhoPimpleFOAM` solver. The magnitude of the velocity field (in colour) and pressure fluctuations $\delta p = p - p_{ref}$ (black and white in log scale) are shown. Figure taken from Brogi et al. (2024).

1000 K) and denser than the surrounding air (above 3 kg/m$^3$). Shocks, turbulence and acoustic fluctuations start to develop immediately after the beginning of the eruption. The plume initially rises because of its initial momentum. Then, turbulent mixing decreases its density due to atmospheric air entrainment and expansion and the plume may reach a level where the buoyancy starts to be positive (buoyancy reversal). At this level, the column starts to behave as a proper plume, accelerating upwards due to its buoyancy. From the neutral buoyancy level, the updrafting mixture decelerates, to finally spread laterally into the umbrella cloud. More details on the phenomenon can be found e.g. in Woods (2010); Cerminara et al. (2016); Cerminara (2016); Neri et al. (2022). We now consider a test case to be solved with the OpenFOAM-based solver `ASHEE` (Cerminara et al., 2016). The `ASHEE` (ASH Equilibrium Eulerian) model, based on the dynamic LES model and an asymptotic expansion strategy of the full non-equilibrium multiphase Eulerian model, solves gas-polydisperse particle turbulent flows that characterize volcanic plumes. Although this approach is valid for dilute concentrations (volume fraction smaller than 1%) of ash, larger particles can be also included in `ASHEE` using a Lagrangian approach with a two-way coupling regime. For testing, we consider that the fragmented magma is injected into a still atmosphere from a 500 m wide inlet, with an initial velocity, temperature, and gas mass fraction equal to 236 m/s, 1050 K, and 5 wt.%,

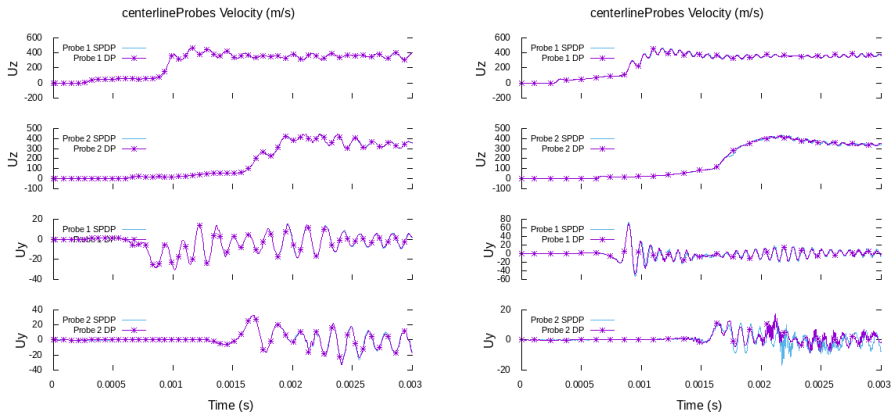


(a) (b)

Figure B.4: Times series of axial ($U_z$) and radial ($U_y$) components of the velocity field as recorded by two probes placed in the computational domain along the jet centre-line for: (a) coarse mesh (16384000 cells); (b) refined mesh (131072000 cells). Figure taken from Brogi et al. (2024).

respectively. This results in a mass flow rate equal to $2 \times 10^8$ kg/s, which is representative of a Plinian eruption. Atmospheric stratification is modelled by using the U.S. Standard Atmosphere. The computational domain is 50 km high and extends along the 2 horizontal directions for 100 km. It is discretised using 40 million cells with an orthogonal mesh with constant grading both in the vertical and horizontal directions. The temporal discretization is based on the second-order Crank-Nicolson scheme, with an adaptive time stepping based on the Courant number (Co $\leq 0.2$). Numerical schemes and boundary conditions are described in detail in (Cerminara et al., 2016; Cerminara et al., 2016; Cerminara, 2016). The bottom of the domain is treated as a thermally insulated slip wall, with a sink condition based on particle settling velocity to allow pyroclasts to deposit. The atmosphere is treated as an open boundary with input-output Dirichlet-Neumann conditions based on the velocity direction and a total pressure condition. The inlet has a prescribed velocity hyperbolic tangent profile to mimic conduit boundary effects. All these characteristics have been implemented in `ASHEE` by using the OpenFOAM infrastructure (OpenFOAM, 2022a).

In figure B.5a, we show a snapshot of the simulation 9 minutes after the

onset of the eruption. The plume, described by an isosurface of ash concentration, reaches a maximum altitude of 30 km. The entire simulation covers 50 minutes of plume dynamics. In figure B.5b, we show vertical profiles of mass flow rate going upward inside the plume. They are obtained by averaging in time and horizontally in space over a 30 minutes time window. These profiles are used to compare the results in double and mixed precision. Mixed precision presents a good level of accuracy to reproduce the averaged properties of the simulated volcanic plume.

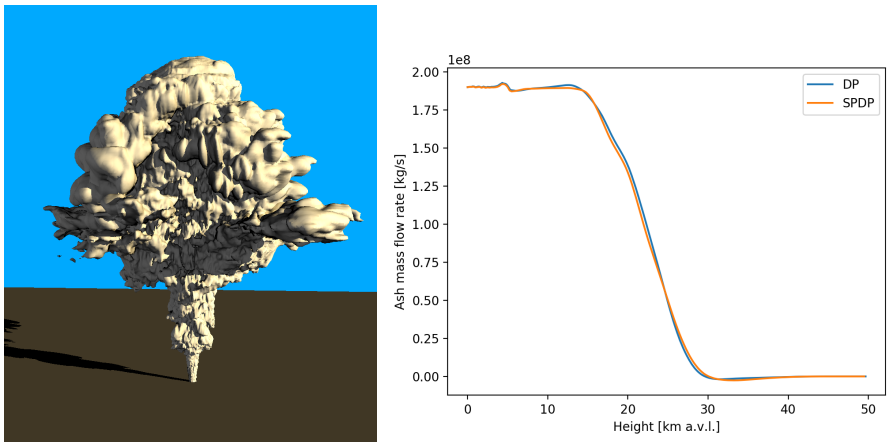


(a) (b)

Figure B.5: Numerical simulations of a volcanic plume with OpenFOAM-based solver `ASHEE` (Cerminara et al., 2016): a) snapshot of the simulation 9 minutes after the onset of the eruption; b) Comparison of vertically averaged profiles for the mass flow rate in double (DP) and mixed precision (SPDP). Figure taken from Brogi et al. (2024).

## B.3 Performance gain of reduced precision computations

Most CFD solver algorithms, as those implemented in OpenFOAM, can be divided into two main steps: the assembly of a matrix that results from the discretisation (Finite Volumes, in OpenFOAM) of the governing partial differential equations, and the solution of the linear algebra system that brings to the numerical solution of the equations. The coupling between the different equations (continuity, momentum, and energy) can be then treated implicitly or explicitly. In the first case, all the coupled PDEs are written as a

single linear system of equations that is solved at once with a linear algebra solver. In the second case, each equation is written as a single linearized system, that is solved separately (segregated strategy) and then the coupling is obtained using well-known iterative pressure- or density-based procedures (SIMPLE, PISO or PIMPLE; (Ferziger et al., 2002)). In particular, the PISO algorithm is used to couple the continuity and momentum equation for transient flow with a two-step iterative strategy. A predictor step, where an intermediate velocity is solved using pressure at the previous time step, is followed by a number of corrector steps that first solve for a pressure equation (derived combining continuity and momentum equations) and then correct the velocity accordingly until continuity is fulfilled. The coupling with the energy equation is also achieved with small time steps with PISO or with larger time steps using the PIMPLE algorithm (see Systems of equations from (Greenshields and Weller, 2022)). The segregated solution strategy is the one adopted in OpenFOAM, although more recently implicitly coupled solvers have been developed (e.g. Oliani et al. (2023); Ferreira et al. (2019)). In this work, we have used only more classical OpenFOAM solvers that adopt a segregated solution strategy.

In the following, we will refer to "matrix assembly" as the set of all the operations necessary for the construction of the matrices. The other main portion of the code, which we will refer to as "linear algebra", includes the set of operations aimed at solving the linear system generated during the "matrix assembly" phase. Finally, the last portion of the code that we will mention is the "flux correction" phase. Passing from double to single precision in an ideal world means that all computational and communication costs involving floating point numbers are halved. Clearly, the parts of the solver involving integer numbers are not affected by the lower precision. When considering mixed precision, the computational gain is less obvious to be predicted. In this case, only the matrix assembly is performed in single precision whereas the linear algebra is still in double precision. The fraction of time spent in linear algebra may vary considerably for different applications (e.g. incompressible and compressible problems) as does the speedup. Moreover, the actual gain obtained with reduced precision depends on how much the application is memory bound and therefore on the details of the numerical setup (e.g. mesh size). Here we consider the lid-driven cavity and starting jet test cases to study and quantify the computational gain associated with reduced precision for incompressible and compressible CFD solvers (i.e. `icoFOAM` and `rhoPimpleFOAM`). The main reported metrics are the time spent for each part of the code in single and mixed precision, as compared to double precision.

A first analysis is conducted by changing the dimension of the computational domain and maintaining the number of cells per core constant (weak scaling analysis). This approach has been chosen to test the consistency of the observed gains while fixing the computational load and the memory bandwidth available per core. Subsequently, the test is repeated with an increased computational load to study its effect on the computational gain with reduced precision. The minimum amount of allocated resources considered is one socket (24 cores, on CINECA's Marconi machine (see (CINECA, 2022a) for hardware specifics) to keep a constant availability of DRAM bandwidth per core.

The results are reported in Tables B.1 and B.2. The maximum gain provided by single precision compared with double precision is 2×. For the lid-driven cavity in single precision, the computational gain is near to 2× (≈ 1.9×) for the test case with a larger computational load per processor (166k cells/core). Instead, for the lower computational load (41k cells/core), the gain obtained is smaller. A deeper inspection reveals that this low value of the total gain is mainly related to the small gain of the linear algebra part, that in this case takes more than 90% of the total time. Hence, as recently well explained by Zounon et al. (2022), the 2× speedup for linear algebra is only obtained for larger problems. In fact, the gain of linear algebra is affected by the performance of the preconditioner, the Sparse Matrix Vector Multiplication (SpMVM) kernel and by the weight of the MPI communications and the slack time due to global synchronizations and not perfect load balancing (in single precision the MPI time is reduced but not halved and it is more than 30% of the total time in the XL case). Regarding the SpMVM kernel, since it is memory bandwidth-bound, the speed-up in theory is given by the ratio of the time required for matrix storage in double precision with respect to the lower precision. For a symmetric ordered LDU-COO matrix (native format in OpenFOAM) the speed-up (S) is given by the following formula:

$$\begin{aligned} S &= \frac{2 * \text{nFaces} * \text{size(int32)} + (\text{nCells} + \text{nFaces}) * \text{size(real64)}}{2 * \text{nFaces} * \text{size(int32)} + (\text{nCells} + \text{nFaces}) * \text{size(real32)}} \\ &= \frac{2 + \frac{\text{nCells}}{\text{nFaces}}}{\frac{1}{2}(3 + \frac{\text{nCells}}{\text{nFaces}})}, \end{aligned} \tag{B.1}$$

where nCells and nFaces are the number of Cells and Faces respectively. For the Lid-driven cavity, M the ratio is approximately 1.4. Our tests have shown that the solver gain is above this theoretical value except for the S case.[1]

[1]For the lid-driven cavity, we used the Conjugate Gradient preconditioned by a

This result is in line with the recent work of Zounon et al. (2022) where they have studied the gain using single precision arithmetic in ILU and SpMVM kernels for a large set of sparse matrices. They found performances below 1.5× in the solution phase of the application of the preconditioner and 1.5× in the SpMVM kernel (using 10 cores).

As expected instead, for the mixed precision the gain obtained in matrix assembly and correction of the fluxes (single precision) is near two, while the gain in the resolution of the linear algebra (double precision) is near 1. Interestingly a small gain can also be observed in the solver phase for both the lid-driven cavity and the starting jet. Overall, the total gains (matrix assembly and solve) for the lid-driven cavity and starting jet are significantly different (1.14× versus 1.40× respectively, in the M test case with high computational load). The reason for this difference lies in the fact that the two applications have completely different time distributions between the matrix assembly and linear algebra phases (Figure B.6). For the lid-driven cavity, most of the time ($> 90\%$) is spent solving the linear algebra (mostly for the pressure equation), while for the starting jet the time is split roughly in half between the two phases. Hence, the gain obtained in the lid-driven cavity is mainly due to the small gain obtained in the solver phase. The total gain for the starting jet is mainly due to the halving of the time spent in the assembly phase. Furthermore, from the Tables B.1 and B.2, it can be noticed that the algebra solver phase percentage increases by increasing the number of cores used. This could be attributed to the increased weight of the communication as the number of cores increases. In particular, this increase might be primarily ascribed to the global MPI calls contained in the solver phase (i.e. `MPIAllReduce`). As expected, in mixed precision an increase of the time spent in linear algebra causes the total gain for both applications to decrease.

## B.4 Parallel computations and precision reduction

### B.4.1 A theoretical model for strong scalability

We here discuss a relatively simple theoretical framework that can be used to describe and analyse the scaling behaviour of an application on parallel machines, including the effect of reduced precision and hardware

diagonal-based Incomplete Cholesky for symmetric equations and the Bi-Conjugate Gradient preconditioned by an incomplete LU factorization for asymmetric equations.

| **Single precision vs Double precision** | | | | | | | |
|---|---|---|---|---|---|---|---|
| Case | nCells/nCores | nCores | Assembly Phase | Solver Phase | Assembly Gain | Solver Gain | Total Gain |
| S | 41.7K | 24 | 4.94% | 93.54% | 1.88 | 1.26 | 1.29 |
| M | 41.7K | 192 | 3.32% | 95.67% | 2.05 | 1.66 | 1.67 |
| XL | 41.7K | 1536 | 1.76% | 97.62% | 2.02 | 1.63 | 1.63 |
| M | 166.7K | 48 | 2.49% | 96.83% | 2.00 | 1.86 | 1.87 |
| XL | 166.7K | 384 | 1.44% | 98.10% | 2.04 | 1.87 | 1.87 |
| **Mixed precision vs Double precision** | | | | | | | |
| Case | nCells/nCores | nCores | Assembly Phase | Solver Phase | Assembly Gain | Solver Gain | Total Gain |
| S | 41.7K | 24 | 4.94% | 93.54% | 1.85 | 1.05 | 1.08 |
| M | 41.7K | 192 | 3.32% | 95.67% | 2.17 | 1.15 | 1.17 |
| XL | 41.7K | 1536 | 1.76% | 97.62% | 1.77 | 1.28 | 1.29 |
| M | 166.7K | 48 | 2.49% | 96.83% | 1.97 | 1.13 | 1.14 |
| XL | 166.7K | 384 | 1.44% | 98.10% | 1.93 | 1.20 | 1.21 |

Table B.1: Lid-driven cavity: performance gain in weak scaling tests using Single and Mixed precision vs Double precision, with a mesh size of $10^6$ cells (S), $8x10^6$ cells (M) and $64x10^6$ cells (XL). Figure taken from Brogi et al. (2024).

specifics (e.g. memory bandwidth or processor). The main outcome here is a model for the strong scalability, that is, the time gain (or the speedup) obtained by increasing the number of processors for a fixed problem size.

Let's start considering a generic numerical problem that is solved using a variable number of processors $P$ (MPI processes). On a first approximation, the total time ($T$) required by a single processor ($p$) to solve its own sub-problem is a function of: the time to transfer the data from the RAM memory of a process to another (intra-node and inter-node), the time to transfer the data from the RAM memory of a process to the registries, the time to process the data. Assuming that these three events occur in three non-overlapped time phases (e.g. Succi et al. (2019)), the total time is then given by the sum of three terms:

$$T = \frac{F}{\dot{F}} + \frac{B}{\dot{B}} + \frac{C}{\dot{C}} \tag{B.2}$$

where $F$ is the sum of floating point instructions done by the processor in FLOP (both in single and double precision), $\dot{F}$ the processor speed in

| Mixed precision vs Double precision | | | | | | | |
|---|---|---|---|---|---|---|---|
| Case | nCells/nCores | nCores | Assembly Phase | Solver Phase | Assembly Gain | Solver Gain | Total Gain |
| S | 42.7K | 48 | 53.05% | 43.25% | 2.14 | 1.30 | 1.66 |
| M | 42.7K | 384 | 48.69% | 47,60% | 2.10 | 1.26 | 1.58 |
| XL | 42.7K | 3072 | 34.40% | 60.48% | 1.86 | 1.15 | 1.34 |
| M | 170.7K | 96 | 48.51% | 47,99% | 1.90 | 1.09 | 1.40 |
| XL | 170.7K | 768 | 43.45% | 52.80% | 1.94 | 1.16 | 1.43 |

Table B.2: Starting jet: performance gain in weak scaling tests using Mixed precision vs Double precision, with a mesh size of 2048000 cells (S), 16384000 cells (M), and 131072000 cells (XL). Figure taken from Brogi et al. (2024).

FLOP/s, $B$ the amount of data, in Bytes, to be transferred from the RAM to the registries, $\dot{B}$ the memory bandwidth in Byte/s, $C$ the amount of data, in Byte, to be transferred from the RAM memory of a process to another, and $\dot{C}$ the network bandwidth, in Byte/s. Now, in order to understand the strong scaling behaviour of an application we need to understand how each term in eq. B.2 scales with the number of processors.

The first term ($F/\dot{F}$) represents the time required for pure calculations (no communication). Increasing the total number of cores simply reduces in general the computational work ($F$) assigned to the single processor. However, determining its exact behaviour is not an easy task. The actual load balancing and the ratio between the number of internal and boundary cells is a function of the algorithm used for domain decomposition. Moreover, the number of iterations for the preconditioned linear solver to converge can increase when switching from a serial to a parallel implementation. Therefore here we simply consider that a perfectly robust solver is used (i.e. the number of iterations does not change from the serial to the parallel case), and the number of internal cells is much higher than boundary cells and is the same among the processors (perfect load balancing). In this case, $F$ can be modelled simply as inversely proportional to the total number of MPI processors ($P$):

$$F = \frac{k_F}{P} \tag{B.3}$$

where $k_F$ is a constant expressing the total number of FLOP, in single and double precision, required to solve the entire numerical problem. By definition, the processor speed ($\dot{F}$) is independent of the number of processors

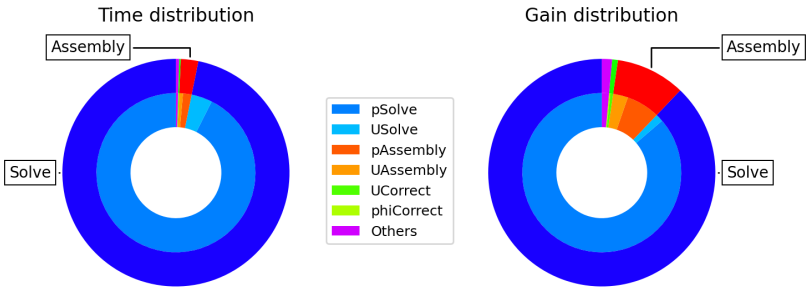


(a) *Lid-driven cavity - Dimension M - 48 Cores.*

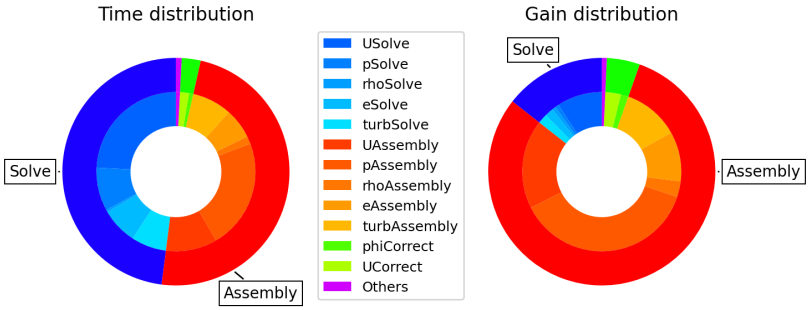


(b) *Starting jet - Dimension M - 96 Cores.*

Figure B.6: CPU-time distribution and performance gain using Mixed precision in the case M of the lid-driven cavity and the compressible starting jet. Figure taken from Brogi et al. (2024).

and is expressed as the product of the average CPU frequency ($f_{CPU}$ in Hz) and the Floating Point Instructions retired Per Cycle ($k_{IPC}$)

$$\dot{F} = k_{IPC} f_{CPU} = k_{\dot{F}} \tag{B.4}$$

where $k_{IPC}$ and $f_{CPU}$, hence also $k_{\dot{F}}$, are assumed to be constant.

For the same reasoning described for $F$, on a first approximation also $B$ can be modelled as inversely proportional to the number of processors:

$$B = \frac{k_B}{P} \tag{B.5}$$

where the constant $k_B$ represents the total amount of data for communications with memory for all processors. Regarding the memory bandwidth ($\dot{B}$), we need instead to distinguish the intra-node from the inter-node case.

Within a computing node, the RAM memory channels are shared among the cores and memory bandwidth contention cannot be avoided. In such a case, the memory bandwidth increases with the number of cores until saturation (Appendix Figure BA1a). The behaviour is almost linear for a few cores and then starts to bend towards the asymptotic value. The memory bandwidth per core slowly decreases until saturation and then drops (Appendix Figure BA1b). We modelled this behaviour with an expression for the inverse of the memory bandwidth equivalent to a first-order Taylor polynomial function of the number of processors (eq. B.6).

When considering multi-node simulations, the RAM channels are still shared inside the node but not among the nodes. Therefore, in an inter-node strong scaling, we can assume that the memory bandwidth for each processor is constant and equal to the value for the single node (considering the full node as a reference and multiples of a single node to measure the speedup). However, the presence of cache levels (L1, L2 and L3) increases the value of $\dot{B}$ as the number of processors grows, due to an increase in the cache efficiency due to an increase in the total cache size available in the system (John and Damodaran, 2009). The bigger the number of processors, the smaller the size of the data representing our discrete problem, until it fits into the cache. In this limit case, we get the maximum memory bandwidth of the system. We modelled this performance augmentation as a linear function (Eq. B.7). As a result, for the intra-node and inter-node scaling test we have two different equations expressing the memory bandwidth available for each processor:

$$\frac{1}{\dot{B}_{intra}} = \frac{1}{k_{\dot{B}}(P)} = k_1 + k_2(P-1) \tag{B.6}$$

$$\dot{B}_{inter} = k_{\dot{B}}(P) = k_3(1 + k_4(\frac{P}{n} - 1)) \tag{B.7}$$

where $n$ is the number of cores in a node, $k_{\dot{B}}$ is the memory bandwidth and $k_1$, $k_2$, $k_3$ and $k_4$ are model constants. When $P = 1$ in the intra-node case and $P = n$ in the inter-node case, $k_1$ and $k_3$ coincides with the memory bandwidth of the serial case.

Finally, we need to consider the third term of Eq. B.2, the time spent by the single process in sending and receiving data from other processes. As it is common in parallel CFD applications, OpenFOAM make use of MPI (e.g. Open MPI) for both point-to-point and collective communications. Asynchronous Point-to-Point communications are required for instance in the assembly phase or in a matrix-vector multiplication, while collective communications are used in `MPIAllreduce` functions required by linear al-

gebra solvers. The total time spent in MPI communications depends on the number of cores in a strong scaling experiment. Typically, as the number of cores is sufficiently small, the wall-time fraction spent in the MPI library ($\frac{C}{\dot{C}}$ in Eq. B.2) is very small, almost negligible. Instead, MPI overhead starts to be significant for a large number of cores or, to be more precise and general, when the number of cells per core is small. For instance, in our simulations with OpenFOAM the MPI communications take less than the 5% of the total time if the number of cells per core is above around 150k. However, when the number of cells per core approaches around 20k, MPI communications become more and more important and may take up to 50% of the total time for many cores (Figure BA3). However, even if the relative weight of MPI increases as the number of core increases, the absolute total time spent in MPI decreases. Indeed, in our test when the number of cells per core is sufficiently small the time spent in MPI communications becomes important and approaches an asymptotic value (Figure BA3). As a result, we model the third term of Eq. B.2 as:

$$\frac{C}{\dot{C}} \asymp k_C \tag{B.8}$$

where $k_C$ is a constant. Let us enforce that this approximation cannot be used in a strong scaling for runs with a large number of cells per core. However, in this case the time spent in MPI communications is not significant with respect to the total time and as a first approximation can be simply neglected. A more accurate approach would require to model the exact behaviour of the dominant type of MPI calls (e.g. `MPIAllReduce`) as a function of the number of cores/cells per core as described in Appendix B.A. Here for practical reasons we simply express $\frac{C}{\dot{C}} \approx k_C w(P)$ where $w(P)$ is a weight function that varies from zero to one passing from runs with large to small number of cells per core.

Now, using eq. (B.3), (B.4) and (B.5) one can write the equation for the time required to solve the problem by a single processor as a function of the number of processors ($P$):

$$T_{intra}(P) = \frac{k_F}{P k_{\dot{F}}} + \frac{k_B}{P k_{\dot{B}}(P)} + w(P) k_C \tag{B.9}$$

where $k_{\dot{B}}(P) = 1/(k_1 + k_2(P-1))$ for the intra-node and $k_{\dot{B}}(P) = k_3(1 + k_4(nP - n))$ for the internode. It is then straightforward, obtain the formula for the speedup, ($S(P) = T(1)/T(P)$) that is commonly measured in strong

scaling experiments for both the intra and inter-node test cases:

$$S(P) = \frac{k_F/k_{\dot{F}} + k_B/k_{\dot{B}}(1) + w(1)k_C}{k_F/(Pk_{\dot{F}}(P)) + k_B/(Pk_{\dot{B}}(P)) + w(P)k_C} \tag{B.10}$$

The above equation is relatively general and, given that all the parameters are known, could be used to predict the scaling behaviour of an application, including the effect due to a change in floating point precision and hardware specifics (e.g. memory bandwidth). In fact, a precision reduction would change the value of most of the parameters appearing in the equation. However, a precise determination of all these constants is beyond the scope of the present work. Instead, in the next sections we will focus on showing how this model can be used to provide qualitative description of the speedup observed in strong scaling experiments of real CFD applications, such as those implemented in OpenFOAM.

### B.4.2 Intra-node scalability

We now demonstrate and analyse the beneficial effects of using reduced precision on the scaling properties at the intra-node level. A scaling experiment with the starting jet test case compiled in double and mixed precision is considered. The size of the test case is relatively large to keep the number of cells per core above the threshold of 40k. In this way, memory communications are expected to play a significant role whereas the contribution from MPI communications should be negligible. The observed speedup deviates quite quickly from the ideal behaviour for both double and mixed precision (Figure B.7), clearly indicating an inefficient use of the computational resources. However, reduced precision helps to improve both the scalability and wall time of the application. In particular, the mixed precision scales better than double precision and provides a computational gain (up to 1.6×) that increases across the node.

To understand the reasons behind this behaviour, we now reconsider the scaling model described in the previous paragraph (eq. B.10). Neglecting the effect of MPI communications ($w(P) = 0$) and applying the approximation for $k_{\dot{B}}$ described in Eq. B.6, after some algebraic manipulation we obtain a simplified form of eq. B.10:

$$S(P) = \frac{1}{\frac{1}{P}(1 + a(P-1))} \tag{B.11}$$

where the constant $a$ is defined as

$$a = (k_B k_2)/(k_F/k_{\dot{F}}(1) + k_B/k_{\dot{B}}(1)) \tag{B.12}$$

Eq. (B.11) is plotted in Figure B.7 for different values of $a$. It is clear that the lower the value of $a$ the closer the curve is to the ideal speed-up. The overall effect of decreasing the parameter $a$ therefore is similar to the effect of the precision reduction observed in our scaling tests (Figure B.7). In other words, one may argue that mixed precision scales better than double precision at the intra-node level thanks to a lower value of the parameter $a$. The decreased value of this parameter with reduced precision can be easily justified by the reduction of the amount of data to be transferred during matrix assembly (lower value of $k_B$) and the increase of the transfer rate of data due to a reduction of memory stalls (lower value of $k_2$), as also confirmed by the level 1 of the Top-Down Microarchitecture Analysis Method (TMAM) analysis (Appendix B.A, Figure BA2). We instead assumed that the other parameters of Eq. B.12 are not influenced by the type of precision: the number of instructions is the same, as a consequence of the same algorithm; the memory bandwidth and the CPU frequency are identical due to the same hardware; IPC is also the same since we assume that floating-point operations are implemented natively in the hardware for both single and double precisions (and vectorization is not present). Thus, the decrease of scalability observed at the intra-node level seems related to memory communication and hence it can be improved by using reduced precision.

### B.4.3 Inter-node scalability analysis

Similarly to the previous section, we discuss the effect of precision reduction on the inter-node scalability by considering the starting jet case compiled in double and mixed precision (OpenFOAM version v2006). In the present scaling analysis, we consider the execution time of the application without pre-processing (e.g. mesh generation) and initialisation time delay at the beginning of the simulation. [2]

The results are reported in (Figure B.8). Both full and reduced precision runs display very similar speedup, with a clear superlinear behaviour up to $10^4$ cells/core (Figure B.8a,b). Below this threshold, MPI communications start to be more important, the scalability quickly deteriorates and double precision scales better than mixed precision. Nonetheless, it is important to notice that mixed precision is always faster than double precision. The computational gain in fact steadily increases from 1.4× up to 1.6× at $20^4$

[2]The initialisation time is usually very small compared with the total execution time, especially for long production runs. However, for our setup, the execution time is also quite small and therefore it might become comparable with the initialisation time.

cells/core and then rapidly decreases to 1.2×, in the MPI-bounded region (Figure B.8c). Hence, as expected, mixed precision does not directly improve the parallel efficiency of the application as in the intra-node case, but it is still computationally convenient up to the number of cells/core where the application present a good parallel efficiency.

For the inter-node case, the MPI overhead cannot be neglected and has to be considered. For simplicity here, in the third term of Eq. B.9, we set $w(P) = 1$ for multiple node runs and $w(1) = 0$ for the reference case (single node). As a result, Eq. B.10 can be written as

$$S(P) = \frac{k_F/k_{\dot{F}}(1) + k_B/k_{\dot{B}}(1)}{k_F/(Pk_{\dot{F}}(P)) + k_B/(Pk_{\dot{B}}(P)) + k_C}\,. \tag{B.13}$$

Then, assuming $k_{\dot{F}}$ to be constant and using equation (B.7), after some algebraic manipulation we get

$$S(P) = \frac{1}{\frac{b_1}{P} + \frac{b_2}{P(1+k_4(\frac{P}{n}-1))} + b_3} \tag{B.14}$$

where the following definitions hold

$$b_1 = \frac{1}{1 + \frac{k_B k_{\dot{F}}}{k_{\dot{B}}(1) k_F}}\,, \tag{B.15}$$

$$b_2 = \frac{1}{1 + \frac{k_F k_{\dot{B}}(1)}{k_{\dot{F}} k_B}}\,, \tag{B.16}$$

$$b_3 = \frac{k_C}{k_F/k_{\dot{F}(1)} + k_B/k_{\dot{B}}(1)}\,. \tag{B.17}$$

Eq. (B.14) is plotted in Figure B.8d. A good agreement between the model and the curve plotted in Figure B.8b) has been found for the Marconi cluster using the parameters $b_1 = 0.3$, $b_2 = 0.5$, $k_4 = 0.003$, $b_3 = 0.00032$ for the mixed precision and $b_1 = 0.22$, $b_2 = 0.85$, $k_4 = 0.002$, $b_3 = 0.00025$ for the double precision. For the same reasons discussed for the intra-node case, the constant $b_3$ is higher in mixed precision with respect to double precision. Regarding the variation of the parameters $b_1$ and $b_2$, it depends on the ratio $\frac{k_B k_{\dot{F}}}{k_{\dot{B}} k_F}$. If the ratio $\frac{k_B}{k_{\dot{B}}}$ decreases more than $\frac{k_F}{k_{\dot{F}}}$, the variation of $b_2$ is negative and of $b_1$ is positive, and viceversa. Since we can reasonably assume that the variation of $\frac{k_F}{k_{\dot{F}}}$ is less pronounced than $\frac{k_B}{k_{\dot{B}}}$ (in the previous paragraph we assumed no variation for the term $\frac{k_F}{k_{\dot{F}}}$), $b_1$ and $b_2$ are higher and lower in

the mixed precision case, respectively. Regarding the parameter $k_4$, we can expect a higher value of this parameter in mixed precision due to a stronger cache effect when working with floats.

In conclusion, the two phenomena that influence the scaling plot are super-linearity and MPI communication. The super-linearity is due to the presence of levels of cache that, as the number of nodes grows, increasingly reduces the memory bandwidth bottleneck and hence provides an additional speedup. The super-linearity is slightly more pronounced in mixed precision at a low number of cores. When the MPI communication starts to play a significant role, the mixed precision scales worst. The reason is that the MPI time is not affected by the mixed precision since most MPI calls are from the linear algebra solvers which is double precision. Moreover, since the MPI time is related to synchronization lags instead of the amount of data to be exchanged by processors, the same conclusion may be valid also if single precision is used everywhere in the code.

## B.5 The role of mixed precision in a hybrid CPU-GPU implementation

In the last decade, a number of GPU implementations of OpenFOAM have been attempted by individual research groups with different strategies and different results in terms of computational performance (e.g. Malecha et al. (2011); Alonazi et al. (2015); Krasnopolsky and Medvedev (2016)). However, none of these attempts have been included yet in the official OpenFOAM distributions.

More recently, Bná et al. (2020) and Zampini et al. (2020) have developed an interface library named PETSc4FOAM that has been included in the OpenFOAM official release as a module. PETSc4FOAM extends the list of available linear solvers with the ones embedded in PETSc and other packages(e.g. HYPRE and ML), with and without GPU support. It basically works with any OpenFOAM solver and allows the user to take advantage of GPU hardware without requiring any change to the source code. Certainly, only the solution of the linear system can be offloaded to the GPU, the assembly of the matrix is still performed on CPU using the original OpenFOAM routines. Therefore this hybrid CPU-GPU strategy provide a speedup that primarily depends on the fraction of time spent in linear algebra by a specific application. For instance, roughly 90% of the computational work ("solve" in figure B.6a) can be accelerated on GPUs for the Lid-driven cavity solved with `icoFoam`. This fraction reduces to 50% (fig-

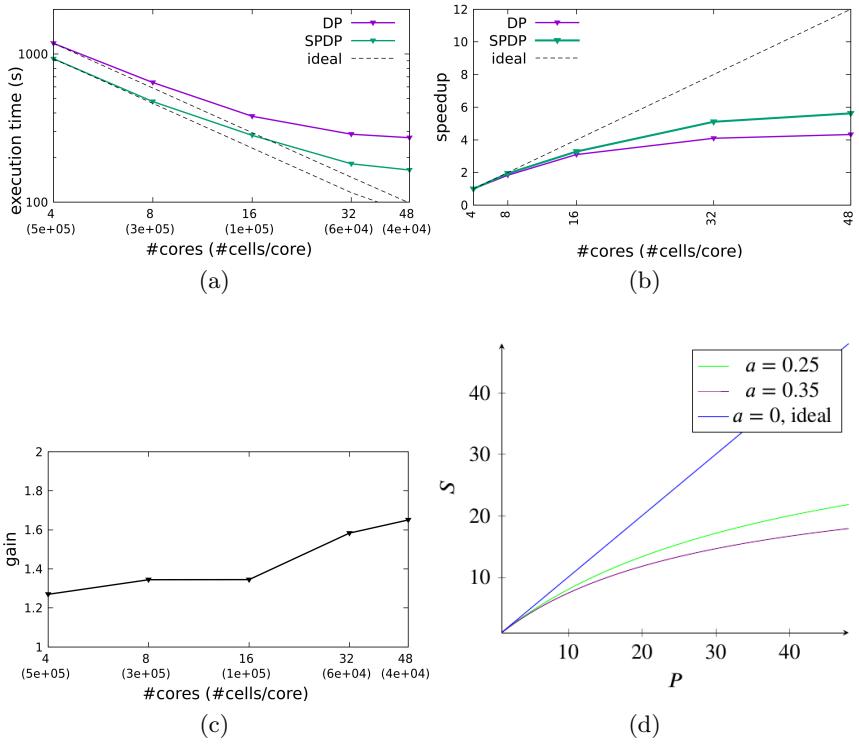


Figure B.7: Intra-node strong scaling for the starting jet using a mesh size of $\approx 2 \times 10^6$ cells performed on Marconi machine (a,b,c). The speedup obtained with the theoretical model (d), is also reported for a qualitative comparison with the experimental one (b). Figure taken from Brogi et al. (2024).

ure B.6b) when considering the starting jet test case with `rhoPimpleFoam`. Morevoer, one has also to consider the time spent in CPU-GPU communication that may have a significant cost. OpenFOAM applications use a segregated solution strategy, that means that each equation is solved separately and then coupled through iterative procedures. The time spent in periodic transfer of the LDU matrix values to the GPU, every time a linear system has to be solved, may therefore increase dramatically with the number of equations to be solved. Nevertheless, the use of mixed precision may come in to rescue this hybrid CPU-GPU strategy. Indeed, with the mixed precision, the amount of data involved in CPU-GPU communication is halved and matrix assembly on CPU becomes twice as fast. Moreover, if the matrix sparsity pattern does not change from one iteration to the

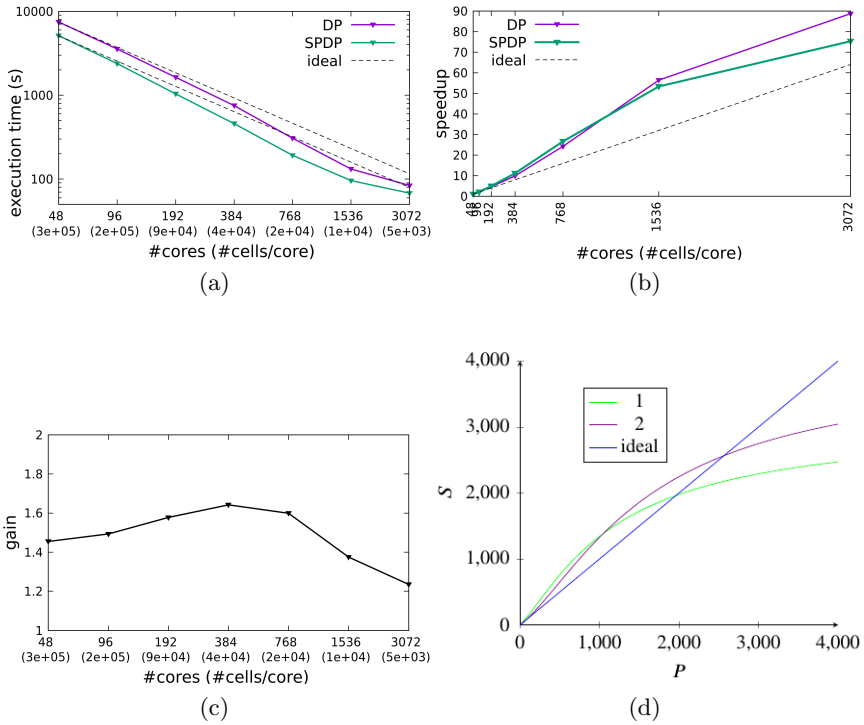


Figure B.8: Inter-node strong scaling for the starting jet using a mesh size of $\approx 16 \times 10^6$ cells performed on Marconi (a,b,c). The speedup obtained with the theoretical model (d), is also reported for a qualitative comparison with the experimental one (b). The inter-node speed-up from the theoretical model is computed with $b_1 = 0.3$, $b_2 = 0.5$, $k_4 = 0.003$, $b_3 = 0.00032$ (line 1, green) and $b_1 = 0.22$, $b_2 = 0.85$, $k_4 = 0.002$, $b_3 = 0.00025$ (line 2, violet). Figure taken from Brogi et al. (2024).

next one, it can be cached on GPU and only the matrix values have to be offloaded (in single precision, in the SPDP case).

If we neglect the time spent for the data transfer and the conversion[3], we can approximately write the total time as the sum of the time spent in the solution of the linear system and the time spent in the assembly of the linear operators. The default in OpenFOAM is to use double precision for

[3]The matrix has to be converted from the native LDU-COO format to CSR each time the solver is called. This operation is performed efficiently on GPU using the radix sort algorithm.

all the computations and a solver based on CPU. In the formula we have

$$T_{tot} = T_{solver\_CPU} + T_{assembly\_DP} \tag{B.18}$$

The fraction of time spent in the assembly is defined as

$$F = \frac{T_{assembly\_DP}}{T_{tot}} \tag{B.19}$$

As we already said, the hybrid CPU-GPU approach has no impact on the assembly loop in terms of computational time but it can be easily combined with mixed precision. On the contrary, mixed precision has no impact on the solution of the linear system but strongly influences the execution time of the matrix assembly part. Therefore, by defining the speedup obtained with the use of GPU linear algebra solvers and mixed precision as:

$$S_{GPU} = \frac{T_{solver\_CPU}}{T_{solver\_GPU}} \qquad S_P = \frac{T_{assembly\_DP}}{T_{assembly\_SPDP}} \tag{B.20}$$

one can apply Amdahl's law and predict the total speedup of mixed precision and GPU linear algebra as:

$$S = \frac{T_{solver\_CPU} + T_{assembly\_DP}}{T_{solver\_GPU} + T_{assembly\_SPDP}} = \frac{1}{\frac{1}{S_{GPU}}(1-F) + \frac{1}{S_P}F} \tag{B.21}$$

In Table B.3 we report the total Execution Time and the total Gain of the starting jet use-case using a different combination of precision and number of equations offloaded to the GPUs. In particular, here we use a recent extension of PETSc4FOAM (Martineau et al., 2021) that provides the possibility to use NVIDIA algebra solvers with GPU support of the AMGx library (Naumov et al., 2015). The best gain is achieved using the mixed precision and the solution of all equations on GPU. The gain can also be estimated using formula (B.21). In section B.3 we showed that a reasonable value for $F$ and $S_P$ is 0.5 and 2, respectively. Using these values, the estimate of the total gain achieved using only the mixed precision is 1.333 (the same value in Table B.21 is 1.31). If the linear equations are solved on GPU, a reasonable value for $S_{GPU}$ taken from our experiments is 3, which gives us an estimate of the total gain equal to 2.4 (compared to 2.43 in Table B.21).

| **Mixed vs Double precision for CPU-GPU OpenFOAM** | | | |
|---|---|---|---|
| Solver | Precision | Execution Time | Gain |
| PBiCG.DILU | DP | 1744 | - |
| PBiCG.DILU | SPDP | 1329 | 1.31× |
| PBiCGStab.JACOBI_L1 Equation (p) on GPU | SPDP | 1237 | 1.41× |
| PBiCGStab.JACOBI_L1 Equation (p\|U) on GPU | SPDP | 931 | 1.87× |
| PBiCGStab.JACOBI_L1 Equation (p\|U\|e) on GPU | SPDP | 833 | 2.09× |
| PBiCGStab.JACOBI_L1 All equations on GPU | SPDP | 733 | 2.38× |
| PBiCGStab.BLOCK_JACOBI All equations on GPU | SPDP | 718 | 2.43× |

Table B.3: Execution time and gain of the starting jet benchmark using different types of algebra solver and a single node of Marconi100 (CINECA, 2022b)

## B.6 Discussions and conclusions

We have analysed the effect of reduced precision on different test cases considering incompressible, compressible as well as multiphase flow problems. Overall, single precision provides numerical solutions that are in good agreement with double precision or the theoretical ones for test cases where the flow is laminar (the lid driven cavity and the shock tube benchmark). Moreover, the low order of accuracy of the tested OpenFOAM solvers seems not to be affected significantly by the precision reduction. Single precision therefore may be expected to be sufficiently accurate for most laminar fluid problems except for those cases where the initial conditions require double precision or the solution is required with a particular degree of accuracy. When considering turbulent flows, single precision seems not to be an option instead. In this case, the nonlinear terms in the governing equations amplify the numerical noise, and in some cases (e.g. depending on the grid size) compromise the convergence of linear algebra solvers. In particular, `rhoPimpleFoam` and `ASHEE` solvers have not converged to physical solutions when considering the dynamics of decaying isotropic turbulence, starting compressible jet and turbulent multiphase flow of a volcanic plume. However, for these cases, one may rely on the implementation of a mixed precision concept in which linear algebra solvers work in double precision.

In this case, all the aforementioned computations converge to consistent physical solutions. The spectrum of the kinetic energy of decaying isotropic turbulence in mixed precision results to be accurate with respect to double precision (error $\approx 10^{-}7$) for both DNS and LES simulations. As well, in complex volcanic plume simulations, the average properties of flow are well recovered with mixed precision.

In general, the computational gain one may obtain in reduced precision varies significantly depending on the characteristics of the CFD application and the computational load per core of the test case. The latter, in particular, is directly related to how much the application is bounded by memory or MPI related communications. Test with the lid-driven cavity in single precision shows that a speedup near to the expected $2\times$ is observed only for the test cases with a larger computational load (166k cells/core). Smaller test cases (40k cells/core) present much smaller gains (1.1-3$\times$), due to the smaller speedup of the linear algebra part of the fluid solver. Changing the application may also affect the computational gain in reduced precision, since the fraction of time spent on different parts of the fluid solver may change significantly. For instance, with respect to the lid-driven cavity where the linear algebra takes more than $> 90\%$ of the total time, the starting jet requires only half of the total time. This aspect becomes even more important when considering the computational gain one may obtain with OpenFOAM in mixed precision, for which only the matrix assembly is done in single precision and linear algebra in double precision. The lid-driven cavity solved with `icoFoam` presents indeed in general a much smaller maximum gain ($1.3\times$) than the starting jet with `rhoPimpleFoam` ($1.7\times$) or volcanic plume simulations with ASHEE. Despite all this variability, in reduced precision (single or mixed) the matrix assembly is observed to be significantly faster for all test cases (1.7-2.2$\times$). As well, in mixed precision linear algebra is also a bit faster (1.1-1.3$\times$).

Reduced precision has also an impact on scalability. This aspect has been studied here interpreting the results of the scaling tests with the aid of an ad hoc developed theoretical model. Despite the strong assumptions, the model qualitatively reproduces the observed scaling behaviours when passing from full to reduced precision and allows us to understand and generalise the test outcomes. At the intra-node level, the use of reduced precision improves the scalability, because the latter is affected by memory communications, as also confirmed by the modelling results and TMAM analysis. This aspect seems to be relevant for OpenFOAM (v1912) which is characterised by a low intra-node scalability performance. Moreover, the computational gain of reduced precision increases with the number of cores since the mem-

ory bandwidth per core decreases across the node. At the inter-node level, the scalability is more complex since both memory and MPI communications need to be considered. Supported by our scalability model results, we have shown that memory communications are mainly responsible for the superlinear behaviour observed for both double and mixed precision up to $\approx 10^4$ cells/core. In this memory bound region, the application is indeed scaling better than in the ideal case since, as the number of nodes grows, the total cache available in the system increases, thus reducing the memory bandwidth bottleneck. The overall effect is that the application receives an additional performance boost and hence an additional contribution to the speedup. In the memory bound region of the speedup plot, mixed and double precision present similar scalability, with mixed precision performing slightly better. It is important also to note that the degree of super-linearity in a speedup plot is related to how much the reference case (in our case the one run on a single node) is bounded by memory bandwidth. Indeed, when the reference case is not strongly affected by the bandwidth bottleneck (in our case, on multiple nodes) the super-linear behaviour is not observed at all. When MPI communications start to play a role (i.e., when the number of cells/core becomes too small), the parallel efficiency decreases quite rapidly as more computational nodes are used and the full precision even scales better than reduced precision. Nevertheless, the computational gain in reduced precision with respect to the full precision is significant, up to the number of cells/core for which the application presents good parallel scalability. Although the conclusions regarding the scalability are based on the comparison between double and mixed precision, we believe they can apply also for the single precision case.

Finally, reduced precision computation is also desirable when working with GPUs, given that efficient data communication is needed to properly exploit the potential of such hardware. In the near future, all computationally intensive applications will be required to use GPUs, since they are becoming an increasingly common and fundamental part of modern heterogenous cluster architectures. In this work, we have demonstrated the power of using mixed precision for a hybrid CPU-GPU OpenFOAM implementation, which, at the moment, is the only option available to the end user (from the up-to-date official OpenFOAM repository). In the hybrid CPU-GPU approach, only the linear algebra part is offloaded on the GPU. Therefore, the total speedup achievable is primarily a function of the fraction of time spent by the application on the linear solver. The latter is application dependent and, in our tests, it may vary from 90% for the lid-driven cavity to 50% with the compressible starting jet. Neglecting CPU-GPU

communication cost and applying Amdahl's Law, it is easy to predict the total speedup for an application. When considering the starting jet (i.e., the worst-case scenario in terms of the time spent in the linear algebra solvers), the combination of mixed precision with the hybrid CPU-GPU implementation may theoretically provide up to 2.4× speedup (w.r.t double precision on pure CPU architecture). This value in fact matches the one measured in our single node tests. Although preliminary, this result may represent a first indication for the end user who wants to speed up CFD simulations with hybrid CPU-GPU and mixed precision implementation. Multi-node GPU scaling tests are left for future work. As well as more work remains to be done to test the use of mixed precision linear algebra solvers with GPUs or tensor cores that can even work in half precision (Haidar et al., 2018). Interestingly, these solvers may further speed up the resolution of linear algebra without compromising the convergence or accuracy of computed solutions. Finally, in this study, we did not consider IO and power consumption, two important aspects that we believe deserve dedicated works. Let us also recall that all the fluid solvers used in this work use a segregated solution strategy (explicit equation coupling), which is the one traditionally adopted in OpenFOAM. Only, more recently, a few solvers with implicit coupling have been developed (Oliani et al., 2023; Ferreira et al., 2019). Depending on the flow problem type, the coupling strategy (explicit vs. implicit) may play a role in determining the accuracy, stability, and computational performances of a fluid solver (Oliani et al., 2023), and therefore may also change the impact of a precision reduction. However, the evaluation of this aspect is left for future investigations.

# Appendices to the article

## Appendix B.A: Top-Down Microarchitecture Analysis Method (TMAM) of an OpenFOAM application

We performed Top-Down Microarchitecture Analysis Method (TMAM) of the lid-driven cavity benchmark varying the number of cores (aka strong scaling). According to the TMAM analysis (Supalov et al., 2014), a slot in a CPU pipeline can be found in a binary state, stalled or not. Our analysis has found that Retiring and Back End bound are the two most frequent states in the first level of the TMAM. Bad speculation and Front End Bound can be neglected. At the second level, Memory Bound is the dominant state and Core Bound can be neglected. Figure BA2 shows the slot fraction of Retiring and Memory Bound for the M-version of the lid-driven cavity run in double

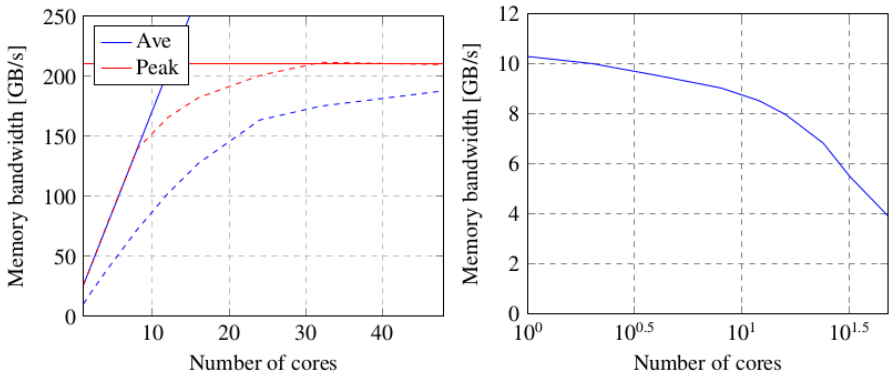


(a) *Average and Peak Memory bandwidth of the node* (b) *Memory bandwidth per core*

Figure BA1: Average and Peak Memory bandwidth registered in the MARCONI cluster using the 3D Lid-driven cavity benchmark (case M). Figure taken from Brogi et al. (2024).

and mixed precision. Both intra-node and inter-node tests have shown that the slot fraction of Retiring is shifted higher in the mixed precision than the double precision. As a consequence, the complementary slot fraction of Memory Bound is shifted lower. In other words, the mixed precision increases the efficiency of the simulation but does not influence the trend with the variation of the number of cores. This trend is characterized by an increasing of the slot fraction of the memory stalls in the intra-node case due to the memory bandwidth contention. In the inter-node case, due to the increasing of the RAM and cache size of the system and the decreasing of the problem size per node, the efficiency increases until saturation, see Figure BA2.

## Appendix B.B: Modelling MPI communication in strong scaling experiment

Our profiler analysis has shown that in double precision the most expensive and dominant MPI function is `MPI_Allreduce` (see Figure BA3). The same profiling analysis repeated with the code compiled in mixed precision provides evidence that `MPI_Recv` is the most used. However, we think that this result is only due to the way the mixed precision code is implemented.

In (Hoefler et al., 2010) the authors have shown that the behaviour of `MPI_All- reduce` is asymptotically logarithmic. However, if the number of cores is relatively low ($P < P*$, where $P*$ is in the order of thousands), the time is constant. This behaviour has not been registered by our tests since

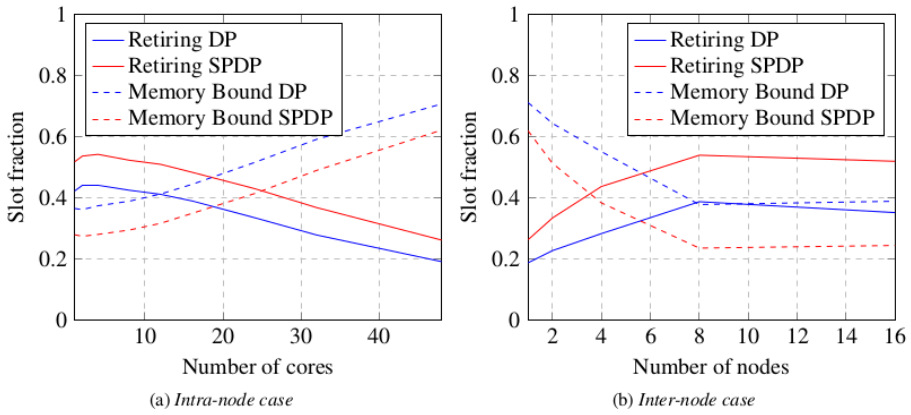


(a) *Intra-node case* (b) *Inter-node case*

Figure BA2: Retiring and Memory Bound slot fraction in the TMAM analysis of the 3D lid-driven cavity benchmark (case M) using double and mixed precision. Figure taken from Brogi et al. (2024).

they include the slack time due to load unbalance; this term is not negligible, as confirmed by our tests, but decreases of importance as the number of cells per core decreases (see Figure BA3).

## Appendix B.C: Convergence analysis and order of accuracy

Here, we report the order of accuracy (table B.4), that is the convergence of the error with respect to the mesh size, for three different test cases: the lid-driven cavity (figure BA4(a)), the shock tube (figure BA4(b)) and isotropic turbulence (figure BA5). The error is computed as an L2-norm:

$$E_{L2} = \sqrt{\frac{\sum_i^{Ncells}(V_i - V_i^{ref})^2}{\sum_i^{Ncells}(V_i^{ref})^2}} \tag{B.22}$$

where $V_i$ is a generic fluid variable (density, velocity, pressure or temperature) at ith cell. As a reference solution ($V^{ref}$), we used the theoretical solution for the shock tube, and the solution with larger mesh size for the lid-driven cavity ($8^6$ cells) and isotropic turbulence ($256^3$ cells).

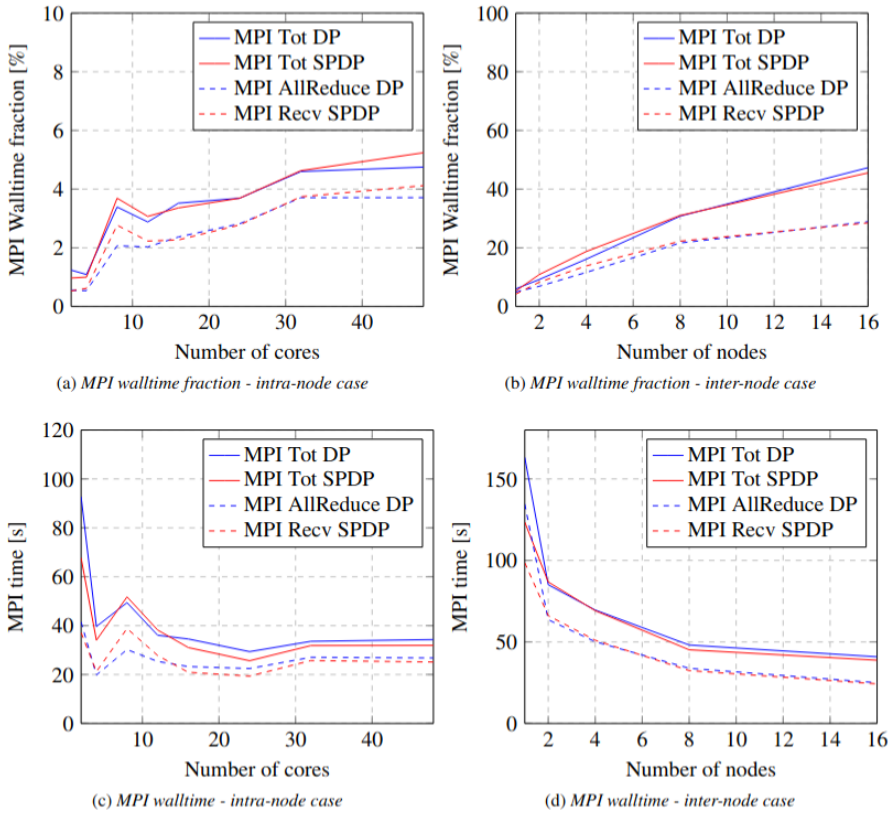


(a) *MPI walltime fraction - intra-node case*
(b) *MPI walltime fraction - inter-node case*
(c) *MPI walltime - intra-node case*
(d) *MPI walltime - inter-node case*

Figure BA3: MPI walltime fraction and absolute walltime in the strong scaling test (intra-node and inter-node) of the 3D lid-driven cavity benchmark (case M) using double and mixed precision. Figure taken from Brogi et al. (2024).

## Appendix B.D: Stability of computed solution and maximum Courant number

Here, we report the test for the maximum Courant number with the shock tube benchmark in single and double precision for two different grids (figure BA6 (a) and (b)). In particular, here we tested the solver stability by performing a finite set of simulations with increasing the maximum Courant number but keeping the time step in each simulation fixed (using PIMPLE). In this way, our test results are more general and not affected by the particular way the time step is adapted during the simulation, to keep the CFL number below a predefined threshold (which in turn depends on the time step used to start the simulation and the algorithm used to keep the CFL

| Cavity | Ux | Uy | Uz | p |
|---|---|---|---|---|
| DP | 0.9639 | 0.95444 | 1.1649 | 0.4507 |
| SP | 0.96393 | 0.95439 | 1.1648 | 0.45057 |

| Shock tube | U | p | T |
|---|---|---|---|
| DP | 0.43603 | 0.57843 | 0.37251 |
| SP | 0.43533 | 0.57767 | 0.37228 |

| Iso. Turbulence | kinetic energy spectrum |
|---|---|
| DP | 0.51334 |
| SP | 0.54116 |

Table B.4: Order of accuracy of the fluid solvers used in this study for the lid-driven cavity (`icoFoam`), shock tube (`rhoPimpleFoam`), isotropic turbulence (`ASHEE`).

number below the defined threshold). Given that the analytical solution for the shock tube has a constant maximum velocity, fixing the time step, in theory, implies that the maximum Courant number is also fixed. However, in the simulations, the maximum Courant number deviates significantly from the expected one due to the numerical error in the computed velocity in a similar fashion for both single and double precision. In particular at the very beginning of the simulations (few time steps), the maximum Courant is much larger than the theoretical one. This is most probably due to a larger numerical error related to the initial conditions to which the solver has to adapt.

(a) (b)

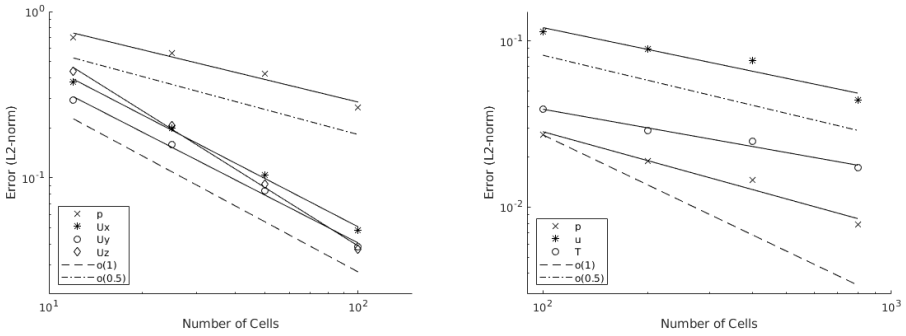


Figure BA4: Convergence test for the lid-driven cavity (Re = 100) (a) and for the shock tube (b) in double precision. In single precision, both figures looks exactly the same since the error values are very similar. Differences in the order of accuracy are reported in Table B.4. Figure taken from Brogi et al. (2024).

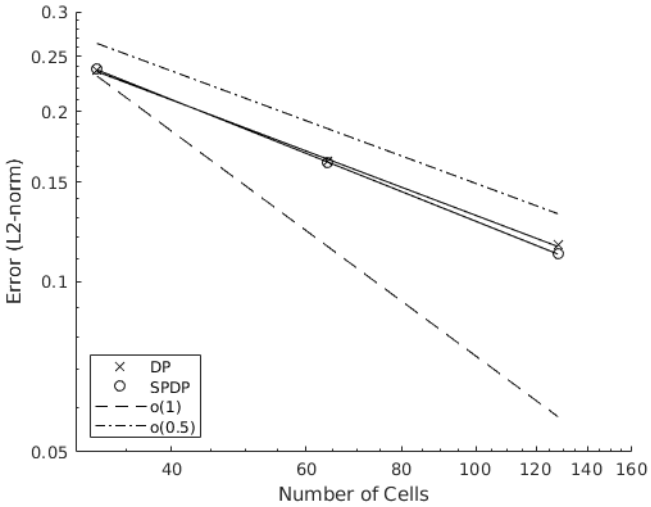


Figure BA5: Convergence test for the isotropic turbulence test in double and single precision. The order of accuracy is reported in Table B.4. Figure taken from Brogi et al. (2024).

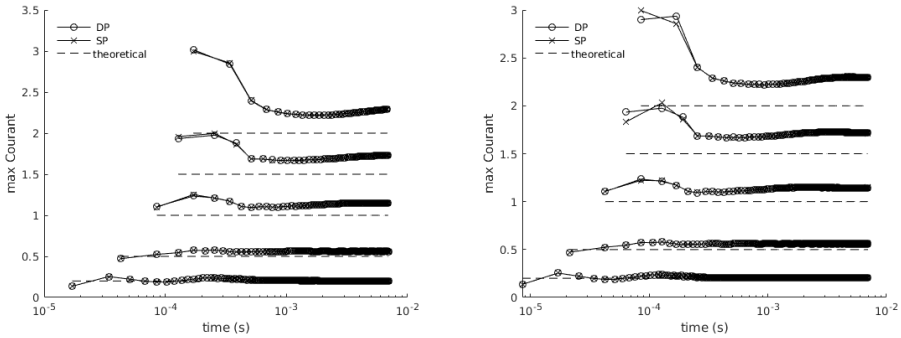


Figure BA6: Evolution of the maximum Courant number in the shock tube simulations with 400 cells, in single and double precision, with five different constant time steps. For each simulation (a) and with 800 cells (b), the theoretical Courant number (dashed line), computed using the theoretical maximum velocity, is also reported. The time axis is set with a logarithmic scale to better visualize the beginning of the simulation (first few time steps), that is when the numerical error is larger, especially for high Courant number simulations. Figure taken from Brogi et al. (2024).

# Acknowledgements

Finally, I would like to dedicate a small space in this thesis to thank all the people who supported me during my PhD journey, both on a professional and personal level.

First of all, I would like to sincerely thank my supervisor, Professor Andrea Cimarelli, for his guidance and teachings both in the field of fluid dynamics research and in the broader field of life with unfailing wisdom and helpfulness. My thanks also go to the people with whom I have had the opportunity to discuss and learn from. In particular to Professor Enrico Stalio, with whom I enjoyed my time in Modena between work-related and non-work-related discussions. Thanks to Professors Carlos da Silva, Sergio Chibbaro and Pedro Costa, for their help during their visiting periods in Modena and with whom I hope to continue and consolidate fruitful collaborations. Thanks to Professors Guido Boffetta and Stefano Musacchio for their valuable feedback, for the scientific sharing and for the enjoyable time spent together during conferences.

I also express my gratitude to Professor Charles Meneveau and Professor J. Christos Vassilicos for dedicating time to review my PhD thesis and for the useful suggestions and comments provided.

I would also like to thank my colleagues from Modena (with whom I have become good friends) for the time spent together, between technical discussions and convivial moments: Roberto, Anna, Lorenzo, Marco, Filippo and Yves. My thanks also go to the friends I met in Madrid: Daniele and Antonio.

Un grazie anche ai miei amici storici (Silvio, Eugenio, Nicholas per nominarne alcuni), che mi hanno supportato nei momenti più difficili. Un grazie infinito ai miei genitori, Rita e Riccardo, che hanno reso possibile che io seguissi la mia strada, e senza i quali niente sarebbe stato possibile, nonostante non abbiano potuto assistere ai traguardi che ho raggiunto durante questi tre anni. Infine un immenso grazie a Sara, che è la mia famiglia.

# Bibliography


A. Abdelfattah, S. Tomov, and J. Dongarra. Towards half-precision computation for complex matrices: A case study for mixed precision solvers on gpus. In *2019 IEEE/ACM 10th Workshop on Latest Advances in Scalable Algorithms for Large-Scale Systems (ScalA)*, pages 17–24. IEEE, 2019.

A. Abdelfattah, H. Anzt, E. G. Boman, E. Carson, T. Cojean, J. Dongarra, A. Fox, M. Gates, N. J. Higham, X. S. Li, J. Loe, P. Luszczek, S. Pranesh, S. Rajamanickam, T. Ribizel, B. F. Smith, K. Swirydowicz, S. Thomas, S. Tomov, Y. M. Tsai, and U. Meier Yang. A survey of numerical linear algebra methods utilizing mixed-precision arithmetic. *The International Journal of High Performance Computing Applications*, 35 (4):344–369, 2021. doi: 10.1177/10943420211003313.

A. Alonazi, D. Keyes, A. Lastovetsky, and V. Rychkov. Design and optimization of openfoam-based cfd applications for hybrid and heterogeneous hpc platforms. *arXiv preprint arXiv:1505.07630*, 2015.

K. Alvelius. Random forcing of three-dimensional homogeneous turbulence. *Physics of Fluids*, 11(7):1880–1889, 1999. doi: 10.1063/1.870050.

A. Apostolidis, J.P. Laval, and J.C. Vassilicos. Turbulent cascade in fully developed turbulent channel flow. *Journal of Fluid Mechanics*, 967:A22, 2023. doi: 10.1017/jfm.2023.487.

G. Axtmann and U. Rist. Scalability of openfoam with large eddy simulations and dns on high-performance systems. In *High Performance Computing in Science and Engineering´ 16*, pages 413–424. Springer, 2016.

M. Baboulin, A. Buttari, J. Dongarra, J. Kurzak, J. Langou, J. Langou, P. Luszczek, and S. Tomov. Accelerating scientific computations with mixed precision algorithms. *Computer Physics Communications*, 180(12): 2526–2533, 2009.

P. Baj, F. Alves Portela, and D.W. Carter. On the simultaneous cascades of energy, helicity, and enstrophy in incompressible homogeneous turbulence. *Journal of Fluid Mechanics*, 952:A20, 2022. doi: 10.1017/jfm.2022.912.

G. K. Batchelor. Small-scale variation of convected quantities like temperature in turbulent fluid part 1. general discussion and the case of small conductivity. *Journal of Fluid Mechanics*, 5(1):113–133, 1959. doi: 10.1017/S002211205900009X.

P. Bechlars and R. D. Sandberg. Variation of enstrophy production and strain rotation relation in a turbulent boundary layer. *Journal of Fluid Mechanics*, 812:321–348, 2017. doi: 10.1017/jfm.2016.794.

M. Bernardini. Reynolds number scaling of inertial particle statistics in turbulent channel flows. *Journal of Fluid Mechanics*, 758:R1, 2014. doi: 10.1017/jfm.2014.561.

M. Bernardini and S. Pirozzoli. A general strategy for the optimization of Runge–Kutta schemes for wave propagation phenomena. *J. Comput. Phys.*, 228(11):4182–4199, 2009.

M. Bernardini, S. Pirozzoli, and P. Orlandi. Velocity statistics in turbulent channel flow up to $Re_\tau = 4000$. *Journal of Fluid Mechanics*, 742:171–191, 2014. doi: 10.1017/jfm.2013.674.

M. Bernardini, D. Modesti, F. Salvadore, and S. Pirozzoli. STREAmS: A high-fidelity accelerated solver for direct numerical simulation of compressible turbulent flows. *Computer Physics Communications*, 263: 107906, 2021. doi: 10.1016/j.cpc.2021.107906.

D. K. Bisset, J. C. R. Hunt, and M. M. Rogers. The turbulent/non-turbulent interface bounding a far wake. *Journal of Fluid Mechanics*, 451:383–410, 2002.

G. A. Blaisdell, N. N. Mansour, and W. C. Reynolds. *Numerical simulation of compressible homogeneous turbulence.* Stanford University, Dept. of Mech. Eng., Thermosciences Div. Rep. TF-50, 1991.

S. Bná, I. Spisso, M. Olesen, and G. Rossi. Petsc4foam: A library to plug-in petsc into the openfoam framework. *PRACE White paper*, 2020.

G. Boffetta and R. E. Ecke. Two-dimensional turbulence. *Annu. Rev. Fluid Mech.*, 44:427–451, 2012.

G Boga, A. Giancola, and A. Cimarelli. Numerical experiments on scalar transport and mixing in turbulent boundary layers. *Journal of Physics: Conference Series*, 2753(1):012003, 2024. doi: 10.1088/1742-6596/2753/1/012003.

G. Borrell and J. Jiménez. Properties of the turbulent/non-turbulent interface in boundary layers. *Journal of Fluid Mechanics*, 801:554–596, 2016.

F. Brogi, S. Bná, G. Boga, G. Amati, T. Esposti Ongaro, and M. Cerminara. On floating point precision in computational fluid dynamics using openfoam. *Future Generation Computer Systems*, 152:1–16, 2024. doi: 10.1016/j.future.2023.10.006.

P. Burattini, R. A. Antonia, and L. Danaila. Scale-by-scale energy budget on the axis of a turbulent round jet. *J. Turb.*, (6):N19, 2005.

M. Carbone and A. D. Bragg. Is vortex stretching the main cause of the turbulent energy cascade? *Journal of Fluid Mechanics*, 883:R2, 2020. doi: 10.1017/jfm.2019.923.

M. Cerminara. *Modeling dispersed gas–particle turbulence in volcanic ash plumes*. Phd thesis, Scuola Normale Superiore, 2016.

M. Cerminara, T. Esposti Ongaro, and L. C. Berselli. Ashee-1.0: a compressible, equilibrium–eulerian model for volcanic ash plumes. *Geoscientific Model Development*, 9(2):697–730, 2016.

M. Cerminara, T. Esposti Ongaro, and A. Neri. Large Eddy Simulation of gas–particle kinematic decoupling and turbulent entrainment in volcanic plumes. *Journal of Volcanology and Geothermal Research*, 326:143–171, oct 2016. doi: 10.1016/j.jvolgeores.2016.06.018.

C. Chan, P. Schlatter, and R. C. Chin. Interscale transport mechanisms in turbulent boundary layers. *J. Fluid Mech.*, 921:A13, 2021.

X. Chen and K. R. Sreenivasan. Reynolds number scaling of the peak turbulence intensity in wall flows. *Journal of Fluid Mechanics*, 908:R3, 2021. doi: 10.1017/jfm.2020.991.

M. Chevalier, P. Schlatter, A. Lundbladh, and D. S. Henningson. *SIMSON: A pseudo-spectral solver for incompressible boundary layer flows*. (Trita-MEK). Available from: http://urn.kb.se/resolve?urn=urn:nbn:se:kth:diva-86771, 2007.

A. Chiarini, M. Mauriello, D. Gatti, and M. Quadrio. Ascending–descending and direct–inverse cascades of reynolds stresses in turbulent couette flow. *J. Fluid Mech.*, 930:A9, 2022.

M. Cho, Y. Hwang, and H. Choi. Scale interactions and spectral energy transfer in turbulent channel flow. *J. Fluid Mech.*, 854:474–504, 2018.

A. Cimarelli and G. Boga. Numerical experiments on turbulent entrainment and mixing of scalars. *Journal of Fluid Mechanics*, 927:A34, 2021. doi: 10.1017/jfm.2021.779.

A. Cimarelli and E. De Angelis. Anisotropic dynamics and sub-grid energy transfer in wall-turbulence. *Phys. Fluids*, 24(1):015102, 2012.

A. Cimarelli and E. De Angelis. The physics of energy transfer toward improved subgrid-scale models. *Phys. Fluids*, 26(5):055103, 2014.

A. Cimarelli, E. De Angelis, and C.M. Casciola. Paths of energy in turbulent channel flows. *J. Fluid Mech.*, 715:436–451, 2013.

A. Cimarelli, G. Cocconi, B. Frohnapfel, and E. De Angelis. Spectral enstrophy budget in a shear-less flow with turbulent/non-turbulent interface. *Phys. Fluids*, 27(12):125106, 2015a.

A. Cimarelli, E. De Angelis, P. Schlatter, G. Brethouwer, A. Talamelli, and C. M. Casciola. Sources and fluxes of scale energy in the overlap layer of wall turbulence. *J. Fluid Mech.*, 771:407–423, 2015b.

A. Cimarelli, E. De Angelis, J. Jiménez, and C.M. Casciola. Cascades and wall-normal fluxes in turbulent channel flows. *J. Fluid Mech.*, 796: 417–436, 2016.

A. Cimarelli, J.-P. Mollicone, M. Van Reeuwijk, and E. De Angelis. Spatially evolving cascades in temporal planar jets. *J. Fluid Mech.*, 910:A19, 2021.

A. Cimarelli, G. Boga, A. Pavan, P. Costa, and E. Stalio. Energy cascade phenomena in temporal boundary layers. *Flow Turb. Comb.*, 112:129–145, 2024a.

A. Cimarelli, G. Boga, A. Pavan, P. Costa, and E. Stalio. Spatially evolving cascades in wall turbulence with and without interface. *Journal of Fluid Mechanics*, 987:A4, 2024b. doi: 10.1017/jfm.2024.359.

CINECA. Marconi machine web page, 2022a. URL `https://wiki.u-gov.it/confluence/pages/viewpage.action?pageId=132481870`.

CINECA. Marconi100 machine web page, 2022b. URL `https://wiki.u-gov.it/confluence/pages/viewpage.action?pageId=336727645#UG3.2:MARCONI100UserGuide-M100specificinformation`.

S. Corrsin and A. L. Kistler. Free-stream boundaries of turbulent flows. *NACA Tech. Rep.*, TN-1244, 1955.

P. Costa. A FFT-based finite-difference solver for massively-parallel direct numerical simulations of turbulent flows. *Comput. & Math. App.*, 76(8): 1853–1862, 2018.

C. B. da Silva and R. R. Taveira. The thickness of the turbulent/nonturbulent interface is equal to the radius of the large vorticity structures near the edge of the shear layer. *Phys. Fluids*, 22:121702, 2010.

C. B. da Silva, J. C. R. Hunt, I. Eames, and J. Westerweel. Interfacial layers between regions of different turbulence intensity. *Annu. Rev. Fluid Mech.*, 46:567–590, 2014.

L. Danaila, F. Anselmet, T. Zhou, and R. A. Antonia. Turbulent energy scale budget equations in a fully developed channel flow. *J. Fluid Mech.*, 430:87–109, 2001.

P. A. Davidson, K. Morishita, and Y. Kaneda. On the generation and flux of enstrophy in isotropic turbulence. *Journal of Turbulence*, 9:N42, 2008. doi: 10.1080/14685240802491345.

B. Di Paolo, J. L. Lara, G. Barajas, and Í. Losada. Waves and structure interaction using multi-domain couplings for navier-stokes solvers in openfoam®. part ii: Validation and application to complex cases. *Coastal Engineering*, 164:103818, 2021.

J. A. Domaradzki, W. Liu, C. Härtel, and L. Kleiser. Energy transfer in numerically simulated wall-bounded turbulent flows. *Phys. Fluids*, 6(4): 1583–1599, 1994.

D. C. Dunn and J. F. Morrison. Analysis of the energy budget in turbulent channel flow using orthogonal wavelets. *Computers & Fluids*, 34(2):199–224, 2005.

G. L. Eyink. Turbulent flow in pipes and channels as cross-stream "inverse cascades" of vorticity. *Physics of Fluids*, 20(12):125101, 2008. doi: 10.1063/1.3013635.

G. G. S. Ferreira, P. L. C. Lage, L. F. L. R. Silva, and H. Jasak. Implementation of an implicit pressure–velocity coupling for the eulerian multi-fluid model. *Computers & Fluids*, 181:188–207, 2019. ISSN 0045-7930. doi: 10.1016/j.compfluid.2019.01.018.

J. H. Ferziger, M. Perić, and R. L. Street. *Computational methods for fluid dynamics*, volume 3. Springer, 2002.

A. Folch, C. Abril, M. Afanasiev, G. Amati, M. Bader, R. M. Badia, H. B. Bayraktar, S. Barsotti, R. Basili, F. Bernardi, et al. The eu center of excellence for exascale in solid earth (cheese): Implementation, results, and roadmap for the second phase. *Future Generation Computer Systems*, 146:47–61, 2023.

E. Garnier, M. Mossi, P. Sagaut, P. Comte, and M. Deville. On the Use of Shock-Capturing Schemes for Large-Eddy Simulation. *J. Comput. Phys.*, 153(2):273–311, 1999. doi: 10.1006/jcph.1999.6268.

D. Gatti, A. Chiarini, A. Cimarelli, and M. Quadrio. Structure function tensor equations in inhomogeneous turbulence. *J. Fluid Mech.*, 898:A5, 2020.

M. Germano. Turbulence: the filtering approach. *Journal of Fluid Mechanics*, 238:325–336, 1992. doi: 10.1017/S0022112092001733.

A. A. Ghira, G. E. Elsinga, and C. B. da Silva. Characteristics of the intense vorticity structures in isotropic turbulence at high reynolds numbers. *Phys. Rev. Fluids*, 7:104605, 2022. doi: 10.1103/PhysRevFluids.7.104605.

R. Gomes-Fernandes, B. Ganapathisubramani, and J. C. Vassilicos. The energy cascade in near-field non-homogeneous non-isotropic turbulence. *J. Fluid Mech.*, 771:676–705, 2015.

C. J. Greenshields and H. G. Weller. *Note on Computational Fluid Dynamics: General Principles*. CFD Direct https://cfd. direct., 2022.

A. Haidar, S. Tomov, J. Dongarra, and N. J. Higham. Harnessing gpu tensor cores for fast fp16 arithmetic to speed up mixed-precision iterative refinement solvers. In *SC18: International Conference for High Performance Computing, Networking, Storage and Analysis*, pages 603–613. IEEE, 2018.

F. Hamba. Turbulent energy density in scale space for inhomogeneous turbulence. *J. Fluid Mech.*, 842:532–553, 2018.

F. Hamba. Inverse energy cascade and vortical structure in the near-wall region of turbulent channel flow. *Phys. Rev. Fluids*, 4(11):114609, 2019.

C. Härtel, L. Kleiser, F. Unger, and R. Friedrich. Subgrid-scale energy transfer in the near-wall region of turbulent flows. *Phys. Fluids*, 6(9): 3130–3143, 1994.

R.J. Hill. Exact second-order structure-function relationship. *J. Fluid Mech.*, 468:317–326, 2002.

T. Hoefler, W. Gropp, R. Thakur, and J. Träff. Toward performance models of mpi implementations for understanding application scaling issues. pages 21–30, 09 2010. doi: 10.1007/978-3-642-15646-5_3.

A. E. Honein and P. Moin. Higher entropy conservation and numerical stability of compressible turbulence simulations. *J. Comput. Phys.*, 201 (2):531–545, dec 2004. doi: 10.1016/j.jcp.2004.06.006.

R. Jahanbakhshi and C. K. Madnia. Entrainment in a compressible turbulent shear layer. *Journal of Fluid Mechanics*, 797:564–603, 2016. doi: 10.1017/jfm.2016.296.

J. Jiménez and A. Pinelli. The autonomous cycle of near-wall turbulence. *J. Fluid Mech.*, 389:335–359, 1999.

B. John and M. Damodaran. *Parallel Three Dimensional Direct Simulation Monte Carlo for Simulating Micro Flows*, volume 67, pages 91–98. 04 2009. doi: 10.1007/978-3-540-92744-0_11.

P. L. Johnson. Energy transfer from large to small scales in turbulence by multiscale nonlinear strain and vorticity interactions. *Phys. Rev. Lett.*, 124:104501, 2020. doi: 10.1103/PhysRevLett.124.104501.

P. L. Johnson. On the role of vorticity stretching and strain self-amplification in the turbulence energy cascade. *Journal of Fluid Mechanics*, 922:A3, 2021. doi: 10.1017/jfm.2021.490.

P. L. Johnson and M. Wilczek. Multiscale velocity gradients in turbulence. *Annual Review of Fluid Mechanics*, 56:463–490, 2024. doi: https://doi.org/10.1146/annurev-fluid-121021-031431.

T. von Kármán and L. Howarth. On the statistical theory of isotropic turbulence. *Proc. Royal Soc. London A.: Math. Phys. Sci.*, 164(917): 192–215, 1938.

A.N. Kolmogorov. Dissipation of energy in the locally isotropic turbulence. *Dokl. Akad. SSSR 32, 301 (1941); reprinted in Proc. R. Soc. Lond. A, 434, 15*, 434:15–17, 1991.

M. Kozul, D. Chung, and J. P. Monty. Direct numerical simulation of the incompressible temporally developing turbulent boundary layer. *J. Fluid Mech.*, 796:437–472, 2016.

M. Kozul, R. J. Hearst, J. P. Monty, B. Ganapathisubramani, and D. Chung. Response of the temporal turbulent boundary layer to decaying free-stream turbulence. *Journal of Fluid Mechanics*, 896:A11, 2020. doi: 10.1017/jfm.2020.320.

B. Krasnopolsky and A. Medvedev. Acceleration of large scale openfoam simulations on distributed systems with multicore cpus and gpus. In *Parallel Computing: On the Road to Exascale*, pages 93–102. IOS Press, 2016.

H. C. Ku, R. S. Hirsh, and T. D. Taylor. A pseudospectral method for solution of the three-dimensional incompressible navier-stokes equations. *Journal of Computational Physics*, 70(2):439–462, 1987.

S. Kumar, C. Meneveau, and G. Eyink. Vorticity cascade and turbulent drag in wall-bounded flows: plane poiseuille flow. *Journal of Fluid Mechanics*, 974:A27, 2023. doi: 10.1017/jfm.2023.609.

F. Laadhari. On the evolution of maximum turbulent kinetic energy production in a channel flow. *Physics of Fluids*, 14(10):L65–L68, 2002. doi: 10.1063/1.1511731.

M. Lee and R. D. Moser. Direct numerical simulation of turbulent channel flow up to $Re_\tau \approx 5200$. *Journal of Fluid Mechanics*, 774:395–415, 2015. doi: 10.1017/jfm.2015.268.

M. Lee and R. D. Moser. Spectral analysis of the budget equation in turbulent channel flows at high reynolds number. *J. Fluid Mech.*, 860:886–938, 2019.

M. Lehmann, M. J. Krause, G. Amati, M. Sega, J. Harting, and S. Gekle. Accuracy and performance of the lattice boltzmann method with 64-bit, 32-bit, and customized 16-bit number formats. *Phys. Rev. E*, 106:015308, 2022. doi: 10.1103/PhysRevE.106.015308.

M. Lesieur, O. Métais, and P. Comte. *Large-Eddy Simulations of Turbulence*, volume 1. Cambridge University Press, 2005.

W. Liao, Y. Peng, and L.-S. Luo. Gas-kinetic schemes for direct numerical simulations of compressible homogeneous turbulence. *Phys. Rev. E*, 80 (4):046702, 2009. doi: 10.1103/PhysRevE.80.046702.

M.J. Lighthill. Introduction: boundary layer theory. In *Laminar Boundary Layers* (ed. L. Rosenhead). Oxford University Press, 1963.

A. Lozano-Durán and J. Jiménez. Time-resolved evolution of coherent structures in turbulent channels: characterization of eddies and cascades. *J. Fluid Mech.*, 759:432–471, 2014.

F.A. Lyman. Vorticity production at a solid boundary. *Appl. Mech. Rev.*, 43(8):157–158, 1990.

Z. Malecha, Ł. Mirosław, T. Tomczak, Z. Koza, M. Matyka, W. Tarnawski, D. Szczerba, et al. Gpu-based simulation of 3d blood flow in abdominal aorta using openfoam. *Archives of Mechanics*, 63(2):137–161, 2011.

N. Marati, C.M. Casciola, and R. Piva. Energy cascade and spatial fluxes in wall turbulence. *J. Fluid Mech.*, 521:191–215, 2004.

M. Martineau, S. Bná, S. Posey, and F. Spiga. OpenFOAM with GPU solver support. In *9th ESI-OpenFOAM conference*, October 2021.

I. Marusic and J. P. Monty. Attached eddy model of wall turbulence. *Annu. Rev. Fluid Mech.*, 51:49–74, 2019.

I. Marusic, B. J. McKeon, P. A. Monkewitz, H. M. Nagib, A. J. Smits, and K. R. Sreenivasan. Wall-bounded turbulent flows at high reynolds numbers: Recent advances and key issues. *Physics of Fluids*, 22(6):065103, 2010. doi: 10.1063/1.3453711.

I. Marusic, W. J. Baars, and N. Hutchins. Scaling of the streamwise turbulence intensity in the context of inner-outer interactions in wall turbulence. *Phys. Rev. Fluids*, 2:100502, 2017. doi: 10.1103/PhysRevFluids.2.100502.

J. Mathew and A. J. Basu. Some characteristics of entrainment at a cylindrical turbulence boundary. *Physics of Fluids*, 14(7):2065–2072, 2002. ISSN 1070-6631. doi: 10.1063/1.1480831.

C. Meneveau. Lagrangian dynamics and models of the velocity gradient tensor in turbulent flows. *Annual Review of Fluid Mechanics*, 43(Volume 43, 2011):219–245, 2011. doi: 10.1146/annurev-fluid-122109-160708.

Y. Mizuno. Spectra of energy transport in turbulent channel flows for moderate reynolds numbers. *J. Fluid Mech.*, 805:171–187, 2016.

Y. Mizuno and J. Jiménez. Wall turbulence without walls. *Journal of Fluid Mechanics*, 723:429–455, 2013. doi: 10.1017/jfm.2013.137.

J.-P. Mollicone, F. Battista, P. Gualtieri, and C. M. Casciola. Turbulence dynamics in separated flows: the generalised Kolmogorov equation for inhomogeneous anisotropic conditions. *J. Fluid Mech.*, 841:1012–1039, 2018.

A. S. Monin and A. M. Yaglom. *Statistical fluid mechanics: mechanics of turbulence*. The MIT press, Cambridge, Massachusetts, and London, England, 1975.

P. A. Monkewitz, K. A. Chauhan, and H. M. Nagib. Self-consistent high-reynolds-number asymptotics for zero-pressure-gradient turbulent boundary layers. *Physics of Fluids*, 19(11):115101, 2007. doi: 10.1063/1.2780196.

B. R. Morton. The generation and decay of vorticity. *Geophysical & Astrophysical Fluid Dynamics*, 28(3-4):277–308, 1984. doi: 10.1080/03091928408230368.

M. Naumov, M. Arsaev, Patrice Castonguay, J. Cohen, J. Demouth, Joe Eaton, S. Layton, N. Markovskiy, I. Z. Reguly, N. Sakharnykh, V. Sellappan, and R. Strzodka. Amgx: A library for gpu accelerated algebraic multigrid and preconditioned iterative methods. *SIAM Journal on Scientific Computing*, 37:S602–S626, 2015. doi: 10.1137/140980260.

A. Neri, T. Esposti Ongaro, M. de' Michieli Vitturi, and M. Cerminara. Multiphase Flow Modeling of Explosive Volcanic Eruptions. pages 243–281. 2022. doi: 10.1007/978-3-030-68578-2_10.

Q. Nie and S. Tanveer. A note on third–order structure functions in turbulence. *Proc. Royal Soc. London A.: Math. Phys. Eng. Sci.*, 455(1985): 1615–1635, 1999.

V. Nikora. Origin of the " $-1$" spectral law in wall-bounded turbulence. *Phys. Rev. Lett.*, 83:734–736, Jul 1999. doi: 10.1103/PhysRevLett.83.734.

S. Oliani, N. Casari, and M. Carnevale. Icsfoam: An openfoam library for implicit coupled simulations of high-speed flows. *Computer Physics Communications*, 286:108673, 2023. doi: 10.1016/j.cpc.2023.108673.

OpenFOAM. OpenFOAM project web page of the OpenCFD LTD, 2022a. URL `https://www.openfoam.com`.

OpenFOAM. OpenFOAM project web page of OpenFOAM Foundation, 2022b. URL `https://www.openfoam.org`.

P. Orlandi. *Fluid Flow Phenomena: A Numerical Toolkit*, volume 55. Springer, 2000.

R. L. Panton. Overview of the self-sustaining mechanisms of wall turbulence. *Progress in Aerospace Sciences*, 37(4):341–383, 2001.

A. E. Perry and M. S. Chong. On the mechanism of wall turbulence. *Journal of Fluid Mechanics*, 119:173–217, 1982. doi: 10.1017/S0022112082001311.

U. Piomelli, W. H. Cabot, P. Moin, and S. Lee. Subgrid-scale backscatter in turbulent and transitional flows. *Phys. Fluids A*, 3(7):1766–1771, 1991.

U. Piomelli, Y. Yu, and R. J. Adrian. Subgrid-scale energy transfer and near-wall turbulence structure. *Phys. Fluids*, 8(1):215–224, 1996.

S. Pirozzoli and F. Grasso. Direct numerical simulations of isotropic compressible turbulence: Influence of compressibility on dynamics and structures. *Phys. Fluids*, 16(12):4386, 2004. doi: 10.1063/1.1804553.

S. Pirozzoli, J. Romero, M. Fatica, R. Verzicco, and P. Orlandi. One-point statistics for turbulent pipe flow up to $Re_\tau \approx 6000$. *Journal of Fluid Mechanics*, 926:A28, 2021. doi: 10.1017/jfm.2021.727.

S. B. Pope. *Turbulent flows*. Cambridge university press, Cambridge, 2000.

F. A. Portela, G. Papadakis, and J. C. Vassilicos. The turbulence cascade in the near wake of a square prism. *J. Fluid Mech.*, 825:315–352, 2017.

L. Prandtl. *Bericht uber die entstehung der turbulenz*. Z. Angew. Math., 1925.

M. Rauter, L. Hoße, R. P. Mulligan, W. A. Take, and F. Løvholt. Numerical simulation of impulse wave generation by idealized landslides with openfoam. *Coastal Engineering*, 165:103815, 2021.

L.F. Richardson. *Weather prediction by numerical process*. Cambridge University Press, 1922.

F. Rincon. Anisotropy, inhomogeneity and inertial-range scalings in turbulent convection. *J. Fluid Mech.*, 563:43–69, 2006.

H. P. Robertson. The invariant theory of isotropic turbulence. In *Mathematical Proceedings of the Cambridge Philosophical Society*, volume 36, pages 209–223. Cambridge University Press, 1940.

S. K. Robinson. Coherent motions in the turbulent boundary layer. *Annual Review of Fluid Mechanics*, 23(Volume 23, 1991):601–639, 1991. doi: 10.1146/annurev.fl.23.010191.003125.

A. I. Ruban and K. N. Vonatsos. Discontinuous solutions of the boundary-layer equations. *Journal of Fluid Mechanics*, 614:407–424, 2008. doi: 10.1017/S0022112008003303.

R. Sakamoto, M. Kondo, K. Fujita, T. Ichimura, and K. Nakajima. The effectiveness of low-precision floating arithmetic on numerical codes: A case study on power consumption. In *Proceedings of the International Conference on High Performance Computing in Asia-Pacific Region*, HPCAsia2020, page 199–206, New York, NY, USA, 2020. Association for Computing Machinery. doi: 10.1145/3368474.3368492.

P. Schlatter and R. Örlü. Assessment of direct numerical simulation data of turbulent boundary layers. *Journal of Fluid Mechanics*, 659:116–126, 2010. doi: 10.1017/S0022112010003113.

P. Schlatter, Q. Li, G. Brethouwer, A. V. Johansson, and D. S. Henningson. Simulations of spatially evolving turbulent boundary layers up to $Re_\theta = 4300$. *International Journal of Heat and Fluid Flow*, 31(3):251–261, 2010. doi: 10.1016/j.ijheatfluidflow.2009.12.011.

H. Schlichting and J Kestin. *Fluid Flow Phenomena: A Numerical Toolkit*, volume 121. Springer, 1961.

J. Schumacher and K. R. Sreenivasan. Statistics and geometry of passive scalars in turbulence. *Physics of Fluids*, 17(12):125107, 2005. doi: 10.1063/1.2140024.

J. Schumacher, K. R. Sreenivasan, and P. K. Yeung. Very fine structures in scalar mixing. *Journal of Fluid Mechanics*, 531:113–122, 2005. doi: 10.1017/S0022112005004040.

P. N. Shankar and M. D. Deshpande. Fluid mechanics in the driven cavity. *Annual review of fluid mechanics*, 32(1):93–136, 2000.

T. S. Silva, M. Zecchetto, and C. B. da Silva. The scaling of the turbulent/non-turbulent interface at high reynolds numbers. *Journal of Fluid Mechanics*, 843:156–179, 2018. doi: 10.1017/jfm.2018.143.

A. J. Smits, B. J. McKeon, and I. Marusic. High–reynolds number wall turbulence. *Annual Review of Fluid Mechanics*, 43(Volume 43, 2011): 353–375, 2011. doi: 10.1146/annurev-fluid-122109-160753.

G. A. Sod. A survey of several finite difference methods for systems of non-linear hyperbolic conservation laws. *Journal of Computational Physics*, 27(1):1–31, 1978. ISSN 0021-9991. doi: 10.1016/0021-9991(78)90023-2.

K. R. Sreenivasan. The passive scalar spectrum and the obukhov–corrsin constant. *Physics of Fluids*, 8(1):189–196, 01 1996. doi: 10.1063/1.868826.

K. R. Sreenivasan. Turbulent mixing: A perspective. *Proceedings of the National Academy of Sciences*, 116(37):18175–18183, 2019. doi: 10.1073/pnas.1800463115.

K. R. Sreenivasan, R. Ramshankar, and C. Meneveau. Mixing, entrainment and fractal dimensions of surfaces in turbulent flows. *Proceedings of the Royal Society of London. A. Mathematical and Physical Sciences*, 421 (1860):79–108, 1989. doi: 10.1098/rspa.1989.0004.

S. Succi, G. Amati, M. Bernaschi, G. Falcucci, M. Lauricella, and A. Montessori. Towards exascale lattice boltzmann computing. *Computers & Fluids*, 181:107–115, 2019.

A. Supalov, A. Semin, M. Klemm, and C. Dahnken. *Optimizing HPC Applications with Intel Cluster Tools: Hunting Petaflops*. Apress, New York, 2014.

S.J. Terrington, K. Hourigan, and M.C. Thompson. The generation and diffusion of vorticity in three-dimensional flows: Lyman's flux. *Journal of Fluid Mechanics*, 915:A106, 2021. doi: 10.1017/jfm.2021.179.

S.J. Terrington, K. Hourigan, and M.C. Thompson. The lyman–huggins interpretation of enstrophy transport. *Journal of Fluid Mechanics*, 958: A30, 2023. doi: 10.1017/jfm.2023.95.

R. Togni, A. Cimarelli, and E. De Angelis. Physical and scale-by-scale analysis of Rayleigh–Bénard convection. *J. Fluid Mech.*, 782:380–404, 2015.

A. A. Townsend. The structure of the turbulent boundary layer. *Math. Proc. Camb. Philos. Soc.*, 47:375–95, 1951.

A. A. Townsend. Equilibrium layers and wall turbulence. *J. Fluid Mech*, 11:97–120, 1961.

A. A. Townsend. *The Structure of Turbulent Shear Flows*. Cambridge: Cambridge University Press. 2nd ed., 1976.

L.-P. Wang and M. R. Maxey. Settling velocity and concentration distribution of heavy particles in homogeneous isotropic turbulence. *J. Fluid Mech.*, 256(-1):27, 1993. doi: 10.1017/S0022112093002708.

W. Wang, C. Pan, and J. Wang. Energy transfer structures associated with large-scale motions in a turbulent boundary layer. *J. Fluid Mech.*, 906: A14, 2021.

T. Watanabe, Y. Sakai, K. Nagata, Y. Ito, and T. Hayase. Turbulent mixing of passive scalar near turbulent and non-turbulent interface in mixing layers. *Physics of Fluids*, 27(8):085109, 2015.

T. Watanabe, C. B. da Silva, and K. Nagata. Scale-by-scale kinetic energy budget near the turbulent/nonturbulent interface. *Phys. Rev. Fluids*, 5: 124610, 2020. doi: 10.1103/PhysRevFluids.5.124610.

J. Westerweel, C. Fukushima, J. M. Pedersen, and J. C. R. Hunt. Mechanics of the turbulent-nonturbulent interface of a jet. *Phys. Rev. Lett.*, 95: 174501, 2005.

J. Westerweel, C. Fukushima, J. M. Pedersen, and J. C. R. Hunt. Momentum and scalar transport at the turbulent/non-turbulent interface of a jet. *Journal of Fluid Mechanics*, 631:199–230, 2009. doi: 10.1017/S0022112009006600.

A. W. Woods. Turbulent Plumes in Nature. *Annual Review of Fluid Mechanics*, 42(1):391–412, 2010. doi: 10.1146/annurev-fluid-121108-145430.

J.Z. Wu and J.M. Wu. Interactions between a solid surface and a viscous compressible flow field. *Journal of Fluid Mechanics*, 254:183–211, 1993a. doi: 10.1017/S0022112093002083.

J.Z. Wu and J.M. Wu. Boundary vorticity dynamics since lighthill's 1963 article: Review and development. *Theoretical and Computational Fluid Dynamics*, 10(1-4):459–474, 1993b. doi: 10.1007/s001620050077.

J.Z. Wu and J.M. Wu. Vorticity dynamics on boundaries. volume 32 of *Advances in Applied Mechanics*, pages 119–275. Elsevier, 1996. doi: 10.1016/S0065-2156(08)70077-2.

H. Yao, J.-P. Mollicone, and G. Papadakis. Analysis of interscale energy transfer in a boundary layer undergoing bypass transition. *J. Fluid Mech.*, 941:A14, 2022.

A. Yoshizawa. Statistical theory for compressible turbulent shear flows, with the application to subgrid modeling. *The Physics of fluids*, 29(7):2152–2164, 1986.

S. Zampini, S. Bná, M. Valentini, and I. Spisso. GPU-accelerated OpenFOAM simulations using PETSc4FOAM. In *8th ESI-OpenFOAM conference*, October 2020.

M. Zecchetto and C. B. da Silva. Universality of small-scale motions within the turbulent/non-turbulent interface layer. *Journal of Fluid Mechanics*, 916:A9, 2021. doi: 10.1017/jfm.2021.168.

M. Zecchetto, R. P. Xavier, M. A. C. Teixeira, and C. B. da Silva. Generalized scaling laws for the irrotational motions bordering a turbulent region. *Phys. Rev. E*, 109:065107, 2024. doi: 10.1103/PhysRevE.109.065107.

X. Zhang, T. Watanabe, and K. Nagata. Turbulent/nonturbulent interfaces in high-resolution direct numerical simulation of temporally evolving compressible turbulent boundary layers. *Phys. Rev. Fluids*, 3:094605, Sep 2018. doi: 10.1103/PhysRevFluids.3.094605.

X. Zhang, T. Watanabe, and K. Nagata. Reynolds number dependence of the turbulent/non-turbulent interface in temporally developing turbulent boundary layers. *Journal of Fluid Mechanics*, 964:A8, 2023. doi: 10.1017/jfm.2023.329.

Y. Zhou and J. C. Vassilicos. Related self-similar statistics of the turbulent/non-turbulent interface and the turbulence dissipation. *Journal of Fluid Mechanics*, 821:440–457, 2017. doi: 10.1017/jfm.2017.262.

Y. Zhou and J. C. Vassilicos. Energy cascade at the turbulent/nonturbulent interface. *Phys. Rev. Fluids*, 5:064604, 2020. doi: 10.1103/PhysRevFluids.5.064604.

S. J. Zimmerman, R. A. Antonia, L. Djenidi, J. Philip, and J. C. Klewicki. Approach to the 4/3 law for turbulent pipe and channel flows examined through a reformulated scale-by-scale energy budget. *J. Fluid Mech.*, 931: A28, 2022.

M. Zounon, N. J. Higham, C. Lucas, and F. Tisseur. Performance impact of precision reduction in sparse linear systems solvers. *PeerJ Computer Science*, 8:e778, 2022. doi: 10.7717/peerj-cs.778.